

Multidisciplinary Imaging of Rock Properties in Carbonate Reservoirs for Flow-Unit Targeting

FINAL TECHNICAL REPORT

10/15/01 – 7/31/04

Stephen C. Ruppel, editor

Prepared for U.S. Department of Energy
Under Contract No. DE-FC26-01BC15351

Bureau of Economic Geology
Scott W. Tinker, Director
John A. and Katherine G. Jackson School of Geosciences
The University of Texas at Austin
Austin, TX 78713-8924

December 2004

Disclaimer

This report was prepared as an account of work sponsored by an agency of the United States Government. Neither the United States Government nor any agency thereof, nor any of their employees, makes any warranty, express or implied, or assumes any legal liability or responsibility for the accuracy, completeness, or usefulness of any information, apparatus, product, or process disclosed, or represents that its use would not infringe privately owned rights. Reference herein to any specific commercial product, process, or service by trade name, trademark, manufacturer, or otherwise does not necessarily constitute or imply its endorsement, recommendation, or favoring by the United States Government or any agency thereof. The views and opinions of authors expressed herein do not necessarily state or reflect those of the United States Government or any agency thereof.

Contents

| | |
|---|-------|
| Disclaimer | ii |
| | |
| Summary of Research Accomplishments | |
| <i>Stephen C. Ruppel</i> | |
| INTRODUCTION | xix |
| OVERVIEW OF PROJECT | xix |
| SUMMARY OF PROJECT ACCOMPLISHMENTS AND FINDINGS | xxii |
| Accomplishments..... | xxii |
| Data Collection and Interpretation..... | xxii |
| Stratigraphic Architecture..... | xxii |
| Petrophysical Modeling | xxiii |
| Interpretation of 3D Seismic Data | xxiii |
| Reservoir Modeling | xxiii |
| Flow Simulation..... | xxiv |
| Definition of Opportunities for Drilling and Recompletion | xxiv |
| Definition of Resource Volumetrics | xxiv |
| Technology Transfer..... | xxiv |
| Major Findings..... | xxv |
| Stratigraphic Architecture..... | xxv |
| Petrophysics | xxv |
| Reservoir Simulation | xxv |
| 3D Geophysics | xxvi |
| Porosity Characterization..... | xxvi |
| Architecture..... | xxvi |
| Reservoir Resources..... | xxvi |
| ACKNOWLEDGMENTS | xxvi |

Facies, Sequence Stratigraphy and Porosity Development in the Fullerton Clear Fork Reservoir

Stephen C. Ruppel and Rebecca H. Jones

ABSTRACT9

INTRODUCTION9

METHODS10

PREVIOUS WORK.....11

GEOLOGIC SETTING12

OUTCROP ANALOGS.....13

 Abo Facies, Cyclicality, and Sequence Architecture14

 Lower Clear Fork Facies, Cyclicality, and Sequence Architecture15

FULLERTON RESERVOIR FACIES AND STRATIGRAPHY16

 Facies and Depositional Setting.....17

 Peritidal Mudstone-Wackestone18

 Clay-rich Carbonate Mudstone19

 Exposed Tidal Flat19

 Peloid Wackestone.....20

 Peloid Packstone21

 Peloid Grain-dominated Packstone.....21

 Ooid-Peloid Grain-dominated Packstone-Grainstone.....22

 Fusulinid Wackestone-Packstone22

 Skeletal Wackestone-Packstone.....23

 Oncoid Wackestone-Packstone.....23

 Siltstone-Sandstone.....24

 Lithoclast Wackestone25

 Depositional Model.....25

 Sequence Stratigraphy27

 Abo Formation27

 Wichita Formation29

| | |
|--|-----------|
| Lower Clear Fork Formation | 31 |
| High-Frequency Sequence L 2.0..... | 31 |
| High-Frequency Sequence L 2.1..... | 31 |
| High-Frequency Sequence L 2.2..... | 33 |
| High-Frequency Sequence L 2.3..... | 34 |
| Tubb Formation | 35 |
| Cycle-Scale Stratigraphy | 35 |
| Wichita Cyclicity | 36 |
| Lower Clear Fork Cyclicity: HFS L 2.1 | 36 |
| Lower Clear Fork Cyclicity: HFS L 2.2 | 38 |
| Lower Clear Fork Cyclicity: HFS L 2.3 | 38 |
| MINERALOGY AND DIAGENESIS | 39 |
| Dolomite and Limestone Distribution | 39 |
| Stable Isotope Chemistry | 40 |
| Karst Development | 42 |
| Karst Fabrics | 42 |
| Causes and Timing of Karst..... | 44 |
| Impact of Karsting on Reservoir Quality..... | 45 |
| RESERVOIR IMAGING..... | 46 |
| Identifying Facies and Cyclicity from Borehole Image Logs..... | 46 |
| Imaging Stratigraphic Architecture and Reservoir Development from 3-D Seismic | 51 |
| Constraining Reservoir Architecture | 52 |
| Defining Reservoir Quality..... | 52 |
| RESERVOIR ARCHITECTURE..... | 54 |
| Cyclicity and Flow-Unit Definition | 54 |
| Lower Clear Fork Reservoir Architecture | 56 |
| Wichita Reservoir Architecture | 58 |
| Abo Reservoir Architecture | 59 |

| | |
|---------------------------------------|----|
| Reservoir Model..... | 60 |
| Porosity Distribution..... | 60 |
| Models for Porosity Development | 63 |
| SUMMARY | 65 |
| ACKNOWLEDGMENTS | 67 |
| REFERENCES | 68 |

Figures

| | |
|---|----|
| 1. Chart showing the Leonardian stratigraphic section in the Permian Basin including the Clear Fork Group and analogous units in New Mexico and in outcrop | 73 |
| 2. Regional map of the Permian Basin showing location of Fullerton field and analogous outcrops in the Sierra Diablo mountains..... | 73 |
| 3. Map of Fullerton Clear Fork field showing location of focused study areas, cores, and 3-D seismic data..... | 74 |
| 4. Type log of producing reservoir section at Fullerton Clear Fork field showing cyclicity and general facies patterns | 75 |
| 5. Structure of the Fullerton Clear Fork field | 76 |
| 6. Outcrop photographs showing Abo–Lower Clear Fork section equivalent to producing reservoir interval at Fullerton field | 77 |
| 7. Cross section depicting lateral changes in facies and cyclicity in Sierra Diablo outcrops partly equivalent to Lower Clear Fork (sequence L2) reservoir rocks at Fullerton field | 77 |
| 8. Cross section (A-A’) illustrating sequence stratigraphy and facies in the central part of the Clear Fork reservoir at Fullerton field based on cores | 78 |
| 9. 3-D seismic section from southern part of Fullerton field showing seismic definition of the Clear Fork reservoir section..... | 79 |
| 10. Core and thin-section photographs of typical Wichita tidal-flat facies | 80 |
| 11. Core and thin-section photographs of typical tidal-flat facies and shallow subtidal facies in the Wichita and Lower Clear Fork | 81 |
| 12. Core and thin-section photographs of typical peloid wackestone facies in the Lower Clear Fork..... | 82 |
| 13. Core and thin-section photomicrographs of mud-rich peloid packstone-wackestone | 83 |
| 14. Core and thin-section photomicrographs of peloid, grain-rich packstones and grainstones..... | 84 |

| | |
|---|-----|
| 15. Core and thin-section photomicrographs of Lower Clear Fork and Abo grainstones | 85 |
| 16. Core and thin-section photomicrographs of the fusulinid wackestone-packstone facies | 86 |
| 17. Core and thin-section photomicrographs of the oncoid, wackestone-packstone facies..... | 87 |
| 18. Depositional model for Permian shallow-water carbonate platforms in the Permian Basin | 88 |
| 19. Generalized sequence-stratigraphic model of the lower Leonardian succession at Fullerton field showing primary facies tracts and stratigraphic nomenclature..... | 88 |
| 20. Map of limestone abundance in the Wichita Formation | 89 |
| 21. Thickness of the Wichita Formation in the Fullerton field area | 90 |
| 22. Northwest-southeast cross section (B-B') across the Fullerton field area showing the sequence architecture and general facies development based on cored well control | 91 |
| 23. Map showing the distribution of limestone and dolostone in Lower Clear Fork HFS L 2.1 based on cores and wireline logs..... | 92 |
| 24. Map of the thickness of the Lower Clear Fork L 2.1 sequence at Fullerton field | 93 |
| 25. Map showing the distribution of limestone and dolostone in Lower Clear Fork HFS L 2.2 based on cores and wireline logs..... | 94 |
| 26. Map of the thickness of the Lower Clear Fork L 2.2 sequence at Fullerton field | 95 |
| 27. Facies stacking and cycle development in the fusulinid- and oncoid-rich, transgressive systems tract of Lower Clear Fork HFS L 2.1 | 96 |
| 28. Facies stacking and cycle development in the grain-rich, highstand systems tract of Lower Clear Fork HFS L 2.1 | 97 |
| 29. Facies stacking and cycle development in the grain-rich, late transgressive systems tract/early highstand systems tract of Lower Clear Fork HFS L 2.2 | 98 |
| 30. Facies stacking and cycle development in the nonreservoir Lower Clear Fork HFS L 2.3..... | 98 |
| 31. Core slab photos of polymict conglomerate in the Wichita Formation of probable karst origin..... | 99 |
| 32. Core slab box photo of breccias developed at the Abo/Wichita contact in FM-1 core | 100 |
| 33. Core slab photos of contact zone of Abo/Wichita | 101 |
| 34. Core slab photos of monomict breccias from the Wichita..... | 102 |
| 35. Image log and core photo images of laminated tidal-flat facies | 103 |
| 36. Image log and core photo images of fusulinid wackestone-packstone facies | 104 |

| | |
|--|-----|
| 37. Image log and core photo images of crossbedded grainstone..... | 105 |
| 38. Image log and core photo images of peloid wackestone-packstone facies..... | 106 |
| 39. Image log and core photo images of nodular peloid wackestone typical of the Lower Clear Fork HFS L 2.2 | 107 |
| 40. Image log and core photo images of “vuggy” fabric | 108 |
| 41. Image log and core photo images of polymict karst conglomerate | 109 |
| 42. 3-D seismic section from Fullerton field showing general continuity and isopachous nature of Lower Clear Fork and Wichita reservoir intervals | 110 |
| 43. Map of negative amplitude data extracted from Fullerton 3-D data..... | 111 |
| 44. Porosity development in HFS 2.1 | 112 |
| 45. Comparison of core-defined facies and cyclicity with porosity logs in tidal-flat-capped cycles of HFS L 2.3. FCU 6122..... | 113 |
| 46. Comparison of core-defined facies and cyclicity with porosity logs in subtidal cycles of HFS L 2.2. FCU 6122 | 114 |
| 47. Schematic depiction of reservoir framework used for model construction at the Fullerton Clear Fork reservoir | 115 |
| 48. Map of total phi in the Wichita | 116 |
| 49. Maps of porosity distribution in the lower and upper parts of the lower Wichita (Sequence L 1) | 117 |
| 50. Maps of porosity distribution in the lower and upper parts of the upper Wichita (Sequence L 2.0) | 118 |
| 51. Maps of porosity distribution in the Lower Clear Fork | 119 |
| 52. Models of porosity formation in the upper Wichita and the Lower Clear Fork (L2 sequence)..... | 120 |

**Integration of Rock Fabric, Petrophysical Class, and Stratigraphy for Petrophysical
Quantification of Sequence-Stratigraphic Framework, Fullerton Clear Fork Field, Texas**

Rebecca H. Jones and F. Jerry Lucia

| | |
|--------------------|-----|
| ABSTRACT..... | 125 |
| INTRODUCTION | 126 |
| METHODS | 128 |
| RESULTS | 129 |

| | |
|---|-----|
| Abo Formation | 130 |
| Wichita Formation | 130 |
| Lower Clear Fork Formation | 131 |
| Lower Clear Fork L2.0 | 131 |
| Lower Clear Fork L2.1 | 132 |
| Lower Clear Fork L2.2 | 133 |
| Lower Clear Fork L2.3 | 134 |
| DISCUSSION..... | 135 |
| Limitations Due to Petrophysical Data Distribution..... | 135 |
| CONCLUSIONS..... | 137 |
| ACKNOWLEDGMENTS | 138 |
| REFERENCES | 139 |
| APPENDIX I: ROCK-FABRIC INSTRUCTIONS: Classifying Carbonate Pore Space from Thin Sections..... | 157 |

Figures

| | |
|--|-----|
| 1. Diagram showing fabrics composing petrophysical classes 1, 2, and 3 and a cross plot showing interparticle porosity vs. permeability, petrophysical class fields, and associated transforms | 141 |
| 2. Photomicrographs of class 1 fabrics observed in this study | 142 |
| 3. Photomicrographs of class 2 fabrics observed in this study | 143 |
| 4. Photomicrographs of class 3 fabrics observed in this study | 144 |
| 5. Location and boundaries of Fullerton field, Andrews County, Texas..... | 145 |
| 6. Type log showing nomenclature used in this study and general vertical stacking of petrophysical classes..... | 146 |
| 7. Porosity-permeability plot of old Abo interval core analysis from wells throughout the field with core described in this study | 147 |
| 8. Photomicrographs of tidal-flat, class 3 fabrics observed in this study | 148 |

| | |
|---|-----|
| 9. Distribution of limestone, dolostone, and petrophysical classes in the Wichita..... | 149 |
| 10. Wichita facies core analysis porosity-permeability plot and petrophysical class 3 transform used to calculate permeability | 150 |
| 11. Plot and histogram for Lower Clear Fork L2.1 subtidal unit high-resolution samples from wells FCU 5927 and 6429..... | 151 |
| 12. Porosity-permeability plot of core analysis from wells with core displaying dominantly class 1 fabrics in the subtidal portion of high-frequency sequence L2.1..... | 152 |
| 13. Regions of different petrophysical classes and mineralogy in the subtidal portion of HFS L2.1 | 153 |
| 14. Regions of different petrophysical classes and mineralogy in HFS L2.2..... | 154 |
| 15. Porosity-permeability plot of Lower Clear Fork L2.2 showing that most samples plot in the class 1 field and photomicrograph example of poikilotopic anhydrite in a class 2 medium-crystalline dolostone | 155 |
| 16. Typical preexisting core analysis data vs. core analysis data resulting from unbiased sampling and careful cleaning of plugs | 156 |

Development of the Wireline-Log Database and Determination of Porosity Using Wireline Logs

Jeffrey A. Kane and James W. Jennings, Jr.

| | |
|--|-----|
| ABSTRACT..... | 167 |
| INTRODUCTION | 167 |
| OVERVIEW OF WIRELINE-LOG DATABASE..... | 168 |
| DATABASE ASSEMBLY PROCEDURES | 170 |
| QUALITY CONTROL..... | 170 |
| POROSITY-LOG NORMALIZATION..... | 172 |
| MOVING AVERAGE COMPUTATION..... | 175 |
| CORE CALIBRATION..... | 175 |
| CONCLUSIONS..... | 177 |
| REFERENCE..... | 178 |

Figures

1. Map showing 316 wells with Sidewall neutron logs (SNP) used to calculate porosity for Fullerton Clear Fork field.....179

2. Map showing 437 wells with compensated neutron logs (NPHI) used to calculate porosity for Fullerton Clear Fork field180

3. Map showing all 733 wells used in porosity calculation for Fullerton Clear Fork field181

4. An example of the Gaussian weighting function using various scale factors182

5. Examples of average SNP porosity areally averaged with different scale factors183

6. Plot of layer averaged core porosity (y-axis) as a function of layer averaged normalized compensated neutron porosity (x-axis) showing the calibration line for dolomites.....184

7. Plot of layer averaged core porosity (y-axis) as a function of layer averaged normalized sidewall neutron porosity (x-axis) showing the calibration line for dolomites185

8. Plot of core porosity (y-axis) as a function of normalized compensated neutron porosity (x-axis) showing the calibration line for limestone186

9. Plot of core porosity (y-axis) as a function of normalized sidewall neutron porosity (x-axis) showing the calibration line for limestone187

Calculations of Permeability and Initial Water Saturations from Wireline Logs

F. Jerry Lucia and Jeffrey A. Kane

ABSTRACT.....193

PERMEABILITY CALCULATIONS FROM WIRELINE LOGS194

ESTIMATION OF ORIGINAL WATER SATURATION.....196

COMPARISON OF MODEL S_w WITH ARCHIE S_w 200

DISCUSSION.....201

REFERENCES202

Tables

1. Thomeer and core analysis values for class 2 samples203

2. Thomeer and core analysis values for class 3 samples203

3. List of electrical measurements from the Lower Clear Fork.....204

Figures

| | |
|---|-----|
| 1. Map showing location of calibration wells in the simulation area | 205 |
| 2. Cross plots showing development of permeability transforms for dolostone in sequence L2.2 | 206 |
| 3. Comparison of core and calculated permeability in sequence L2.2 | 207 |
| 4. Porosity-permeability cross plot for moldic limestone in sequence L2.2..... | 208 |
| 5. Comparison of core and calculated permeability in sequence L2.1 | 208 |
| 6. Comparison of core and calculated permeability in the Wichita peritidal facies | 209 |
| 7. An example of fitting Thomeer parameters to a class 2 medium crystalline dolostone | 210 |
| 8. Cross plots of Thomeer G factor and porosity for class 3 fabrics and class 2 fabrics showing little relationship between porosity and G factor | 211 |
| 9. Cross plots of extrapolated entry pressures and porosity for class 3 fabrics and class 2 fabrics showing statistical relationships between entry pressure and porosity | 212 |
| 10. Comparison of class 3 curves with curves calculated using the Thomeer model..... | 213 |
| 11. Comparison of Thomeer class 3 capillary pressure model with generic class 3 model | 214 |
| 12. Comparison of class 2 curves with curves calculated using the Thomeer model..... | 215 |
| 13. Comparison of Thomeer class 2 capillary pressure model with generic class 2 model | 216 |
| 14. Capillary pressure curves from moldic limestone | 217 |
| 15. Comparison of capillary pressure curves from class 1 anhydritic dolostones with curves using the generic class 1 model | 217 |
| 16. Example of model and Archie S_w from well FCU 5727..... | 218 |

Reservoir Modeling and Simulation of Fullerton Clear Fork Field, Andrews County, Texas

Fred Wang and F. Jerry Lucia

| | |
|-----------------------------|-----|
| ABSTRACT | 225 |
| INTRODUCTION | 226 |
| 3-D RESERVOIR MODELING..... | 227 |
| Stratigraphic Modeling..... | 227 |

| | |
|--|-----|
| Upscaling | 229 |
| Petrophysical Modeling | 230 |
| Porosity Distribution..... | 231 |
| Permeability (k) and kh Distribution | 232 |
| S_w and $S_o\phi h$ Distribution..... | 234 |
| VOLUMETRICS | 235 |
| Sensitivity Analysis | 236 |
| Search Radius in Mapping..... | 236 |
| Grid Resolution..... | 237 |
| Water-Oil Contact..... | 237 |
| Porosity Cutoffs | 238 |
| Water Saturation Cutoffs | 239 |
| Permeability Cutoffs | 239 |
| Compound Effects of Vertical Resolution and Cutoff Values..... | 240 |
| PRODUCTION-TREND ANALYSIS | 242 |
| FLOW-UNIT MODEL AND RESERVOIR SIMULATION | 243 |
| Flow-unit Model | 243 |
| Flow Simulation..... | 249 |
| Sensitivity Study | 250 |
| SUMMARY | 253 |
| REFERENCES | 256 |
| APPENDIX A: UPSCALING | 295 |

Tables

| | |
|---|-----|
| 1. Geologic and reservoir parameters of Fullerton Clear Fork Unit..... | 257 |
| 2. Geologic frameworks used in 3-D reservoir models..... | 258 |
| 3. Dimensions of 3-D field models..... | 259 |
| 4. Formation volume factor, oil-gas ratio, and WOC used in OOIP estimates | 259 |
| 5. Effect of variable search radius on OOIP estimates of FCU | 259 |
| 6. Effect of water-oil contact on OOIP estimates of FCU..... | 260 |
| 7. Effect of cutoff values on OOIP..... | 260 |
| 8. Effect of cutoff values on OOIP in FCU for WOC at -3940 ft summarized by ExxonMobil zonation | 261 |
| 9. Effect of cutoff values on OOIP in Fullerton field for WOC at -3940 ft summarized by ExxonMobil zonation | 261 |
| 10. Effect of cutoff values on OOIP in FCU for WOC at -3940 ft summarized by high frequency cycles | 262 |
| 11. Effect of cutoff values on OOIP in Fullerton Clear Fork field for WOC at -3940 ft summarized by high frequency cycles | 263 |
| 12. Effect of vertical resolution on OOIP..... | 264 |
| 13. Summary of parameters affecting OOIP | 264 |
| 14. Dimensions of 3-D Model of Initial 2,000 acre model (simulation area) | 264 |

Figures

| | |
|--|-----|
| 1. Production history of waterflooding in Fullerton Clear Fork Unit..... | 265 |
| 2. Workflow of 3-D modeling..... | 265 |
| 3. Geologic framework used to build 3-D models of Fullerton Clear Fork field..... | 266 |
| 4. Effect of search radius of 2,500 ft and 5,000 ft on porosity mapping..... | 266 |
| 5. Porosity distribution in fine-grid model | 267 |
| 6. Average porosity distribution in Zone 1, Zone 2, Wichita, Zone 3, Zone 3B, and Zone 4 | 267 |

| | |
|---|-----|
| 7. ϕ_h distribution in reservoir Zone 1 (Lower Clear Fork HFS 2.2) by cycle | 268 |
| 8. Porosity distribution in reservoir Zone 1 (Lower Clear Fork. HFS 2.2) by cycle..... | 268 |
| 9. Porosity distribution in reservoir Zone 2 (Lower Clear Fork. HFS 2.1) by cycle..... | 268 |
| 10. Porosity distribution in Zones Wichita, 3, 3B, and 4, in the Wichita Formation | 269 |
| 11. Permeability distribution in 3-D model..... | 269 |
| 12. Permeability distribution in reservoir zones 1, 2, Wichita, 3, 3B, and 4..... | 270 |
| 13. Kh distributions in Zone 1, Zone 2, Wichita, Zone 3, Zone 3B, and Zone 4..... | 270 |
| 14. Results of petrophysical analysis in FCU 5927, 1284, and 1435..... | 271 |
| 15. Water saturation distribution in 3-D model with oil-water contact at -3,940 ft | 271 |
| 16. Water saturation distributions in Zone 1, Zone 2, Wichita, Zone 3, Zone 3B, and Zone 4..... | 272 |
| 17. Hydrocarbon volume distributions in Zone 1, Zone 2, Wichita, Zone 3, Zone 3B, and Zone 4 | 272 |
| 18. Hydrocarbon volume distribution in six reservoir zones | 273 |
| 19. Hydrocarbon volume (distribution in Zone 1 (Lower Clear Fork HFS L 2.2))..... | 273 |
| 20. Hydrocarbon volume distribution in Zone 2 (Lower Clear Fork HFS 2 L 2.1) | 273 |
| 21. Hydrocarbon volume distribution in the Wichita Formation | 274 |
| 22. Formation volume factor and oil-gas ratio of two types of crude in FCU | 274 |
| 23. Effect of water-oil contact on vertical coverage in Zone 3B, Zone 4, and Zone 5 (Abo) | 275 |
| 24. Effect of water-oil contact on areal coverage in Zone 3, Zone 3B, Zone 4, and Zone 5 (Abo) | 275 |
| 25. Effect of water-oil contacts on OOIP estimate..... | 276 |
| 26. Effects of porosity cutoffs of 3%, 5% and 10%, and permeability cutoffs of 0.1, 0.5, and 1 mD on volumetrics | 276 |
| 27. Effects of cutoff values on OOIP estimate porosity, water saturation, and permeability | 277 |

| | |
|--|-----|
| 28. Relationship between permeability and porosity cutoff values. A specific permeability cutoff represents rock-fabric-dependent porosity cutoffs..... | 277 |
| 29. Effects of porosity cutoffs and grid vertical resolution on volumetrics, 3%, 5%, and 10% on fine-grid model, and 3%, 5% and 10% on cycle-based model | 278 |
| 30. Effects of porosity cutoffs and grid vertical resolution on volumetrics, 0.1, 0.5, and 1.0 mD on fine-grid model, and 0.1, 0.5, and 1.0 mD on cycle-based model..... | 279 |
| 31. Changes in OOIP between high-resolution and cycle-based models with respect to porosity cutoff, water saturation cutoff, and permeability cutoff values | 279 |
| 32. Production data and trends in primary and waterflooding | 280 |
| 33. Initial 3:1 line-drive waterflooding pattern | 280 |
| 34. Porosity and $S_{o\phi h}$ in Zone 2, Wichita, and Zone 3, overlaid with production trends | 281 |
| 35. Water-injection patterns in the initial reservoir model area in 2001 | 281 |
| 36. Production data and trends in primary and waterflooding in simulation area..... | 282 |
| 37. Lawyer Canyon cycle 1 flow-layer model | 283 |
| 38. Average porosity for various rock fabrics in sequences L2.1 and L2.2 | 284 |
| 39. Flow layers and cycles in sequence L2.1 | 285 |
| 40. Flow layers in sequence L2.2 | 286 |
| 41. Flow layers in the Wichita..... | 287 |
| 42. Lower Clear Fork and Wichita flow layers in cored wells of simulation area illustrating the use of porosity to build a flow model..... | 288 |
| 43. Porosity distribution in the simulation area..... | 288 |
| 44. Permeability distribution in the simulation area..... | 289 |
| 45. Water saturation distribution in the simulation area..... | 289 |
| 46. Porosity and $S_{o\phi h}$ trends in the simulation area..... | 290 |
| 47. Porosity distribution in simulation model | 290 |
| 48. Initial oil saturation in simulation model..... | 291 |
| 49. Simulated oil saturation in 1960, 1970, 1980, and 2002, simulation area | 291 |

| | |
|---|-----|
| 50. Simulated oil saturation in 2002, in Zone 1 | 292 |
| 51. Simulated oil saturation in 2002, in selected model layer slices of the Lower Clear Fork HFS L2.1 (reservoir Zone 2) | 292 |
| 52. Simulated oil saturation in 2002, in upper model layers of the Wichita | 293 |
| 53. Simulated oil saturation in 2002, in model layers of Wichita reservoir Zone 3B | 293 |
| 54. Corey correlations for relative permeability..... | 293 |
| 55. Effect of relative permeability on simulated oil rate, water rate, pressure, and oil recovery | 294 |
| 56. Effect of permeability multiplication on simulated water production..... | 294 |

Construction and Analysis of 3-D Seismic Porosity Inversion Models

Hongliu Zeng

| | |
|--|-----|
| ABSTRACT | 309 |
| INTRODUCTION | 309 |
| METHODOLOGY | 311 |
| DATA AND TIE..... | 313 |
| IMPROVEMENT OF SEISMIC DATA INTERPRETABILITY | 314 |
| 90°-phasing | 314 |
| High-frequency Signal Enhancement | 315 |
| WELL-BASED AI MODEL..... | 316 |
| MODEL-BASED SEISMIC INVERSION..... | 317 |
| Why Model-based? | 317 |
| How Well and Seismic Data Are Integrated | 319 |
| PROGRESSIVE INVERSION | 320 |
| Problems in Model-based Inversion | 320 |
| Solution..... | 322 |
| Blind Test..... | 324 |
| CONCLUSIONS..... | 325 |
| REFERENCES | 326 |

Figures

| | |
|--|-----|
| 1. Location of well and seismic data in Fullerton field, Andrews County, Texas, and 3-D seismic inversion area around Phase 2 area..... | 327 |
| 2. Synthetic seismogram of lower Clear Fork and Wichita and surrounding formation in well Cal/Mon 1 across 2-D seismic line 0123 | 328 |
| 3. Linear relationship between AI and log porosity of carbonate rocks in the lower Clear Fork and Wichita, Fullerton field, Andrews County, Texas | 328 |
| 4. A 0°-phase seismic section (trace 2382) in the 3-D survey area showing poor tie between high-porosity/low-AI units and amplitude/polarity and difficulty in picking high-frequency sequence boundaries..... | 329 |
| 5. A 90°-phase seismic section (trace 2382) in the 3-D survey area showing improved tie between high-porosity/low-AI units and amplitude/polarity | 330 |
| 6. A high-frequency-enhanced (spectral-balanced) version of Figure 5 showing improvement in seismic resolution | 331 |
| 7. Wireline log-based AI models for reservoir characterization and seismic inversion..... | 332 |
| 8. Procedure of a model-based inversion..... | 333 |
| 9. Model based inversion from background model, blocky model, smoothed log model, and log model..... | 334 |
| 10. Differences of AI inversion corresponding to different initial model inputs | 335 |
| 11. Initial models for progressive inversion | 336 |
| 12. Progressive inversion..... | 337 |
| 13. Differences of stratigraphic framework used in initial model construction | 338 |
| 14. Difference in AI estimation through progressive inversion..... | 339 |
| 15. Blind test showing value and limit of progressive inversion (example 1)..... | 340 |
| 16. Blind test showing value and limit of progressive inversion (example 2)..... | 341 |
| 17. Blind test showing value and limit of progressive inversion (example 3)..... | 342 |

Summary of Research Accomplishments

Stephen C. Ruppel

INTRODUCTION

Despite declining production rates, existing reservoirs in the United States contain large quantities of remaining oil and gas that constitute a huge target for improved diagnosis and imaging of reservoir properties. The resource target is especially large in carbonate reservoirs, where conventional data and methodologies are normally insufficient to resolve critical scales of reservoir heterogeneity. The objectives of the research described in this report were to develop and test such methodologies for improved imaging, measurement, modeling, and prediction of reservoir properties in carbonate hydrocarbon reservoirs. The focus of the study is the Permian-age Fullerton Clear Fork reservoir of the Permian Basin of West Texas. This reservoir is an especially appropriate choice considering (a) the Permian Basin is the largest oil-bearing basin in the United States, and (b) as a play, Clear Fork reservoirs have exhibited the lowest recovery efficiencies of all carbonate reservoirs in the Permian Basin.

OVERVIEW OF PROJECT

The elements of the research carried out on Fullerton field are presented in six chapters. In the first chapter, Ruppel and Jones describe the depositional facies and sequence stratigraphy of the reservoir based on integrated study of outcrops and subsurface data from Fullerton field. They also describe the key steps in using outcrop- and core-based facies-stacking patterns and wireline log response relationships to develop a robust reservoir framework having sufficient resolution and accuracy to form the basis for reservoir modeling and simulation. In addition, they document the products of diagenesis and using three-dimensional relationships of geochemical

and porosity distribution data suggest models for dolomitization and porosity development. Finally, they describe the use of two modern techniques for improved reservoir imaging: (1) borehole imaging logs for improved definition of facies distribution and cycles, and (2) 3D seismic data, to better define the distribution of reservoir porosity.

Jones and Lucia document the nature and distribution of reservoir rock fabrics in the field. A knowledge of rock fabrics, groupings of rock types with similar petrophysical relationships, is critical for accurate modeling of permeability and saturation. Jones and Lucia show that each of the three major stratigraphic units in the reservoir contains distinct rock-fabric types that belong to three petrophysical classes. These classes vary substantially in petrophysical character. For example, rocks from Petrophysical Class 3 exhibit two orders of magnitude lower permeability for a given porosity value than do rocks of Petrophysical Class 1. Rock-fabric types and petrophysical classes were mapped throughout the field, thus providing an improved basis for calculating permeability and original oil saturation in the reservoir.

Kane and Jennings describe the procedures and methods used to develop a robust calculation of well-log porosity for each well in the field. This work includes the process used to assemble and quality-check the original wireline log data to create a workable database and the methodology used to create a final calculated porosity. Because calculations of reservoir porosity and saturation are based on porosity, this process is fundamental to accurate reservoir characterization and modeling.

Lucia and Kane discuss the approaches used to calculate permeability from wireline logs. As the chapter documents, accurate permeability calculation depends on two primary factors: porosity and rock fabric. As such, their work is built on the procedures documented by Kane and Jennings for porosity determination and interpretation and distribution of rock-fabric properties

described by Jones and Lucia. Lucia and Kane also describe the approaches used to calculate initial water saturation using capillary pressure and rock-fabric data. This approach, which is commonly the best way to define original saturations in carbonates, is the key to calculating original oil in place and remaining oil resource.

Wang and Lucia present the methods and results of reservoir modeling and simulation activities undertaken during the project. The primary goal of these studies was to better define the distribution of original and remaining oil resource in the reservoir. Key parts of this effort were (1) the construction of a 2,000-acre flow-unit model and a flow simulation sensitivity study of the model, and (2) the construction of a 35,000-acre full-field, static reservoir model. The simulation study produced an excellent image of waterflood performance and provides fundamental guidelines to predicting the distribution of remaining oil resources across the entire reservoir. The full-field model, which is based on integration of research completed on stratigraphy, reservoir architecture, porosity distribution, rock fabrics, and petrophysics, provides an excellent modern image of the 3D distribution of reservoir properties that will serve as a future guide to model effective recovery operations in the field. Calculations of original resource volume based on this new model will also provide a needed economic incentive for these plans.

Finally, Zeng reports on research carried out to recondition 3D seismic data and to develop an integrated wireline log–3D seismic inversion model of porosity. The data reconditioning work demonstrates how relatively simple procedures can lead to greatly improved seismic resolution, in turn leading to better definition of reservoir architecture and porosity distribution. Zeng also describes procedures used to construct a robust wireline inversion model of porosity for the reservoir. The results of this work illustrate the tremendous untapped potential

that exists for utilizing 3D seismic data in improved imaging of reservoir properties in incompletely exploited carbonate reservoirs.

Collectively, the work carried out on this project represents one of the most comprehensive studies of a major carbonate reservoir ever published. As such it contains lessons of value for geoscientists, engineers, and managers—not just of Fullerton field, but of all carbonate platform reservoirs in the United States.

SUMMARY OF PROJECT ACCOMPLISHMENTS AND FINDINGS

Accomplishments

Data Collection and Interpretation

- Completed quality control procedures on 18,000 logs
- Assembled core, log, and interpretive data into integrated database (Landmark OpenWorks) including
 - 1,500 well files (23,000 log files)
 - 30 core analysis files
 - Core facies descriptions (27 wells)
 - Stratigraphic tops (~45,000)
 - Calculated porosity (733 wells)
 - Calculated permeability (733 wells)
 - Calculated saturation (733 wells)
 - Flow-unit tops (265 wells)

Stratigraphic Architecture

- Integrated subsurface data with outcrop models
- Defined facies and cyclicity in 27 cored wells (14,383 ft of core)
- Correlated cycles and tops in more than 850 wells (~ 45,000 tops)
- Described more than 1,700 thin sections (19 wells)
- Integrated core and log data with 3D and 2D seismic data

- Defined sequence and cycle stratigraphic framework for entire field
- Mapped structure and thickness of major sequences
- Demonstrated key architectural differences within reservoir
- Demonstrated presence of karst features
- Developed model for porosity development
- Utilized 3D seismic inversion for improved imaging of porosity distribution

Petrophysical Modeling

- Obtained new conventional core analyses (705)
- Obtained new special core analyses (30)
- Obtained new thin sections for rock-fabric analysis (950)
- Analyzed core data from 63 cored wells
- Calculated log porosity for 733 wells
- Created and applied porosity log normalization procedures for entire field
- Defined and mapped petrophysical classes throughout field
- Defined porosity-permeability transforms for all petrophysical classes
- Constructed original saturation model from capillary pressure and petrophysical class data

Interpretation of 3D Seismic Data

- Reprocessed 3D and 2D data for phase character and resolution
- Integrated 222 miles of 2D and 33,000 acres of 3D data with wireline and core data
- Mapped time structure and isochrons of major horizons
- Correlated major sequences in 3D and 2D data volumes
- Defined relationships between deep structure and reservoir quality
- Employed amplitude extractions for reservoir-quality mapping
- Demonstrated robust relationship between impedance and porosity
- Constructed wireline log/3D seismic inversion model

Reservoir Modeling

- Constructed 2,000-acre flow model comprising 39 flow units, 85 wells, 265 layers, and 3.2 million cells (150 ft × 150 ft × 3–5 ft cell size)

- Constructed 35,000-acre, full-field reservoir model comprising 35 stratigraphic surfaces/cycles, 730 wells, 380 layers, and 42 million cells (150 ft × 150 ft × 10–15 ft cell size)

Flow Simulation

- Performed history match and sensitivity study for 1,600-acre flow model
- Completed flow simulation in Eclipse
- Used simulation results to characterize sweep characteristics of field

Definition of Opportunities for Drilling and Recompletion

- Completed 3D amplitude analysis and provided recommendations on eight proposed infill locations
- Completed production streamline analysis of 15 proposed infill wells and recommended alternatives
- Reservoir models and simulation results provide invaluable guides to additional drilling and recompletion opportunities
- Completed study is being used as basis for designing and implementing a tertiary, CO₂ flood program

Definition of Resource Volumetrics

- Calculated volumetrics for entire reservoir using multiple petrophysical and stratigraphic scenarios:
 - Two oil-water contact cases
 - Four porosity-cutoff cases
 - Three permeability-cutoff cases
 - Four water saturation-cutoff cases

Technology Transfer

- Met regularly with operator staff to maintain focus of research.
- Responded to interim operator requests for data and interpretations
- Provided analysis of infill drilling locations
- Delivered final digital data sets to operator
 - OpenWorks database
 - GoCad and RMS reservoir models

- Eclipse simulation
- Interpreted 2D seismic data set
- Delivered final report
 - Written report with illustrations
 - Digital data files
- Created computer animation of project for Web-site distribution
- Presented oral papers and posters on major aspects of the study
- Disseminated final report and other project products through Web site and CD's

Major Findings

Stratigraphic Architecture

- 3D seismic data can provide inaccurate images of reservoir architecture
- Porosity development is a function of early diagenesis
- Borehole image logs provide almost as much facies and cyclicity data as cores
- Cycle-scale architecture is not definable in peritidal facies tracts
- Karst features are widespread but discontinuous
- Porosity development is partially controlled by deep structure
- Permeability is a function of facies, but porosity is a function of diagenesis

Petrophysics

- Peritidal successions (Wichita Formation) contain high-porosity, low-permeability rock fabrics
- Subtidal successions (Lower Clear Fork and Abo Formations) contain higher permeability rock fabrics than peritidal successions
- Peritidal limestones are flow baffles; subtidal limestones are high-flow zones
- Petrophysical classes and rock fabrics can be mapped throughout the field using stratigraphic framework
- A single porosity cutoff or permeability transform is inadequate
- Permeability models must consider rock-fabric distribution

Reservoir Simulation

- Provides key insights to sweep and remaining oil distribution for *much* of the reservoir

- Dominant issues controlling sweep efficiency are rock fabric, continuity, and completion coverage

3D Geophysics

Porosity Characterization

- Strong relationship between amplitude and porosity
- Progressive 3D inversion provides excellent constraints on interwell and extrawell porosity distribution
- Simple amplitude extractions provide robust qualitative guide to interwell and extrawell porosity distribution

Architecture

- Seismic response controlled by porosity (facies and diagenesis)
- Seismic architecture must be vetted by geological models
- Continuing and differential fault motion through Permian

Reservoir Resources

- Total hydrocarbon pore volume is conservatively estimated at 1.58 billion barrels
- Peritidal facies (Wichita Formation) contains 55 percent of the total pore volume but only 43 percent of the original hydrocarbon pore volume
- Resource estimations provide critical data for developing economically sound plans for further exploitation of the reservoir

ACKNOWLEDGMENTS

The research documented here was co-funded by the U.S. Department of Energy, The University of Texas System, ExxonMobil Corporation, and the Reservoir Characterization Research Laboratory of the Bureau of Economic Geology. I thank John Stout, Jeff Simmons, and Craig Kemp of Occidental Permian for providing important data for the study and for providing thoughtful insights into project planning. Steve Krohn and Amy Powell helped develop and promote the project within ExxonMobil. Terry Anthony and David Smith, also with ExxonMobil, provided ongoing operator liaison, data exchange, and input on project activities

and deliverables. Tim Hunt, University of Texas System West Texas Operations Office, helped with technology transfer activities and gathered new GPS location data for wells in the field. Dan Ferguson served as contract officer for DOE. The Bureau acknowledges support of this research by Landmark Graphics Corporation via the Landmark University Grant Program.

FACIES, SEQUENCE STRATIGRAPHY AND POROSITY DEVELOPMENT IN THE
FULLERTON CLEAR FORK RESERVOIR

Stephen C. Ruppel and Rebecca H. Jones

Bureau of Economic Geology
Scott W. Tinker, Director
John A. and Katherine G. Jackson School of Geosciences
The University of Texas at Austin
Austin, Texas 78713-8924

| | |
|---|----|
| ABSTRACT..... | 9 |
| INTRODUCTION | 9 |
| METHODS | 10 |
| PREVIOUS WORK..... | 11 |
| GEOLOGIC SETTING | 12 |
| OUTCROP ANALOGS..... | 13 |
| Abo Facies, Cyclicality, and Sequence Architecture | 14 |
| Lower Clear Fork Facies, Cyclicality, and Sequence Architecture | 15 |
| FULLERTON RESERVOIR FACIES AND STRATIGRAPHY | 16 |
| Facies and Depositional Setting..... | 17 |
| Peritidal Mudstone-Wackestone | 18 |
| Clay-rich Carbonate Mudstone | 19 |
| Exposed Tidal Flat | 19 |
| Peloid Wackestone..... | 20 |
| Peloid Packstone | 21 |
| Peloid Grain-dominated Packstone..... | 21 |
| Ooid-Peloid Grain-dominated Packstone-Grainstone..... | 22 |
| Fusulinid Wackestone-Packstone | 22 |
| Skeletal Wackestone-Packstone..... | 23 |
| Oncoid Wackestone-Packstone..... | 23 |
| Siltstone-Sandstone..... | 24 |
| Lithoclast Wackestone | 25 |
| Depositional Model..... | 25 |
| Sequence Stratigraphy | 27 |
| Abo Formation | 27 |

| | |
|---|----|
| Wichita Formation | 29 |
| Lower Clear Fork Formation | 31 |
| High-Frequency Sequence L 2.0..... | 31 |
| High-Frequency Sequence L 2.1..... | 31 |
| High-Frequency Sequence L 2.2..... | 33 |
| High-Frequency Sequence L 2.3..... | 34 |
| Tubb Formation | 35 |
| Cycle-Scale Stratigraphy | 35 |
| Wichita Cyclicity | 36 |
| Lower Clear Fork Cyclicity: HFS L 2.1 | 36 |
| Lower Clear Fork Cyclicity: HFS L 2.2 | 38 |
| Lower Clear Fork Cyclicity: HFS L 2.3 | 38 |
| MINERALOGY AND DIAGENESIS | 39 |
| Dolomite and Limestone Distribution | 39 |
| Stable Isotope Chemistry | 40 |
| Karst Development | 42 |
| Karst Fabrics | 42 |
| Causes and Timing of Karst..... | 44 |
| Impact of Karsting on Reservoir Quality..... | 45 |
| RESERVOIR IMAGING..... | 46 |
| Identifying Facies and Cyclicity from Borehole Image Logs..... | 46 |
| Imaging Stratigraphic Architecture and Reservoir Development from 3D Seismic | 51 |
| Constraining Reservoir Architecture | 52 |
| Defining Reservoir Quality..... | 52 |

| | |
|---|----|
| RESERVOIR ARCHITECTURE..... | 54 |
| Cyclicality and Flow-Unit Definition..... | 54 |
| Lower Clear Fork Reservoir Architecture | 56 |
| Wichita Reservoir Architecture | 58 |
| Abo Reservoir Architecture | 59 |
| Reservoir Model..... | 60 |
| Porosity Distribution..... | 60 |
| Models for Porosity Development | 63 |
| SUMMARY | 65 |
| ACKNOWLEDGMENTS | 67 |
| REFERENCES | 68 |

Figures

| | |
|---|----|
| 1. Chart showing the Leonardian stratigraphic section in the Permian Basin including the Clear Fork Group and analogous units in New Mexico and in outcrop | 73 |
| 2. Regional map of the Permian Basin showing location of Fullerton field and analogous outcrops in the Sierra Diablo mountains..... | 73 |
| 3. Map of Fullerton Clear Fork field showing location of focused study areas, cores, and 3-D seismic data..... | 74 |
| 4. Type log of producing reservoir section at Fullerton Clear Fork field showing cyclicality and general facies patterns | 75 |
| 5. Structure of the Fullerton Clear Fork field | 76 |
| 6. Outcrop photographs showing Abo–Lower Clear Fork section equivalent to producing reservoir interval at Fullerton field | 77 |
| 7. Cross section depicting lateral changes in facies and cyclicality in Sierra Diablo outcrops partly equivalent to Lower Clear Fork (sequence L2) reservoir rocks at Fullerton field | 77 |
| 8. Cross section (A-A’) illustrating sequence stratigraphy and facies in the central part of the Clear Fork reservoir at Fullerton field based on cores | 78 |

| | |
|---|----|
| 9. 3-D seismic section from southern part of Fullerton field showing seismic definition of the Clear Fork reservoir section..... | 79 |
| 10. Core and thin-section photographs of typical Wichita tidal-flat facies | 80 |
| 11. Core and thin-section photographs of typical tidal-flat facies and shallow subtidal facies in the Wichita and Lower Clear Fork | 81 |
| 12. Core and thin-section photographs of typical peloid wackestone facies in the Lower Clear Fork..... | 82 |
| 13. Core and thin-section photomicrographs of mud-rich peloid packstone-wackestone | 83 |
| 14. Core and thin-section photomicrographs of peloid, grain-rich packstones and grainstones..... | 84 |
| 15. Core and thin-section photomicrographs of Lower Clear Fork and Abo grainstones | 85 |
| 16. Core and thin-section photomicrographs of the fusulinid wackestone-packstone facies | 86 |
| 17. Core and thin-section photomicrographs of the oncoïd, wackestone-packstone facies..... | 87 |
| 18. Depositional model for Permian shallow-water carbonate platforms in the Permian Basin | 88 |
| 19. Generalized sequence-stratigraphic model of the lower Leonardian succession at Fullerton field showing primary facies tracts and stratigraphic nomenclature..... | 88 |
| 20. Map of limestone abundance in the Wichita Formation | 89 |
| 21. Thickness of the Wichita Formation in the Fullerton field area | 90 |
| 22. Northwest-southeast cross section (B-B') across the Fullerton field area showing the sequence architecture and general facies development based on cored well control | 91 |
| 23. Map showing the distribution of limestone and dolostone in Lower Clear Fork HFS L 2.1 based on cores and wireline logs..... | 92 |
| 24. Map of the thickness of the Lower Clear Fork L 2.1 sequence at Fullerton field | 93 |
| 25. Map showing the distribution of limestone and dolostone in Lower Clear Fork HFS L 2.2 based on cores and wireline logs..... | 94 |
| 26. Map of the thickness of the Lower Clear Fork L 2.2 sequence at Fullerton field | 95 |
| 27. Facies stacking and cycle development in the fusulinid- and oncoïd-rich, transgressive systems tract of Lower Clear Fork HFS L 2.1 | 96 |

| | |
|---|-----|
| 28. Facies stacking and cycle development in the grain-rich, highstand systems tract of Lower Clear Fork HFS L 2.1 | 97 |
| 29. Facies stacking and cycle development in the grain-rich, late transgressive systems tract/early highstand systems tract of Lower Clear Fork HFS L 2.2 | 98 |
| 30. Facies stacking and cycle development in the nonreservoir Lower Clear Fork HFS L 2.3..... | 98 |
| 31. Core slab photos of polymict conglomerate in the Wichita Formation of probable karst origin..... | 99 |
| 32. Core slab box photo of breccias developed at the Abo/Wichita contact in FM-1 core | 100 |
| 33. Core slab photos of contact zone of Abo/Wichita | 101 |
| 34. Core slab photos of monomict breccias from the Wichita..... | 102 |
| 35. Image log and core photo images of laminated tidal-flat facies | 103 |
| 36. Image log and core photo images of fusulinid wackestone-packstone facies | 104 |
| 37. Image log and core photo images of crossbedded grainstone..... | 105 |
| 38. Image log and core photo images of peloid wackestone-packstone facies..... | 106 |
| 39. Image log and core photo images of nodular peloid wackestone typical of the Lower Clear Fork HFS L 2.2 | 107 |
| 40. Image log and core photo images of “vuggy” fabric | 108 |
| 41. Image log and core photo images of polymict karst conglomerate | 109 |
| 42. 3-D seismic section from Fullerton field showing general continuity and isopachous nature of Lower Clear Fork and Wichita reservoir intervals | 110 |
| 43. Map of negative amplitude data extracted from Fullerton 3-D data..... | 111 |
| 44. Porosity development in HFS 2.1 | 112 |
| 45. Comparison of core-defined facies and cyclicity with porosity logs in tidal-flat-capped cycles of HFS L 2.3. FCU 6122..... | 113 |
| 46. Comparison of core-defined facies and cyclicity with porosity logs in subtidal cycles of HFS L 2.2. FCU 6122 | 114 |
| 47. Schematic depiction of reservoir framework used for model construction at the Fullerton Clear Fork reservoir | 115 |

| | |
|---|-----|
| 48. Map of total porosity in the Wichita | 115 |
| 49. Maps of porosity distribution in the lower and upper parts of the lower Wichita (Sequence L 1) | 116 |
| 50. Maps of porosity distribution in the lower and upper parts of the upper Wichita (Sequence L 2.0) | 117 |
| 51. Maps of porosity distribution in the Lower Clear Fork | 118 |
| 52. Models of porosity formation in the upper Wichita and the Lower Clear Fork (L2 sequence)..... | 119 |

Facies, Sequence Stratigraphy and Porosity Development in the Fullerton Clear Fork Reservoir

Stephen C. Ruppel and Rebecca H. Jones

ABSTRACT

The analysis of reservoir sequence and cycle stratigraphy, of depositional and diagenetic facies, and of the interrelationships between these attributes and reservoir properties is key to the construction of an accurate reservoir framework needed for reservoir modeling and improved imaging of remaining hydrocarbons. In the Fullerton Clear Fork field, fundamental steps in the process included (1) creating and applying an analogous outcrop depositional model, (2) describing and interpreting subsurface core and log data in terms of this initial model, (3) defining the sequence-stratigraphic architecture of the reservoir section, and (4) developing a cycle-based reservoir framework. Key data in this analysis included 29 cores totaling 14,383 ft, more than 1,700 rock thin sections, nearly 800 wells, 3-D and 2-D seismic, a borehole image log, and applicable outcrop models.

INTRODUCTION

The Clear Fork Group (fig. 1) in the Permian Basin comprises a thick (as much as 2,500 ft; 800 m) succession of dominantly shallow-water-platform carbonates that were deposited across West Texas and New Mexico during the Early Permian (Leonardian). Reservoirs developed in these carbonates (fig. 2) have accounted for more than 3.2 billion barrels of oil production (Dutton and others, 2004)—more than 10 percent of the total recovered from the Permian Basin to date. Despite this substantial production, estimates of original oil in place (OOIP) indicate that, overall, Leonardian reservoirs contained more than 14.5 billion barrels of

oil at discovery. Recovery efficiency is thus only about 22 percent, considerably below the 32-percent average for carbonate reservoirs in the Permian Basin (Tyler and Banta, 1989; Holtz and Garrett, 1990). Recovery from the shallow-water-platform reservoirs of the Clear Fork Group has been even less efficient. Holtz and others (1992) estimated a recovery efficiency of only 18 percent of OOIP for these reservoirs.

To recover the remaining oil in Clear Fork reservoirs, operators must turn to increasingly sophisticated recovery technologies: e.g., waterflooding, gas injection, horizontal wells, etc. To effectively deploy these technologies, however, it is critical that an accurate reservoir framework first be constructed to form the basis for modeling and interpreting past, present, and future recovery operations.

This report details the approaches used to develop such a framework in the Fullerton Clear Fork field in West Texas. Like many mature Clear Fork reservoirs in the Permian Basin, Fullerton field has undergone a major decline in oil production rate and a major increase in water production rates for several years. Current production from the field stands at about 310 million bbl, representing only about 25 percent of the calculated OOIP. An understanding of the depositional and diagenetic facies, the cycle and sequence stratigraphy, and the architecture of these stratigraphic elements is the crucial first step to determining the probable oil distribution at discovery and defining the best strategies for recovering the sizeable remaining oil volume.

METHODS

The focus of this study of the Fullerton reservoir is the Fullerton Clear Fork Unit, a unitized production area in Fullerton field operated by ExxonMobil Corporation. Data and interpretations presented in this report were derived from investigation of 29 cores totaling 14,383 ft, the examination of more than 1,700 rock thin sections, and the correlation of

approximately 45,000 stratigraphic tops in nearly 800 wells. The basic procedure followed in this study to develop a full-field sequence-stratigraphic model and reservoir framework is as follows: (1) identify depositional facies and vertical facies-stacking patterns and cycles in cores, (2) calibrate facies and cycle patterns to wireline logs, (3) construct 2D cross sections of core/log data sections, (4) define 2D cycle and sequence stratigraphy from core/log sections, and (5) extrapolate 2D cycle and sequence correlations into 3-D space by correlating all available well logs. Stratigraphic sequences were tied into available 3-D seismic data to check their accuracy and geometry. Conventional core analysis data were available for all cores; these data were used to determine relationships between facies, cyclicity, and porosity and permeability development. Figure 3 depicts the distribution of cores and 3-D seismic data in the field.

PREVIOUS WORK

Mazzullo (1982) and Mazzullo and Reid (1989) presented overviews of lower Leonardian stratigraphy and depositional systems in the Midland Basin. Presley and McGillis (1982; see also Presley, 1987) documented the highly cyclic, predominantly evaporitic facies of the upper Leonardian Glorieta and Upper Clear Fork units in the Texas Panhandle. Ruppel (1992; 2002) described the facies, cyclicity, and diagenesis in the Glorieta and Upper Clear Fork at Monahans Clear Fork field on the Central Basin Platform and postulated that reservoir development was caused by cyclic deposition and diagenesis driven by episodic sea-level rise and fall. Atchley and others (1999) described Clear Fork facies at Robertson field at the north end of the Central Basin Platform and proposed a similar model for structural control over facies deposition and reservoir development. Ruppel and others (2000) described outcrop equivalents of the producing subsurface Clear Fork reservoirs from outcrops in the Sierra Diablo mountains of West Texas. Kerans and others (2000) documented the depositional setting, facies, and

architecture of the Abo from outcrops in the Sierra Diablo (fig. 2) and showed that karsting has had a major effect on both the Abo and the overlying Lower Clear Fork succession.

GEOLOGIC SETTING

The Fullerton Clear Fork field is the largest of a large number of fields developed in the Leonardian Series on the Central Basin Platform of the Permian Basin (fig. 2). In some parts of the Basin, the Leonardian is productive from all of its component stratigraphic units (fig. 1). The productive reservoir section at Fullerton, however, is essentially restricted to the Lower Clear Fork, Wichita, and Abo stratigraphic units (fig. 4); very minor production has also been reported from the Upper Clear Fork section. By far the bulk of the oil production has come from the lower two-thirds of the Lower Clear Fork and the Wichita sections of the reservoir. Even where oil saturated, the Abo has proven difficult to exploit in part owing to its active water drive (as opposed to the pressure depletion drive that characterizes the overlying parts of the reservoir) and the fact that it is at or near the oil-water contact throughout most of the field.

Regionally, the Leonardian is dominated by shallow-water-platform carbonates. Each of the component stratigraphic units contains updip peritidal tidal-flat carbonates and downdip subtidal carbonates. Mineralogy in each is dominated by dolomite and anhydrite. Calcite, in the form of limestone, is relatively uncommon; however, where present it is most common in the lower part of the Leonardian and in the distal, downdip sections (Ruppel, 2002). The reservoir section at Fullerton is generally consistent with this regional pattern, but it does contain a higher volume of limestone than most other Leonardian platform reservoir successions in the Basin.

Structurally, Fullerton field is developed over a large compound structural high (fig. 5) that reflects deep-seated faulting and differential uplift of the area that began in the Pennsylvanian (Jones and Ruppel, 2004). Deeper oil production comes from block-faulted

Silurian (Wristen Group) carbonates in the southern and central parts of the fields. The Clear Fork reservoir seal is provided by evaporite-rich carbonates in the Lower Clear Fork, Tubb, Upper Clear Fork, and Glorieta.

The reservoir is currently drilled to well spacings of 40 to 10 acres and is under active waterflood. The greatest well density is in the northern part of the field (mostly 20- and 10-acre well spacings); poorer well control exists in the southern half of the field. In general, these closely spaced wells provide good control for definition of stratigraphic horizons and reservoir attributes. In many parts of the field, especially along the western edge of the field and in the southern half of the field wells are represented only by poor-quality (old gamma-ray/neutron) logs and cannot be correlated or interpreted with any precision.

OUTCROP ANALOGS

Studies of analogous reservoir outcrops in the Sierra Diablo in Hudspeth and Culberson Counties (fig. 2), Texas, provide important insights into the geological controls on reservoir development in the Fullerton reservoir and on the reservoir architecture. The Leonardian of the Sierra Diablo contains direct analogs of all major reservoir intervals at Fullerton field, including the shallow-water-platform carbonates of the Lower Clear Fork Group (Fitchen and others, 1995; Ruppel and others, 2000) and Wichita units, and the karsted, platform-margin subtidal carbonates of the Abo (Fitchen and others, 1995; Kerans and others, 2000). The overall Leonardian stratigraphic section and its component sequences are thinner in the Sierra Diablos than in the subsurface of the Permian Basin. This seems most likely due to a more dominant control of local tectonics in the outcrop area during the Leonardian (e.g., King, 1942). However, styles of depositional architecture and facies development are very representative of subsurface

succession and thus form excellent, if not essential, models for interpreting sparser subsurface data sets. Key observations established from these outcrops are described below.

Abo Facies, Cyclicity, and Sequence Architecture

Integrated studies of outcrops and subsurface data sets indicate that the Abo represents the basal depositional sequence (sequence L1) of the Leonardian (Fitchen and others, 1995). Studies of Abo outcrops in the Sierra Diablo (Fitchen and others, 1995 ; Kerans and others, 2000) demonstrate three important aspects of this succession in the Permian Basin: (1) it consists of dominantly open-marine, outer platform facies, (2) it displays clinoformal architecture, and (3) it is overprinted by karst features (sinkholes, caves, cave fill, and collapse features). The dominance of clinoformal, outer ramp, fusulinid-crinoid packstones and wackestones and less common ramp-crest, ooid-peloid, grain-rich packstones and grainstones in the Abo contrasts with the flat-lying, alternating tidal-flat and shallow subtidal wackestone-packstone successions of the Wichita and Lower Clear Fork. The top-lapping clinoforms of the Abo document rapid basinward progradation, a forced regression probably caused by a rapid fall in sea level. Karsting in the Abo, although initiated at the exposed top of the Abo during sea-level fall, is manifested downsection in the Abo by caves and sinkholes and upsection in the overlying Lower Clear Fork as collapse features. Where karsting and associated thickness variations are developed, largely in platform-marginal settings, the contact between the Abo and Lower Clear Fork is a relatively sharp and undulating, unconformable surface. Updip, karsting is less apparent and the contact less pronounced.

Lower Clear Fork Facies, Cyclicity, and Sequence Architecture

The outcropping Lower Clear Fork succession in the Sierra Diablo represents a single depositional sequence (L2). Key elements of this succession are (1) basal backstepping tidal-flat deposits that locally fill relief on the underlying, karsted Abo surface (fig. 6), (2) an updip succession of amalgamated tidal-flat facies, (3) a cyclic, downdip succession of alternating tidal-flat and midramp, subtidal facies, and (4) an overall backstepping (upward-deepening) trend (fig. 7).

The Lower Clear Fork outcrop succession records the gradual flooding of the previously exposed Abo platform and a continued, although punctuated, increase in accommodation and water depth. Downdip Lower Clear Fork deposits are characterized by alternating peritidal, tidal-flat deposits and subtidal, skeletal wackestones and packstones that document cyclic rise and fall of sea level at the high-frequency sequence and cycle scale. These cycles, which average about 20 ft in thickness, display consistent patterns of facies stacking (cycle-base skeletal wackestones and overlying peloidal grain-rich packstones) and appear to be widely continuous (Ruppel and others, 2000). Recent studies undertaken in the course of this project reveal that these shallow subtidal platform rocks pass downdip into clinoformal fusulinid-crinoid wackestones and packstones of the outer ramp/slope within less than 2 mi basinward. Updip, in the platform interior (landward), the Lower Clear Fork is characterized by amalgamated, peritidal tidal-flat deposits (fig. 7). These updip tidal flats are analogous to the Wichita of the subsurface. The absence of shallow-water highstand deposits at the top of the Lower Clear Fork suggests a rapid, perhaps forced, regression followed by exposure and possible erosion at the top of the L2 sequence.

Lower Clear Fork outcrops in the Sierra Diablo also provide important insights into the cycle architecture of analogous subsurface reservoir sections like that at Fullerton. In tidal-flat-capped successions, and less commonly in subtidal successions, 3- to 6-ft-thick (1- to 2-m-thick) cycles are definable in vertical sections but, because of poor outcrop continuity, are not readily correlatable. However, subtidal cycle bundles, which average 15 to 30 ft (5 to 9 m) in thickness, can be correlated at typical interwell distances. These bundles typically consist of upward-shallowing successions that have skeletal wackestones at their bases and peloid-oid packstones at their tops (fig. 7).

FULLERTON RESERVOIR FACIES AND STRATIGRAPHY

The productive reservoir section at Fullerton field includes parts of the Abo, Wichita, and Lower Clear Fork Formations (fig. 4). Like many stratigraphic names used in the subsurface, each of these units is commonly considered to display both regional time equivalency and facies constancy across the region. In other words, each is considered to be both a rock-stratigraphic and a time-stratigraphic unit. In fact, these names are best considered rock-stratigraphic terms (essentially facies) at the formation level of nomenclature. To place these units in their proper perspective, however, it is best to consider both facies and time interrelationships. In this report we treat these named stratigraphic units (i.e., formations) as facies or rock-stratigraphic units but place them in an interpreted sequence-stratigraphic (i.e., time-stratigraphic) framework that has been developed from previous studies (e.g., Fitchen and others, 1995; Kerans and others, 2000; Ruppel and others, 2000). In this framework, the Abo and part of the Wichita Formation are time-equivalent facies of the earliest composite (third-order) depositional sequence of the Leonardian (sequence L1). Sequence L 2 comprises part of the Wichita Formation (updip peritidal deposits) and the Lower Clear Fork Formation (downdip, dominantly subtidal deposits).

The L 3 sequence contains siliciclastics of the Tubb Formation and carbonates of the part of the overlying Upper Clear Fork (fig. 4). Stratigraphic data at Fullerton field are consistent with this interpretation of time and rock interrelationships.

Correlations of usable wireline log suites (about 750) show that across most of the area of the Fullerton Clear Fork Unit (figs. 3, 5), stratigraphic units are relatively isopachous (fig. 8). This is consistent with the depositional setting of the field area on the Central Basin Platform, a broad, flat carbonate platform not unlike the modern-day Bahamas platform.

The same generally isopachous nature of the Wichita and Lower Clear Fork shows up in 3-D and 2-D seismic data. These data, however, show that the Wichita and Abo vary considerably in thickness across the field. Wichita deposits thin and Abo deposits thicken to the east and southeast (fig. 9). Synthesis of core, wireline, and seismic data indicates that this reciprocal thickness relationship is the result of facies change, i.e., the Wichita represents the updip, shallower water (inner platform) equivalent of the distal, deeper water (outer platform to slope) Abo. Support for this conclusion will be presented in subsequent sections.

Facies and Depositional Setting

The facies encountered at Fullerton field are typical of those observed throughout most carbonate platform successions of Leonardian and early Guadalupian age in the Permian Basin. The characteristics of these and similar facies have been documented by many authors, including Bebout and others (1987), Ruppel and Cander (1988a, 1988b), Garber and Harris (1990), Longacre (1990), Kerans and others (1994; see also Kerans and Fitchen, 1995; Kerans and Kempter, 2002), and Ruppel and Bebout (2001). Leonardian facies successions have been documented both in outcrop (Ruppel and others, 2000) and in the subsurface (Ruppel (2002).

The facies groupings defined in this study and presented below were defined with three goals in mind: (1) to document the characteristics of distinct depositional settings, (2) to document widespread and potentially correlatable sediment packages, and (3) to create a sound geological basis for assessing relationships between rock textures and fabrics and petrophysics. In many ways, it is the last of these goals that is most important, for it provides the foundation for reservoir modeling. However, as a result of this, facies characteristics used for subdivision are dominantly small-scale matrix properties, e.g., grain size and shape, grain type. Larger scale features such as fractures, anhydrite nodules, and evidence of burrowing, although noted, are not used for facies subdivision.

Twelve facies can be at least locally identified in the Fullerton reservoir succession. Most of these are intergradational with one or more others. In many cases, their distinction is somewhat subjective, based on differences in grain preservation, diagenesis, grain size, etc. Most can be found in any part of the reservoir succession.

Peritidal Mudstone-Wackestone

These rocks are most abundant in the Wichita but are also locally common in the Lower Clear Fork. They are massive to parallel-laminated mud-rich rocks that only rarely contain any grains other than a few peloids (fig. 10. a, b). They are most typically associated with the exposed tidal-flat facies and the clay-rich carbonate mudstone facies and are assumed to represent peritidal deposition on a very low energy tidal flat. They are dominantly dolomitized. Where dolomite, they may display very high porosities (as much as 15 percent). Because this porosity is due to intercrystalline pores within fine crystalline dolomite, however, the permeability is generally low. Where limestone, they invariably exhibit very low porosity

(typically less than 2 percent) and permeability. Gamma-ray signature is medium to high and highly variable in these rocks owing to the local presence of clay minerals.

Clay-rich Carbonate Mudstone

These rocks are found intimately associated with rocks of the Peritidal mudstone-wackestone facies in the Wichita. They are typically dark gray to nearly black and 1 to 8 cm in thickness (fig. 10, c). Where cyclic upward-shallowing successions can be identified, these deposits are found at or near cycle tops in both the Lower Clear Fork and the Wichita. Although they are probably contributors to the high gamma-ray response observed in the Wichita and in Lower Clear Fork peritidal intervals, because of their thinness, they cannot be discretely defined by logs and therefore are not correlatable. Their color and clay content and lack of apparent lateral continuity suggest that they were formed as local organic-rich ponds or stagnant pools on the tidal flat. They may act as local baffles to reservoir fluid flow but are probably very discontinuous laterally.

Exposed Tidal Flat

These deposits show obvious evidence of exposure such as fenestral pores, pisolites, mudcracks, insect burrows, sheet cracks, tepee structures, and cyanobacterial or microbial laminations (fig. 11). They are locally common in both the Lower Clear Fork and the Wichita. In the Lower Clear Fork, they define cycle tops; in the Wichita, their relative sea-level significance is less apparent. Their sedimentary structures demonstrate, however, that they were formed during at least local sea-level fall and exposure. Porosity is locally very high (at least 30 percent) and is associated with a combination of fenestral pores and intercrystalline and interparticle pores. Permeability is lower than in grain-dominated subtidal rocks but can be significant where high porosities are present. Like the peritidal mudstone-wackestone facies, these rocks typically

display somewhat elevated and variable gamma-ray response. This can sometimes be used to distinguish these rocks from overlying and underlying subtidal facies.

Peloid Wackestone

This grain-poor facies differs from the rocks of the Peritidal mudstone-wackestone facies in its association and sedimentary structures. The rocks are invariably associated with other, demonstrably subtidal, facies; they are burrowed; and they locally contain skeletal debris (fig. 11 c). These features suggest they were deposited in low-energy subtidal settings. Dominant grains (usually 80 to 150 μm in diameter) are probably fecal pellets created by infaunal burrowers. The absence of skeletal allochems supports a low-energy, perhaps restricted, setting.

Anhydrite nodules are locally common in these rocks, probably reflecting the postdepositional entry of sulfate-bearing diagenetic fluids into permeability pathways created by burrowers. In many cases, anhydrite nodules occupy solution-widened vertical burrow pathways that are surrounded by alteration halos (fig. 12). These halos (which have been reported from most Permian platform carbonate successions) commonly display a more grain-rich texture, higher porosity and permeability, and a depleted oxygen isotope signature (Major and others, 1990; Ruppel and Bebout, 2002). At Fullerton, they are most commonly developed in HFS L 2.2. This stratigraphic position (in the late highstand of the L2 composite sequence) is analogous in terms of accommodation to similar features documented from the younger Grayburg Formation at (Ruppel and Bebout, 2001), suggesting that these features are an expected and perhaps predictable feature of late highstand sedimentation on Permian shallow-water-carbonate platforms.

Peloid Packstone

The distinction between these rocks and those assigned to the Peloid wackestone facies is usually based on apparent peloid abundance and can be subjective. As with the Peloid wackestone facies, peloids are mostly fecal pellets created by burrowing infauna, although skeletal debris (chiefly mollusk fragments) are locally common. It should be noted that the preservation of these pellets is largely a function of diagenesis, both early and late. Nearly all of the low-energy mud-dominated facies in the Permian contain obvious pellets indicating that burrowers were ubiquitous in these deposits. There is a complete gradation in texture between pelleted mudstones and peloid packstones. Differences in texture are probably most commonly due to differences in early diagenesis. Pellets that were early lithified and stabilized are more likely to be preserved. Thus, peloid (i.e., pellet) packstones are sediments that underwent significant amounts of early diagenesis, whereas peloid wackestones and pelleted mudstones underwent relatively little. The textural significance of these pelleted facies is thus more diagenetic than depositional. Accordingly, apparent variations in peloid abundance in these mud-dominated facies packstones, wackestones, and mudstones is not necessarily an indication of differing depositional environment or fluctuations in wave energy. Rather, they may be predominantly due to local changes in rates and effects of early diagenesis. Porosity in these rocks is usually associated with intercrystalline pores and rare skeletal moldic pores (fig. 13).

Peloid Grain-dominated Packstone

Unlike mud-rich peloid facies discussed above, grain-dominated (or grain-rich) peloid packstones commonly display evidence of possible wave-related transport. These rocks are typically well sorted and contain interparticle pores that are either open or filled with cements (fig. 14). The interparticle pores indicate that these peloids acted as true grains rather than

pelleted mud, in contrast with the intercrystalline and moldic pores that typify mud-dominated facies. It should be noted, however, that in some instances the grain-dominated texture is associated with vertical burrows and probably owes its origin to burrow-related diagenesis. For the most part, this facies is restricted to the subtidal legs of Lower Clear Fork depositional sequences. These rocks are among the highest quality reservoir facies in the field. Highest porosity and permeability are encountered in peloid grain-dominated packstone limestones (as much as 20 percent porosity), although dolostones also exhibit good porosity and permeability.

Ooid-Peloid Grain-dominated Packstone-Grainstone

These rocks differ from the peloid grain-dominated packstone facies, with which they are often closely associated, in having recognizable ooids (as much as 250 μm in diameter) in addition to pervasive pellets (fig. 15). Skeletal grains in the form of fusulinids, mollusks, and crinoids are also common. In most cases, these deposits, which are restricted to subtidal sections of the Lower Clear Fork, are also well sorted, possibly due to wave action. Grainstones, although relatively rare, display excellent size sorting and in some cases possess inclined or cross laminations (fig. 15a). These rocks, which occur as both dolostone and limestone, represent the highest energy facies in the reservoir succession and in many cases display the best porosity and permeability. Pores are dominantly interparticle, but moldic pores are very abundant, especially in limestone-dominated intervals.

Fusulinid Wackestone-Packstone

Fusulinid-bearing rocks are found in all three formations (Abo, Wichita, and Lower Clear Fork), although they are very limited in the Wichita. In all occurrences they are most commonly dolomitized. The fusulinids that dominate this facies can constitute as much as 40 percent of the rock (fig. 16). Fusulinids are preserved either as open or anhydrite-filled molds or as well-

preserved fossil tests. In the Lower Clear Fork and Wichita, they are associated with abundant peloids (probably pellets). In the Abo, they commonly co-occur with crinoids, and less commonly with brachiopods. Fusulinids are thought to have occupied water depths of 30 m or more and here represent the deepest water facies observed at Fullerton field. Accordingly, their presence is an indicator of platform flooding and relative sea-level rise, making them key indicator facies of cycle and sequence boundaries.

Skeletal Wackestone-Packstone

Typically these rocks contain small volumes of skeletal debris (most commonly mollusks fragments but also including crinoids and less common ostracodes) and the ubiquitous peloids. They are gradational into peloid wackestones and packstones. Evidence of burrowing is common. The dominance of mollusks and the essential absence of more normal marine organisms in these rocks suggests they were deposited in an inner platform setting. Typically they exhibit low porosity; pore space is created by skeletal molds and intercrystalline pores.

Oncoid Wackestone-Packstone

Oncoids (or oncolites) are large microbial-coated grains (fig. 17) formed under conditions of continuous wave agitation in shallow water. They are abundant at the base of the Lower Clear Fork throughout the entire field area. Invariably they are associated with fusulinids and other faunas indicative of open-marine deposition. This association and their stratigraphic position immediately above the top of the tidal-flat-dominated Wichita indicates that they represent marine flooding of the platform during sea-level rise (transgression). In some downdip some wells (e.g., the Amoco FM-1 well; fig. 3), they are present at many intervals in the Lower Clear Fork. Overall, they are most abundant at cycle bases. Their distribution suggests that they document relatively high energy conditions developed during platform flooding. Like the

fusulinid facies, the oncoïd wackestone-packstone facies is a marker facies indicative of transgression or platform deepening (i.e., sea-level rise).

Siltstone-Sandstone

Quartz silt- and sand-bearing rocks are common only at the top of the Lower Clear Fork and in the overlying Tubb Formation. Because the quartz is associated with potassium- and thorium-rich clay minerals, its presence in the Lower Clear Fork and Tubb is well defined by high CGR (corrected gamma ray) wireline log response (figs. 4 and 8). Their size (fine sand to coarse silt) and shape (generally subangular) suggests these sediments were originally windblown. This indicates that most of the quartz in the section was delivered to the area during sea-level lowstands when the platform was emergent. Quartz silt/sand occurs in two scenarios: (1) in peritidal tidal-flat facies and (2) in reworked subtidal facies. The former are probably formed as small volumes of silt, sand, and clay are blown onto intermittently exposed, slowly accumulating tidal flats and admixed with peritidal carbonate sediment. The presence of potassium and thorium in these clastics produces the increased gamma-ray response that is associated with many tidal-flat deposits in the Clear Fork and facilitates recognition of these cycle-capping deposits in these sediments (Ruppel, 2002). Most of the occurrences of silt, sand, and clay in the Lower Clear Fork at Fullerton are of this type.

Subtidal silt, sand, and clay deposits are most common in the Tubb. These rocks were formed first by large-volume eolian deposition during extended sea-level lowstand and carbonate nondeposition, then reworked during the ensuing sea-level rise and marine flooding of the platform. These deposits are generally richer in clastic content, are intermixed with carbonate mud, and show evidence of subtidal conditions (e.g., burrows, stratification). Although these

rocks may locally exhibit some minor porosity, they do not appear to display any significant reservoir permeability.

Lithoclast Wackestone

Thin intervals (usually less than 1 ft) containing scattered lithoclasts are locally encountered at the contacts between transgressive marine facies and underlying tidal-flat deposits or other facies showing evidence of subaerial exposure (fig. 11c). Clasts are variable in composition but most commonly consist of fragments or intraclasts derived from the underlying bed. Clasts typically are 1 cm in width or less. Although volumetrically minor, these rocks are an important indicator facies of lithification due to exposure or nondeposition and subsequent sea-level rise and thus of cycle boundaries.

Depositional Model

The relative distribution of the facies described above can best be understood when considered in light of a conceptual geological model. Figure 10 portrays idealized three-dimensional relationships among major facies types and depositional environments typical of most middle Permian (Leonardian and Guadalupian) platform carbonate successions in the Permian Basin. It should be understood that this model reflects only the relative interrelationships among facies tracts. The actual position of individual facies tracts at a given point in time is a function of many factors, including accommodation, rates and magnitude of sea-level rise, rising versus falling sea-level trends, climate, tectonics, etc. However, during normal relative rises in sea level facies tracts normally step landward, whereas during falls they step basinward. Exceptions to this general pattern are common. For example, ramp-crest facies may be much better developed during sea-level highstand and fall than during transgression and rise. The basal Leonardian (L1) depositional sequence at Fullerton, for example, appears to be

dominated by an updip inner ramp succession (Wichita) and a downdip outer platform succession (Abo) with a very poorly developed middle-ramp to ramp-crest facies tract. Nevertheless, the vertical successions (facies stacking patterns) formed by sea-level-driven migrations of these facies tract are the key to identifying depositional cycles in cycles from cores and logs.

Among the identified facies at Fullerton, the peritidal mudstone-wackestone facies, the clay-rich carbonate mudstone facies, and the exposed tidal-flat facies for the most part represent deposition on the inner ramp in sabkha–tidal flat setting as low-exposure index (cf. Hardie and Garrett, 1977) peritidal deposits, tidal-flat ponds, and high-exposure tidal-flat deposits, respectively (fig. 18). It should be noted, however, that exposure fabrics like those developed in the inner platform can also form on the ramp crest following complete aggradation and exposure at any time.

The peloid/pellet-rich facies at Fullerton (peloid wackestone facies, peloid packstone facies, peloid grain-dominated packstone facies, and skeletal wackestone-packstone facies) are also dominantly associated with the inner ramp but occupy a somewhat more distal, lagoonal to restricted subtidal setting where sediment formation is dominated by infaunal and epifaunal burrowing activities (fig. 18).

The oid-peloid grain-dominated packstone – grainstone facies in the Lower Clear Fork at Fullerton is typical of facies deposited in a platform ramp crest at the platform-margin setting where relatively high wave energies are developed (fig. 18). However, none of the cored wells in the field reveal the kind of vertically stacked succession of these deposits that typically defines a well-developed ramp crest (see, for example, Ruppel and others, 2000). This may reflect

insufficient core control or the absence of a true ramp crest on the Lower Clear Fork platform. As previously stated, the Abo appears to lack a ramp-crest facies succession.

As in most middle Permian carbonate-platform successions, the fusulinid wackestone-packstone facies documents outer platform deposition. These rocks are well developed in both the Lower Clear Fork and the Abo. In the Abo, these rocks display classic clinoformal bedding and the general lack of cyclicity that typifies a distal outer platform setting (fig. 18). By contrast, fusulinid wackestone-packstone facies rocks in the Lower Clear Fork are horizontally bedded and interbedded with middle and inner platform facies. This suggests that these fusulinid-rich rocks were deposited in a much more proximal outer ramp position.

The oncoïd wackestone-packstone facies is closely associated with the fusulinid wackestone-packstone facies in the Lower Clear Fork at Fullerton, indicating that the former was deposited during platform deepening. This facies has not previously been reported from middle Permian rocks in the Permian Basin. Its occurrence at Fullerton field may indicate the development of relatively higher energy conditions on the outer platform in the Fullerton area than is generally developed in other regions in the Basin.

Sequence Stratigraphy

Figure 11 illustrates diagrammatically the sequence architecture, basic facies tracts interrelationships, and rock and time terminology of the lower Leonardian at Fullerton field. In this section, we describe the sequence-stratigraphic characteristics of each of the major Leonardian units at Fullerton.

Abo Formation

As already discussed, the Abo represents the distal facies or systems tract of the earliest (oldest) Leonardian sequence in the Permian Basin: the L 1 sequence (fig. 11). Regionally, the

Abo consists of outer ramp to slope, skeletal crinoid-fusulinid-dominated subtidal facies and less common ramp-crest ooid-peloidal grainstones (Kerans and others, 2000). In both outcrop and in the subsurface, the Abo is dominantly characterized by clinoformal, top-lapping geometries (Kerans and others, 2000; Zeng and Kerans, 2003; figs. 6 and 9). This typical Abo architecture is very apparent in 3-D and 2D data from Fullerton field. The Abo is readily defined by its clinoformal reflectors and its top by a prominent toplap surface that is apparent throughout the field (fig. 9).

Although the Abo at Fullerton field is penetrated by relatively few wells and has been cored in even fewer, existing cores display facies and bedding characteristics typical of sediments deposited in an outer ramp/slope setting. Facies consists of alternating beds of fusulinid-crinoid packstones and wackestones, and peloidal packstones. No true cyclicity is apparent in the Abo, although there are alternations between skeletal-rich and skeletal-poor intervals. Inclined beds are locally common. Additionally, correlations within the Abo are not apparent either from core sections or from wireline logs. In part this is the result of limited core and well-log control through the Abo section. But poor correlatability is typical of outer platform depositional successions that display clinoformal architectures because of the associated dipping bedding surfaces, discontinuous facies packages, and poor vertical facies contrasts.

Abo rocks are almost entirely composed of dolomite at Fullerton field. Porosity is locally very high, reaching values of as much as 25 percent. Pore types vary among fusumolds, intercrystalline pores within coarse crystalline dolostones, and interparticle pores in skeletal/peloidal packstones.

The thickness of the Abo is indeterminate largely for two reasons. First, few wells and no cores penetrate the complete Abo to Wolfcamp section. Second, outcrop studies reveal that the

Abo–Wolfcamp contact may be lithologically indistinct in many areas: in outcrop both the uppermost Wolfcamp and the Abo are composed of clinoformal, outer platform fusulinid/crinoid wackestones. A minimum thickness of 300 ft is established by the Amoco FM-1 cored well in the southeastern corner of the field (fig. 3).

The contact between the Abo and the overlying Wichita varies from sharp to gradational. In many cores, the contact is marked by an interval (up to several feet thick) of intermixed clasts and fragments of Wichita tidal-flat deposits and Abo fusulinid-bearing subtidal deposits. The brecciated nature of this contact interval suggests strongly that it is the result of karst-related dissolution and collapse. These breccias and their distribution are discussed more fully in a later section of this report.

Wichita Formation

The Wichita at Fullerton field consists of a diverse assemblage of peritidal to supratidal tidal-flat deposits. Integrated outcrop and subsurface studies indicate that the Wichita Formation represents an updip, proximal facies equivalent of both the Abo outer platform succession and the subtidal Lower Clear Fork. These data also suggest that the Wichita actually comprises parts of two depositional sequences: the highstand leg of sequence L1 and the transgressive leg of sequence L2 (fig. 19). The lower Wichita represents the updip, tidal-flat facies tract equivalent of the downdip, outer platform facies tract of the Abo in Leonardian sequence L1, whereas the upper Wichita represents the updip tidal-flat facies equivalent of the basal Lower Clear Fork subtidal facies in sequence L2 (fig.11).

The Wichita is dominantly composed of dolostone; however, intervals of limestone are common in the upper Wichita in the northern part of the field (fig. 20). The limestone intervals

are relatively persistent laterally and are generally subparallel to stratigraphic markers in the field (fig. 8).

The thickness of the Wichita is fairly consistent over the northern two-thirds of the field, ranging from about 350 ft in the center of the field to about 280 ft along the western, northern, and eastern margins of the field area (fig. 21). Thickness decreases, however, to as little as 110 ft in the southeastern part of the field (fig. 21). This decrease in thickness, which occurs relatively abruptly along a generally northeast trending belt, marks the change from the updip Wichita tidal-flat facies to the downdip Abo outer ramp fusulinid facies. This relationship, is well displayed in figure 22, a NW-SE cross section through the field.

Correlations within the thick Wichita succession of relatively similar tidal-flat deposits are difficult owing to (1) the discontinuous nature of tidal-flat deposits, (2) the lack of any systematic vertical stacking relationships among facies to define cycles, (3) the nonuniform response of wireline logs to these facies, and (4) the overprinting effects of diagenesis. One exception to this is a thin (average 10 ft thick) bed of subtidal fusulinid to peloidal packstone that is apparent in the middle of the Wichita in many cores and logs (figs. 8, 22). Because of its subtidal character, this bed is actually well imaged by wireline gamma logs. Its low gamma-ray response provides a strong contrast to the generally high and variable gamma-ray aspect of the underlying and overlying tidal-flat deposits (figs. 6, 22). This subtidal deposit, which appears to be present over the entire field area, documents a widespread sea-level rise and transgression and is essentially the only definable time line in the Wichita succession. This marine flooding event appears to represent a late L1 transgression of the platform and probably correlates to the uppermost part of the Abo in downdip areas of the field.

Lower Clear Fork Formation

Rocks assigned to the Lower Clear Formation represent the subtidal systems tract of the Leonardian 2 (L2) sequence. Core studies show that the Lower Clear Fork can be subdivided into three high-frequency sequences HFS (L 2.1, L2.2, L2.3) throughout most of the Fullerton field area (figs. 4 and 8). A fourth HFS (L 2.0) can be defined at the margins of the field. Each of these can be identified as having a transgressive, dominantly subtidal lower leg and an overlying, highstand upper leg.

High-Frequency Sequence L 2.0

HFS L 2.0 documents the initial flooding of the platform following sea-level fall and exposure at the end of L1 deposition. In most of the field area, HFS 2.0 consists of amalgamated tidal-flat deposits of the upper Wichita. Subtidal Lower Clear Fork deposits of L 2.0 are only present at the margins the field (figs. 8 and 22). At the downdip edge of the field, HFS L 2.0 consists of a basal transgressive leg of peritidal tidal-flat deposits, a middle maximum flooding leg of subtidal, outer platform, fusulinid-rich packstones, and an upper leg of peritidal tidal-flat deposits (fig. 22).

High-Frequency Sequence L 2.1

In most of the Fullerton field area, HFS L 2.1 forms the base of the Lower Clear Fork. As defined for this study, L 2.1 consists of a basal section of transgressive to early highstand subtidal platform facies and an upper section of highstand tidal-flat facies (figs. 8, 11, and 22). The basal transgressive subtidal facies of the Lower Clear Fork represent the first marine flooding of the platform and a sharp change in depositional style from the tidal-flat deposition of the Wichita to subtidal deposition of the Lower Clear Fork.

The basal transgressive leg of L2.1 consists dominantly of fusulinid wackestone-packstone and oncoïd wackestone-packstone facies that document landward backstepping of outer platform facies across the platform. These rocks are generally overlain by a succession of peloid packstones and grain-dominated packstones that represent late transgression and early highstand. Locally, within this succession there are exposed tidal-flat facies indicating periodic exposure. L 2.1 is capped throughout most of the field by a succession of one to three tidal-flat-capped cycles that represent exposure during late highstand (figs. 8, 11, and 22). These tidal-flat facies typically exhibit an elevated gamma-ray log response that aids in their recognition (figs. 8 and 22).

Like most of the Lower Clear Fork in the Permian Basin, HFS 2.1 is dominantly dolostone. However limestone is locally common at Fullerton field, especially in the transgressive leg of 2.1. Areally, limestone is most abundant along the periphery of the northern half of the field and at the southern end of the field (fig. 23).

The thickness of L 2.1 is relatively constant across the Fullerton field area, ranging from about 140 to 150 ft across most of the area (fig. 24). In some cases, thickness changes appear to be a function of differential subsidence along deep-seated faults (see Jones and Ruppel, this report). This is especially apparent along the north-trending fault in the northeastern part of the field, where the thickness changes from less than 140 ft on the western, upthrown side of the fault to more than 160 ft on the eastern, downthrown side of the fault (fig. 23). Examination of modern structure (fig. 5) shows that considerable movement on this fault occurred even after Lower Clear Fork deposition.

Porosity can be developed in any part of L 2.1 but is most abundant in the subtidal (transgressive and early highstand) parts of the sequence. Pore space is dominated by

intercrystalline and moldic pores, the latter being especially abundant in limestone sections. Overall, these rocks are most porous in areas where limestone is present. Tidal-flat rocks are also locally porous but generally contain low permeabilities. The subtidal rocks of L 2.1 probably constitute the most productive reservoir interval in the field.

High-Frequency Sequence L 2.2

HFS L 2.2 is similar to HFS L 2.1 in consisting of a basal transgressive leg composed of backstepping tidal-flat facies, a middle (late transgressive to early highstand) leg composed dominantly of subtidal facies, and an uppermost (late highstand) leg composed of tidal-flat facies (figs. 8, 11, and 22).

As is the case with L 2.1, there is good evidence that the marine flooding of the platform following the post L2.1 lowstand was progressive. Basal L2.2 tidal-flat deposits are thickest in the center of the field area but generally absent along the margins, reflecting greater accommodation and early flooding of downdip areas. The lower abundance of outer ramp fusulinid-rich facies in the TST of L 2.2 relative to L 2.1 suggests that the overall accommodation during the L2.2 sea-level rise was somewhat less than during L2.1. Lower accommodation and attendant lower wave energies are also suggested by the near absence of the oncoïd wackestone-packstone facies in L 2.2. These rocks are found only in the most downdip core in the field. The fusulinid wackestone-packstone facies is also largely restricted to the eastern and southeastern parts of the area (fig. 22).

Throughout most of the field area, L 2.2 is dominated by peloid wackestones and packstones (figs. 8 and 22) typical of middle platform deposition. The sequence is capped by a thin succession of tidal-flat cycles (figs. 8 and 22).

HFS L 2.2 is composed dominantly of dolostone with two important exceptions. Like L 2.1, limestone is dominant in the southern part of the field (fig. 25). Dolomite in this area is largely restricted to mud-rich fusulinid wackestones; virtually all grain-rich facies in this area are limestone. Limestone is also abundant in a small area in the north-central part of the field.

The thickness of L 2.2 is generally significantly less than that of L 2.1 (fig. 26). L 2.2 ranges from about 85 to 90 ft across most of the central part of the area to about 100 ft along the northern and southern field margins.

Porosity development in L 2.2 is similar to that in L 2.1. Porosity is best developed in the subtidal (transgressive and early highstand) parts of the sequence and dominated by intercrystalline and moldic pores. Also like L 2.1, porosity is greatest in sections containing significant limestone.

High-Frequency Sequence L 2.3

The uppermost Lower Clear Fork high-frequency sequence (L 2.3) is composed of tidal-flat-capped restricted subtidal cycles throughout most of the field area (figs. 8, 11, and 22). These tidal-flat caps typically contain fenestral and fine intercrystalline pore space that is definable on porosity logs. Log correlations suggest that these cycle-capping tidal-flat facies are relatively continuous across significant areas of the field. The underlying cycle-base subtidal rocks are dominantly mud-rich packstones and wackestones.

Porosity, as indicated, is mostly restricted to tidal-flat caps. Because these rocks are dominated by fine intercrystalline and moldic pores, they contain little if any reservoir permeability. Accordingly, they locally contain oil stain but rarely contribute to oil production. A possible exception to this occurs along the outer margins of the field where grain-rich peloidal

packstones of the middle ramp become more common (fig. 22). If reservoir permeability is anywhere present in L2.3, it is in these field marginal areas.

Tubb Formation

The Tubb is characterized by fine-grained siliciclastics (coarse siltstone and fine sandstone), which are relatively easily defined by high-gamma-ray log response (fig. 8). These clastics have been interpreted to represent eolian deposits that were deposited during the post-L2 lowstand then reworked during the ensuing L3 sea-level rise. Because of this, most intervals are varying mixtures of siltstone/sandstone and carbonate (typically mud-rich, shallow-water facies). Although locally some Tubb beds appear correlative, they are highly variable in their distribution across the field area. The base of sequence L3 is picked at the first occurrence of siltstone/sandstone about 100 ft below the thickest clastic beds (fig. 8). A prominent marine flooding event of dolostone (peloidal wackestone and dolostone) immediately above these clastics is readily definable on wireline logs throughout the field because of its characteristic low-gamma-ray signature (especially on the spectral gamma-ray log) and provides the most correlative datum in the field. The Tubb is not part of the reservoir at Fullerton field.

Cycle-Scale Stratigraphy

The fundamental goal of cycle stratigraphy is to develop a correlation framework based on time-equivalent surfaces. The basic underlying premise for this approach is the assumption that widely correlative depositional cycles are formed by punctuated, allocyclic processes (e.g., sea-level rise and fall) that affected sedimentation over broad areas. The methodology used to develop a cycle-scale stratigraphic framework in the Leonardian section at Fullerton field consists of the following: (1) characterization of facies stacking patterns and cycle development in analogous outcrops, (2) description, interpretation, and logging of facies, stacking patterns,

and possible cycle tops in cores, (3) integrated log- and core-based correlation of tentative cycle tops, and (4) definition of cycle architecture. At Fullerton field, nearly 15,000 ft of core (from 29 cored wells) was described in detail to provide the basic data for cycle definition.

Wichita Cyclicity

As discussed previously, tidal-flat facies, such as those that characterize the Wichita, are typically highly discontinuous laterally; thus, depositional cycles are generally not definable in these rocks. This assertion is supported both by outcrop studies and by examination of such sediments in modern settings. Only one correlative cycle top has been defined in the Wichita on the basis of facies stacking relationships. This surface, which occurs in about the middle of the Wichita succession in most of the field, is marked by the sharp superposition of clearly subtidal rocks over the more typical tidal-flat facies of the Wichita. These subtidal rocks are in turn overlain by tidal-flat facies (peritidal mudstone-wackestone facies or exposed tidal-flat facies) that mark the cycle top. This cycle averages about 10 ft in thickness and is generally marked by a low-gamma-ray log response (fig. 8). It is probable that this lone subtidal cycle represents maximum transgression (i.e., maximum flooding) and accommodation developed on the inner Lower Clear Fork platform during the L 2.0 HFS sea-level rise. No other true depositional cycle tops (e.g., time surfaces) can be defined in the Wichita.

Lower Clear Fork Cyclicity: HFS L 2.1

Facies stacking patterns define numerous apparent cycle tops, at thicknesses ranging from 2 to 15 ft (fig. 27). Cycles are typically characterized by having mud-rich facies at their bases and grain-rich facies at their tops. Basal transgressive systems tract (TST) cycles in HFS L2.1 contain abundant oncoids at cycle bases along with accompanying fusulinids (fig. 27). These cycles are capped by better sorted, peloid-rich facies. High frequency cycles (typically 5 to 10 ft

in thickness) stack into cycle sets that average 25 to 40 ft in thickness (fig. 27). Cycle sets display similar facies stacking patterns to cycles consisting of fusulinid-rich bases and peloid-rich caps. Locally, tidal-flat facies cap these cycle sets. Porosity is generally highest at both cycle tops and cycle set tops relative to bases. However, because cycles in the lower parts of cycle sets are generally more mud- and fusulinid-rich, overall porosity in these basal TST cycles is usually relatively low.

Cores and outcrop studies suggest that cycles and cycle sets are correlative over significant distances. However, where cores are not available, these correlations can be difficult to establish. Gamma-ray logs display virtually no systematic response to subtidal facies and cycles (figs. 27, 28) and thus cannot be reliably used for cycle-scale correlation throughout most of the Lower Clear Fork. [They are only useful for general definition of tidal-flat cycles at HFS contacts.] In the absence of gamma-ray logs, the most effective way of establishing cycle-scale correlations is through the use of porosity logs. This approach is based on the observation from outcrops and cores that cycle tops consistently contain the most grain-rich facies and that these rocks are most likely to contain high porosity. Accordingly, porosity logs can be used to correlate both the high-porosity facies in the upper part of the cycle and the overlying cycle top.

L2.1 highstand cycles are dominated by mud-rich peloidal facies at their bases and grain-rich peloid- or ooid-bearing facies at their tops (fig. 28). Fusulinids are usually uncommon in these highstand cycles reflecting the basinward shift in facies tracts. In general, these cycles are dominated by peloid packstones and grain-rich packstones. Porosity is commonly highest at both cycle tops and cycle set tops because of the abundance of these grain-rich facies. Cycles typically average 5 to 10 ft in thickness; cycle sets are commonly 20 to 30 ft thick (fig. 28).

Lower Clear Fork Cyclicity: HFS L 2.2

Facies stacking and cycle development in HFS L 2.2 are very similar to those in L 2.1. Cycles average 5 to 10 ft in thickness, and porosity is best developed in cycle tops (fig. 29). L 2.1 cycles differ, however, in the lack of oncoid facies and the relative scarcity of fusulinid facies. This presumably reflects decreasing overall accommodation in L2.2 owing to platform aggradation and slowing rates of long-term sea-level rise. Additionally, cycle sets are not generally definable in L 2.2. This is largely due to the general absence of fusulinid facies that in L 2.1 define these intermediate-scale sea-level rise events.

Lower Clear Fork Cyclicity: HFS L 2.3

High-frequency cyclicity in the Leonardian at Fullerton field is most readily definable in L2.3. These rocks, which are characterized by tidal-flat-capped shallow subtidal cycles (fig. 30), appear to be much more widely correlative than cycles in L 2.1 or L 2.2. Although neither facies nor cyclicity is defined by gamma-ray logs, both are distinguishable on porosity logs because of the typically well developed porosity associated with cycle-capping tidal-flat deposits. The porosity in these rocks is generally caused by the presence of fenestral pores and can be relatively high, especially relative to the generally low porosity exhibited by cycle-base mud-rich wackestones and packstones. However, because of the separate-vug fenestral pores, permeability is generally low and L 2.3 rarely contributes to hydrocarbon production in the field. Porosity-based wireline correlations suggest that cycle and facies continuity is high. This is somewhat unexpected considering outcrop observations that suggest that tidal-flat facies are highly discontinuous. The laterally continuous porosity development at these cycle tops probably reflects the effects of early diagenesis associated with sea-level fall and subsequent rise at these surfaces.

MINERALOGY AND DIAGENESIS

The lower Leonardian section at Fullerton field is similar to most other platform Leonardian successions in the Permian Basin in showing evidence of significant post-depositional diagenesis. Principal products of this diagenesis are matrix-replacive and pore-filling dolomite and anhydrite. However, limestone is locally present in the Leonardian section at Fullerton, including the Abo, the Wichita, and the Lower Clear Fork.

Dolomite and Limestone Distribution

Dolomite is by far the dominant mineral in the reservoir section. The Abo consists entirely of dolomite except in the most downdip wells. In core from the FM-1 well, perhaps the most downdip well in the field, the Abo contains alternating zones of limestone and dolostone. Dolostone is more commonly associated with mud-rich facies (peloid wackestone and fusulinid wackestone) in the Abo clinoformal succession, whereas limestone intervals are more commonly grain-rich, skeletal facies (fig. 22).

Limestone is locally very abundant in the Wichita, especially in the upper half of the formation (fig. 8). In all cases, calcite-rich rocks in the Wichita are peritidal mudstones or wackestones (the peritidal mudstone-wackestone facies). These calcite-dominated facies characteristically exhibit very low porosity (>2 %) and essentially no permeability. Log correlations suggest that limestone intervals are locally correlative (fig. 8). Although facies stacking patterns do not clearly reveal a systematic relationship between mineralogy and cyclicity, it is probable that these limestones are the result of cycle-punctuated diagenesis. Limestone is virtually absent from the lower Wichita (L1) but very common in the upper part (L2) of the formation (fig. 8). This distribution correlates closely with the position of the interpreted L1 – L2 sequence boundary that subdivides the Wichita (fig. 22); limestone is absent

from the L1 (highstand) Wichita but is locally very abundant in the L2 (transgressive) Wichita. Limestone abundance in the upper (L2) Wichita displays a systematic trend across the field. The highest abundance of limestone is in the northwestern part of the field; essentially no limestone is present in the southern part of the field (fig. 20). Because of the low porosity associated with limestones in the Wichita, porosity logs can be reliably used to define and correlate limestone even where cores, or dual porosity, or PE logs are unavailable.

Lower Clear Fork rocks at Fullerton field also contain locally abundant limestone. Limestone is common in HFS L 2.1 across most of the field (fig. 23). Highest abundance is in the southern part of the field where only mud-rich (typically fusulinid-bearing) facies contain significant dolomite. Essentially all grain-rich facies in this area are dominantly calcitic. In the northern part of the field, limestone is also common in L 2.1 but is complexly distributed among all subtidal facies.

Like HFS 2.1, limestone dominates L 2.2 in the southern part of the field. However, outside of this area, limestone is rare except in one small area in the northwestern part of the field (fig. 25).

Porosity is generally high in limestone-rich intervals in the Lower Clear Fork. However, porosity is also well developed in dolostones, so except where cores, dual-porosity log suites, or PE logs are available, it is not possible to differentiate limestone from dolostone in the Lower Clear Fork.

Stable Isotope Chemistry

Samples of dolostone and limestone were collected from the Lower Clear Fork Formation in the FM-1 core and analyzed for stable isotopes. For both rock types $\delta^{13}\text{C}$ data are similar; data average 4.89 ‰ PDB for limestones (n = 13) and 5.44 ‰ PDB for dolostone (n = 2). Such

heavy carbon isotope values are typical of most Permian Leonardian and Guadalupian carbonates (Ruppel and Cander, 1988a, b; Leary and Vogt, 1990; Saller and Henderson, 1998; Ruppel, 2002).

The $\delta^{18}\text{O}$ data from limestones average -2.67‰ PDB ($n = 13$, range: -1.55 to -3.55‰). These data are very different from previously reported values for other calcite-bearing samples in the Leonardian and Guadalupian. For example, most $\delta^{18}\text{O}$ values for Guadalupian calcites have ranged from about -7.6 to -10.4 (Leary, 1985; Vogt, 1986, S. Ruppel, unpublished data from the Grayburg Formation at South Cowden field). These values, however, were recorded from “replacement calcite” interpreted to have precipitated from meteoric water possibly sourced from deep basin fluids. The $\delta^{13}\text{C}$ values from these “replacement calcites” are also very depleted (-19 to -30‰ PDB), suggesting precipitation from bacterially mediated sulfate reduction (Leary, 1985; Vogt, 1986; S. Ruppel, unpublished data). The more “normal” $\delta^{13}\text{C}$ values for the Lower Clear Fork limestones at Fullerton indicate a very different origin for these calcites. It should be noted that these Lower Clear Fork $\delta^{18}\text{O}$ values are very similar to the current best estimate for marine calcite precipitates from seawater during the middle Permian (-2.8‰ PDB; Lohman and Walker, 1989). One interpretation of these data is that these Lower Clear Fork limestones contain a preserved record of original seawater chemistry and by extension that these rocks have undergone relatively little chemical alteration.

The $\delta^{18}\text{O}$ data obtained from Lower Clear Fork dolostones average 2.30‰ ($n = 2$). These data are similar to previous Leonardian data reported by Ye and Mazzullo (1993), Saller and Henderson (1998), and Ruppel (2002) but very different from most data reported for younger Guadalupian rocks. Typical $\delta^{18}\text{O}$ values for these younger Guadalupian (San Andres and Grayburg Formations) platform dolomites are 3 to 6‰ (Vogt, 1986; Ruppel and Cander,

1988a,b; Saller and Henderson, 1998; Ruppel and Bebout, 2001; Ruppel, 2002). The relatively enriched isotopic signatures of these Guadalupian dolomites have invariably been interpreted to have been produced during dolomitization by evaporatively concentrated seawater brines. The significantly depleted values for the Leonardian dolostones at Fullerton and in other Leonardian fields suggest that either (1) dolomitization was caused by brines that were less evaporatively concentrated than those that caused Guadalupian dolomitization, (2) dolomitization was caused by fluids of a mixed water origin, or (3) a combination of cases 1 and 2 above.

Karst Development

Karst Fabrics

Evidence of karst-related diagenesis and dissolution is common in the lower part of the reservoir section at Fullerton field; karst features occur within the Wichita and at the Wichita/Abo contact. These rocks are variable in fabric but include four basic types: (1) polymict conglomerates, (2) monomict breccias, (3) fractured and tilted beds, and (4) void-filling cement.

The predominant style of polymict conglomerate typically consists of rounded clasts of multiple peritidal lithologies (fig. 31). Clasts range in size from a few millimeters to several centimeters in maximum dimension and are usually subequant and rounded. Clasts are usually enclosed in mudstone or abut one another at stylolitic contacts. Polymict fabrics are most common in the middle of the Wichita (fig. 31). Intervals of polymict conglomerate of at least 25 ft to as much as 60 ft thick are present in the FCU 6122 core. The multiple facies character of these clasts and their rounded character indicate that they were formed by sediment transport. Their discontinuous nature and their association with other features indicative of karst processes suggest they originated as cave-fill deposits.

Although probably not true polymict conglomerates, superficially similar deposits that also indicate karst processes are present at the contact of the Wichita and the Abo in the FM-1 core at the downdip edge of the field area. These rocks are usually characterized by a mixture of two or more facies types including Wichita tidal-flat facies, green silty carbonate, dark-gray silty carbonate, and Abo subtidal facies (figs. 32, 33). Rather than being interbedded with one another the first three appear to surround the Abo facies in many cores (fig. 33). This suggests that these “polymict conglomerates” actually represent dissolution and/or erosion of the top of the Abo and subsequent infilling of the irregular surface or differential compaction of the Abo (L1) and overlying transgressive Wichita sediments (L2) at the Abo/Wichita contact. In rare instances, there are also features suggestive of collapse brecciation. All of these features have been observed in analogous outcrops of the Abo/Wichita contact in Apache Canyon in the Sierra Diablo (Kerans and others, 2000). The outcrop succession reveals that karst features (sinkholes and caves) were formed during the post L1 sea-level fall, then filled with transgressive L2 tidal-flat deposits (i.e., Wichita facies). These tidal-flat facies in some instances were brecciated and intermixed with the underlying Abo as sinkholes and caves collapsed.

Monomict conglomerates or breccias consist of broken and rotated clasts of constant lithology and facies (fig. 34). These rocks are restricted to the Wichita, usually the middle of the section. Commonly associated with these deposits are fractures, sediment infill (cracks and fissures), void-filling cement (chiefly anhydrite), and other evidences of dissolution. Most of these features can also be formed by nonkarst processes in tidal-flat intervals not exposed to true karst (e.g., tepee formation is usually accompanied by broken and rotated blocks, cracks and fissures, and cement and sediment infill). Thus it is possible that some of these deposits may not

be the result of true karst processes. However, their thickness, abundance, and association with other features of karst formation suggest that many are also karst related.

Fractured and tilted beds are also observed in some cores especially in the middle of the Wichita section. Tilted beds have clearly been formed by postdepositional collapse. In the FCU 5927 core, they form part of a succession that very much resembles the classic cave fill–cave roof succession described by Loucks (1999). The succession in the 5927 well consists of 20 ft of polymict cave-fill conglomerate composed of mixed tidal-flat facies overlain by 20 ft of fractured and locally tilted but apparently generally in situ beds of tidal-flat and subtidal facies probably representative of a cave roof.

Large zones of void-filling anhydrite cement are also strong indicators of karst-related dissolution. Zones of massive anhydrite up to 1½ ft thick are present in cores in the Wichita at Fullerton field (e.g., FCU 6122, 5927). Smaller anhydrite-filled voids and fractures are ubiquitous within the Wichita and at the Wichita/Abo contact (e.g., fig. 32) and also point to late cementation of dissolution voids by diagenetic fluids associated with reflux dolomitization of the succession.

Causes and Timing of Karst

Outcrop studies demonstrate that major karsting of the Leonardian sequence occurred at the sea-level fall/rise event that is defined by the L1/L2 sequence boundary (Kerans and others, 2000). In downdip areas of Fullerton field, cores demonstrate this same relationship. Here, the top surface of the Abo outer platform facies succession (L1) is karsted and is infilled and overlain by brecciated Wichita tidal-flat facies (L2). In updip areas, however, establishing a spatial and temporal relationship between karst formation and the L1/L2 sequence boundary is more problematic. Most karst features in the Fullerton field area are found in an interval of about

150 ft in the middle of the Wichita section (fig. 8). In general, this interval correlates approximately to the marine flooding event identified within the Wichita in cores and logs that is thought to represent the L2 transgression (fig. 22). However, karst features are developed both below and above this horizon, indicating that karst-related diagenesis was not limited to the L1 sequence. Instead, it appears that two types of karst-related processes occurred as outlined below.

Primary karsting and dissolution probably occurred during the post-L1 lowstand. At this time, the exposed top L1 surface (consisting of Abo subtidal sediments downdip and lower Wichita tidal-flat sediments updip) developed local caves, sinkholes, and an irregular topography. During the subsequent L2 sea-level rise, transgressive peritidal deposits of the Wichita filled the irregular karsted surface including sinkholes and caves. With continued sedimentation and compaction, parts of the overlying L2 (upper Wichita tidal flat) succession underwent local brecciation and collapse probably due to stress differences set up over underlying karst features. This scenario is consistent with outcrops (Kerans and others, 2000) and fits the distribution of karst features seen at Fullerton field.

Impact of Karsting on Reservoir Quality

Some karst-related deposits most certainly exhibit at least local differences in petrophysical properties (i.e., porosity, permeability, and saturation) from surrounding undisturbed and unaltered deposits. Polymict conglomerates and anhydrite voids are two obvious examples of this. However, two factors make quantification of the importance of these differences difficult. First, most karst deposits do not record significantly different porosity or permeability than surrounding nonkarsted deposits based on both wireline and core data. This is probably due to the fact that most karst fills are composed of the same facies as nonkarsted

intervals. Anhydrite void fills are an obvious exception to this, as they contain no porosity or permeability, but they are generally very small and probably of little impact on reservoir flow.

Second, with the exception of areas in which there are cores, the distribution of karst features in the reservoir section is not definable. Efforts to identify karst fill using logs and 3-D seismic appear to be negated by the similar lithological and petrophysical properties these features share with surrounding rocks. It is tempting to conclude from these observations that karst features have no impact of reservoir heterogeneity or fluid flow. However, there are anomalies in water production and flow rates in the Wichita that cannot be readily explained by matrix petrophysical properties (T. Anthony, personal communication, 2003). These phenomena may be the result of karst development.

RESERVOIR IMAGING

Accurate definition of reservoir architecture and the distribution of rock fabrics within this architecture is the key to defining improved methods for recovery of hydrocarbons remaining in these systems. We utilized several methods to better image the reservoir at Fullerton field. Especially important in defining the geologic architecture of the reservoir are (1) the calibration and use of borehole image logs to aid in the identification and mapping of facies, cyclicity, and rock fabrics, and (2) the use of 3-D seismic data to constrain the geologic framework.

Identifying Facies and Cyclicity from Borehole Image Logs

Image logs are highly underutilized in the characterization of carbonate reservoirs. To most, the principal use of such logs is in the identification of fractures. However, image logs also have the potential to accurately image many matrix properties that are key to the proper characterization, modeling, and exploitation of carbonate reservoirs.

Traditionally, cores have been obtained to provide the key data needed for constraining the distribution of reservoir facies, cyclicity, and rock fabrics. However, because of cost, the number of cores typically obtained is generally far smaller than needed to accurately constrain these aspects. If properly calibrated with core observations, borehole image logs can provide most of the required data to construct an accurate reservoir model at a fraction of the cost.

To test this premise and to add to the core database, a borehole image log was obtained in a new well drilled in the field at the beginning of the study. This well (FCU 2564, fig. 3) was drilled in an area where no cores exist. Accordingly, the development of a robust methodology for deriving key geological information from this well such as facies, rock fabric, and cyclicity from this image log has tremendous potential value for efforts to construct a more accurate image of the reservoir architecture.

A critical first step in utilizing image logs for geological analysis is the calibration of the images to known geological features. This is best done with a core taken from the well in which the image log is recovered. However, when a companion core is not available, as was the case with this image log, a satisfactory calibration can often be established by examination and correlation of nearby cores.

It is important to keep in mind that resistivity image logs, like the FMI log, display differences in resistivity. Thus, only those sedimentary features that are associated with resistivity contrasts can effectively be imaged. High-resistivity features are usually those that have very low porosity. In most color scales used on such image logs, the highest resistivity (lowest porosity) features are shown in white). In these rocks, white usually indicates anhydrite. At the other end of the color scale, black indicates lowest resistivity and usually higher porosity.

However, dark colors can also indicate low resistivity associated with clay-rich sediments (e.g., shales).

Examination, correlation, and comparison of the FCU 2664 image log with nearby cores show that seven facies can reliably be identified from the image log. This is fewer than the 12 defined from core studies but is sufficient to provide necessary information to define major facies successions and cyclicity and to provide a strong basis for accurate correlation and interpretation of facies and cyclicity to nearby wells. Facies recognizable on the image log include (1) tidal-flat facies, (2) peloid wackestone-packstone, (3) nodular wackestone-packstone, (4) cross-bedded grainstone, (5) fusulinid wackestone-packstone, (6) karst breccia, and (7) clay-rich mudstone. Additionally, siltstone-sandstone facies can be identified from many wireline logs.

Tidal-flat facies are characterized on image logs principally by their closely spaced parallel and horizontal laminations (fig. 35). The common presence of fenestral pores and small burrows in tidal-flat facies is typically shown on image logs by abundant small black (low resistivity indicating fluid-containing open pores) spots. Tepee structures and sheet cracks are also well imaged where present. The identification of tidal-flat facies is crucial for defining both reservoir architecture and reservoir quality. Because they generally occupy cycle tops their definition makes it possible to define cycle boundaries and thereby facilitates cycle-scale correlation. Equally important is the identification of tidal-flat facies and their petrophysical significance. As discussed previously, tidal-flat facies commonly display relatively high porosities but low permeability. Because of this, it is critical for accurate reservoir-quality mapping to distinguish tidal-flat rocks from subtidal rocks that are typically higher in permeability.

Fusulinid wackestones (fig. 36) are identified on image logs by the presence of small black patches that are in some cases similar to those representing fenestral pores in tidal-flat facies. However, fusulinid pores are typically larger and more irregular in shape. Fusulinid facies can also be distinguished from tidal-flat facies by the general lack of closely spaced laminations. Fusulinid-bearing rocks generally represent the deepest water facies in the Leonardian succession and typically are found at cycle bases. They are thus important indicators of sea-level rise and guides to cycle definition and correlation.

Although generally rare in the Leonardian, cross-bedded grainstones are well imaged on image logs because of their dipping laminations (fig. 37). These rocks also indicate cycle tops and thus are guidelines to cycle definition and correlation. Additionally, where porous, these grainstones can contain very high permeability.

Other subtidal rocks are typically difficult to subdivide using image logs. Peloid-skeletal wackestones and packstones commonly all display a grainy texture, probably caused by their small pore size, and intercrystalline porosity (fig. 38). Burrowing of these rocks is ubiquitous, however, and image logs can readily reveal where this burrowing has caused changes in porosity or promoted differential diagenesis. Nodular wackestones, for example, contain abundant anhydrite nodules that were precipitated in the enhanced permeability pathways created by burrowing organisms (fig. 39). The anhydrite that fills these burrows is easily imaged on the image log as whitish subspherical patches (fig. 39b). Commonly, burrow margins still preserve some of the porosity enhancement caused by the burrowing. These high-porosity margins are expressed on the image logs as black rims around the nodules (fig. 39b). Where anhydrite has not filled the burrows, the result is patches of high porosity (fig. 40a). These are displayed on the

image log as black, low-resistivity patches. It is important to note that these features are not vugs or open molds, as they have commonly been mistaken to be (fig. 40b).

Breccias are relatively easily defined by image logs. This especially the case if the clasts are separated by clay-rich or more porous facies that have lower resistivities (fig. 41). However, the origin of such breccias is not obvious from the images. For example, the image in figure 41b could represent either a tectonic breccia, a deep-water debris flow, or a karst infill breccia. The correct interpretation requires an integrated regional and local understanding of depositional setting and diagenetic processes. At Fullerton, it is clear that these breccias are the result of karsting.

Other facies such as siltstone-sandstones and clay-rich carbonate mudstones can be defined using a combination of image character and wireline log response. For example, most siltstone-sandstones display parallel, horizontal laminations similar to tidal-flat facies on image logs and higher than expected values for neutron and acoustic logs. Gamma-ray response is also typically high, although care must be taken to determine whether gamma-ray response comes from potassium-thorium associated with clastics as opposed to uranium, which is less systematically distributed. The spectral gamma-ray log allows this distinction to be made easily. Clay-rich carbonate mudstones (commonly called shales) can be defined by their dark color (indicating low resistivity) and limited thickness. Like the siltstone-sandstones, they are also commonly associated with clastics and an elevated gamma-ray, neutron, and acoustic log response.

Using the calibrated image log responses described above it is possible to create a very detailed record of facies in wells having good-quality image logs. For the FCU 2564 well, we defined facies through an interval of more than 750 ft (6,600 to 7350 ft). Vertical resolution

through this interval is potentially better than that attainable from cores (because of uncertainties of core/well depth ties). Cycles defined from these facies successions range in thickness from 3 to 20 ft. Highest facies and cycle resolution was obtained in intervals characterized by alternating subtidal and tidal-flat facies in the Lower Clear Fork because of the marked contrast in image log character of these two facies types.

Particularly noteworthy observations from the image log in FCU 2564 is the clear indication that this well occupies a significantly different depositional setting than the nearest cored wells to the east. The greater thickness of relatively deep water fusulinid wackestone-packstone facies in L 2.1 here strongly suggests that accommodation increases to the west. This is counter to the regional trend in depositional dip and paleogeography and would not be recognized without this image (or a continuous core). This finding has potential petrophysical significance for the western part of the field by suggesting that deeper water facies of more favorable petrophysical character may be more prevalent in this area than would otherwise be expected. Thus, because of the ability to image key facies and thus facilitate the definition of cycles, sequences, and rock fabrics, the image log adds critical data that are extremely pertinent to the accurate modeling of reservoir architecture and permeability across the field.

Imaging Stratigraphic Architecture and Reservoir Development from 3-D Seismic

Like image logs, 3-D seismic data are remarkably underutilized in the characterization of carbonate reservoirs. A critical need in developing approaches that lead to improving recovery from reservoirs containing significant volumes of remaining hydrocarbons is a better understanding of the 3-D distribution of reservoir attributes. The approaches outlined in this report for assembling and interpreting well data are the most critical part of this effort. However, because they are limited to well control, they leave important gaps in our understanding. Three-

dimensional seismic data offer valuable data on interwell and extrawell areas (meaning areas of the field where usable well data are absent) and when properly interpreted and applied can greatly improve and thus constrain reservoir attribute models. Here we provide some brief insights into how 3-D data can be used to better image both reservoir framework and porosity distribution. A far more detailed and rigorous application of these 3-D data to the construction of the geological model at Fullerton is described by Zeng (this report).

Constraining Reservoir Architecture

Two- and three-dimensional data at Fullerton field provide important guides to the stratal architecture of the reservoir succession. Seismic amplitude sections through the entire reservoir interval reveal that much of the section is characterized by generally parallel seismic reflectors (fig. 42). This is not unexpected considering the shallow-water-platform depositional setting indicated by the cores and the apparently subhorizontal correlations suggested by wireline logs. However, 3-D and some 2D data suggest a very different architecture for the basal Leonardian, Abo Formation. Seismic data reveal sets of clinoformal reflectors in the Abo that dip generally basinward (toward the east). This apparent clinoformal architecture of the Abo is consistent with observations of clinoformal fusulinid wackestones and packstones in outcropping Abo-equivalent sections in the Sierra Diablo. These clinoforms demonstrate that conventional horizontal correlations of wireline log data are inappropriate for the Abo. In most cases, it is not possible to resolve cycle-scale correlations of either facies or time surfaces in such settings.

Defining Reservoir Quality

Seismic data can also be robust indicators of porosity distribution in carbonate reservoirs. Zeng (this report) demonstrates the strong agreement between 3-D seismic impedance data and reservoir porosity at Fullerton field. Because of this robust relationship, even simple amplitude

extractions reveal field-scale and field-wide changes in porosity development that are important for understanding controls on porosity development and for defining interwell and extrawell distribution of porosity.

Figure 43 is an amplitude extraction map for HFS 2.1 in a small area of the field created to examine possible infill drilling locations. Note that whereas the northern half of the map displays high negative amplitudes indicative of high porosity, the southern half of the area is characterized by markedly lower amplitude. The porosity distribution revealed by this map indicates that only those wells in the northern half of the target area are likely to encounter good porosity in this zone. It should be pointed out that this information on porosity distribution is only obtainable from the 3-D data volume. The quality of the well logs in the area is too poor to determine porosity with any accuracy.

Areas of poor well control like these (caused by either the lack of wells or poor-quality logs) are common through the field, and they greatly compromise efforts to develop a field-wide strategy to identify and target oil resources. This is readily apparent from a comparison of a porosity map based on well logs and a seismic amplitude map for HFS L 2.1 (fig. 44). The value of the seismic data volume is especially apparent in the southern end of the field where the limited well control does not accurately image the east-west-trending area of high porosity shown by the amplitude map (compare fig. 44a with fig. 44b). It is apparent that basic amplitude data like these provide a powerful supplement to well control in defining and predicting porosity distribution in the field. Zeng (this report) documents a more quantitative use of 3-D data in defining porosity development in the field.

RESERVOIR ARCHITECTURE

A critical component of a robust reservoir model is a geologically constrained reservoir framework. Geologically accurate models must be based on correlations of time stratigraphic units, the most readily correlative of which are cycle and sequence boundaries. At Fullerton field, we utilized correlations of cycle tops to construct the reservoir model for the Clear Fork. Although these correlations are ultimately based on correlations of wireline logs (porosity and gamma ray), the underlying basis for the interpretation and correlation of these logs is a knowledge of 1D and 2D facies and cycle-stacking relationships developed from integrated studies of cores and outcrops.

Cyclicity and Flow-Unit Definition

Reservoir flow units are most appropriately based on the definition and mapping of depositional cycle boundaries. This is because, when properly defined and correlated, depositional cycles represent the best available indicator of original depositional surfaces or time lines. The procedure for identifying utilizing cycle boundaries for flow unit definition has been well described by Ruppel and Ariza (2002) and Lucia and Jennings (2002) for the South Wason Clear Fork reservoir.

Ideally, the correlation of depositional cycle tops should be based on a log that can be directly tied to facies and one that is independent of diagenesis or porosity development. The gamma-ray log in certain ideal settings serves this function. However, throughout most of the Leonardian carbonate succession (in fact, throughout most of the Permian carbonate section in the Permian Basin) the gamma-ray log is not accurate for detailed correlation because of variable volumes of uranium, potassium, and thorium. The spectral gamma-ray log can help to distinguish variations in these elements and thus is useful in separating clastic-rich sections (that contain

high levels of potassium and thorium). Because small volumes of clastics are commonly associated with tidal-flat facies the spectral gamma ray is locally helpful in distinguishing tidal-flat facies from subtidal facies (Ruppel, 1992; 2002). However, variations in uranium content are not always systematic, and because of this, gamma-ray response commonly varies independently of facies. Resistivity logs can also locally be used to separate tidal-flat facies from subtidal facies on the basis of differences in saturation (Ruppel 2002). However, even under ideal circumstances, neither gamma-ray logs nor resistivity logs can accurately depict facies in Leonardian rocks.

Accordingly, we used utilized porosity logs to define facies and cycle tops in the Lower Clear Fork section at Fullerton field. The basis for this approach comes from integrated studies of cores and wireline logs at Fullerton that demonstrate two important attributes of Leonardian cycles. First, cycle-capping facies are either grain-rich subtidal or tidal-flat facies. Second, porosity is most commonly associated with these facies and therefore is most typically developed at cycle tops. These relationships are key to the use of wireline logs for correlation of cycles and of flow units.

It is important to understand that there are limitations to the accuracy of the porosity log correlation method. For example, because of diagenesis, all carbonate facies display some variations in porosity. Cycle-top facies in the Leonardian, whether grainstone or tidal flat, do exhibit lateral changes in porosity. So locally, cycle tops defined from porosity may be slightly mispositioned (e.g., due to a local decrease in porosity in the cycle-top facies or a local increase in porosity in the overlying cycle-base facies). From a strict chronostratigraphic point of view, this means that some cycle tops are incorrect and that cycle correlations locally cross time lines. From a reservoir point of view, however, this result is actually probably preferable. That is

because these Leonardian rocks rarely contain cycle-base flow barriers and flow probably does locally cross cycle boundaries. In any case, the porosity log correlation method, if properly constrained by core and outcrop calibration of facies, porosity, and cyclicity, is the most geologically sound basis for constructing cycle correlations and establishing the basis for true flow-unit correlations.

It is also important, however, to correlate geologically defined cycle tops at the highest resolution possible. For example, outcrop studies demonstrate that cycles less than 10 ft thick can be correlatable over large areas of the platform. Where wireline data permit, an effort should be made to correlate these thin cycles through the reservoir as well, even if later upscaling is planned for reservoir modeling. This is important for two reasons. First, coarser scale correlations are much more likely to be in error. At Fullerton, we found that early correlations made at the sequence or cycle set scale were later proven to be off by a cycle or two after we recorrelated the succession at the cycle scale. From a reservoir modeling point of view, this means that flow units defined by coarse scale correlations are more likely to cross-connect flow layers than those defined by finer scale correlations. Second, upscaling (grouping of cycles into thicker flow-unit packages for modeling) is more likely to retain the original geological architecture if based on fine-scale (i.e., cycle scale) correlations. Accordingly, we attempted to correlate the reservoir succession at the highest possible level of detail supported by outcrop and core observations and wireline resolution.

Lower Clear Fork Reservoir Architecture

The robustness of the use of porosity logs for defining facies and cyclicity is apparent from core and log relationships in HFS L 2.3. A comparison of core data and porosity logs in the FCU 6122 well (fig. 45) shows that porosity is nearly entirely associated with cycle-top tidal-flat

facies. Thus, porosity logs can be used to define both facies and cyclicity. Other cored wells in the field exhibit the same core/log relationship. Although not an oil-producing part of the reservoir, the L 2.3 section demonstrates the log/porosity calibration that underlies all cycle-based correlation in the field. The cycles apparent from the porosity log response, which average about 10 ft in thickness, are relatively easily correlated across of the field.

The same approach is applicable to the subtidal sections in the Lower Clear Fork. However, in these cases, cycle tops are typically composed of grain-rich subtidal facies. Here too, however, there is a strong relationship in cored wells between cycle-top facies and porosity (fig. 46).

Using this approach at Fullerton, we defined and correlated 15 cycles in the Lower Clear Fork (fig. 4). The average thickness of these cycles is about 17 ft for the entire interval of L 2.1 and L 2.2. However, cycle thickness varies systematically by sequence within this interval. HFS L 2.2 cycles average about 11 ft in thickness, whereas L 2.1 cycles, with the exception of low-accommodation tidal-flat cycles at the base and top of the sequence, are nearly twice as thick (fig. 8). This is probably due to two factors. First, L 2.1 deposits record the maximum flooding of the platform and probably the development of maximum accommodation. The overall upward thinning of cycles from L2.1 to L 2.2 is consistent with an overall upward decrease in accommodation. Second, lateral changes in facies stacking in L 2.1 cycles suggest local variations in sediment accumulation patterns that may have been caused by topographic relief on the platform during L 2.1 flooding. The resultant complex vertical and lateral facies distribution patterns make accurate definition of cycles difficult. As a result, cycles defined for L 2.1 may actually reflect combinations of cycles or cycle sets.

Wichita Reservoir Architecture

Rigorous cycle definition is not possible for the Wichita because of the preponderance of very low accommodation, tidal-flat facies. Both core and outcrop studies show that rocks deposited in such settings rarely display systematic trends in vertical facies stacking and generally exhibit very low lateral facies continuity. Accordingly, patterns of depositional facies do not define extrinsic controls (e.g., sea-level rise and fall) but rather local controls on sediment accumulation (e.g., paleotopography and climate). Thus for the Wichita, it is necessary to use diagenetic features to develop a reservoir framework.

Key diagenetic features used to define Wichita "cycles" are mineralogy and porosity. In the northern part of the field, the upper Wichita contains multiple intervals of low-porosity limestone (figs. 8, 20). Because these intervals are generally parallel to overlying and underlying cycle and sequence boundaries and because they are relatively continuous (fig. 8), we suspect that their formation was related to cycle deposition, exposure, and diagenesis. For example, early dolomitization of peritidal cycle tops has been widely documented in low-accommodation carbonate platform successions of all ages. By analogy, these limestone beds probably represent undolomitized cycle bases, whereas the intervening dolostone beds define cycle tops. As such, the architecture of these diagenetic "cycles" is closely tied to depositional surfaces and thus represents a good approximation of time surfaces. These surfaces are also especially useful from a reservoir point of view because they define layers of low and high porosity and permeability. The top four "cycles" in the Wichita are defined on the basis of these cyclic dolostone (high porosity) - limestone (low porosity) couplets (fig. 4).

However, no limestone is present in the upper Wichita in the southern part of the field area (fig. 20) nor in the lower part of the Wichita in any part of the field (fig. 8). In these areas, it is necessary to use porosity alone to construct the reservoir framework. Although it still likely

that porosity variations in these areas are closely tied to diagenesis associated with depositional surfaces (i.e., cycle tops), we have little independent evidence (i.e., mineralogical variations) with which to demonstrate this. Accordingly, the framework established for these parts of the Wichita is far less geologically robust than that defined for other parts of the reservoir. For this part of the reservoir we defined and correlated 12 surfaces on the basis of porosity. We have confidence that these surfaces are subparallel to time surfaces on the basis of their parallelism to overlying Lower Clear Fork cycle-top surfaces and to the middle Wichita marine floodback that marks the L1–L2 boundary. However, we cannot tie them rigorously to cyclicity.

Abo Reservoir Architecture

The Abo is dominated by clinoformal bedding typical of outer ramp carbonate deposits; this is demonstrated both by outcrop studies (Kerans and others, 2000) and by 3-D seismic data at Fullerton (fig. 42). It is therefore certain that the Abo architecture differs significantly from the generally subparallel character of the depositional surfaces of the platform-top Wichita and Lower Clear Fork successions. Outcrop studies and seismic studies at Fullerton and elsewhere (Kerans others, 2000; Ruppel and others, 2000) also demonstrate that clinoformal outer platform successions like the Abo do not contain readily correlatable cyclic successions. This is due to changes in sources and distributional patterns and to extreme variations in lateral textures and fabrics of these transported sediments. Accordingly, it is not possible to establish an accurate internal architecture for these deposits. For purposes of reservoir modeling, we have created a series of conceptual clinoform surfaces to constrain the reservoir architecture. Although these surfaces do not accurately describe the architecture of the Abo, they do illustrate the nonparallel and nonhorizontal nature of these deposits.

Reservoir Model

The architecture of the reservoir framework developed for the Clear Fork reservoir at Fullerton is depicted by Figure 47. Key aspects of this model are (1) the subhorizontal and subparallel nature of Clear Fork and upper Wichita (L 2) surfaces, (2) the effective pinch-out of lower Wichita (proximal L 1) surfaces at the facies change from Wichita tidal flats to Abo subtidal, and (3) the clinoformal nature of Abo (distal L 1).

Porosity Distribution

Core and log data from wells that penetrate the Abo indicate that the Abo locally contains high porosity. However, well control is too sparse and incomplete to accurately map porosity distribution. Wang (this report) presents an estimation of the 3-D distribution of Abo porosity using a full field based on available porosity data and a conceptual geological framework. However, the accuracy of this distribution must be considered relatively low.

The Wichita Formation contains higher porosity than either the Abo or the Lower Clear Fork (fig. 48). This total porosity map reveals that highest porosity lies along the field structural crest (compare figs. 48 and 5), suggesting that porosity development may have been a function of structure. However, when porosity is examined by stratigraphic horizon this interpretation seems less obvious. The key element of porosity distribution in the lower parts of the Wichita is the marked decrease in porosity to the southeast due to the southeastward facies transition from Wichita tidal flat to Abo subtidal facies (and accompanying decrease of Wichita thickness) along the margin of the inner platform (fig. 49). Lower Wichita porosity distribution in the interior platform of these L 1 Wichita tidal-flat deposits shows no obvious trend, although localized areas of high porosity are apparent in both intervals.

The lower part of the upper Wichita (Fig. 50), which represents the base of the L 2 composite sequence and the beginning of L2 transgression (HFS L 2.0), displays a very well defined, arcuate trend of porosity that generally parallels the underlying L 1 Wichita/Abo facies transition (fig. 49). Note that both the wireline log data (fig. 50b) and the 3-D seismic amplitude extraction data (fig. 50c) image this trend well. The transition from L 2.0 upper Wichita rocks to L2.0 Lower Clear Fork rocks is located just eastward of this belt of porosity. The decrease in porosity southeastward from this belt is thus associated with a change from tidal-flat rocks to subtidal-flat rocks, presumably the result of topographic dip and changes in bathymetry and accommodation downdip on the lower Wichita-Abo platform. The decrease in porosity to the northwest, however, is not associated with any apparent change in depositional facies. Wichita rocks in the northern part of the field are depositionally similar facies. Accordingly, the cause of porosity development must be more a function of diagenesis than deposition. A model for this diagenesis is presented in the following section.

The uppermost Wichita also displays strong differential development of porosity across the field area that does not appear to be related to depositional facies. Areas of highest porosity are located in the northern and southern parts of the field. Low porosity is encountered in the center and northwest parts of the area (fig. 50a). Like the lower Wichita, there are no apparent systematic differences between the tidal-flat deposits across the field. Thus, these variations must be the result of differential diagenesis. Porosity patterns suggest that upper Wichita porosity may exhibit a similar, albeit westwardly displaced, arcuate trend much like that in the lower Wichita. The high-porosity area in the north extends southwestward and may continue west of the field to link up with the porosity in the southern end of the field. If so, this would imply a link between reservoir development and platform geometry similar to that suggested for the lower Wichita.

The more westward development of this porosity trend is consistent with progressive transgression of the L2 platform and backstepping of the Wichita tidal-flat systems tract.

Limestone is common in the upper Wichita tidal-flat succession throughout the northern part of the field but is not related to areal trends in porosity. It does, however, affect fluid flow through this part of the reservoir.

The Lower Clear Fork HFS L 2.1 displays an arcuate trend in porosity development that is very similar to that seen in the upper Wichita (fig. 51b, c). Like the uppermost Wichita (fig. 50a), there is a strong suggestion that the northern trend may extend west of the field and curve south to link up with the southern areas of porosity as does the lower upper Wichita (fig. 50b). As is the case with the Wichita porosity development, depositional facies do not appear to be the dominant controlling factor in the development of this trend. The eastward decrease in porosity (in the southern part of the field) is associated with a gradual change from middle ramp grain-rich packstones to outer ramp fusulinid-rich wackestones. The area of high porosity may represent a low-energy ramp crest because the abundance of ooid-skeletal grain-dominated packstones and grainstones is somewhat greater. But the change in depositional facies associated with the major decrease in porosity into the northwestern part of the field appears subtle (fig. 51b). Instead, it is apparent that, like the Wichita, high porosity in L 2.1 is dominantly the result of diagenetic patterns. There is almost a 1:1 relationship between the presence of limestone and high-porosity areas (compare figs. 23 and 51b). Areas of high porosity in the northern part of the field contain mixtures of porous dolostones and porous limestone; the high-porosity area at the south end of the field is nearly all limestone.

No obvious trend in porosity is apparent in HFS L 2.2 (fig. 51a). However, like L2.1, the areas of highest porosity are associated with limestone. For L2.2 this is dominantly in the

southern end of the field; however, a small area of limestone also exists in the northwest corner of the field (compare figs. 25 and 51a).

Models for Porosity Development

As we have discussed, porosity is developed in all parts of the Abo–Wichita– Lower Clear Fork reservoir section. However, there are obvious areal variations in porosity that reflect a combination of depositional, diagenetic, and structural controls on reservoir development. Most of the major reservoir intervals exhibit spatial variations in porosity development that parallel platform paleotopography. This is particularly apparent in the lower and upper parts of the upper (L2) Wichita and in the Lower Clear Fork (HFS 2.1) (fig. 20E). In each of these cases, trends of high porosity are situated immediately up depositional dip from the position of the underlying Wichita-Abo facies boundary. However, the mechanism for porosity development must differ between the Wichita (fig. 20Ea,b) and the Lower Clear Fork (fig. 20Ec).

In the case of both Wichita intervals, depositional facies in the high-porosity trend are essentially identical to those in low-porosity areas both updip and downdip depositionally (fig. 20Ea, b). This indicates that porosity formation is the result of local diagenetic processes. Stable isotope data reported for the Fullerton field reservoir by Kaufman (1991) are consistent with those reported herein and suggest that high-porosity dolomites in the Wichita were formed by seawater-dominated fluids perhaps mediated by meteoric mixing. This is indicated by light $\delta^{18}\text{O}$ values (average: 0.1 ‰ ; $\delta^{13}\text{C} = 2.6$ ‰ PDB). The restriction of high-porosity rocks to the downdip margin of the Wichita tidal flat suggests the possibility that porosity development may be the result of early seawater-dominated dolomitization and stabilization along the seaward margin of the Wichita tidal flat. Available data suggest that less porous, updip Wichita tidal-flat deposits were dolomitized during a later event by very different fluids. These rocks contain

heavier isotopes ($\delta^{18}\text{O} = 2.7 \text{ ‰}$; $\delta^{13}\text{C} = 3.0 \text{ ‰}$ PDB) that are typical of younger, Lower and Upper Clear Fork rocks and are more indicative of brines that were evaporatively concentrated (Saller and Henderson, 1998; Ruppel, 2002). Possible sources for such brines based on stratigraphic data are updip tidal flats at the top of HFS 2.1, 2.2, and 2.3 or those developed during Tubb deposition. The presence of limestone interbeds in the Wichita in the northern, less porous part of the field suggests such a distal diagenetic setting (i.e., one that is distal to the source of diagenetic fluids). The lack of porosity in the updip Wichita tidal flats may reflect compaction as well as porosity reduction caused by dolomitization and sulfate emplacement during Clear Fork/Tubb reflux dolomitization.

The Lower Clear Fork HFS 2.1 also displays a trend in porosity development that closely parallels the Wichita-Abo facies transition as well as the Wichita–Clear Fork facies transition (fig. 20Ec). In this case, however, there is a relationship between both facies and mineralogy and porosity development. Facies data suggest that the trend of high porosity may represent a platform ramp crest: an area characterized by more common ooid-bearing, grain-rich packstones and grainstones and by locally more abundant tidal-flat caps. Ramp-crest development was probably controlled by inherited paleotopography over the L1 (Wichita-Abo) inner ramp margin and/or differential subsidence over deep-seated faults in the same way that the position of the Wichita-Abo facies transition is most likely controlled by such deep structures. Mineralogical data show that this trend is also an area of abundant calcite; lower porosity areas to the east and west are nearly entirely dolomite (see fig. 23). Strontium and oxygen isotope data from these calcites indicate that they are essentially unaltered original marine precipitates. Updip dolomites display values that indicate that they were formed from evaporatively concentrated brines after deposition. These data together suggest the HFS L2.1 porosity trend may have been formed by

early marine calcite cementation in well-agitated and -oxygenated conditions along the ramp crest. Lower porosity in updip dolomites is probably the result of predolomitization compaction and possibly by porosity occlusion by dolomite and anhydrite cementation. Both compaction and dolomitization, and thus porosity loss, were probably limited in the ramp crest because of the early calcite cementation and stabilization that took place there.

SUMMARY

Both the procedure used to develop the reservoir framework at Fullerton field and many of the attributes of this framework offer important guidelines for the characterization of Clear Fork reservoirs and for the development of predictive models of the distribution of reservoir properties. Key findings from this study include the following.

The Leonardian reservoir succession in the Permian Basin consists of three formations or facies successions: Abo, Wichita, and Lower Clear Fork. Each of these is characterized by distinctive facies, cyclicity, depositional architecture, and porosity development.

The Abo consists largely of porous outer ramp, open-marine, fusulinid/crinoid facies whose clinoformal architecture is clearly expressed on seismic. Lateral facies continuity is poor. As a result, porosity distribution is complex and probably highly discontinuous.

The Wichita, which includes both highstand systems tract updip equivalents of the Abo (Leonardian sequence L1) and transgressive systems tract updip equivalents of the basal Lower Clear Fork (Leonardian sequence L2), consists of a thick succession of aggradational, restricted tidal-flat facies. These rocks contain high porosity but usually relatively low permeability and display poor small-scale continuity. Cyclicity is poorly developed; reservoir architecture is more controlled by diagenesis than by depositional facies. Limestone intervals in the dominantly

dolomitic Wichita display extremely low porosity and permeability and act as local fluid-flow baffles between the higher porosity intervals of dolostone.

The Lower Clear Fork consists of a succession of three high-frequency sequences (HFS), each of which records sea-level rise (transgression) and fall (regression). Reservoir development is largely restricted to subtidal facies (late transgression and early highstand). Highest porosity and permeability in the Lower Clear Fork is associated with incompletely dolomitized grain-rich packstones and grainstones. Cyclicity is well developed. However, facies are discontinuous at the cycle scale.

Karst features (including inclined beds and monomict and polymict cave-fill breccias) are common in the Wichita. Neither wireline log data nor core analysis data reveal any definitive differences between karsted and unkarsted sections of Wichita. Nevertheless, these karst zones, which are only definable on image logs and cores, may locally affect fluid flow.

Gamma-ray logs are useful for general correlations only. As in other Leonardian reservoirs, high gamma-ray response is usually an indication of the presence of clays and silt in tidal-flat facies; low gamma-ray response indicates subtidal facies. Porosity logs or image logs must be used for high-resolution, cycle-scale correlation. Three-dimensional seismic provides excellent resolution of both the reservoir architecture and the distribution of reservoir porosity at the HFS scale.

Porosity development is largely a function of early diagenesis controlled by platform-margin geometry. Zones of highest porosity in the Wichita are the result of early dolomitization and stabilization along the outer margin of the Wichita inner platform. A similar subparallel zone in the Lower Clear Fork was created by early calcite cementation and mineralogical stabilization in the platform ramp crest.

ACKNOWLEDGMENTS

The results presented in this paper are part of continuing research into the styles and causes of heterogeneity in shallow-water platform carbonate reservoirs in the Permian Basin by the Bureau of Economic Geology. Frequent, sometimes vigorous, discussions with colleagues at the Bureau, including Charlie Kerans, Robert Loucks, Jerry Lucia, and Jim Jennings, have been especially helpful in formulating the interpretations presented herein. Funding for the study was provided by contract no. DE-FC26-01BC15351 from the U. S. Department of Energy. Additional funding was provided by member sponsors of the Bureau's Carbonate Reservoir Characterization Research Laboratory, including Anadarko, Aramco, BP, ChevronTexaco, ExxonMobil, Great Western Drilling, Kinder Morgan, Marathon, Occidental Petroleum, Petroleum Development Oman, Shell International, Statoil, and TotalFinaElf. Additional funding for the study was provided by ExxonMobil and The University of Texas System. Special thanks are extended to David Smith, Terry Anthony, Steve Krohn, and Amy Powell of ExxonMobil and Jeff Simmons, Craig Kemp, and John Stout of Oxy for their contributions to organizing the project and providing data. David Smith and Terry Anthony have been especially helpful in providing insights into the field geology and engineering issues. We also express our appreciation to Stephen Hartman and Tim Hunt of The University of Texas System West Texas Operations Office for providing both collaborative funding and data.

REFERENCES

- Atchley, S. C., Kozar, M. G., and Yose, L. A., 1999, A predictive model for reservoir characterization in the Permian (Leonardian) Clear Fork and Glorieta Formations, Robertson field area, West Texas: American Association of Petroleum Geologists Bulletin, v. 83, p. 1031–1056.
- Bebout, D. G., and others, 1987, Characterization of the Grayburg reservoir, University Lands Dune field, Crane County, Texas: The University of Texas at Austin, Bureau of Economic Geology Report of Investigations No. 168, 98 p.
- Dutton, S. P., Kim, E. M., Broadhead, R. F., Breton, C. L., Raatz, W. D., Ruppel, S. C., and Kerans, C., 2004, Play analysis and digital portfolio of major oil reservoirs in the Permian Basin: application and transfer of advanced geological and engineering technologies for incremental production opportunities: The University of Texas at Austin, Bureau of Economic Geology, Final report to the Department of Energy, contract DE-FC26-02NT15131, 408 p.
- Fitchen, W. M., Starcher, M. A., Buffler, R. T., and Wilde, G. L., 1995, Sequence stratigraphic framework and facies models of the early Permian platform margins, Sierra Diablo, West Texas, *in* Garber, R. A., and Lindsay, R. F., eds., Wolfcampian-Leonardian shelf margin facies of the Sierra Diablo - seismic scale models for subsurface exploration: West Texas Geological Society Publication 95-97, p. 23–66.
- Garber, R. A., and Harris, P. M., 1990, Depositional facies of the Grayburg/San Andres dolomite reservoirs; Central Basin Platform, Permian Basin, *in* Bebout, D. G., and Harris, P. M. (eds.), Geologic and engineering approaches in evaluation of San Andres/Grayburg hydrocarbon reservoirs - Permian Basin: The University of Texas at Austin, Bureau of Economic Geology, p. 1–20.
- Hardie, L. A., and Garrett, P., 1977, General environmental setting, *in* Hardie, L. A., ed., Sedimentation on the modern carbonate tidal flats of the northwest Andros Island, Bahamas: The Johns Hopkins University Press, Baltimore and London, p. 12–50.
- Holtz, M. H., and Garrett, C. M., 1990, Geologic and engineering characterization of Leonardian carbonate oil reservoirs: a framework for strategic recovery practices in four oil plays (abs.), *in* Flis, J. E., and Price, R. C., eds., Permian Basin oil and gas fields: innovative ideas in exploration and development: West Texas Geological Society Publication No. 90-87, p. 76.
- Holtz, M. H., Ruppel, S. C., and Hocott, C. R., 1992, Integrated geologic and engineering determination of oil-reserve-growth potential in carbonate reservoirs: Journal of Petroleum Technology, November, p. 1250–1258.
- Jones, R., and Ruppel, S., 2004, Evidence of post-Wolfcampian fault movement and its impact on Clear Fork reservoir quality: Fullerton field, West Texas, *in* Trentham, R. C., Banking

- on the Permian Basin: plays, field studies, and techniques: West Texas Geological Society Fall Symposium: West Texas Geological Society Publication #04-112, p.207.
- Kaufman, J., 1991, A predictive model for early dolomitization in the Permian Basin: Exxon Production Research Unpublished report EPR.6X.91, 31 p.
- Kerans, Charles, Kempter, K., Rush, J., and Fisher, W. L., 2000, Facies and stratigraphic controls on a coastal paleokarst: Lower Permian, Apache Canyon, West Texas, *in* Lindsay, R., Trentham, R., Ward, R. F., and Smith, A. H. (eds.), Classic Permian geology of West Texas and Southeastern New Mexico, 75 Years of Permian Basin oil & gas exploration & development: West Texas Geological Society Publication 00-108, p. 55–82.
- Kerans, Charles, Lucia, F. J., and Senger, R. K., 1994, Integrated characterization of carbonate ramp reservoirs using Permian San Andres Formation outcrop analogs: American Association of Petroleum Geologists Bulletin, v. 78, no. 2, p. 181–216.
- Kerans, Charles, and Fitchen, W. M., 1995, Sequence hierarchy and facies architecture of a carbonate ramp system: San Andres Formation of Algerita Escarpment and Western Guadalupe Mountains, West Texas and New Mexico: The University of Texas at Austin, Bureau of Economic Geology Report of Investigations No. 235, 86 p.
- Kerans, Charles, and Ruppel, S. C., 1994, San Andres sequence framework, Guadalupe Mountains: implications for San Andres type section and subsurface reservoirs, *in* Garber, R. A., and Keller, D. R., eds., Field guide to the Paleozoic section of the San Andres Mountains: Permian Basin Section - SEPM, Publication No. 94-35, p. 105–115.
- Kerans, Charles, and Kempter, Kirt, 2002, Hierarchical stratigraphic analysis of a carbonate platform, Permian of the Guadalupe Mountains: The University of Texas at Austin, Bureau of Economic Geology (American Association of Petroleum Geologists/Datapages Discovery Series No. 5), CD-ROM.
- King, P. B., 1942, Permian of West Texas and southeastern New Mexico: American Association of Petroleum Geologists Bulletin v. 26, no. 4, p. 535–763.
- King, P. B., 1965, Geology of the Sierra Diablo region, Texas: U.S. Geological Survey Professional Paper 480, 185 p.
- Leary, D. A., 1985, Diagenesis of the Permian (Guadalupian) San Andres and Grayburg Formations, Central Basin Platform, Permian Basin, West Texas: unpublished Master's thesis, The University of Texas at Austin, 125 p.
- Leary, D. A., and Vogt, J. N., 1990, Diagenesis of the San Andres Formation (Guadalupian) reservoirs, University Lands, Central Basin Platform, *in* Bebout, D. G., and Harris, P. M., eds., Geologic and engineering approaches in evaluation of San Andres/Grayburg hydrocarbon reservoirs - Permian Basin: The University of Texas at Austin, Bureau of Economic Geology, p. 21–28.

- Loucks, R. G., 1999, Paleocave carbonate reservoirs: origins, burial-depth modifications, spatial complexity, and reservoir implications: American Association of Petroleum Geologists Bulletin, v. 83, p. 1795–1834.
- Lohman, K. C., and Walker, J. C. G., 1989, The $\delta^{18}\text{O}$ record of Phanerozoic abiotic cements: Geophysical Research Letters v. 16, p. 319–322.
- Longacre, S. A. , 1990, The Grayburg reservoir, North McElroy Unit, Crane County, Texas, *in* Bebout, D. G., and Harris, P. M. (eds.), Geologic and engineering approaches in evaluation of San Andres/Grayburg hydrocarbon Reservoirs - Permian Basin: The University of Texas at Austin, Bureau of Economic Geology, p. 239–273.
- Lucia, F. J. and Jennings, J. W., Jr., 2002, Calculation and distribution of petrophysical properties in the south Wasson Clear Fork field, in Lucia, F. J. (editor), Integrated outcrop and subsurface studies of the interwell environment of carbonate reservoirs: Clear Fork (Leonardian-age) reservoirs, West Texas and New Mexico: Final technical report to the Department of Energy, Contract No. DE-AC26-98BC15105, p. 95-142.
- Major, R. P., Vander Stoep, G. W., and Holtz, M. H., 1990, Delineation of unrecovered mobile oil in a mature dolomite reservoir: East Penwell San Andres Unit, University Lands, West Texas: The University of Texas at Austin, Bureau of Economic Geology Report of Investigations No. 194, 52 p.
- Mazzullo, S. J., 1982, Stratigraphy and depositional mosaics of lower Clear Fork and Wichita groups (Permian), northern Midland Basin, Texas: American Association of Petroleum Geologists Bulletin, v. 66, p. 210–227.
- Mazzullo, S. J., and Reid, A., 1989, Lower Permian platform and basin depositional systems, northern Midland Basin, Texas, *in* Crevello, P. D., Wilson, J. J., Sarg, J. F., and Read, J. F., eds., Controls on carbonate platform and basin development: Society of Economic Paleontologists and Mineralogists Special Publication, v. 44, p. 305–320.
- Presley, M. W., 1987, Evolution of Permian evaporite basin in Texas Panhandle: American Association of Petroleum Geologists Bulletin, v. 71, p. 167–190.
- Presley, M. W., and McGillis, K. A., 1982, Coastal evaporite and tidal-flat sediments of the upper Clear Fork and Glorieta Formations, Texas Panhandle: The University of Texas at Austin, Bureau of Economic Geology Report of Investigations No. 115, 50 p.
- Ruppel, S. C., Kerans, Charles, Major, R. P., and Holtz, M. H., 1994, Controls on reservoir heterogeneity in Permian shallow-water platform carbonate reservoirs, U.S.A.: implications for secondary recovery: The Arabian Journal for Science and Engineering, v. 19, no. 2B, p. 215–236.
- Ruppel, S. C., and Cander, H. S., 1988a, Effects of facies and diagenesis on reservoir heterogeneity: Emma San Andres field, West Texas: The University of Texas at Austin, Bureau of Economic Geology Report of Investigations No. 178, 67 p.

- Ruppel, S. C., and Cander, H. S., 1988b, Dolomitization of shallow-water platform carbonates by sea water and seawater-derived brines: San Andres Formation (Guadalupian), West Texas, *in* Sedimentology and geochemistry of dolostones: Society of Economic Paleontologists and Mineralogists, Special Publication No. 43, p. 245–262.
- Ruppel, S. C., and Bebout, D. G., 2001, Competing effects of depositional architecture and diagenesis on carbonate reservoir development: Grayburg Formation, South Cowden field, West Texas: The University of Texas at Austin, Bureau of Economic Geology Report of Investigations No. 263, 62 p.
- Ruppel, S. C., Park, Y. J., and Lucia, F. J., 2002, Applications of 3-D seismic to exploration and development of carbonate reservoirs: South Cowden Grayburg field, West Texas, *in* Hunt, T. J., and Lufholm, P. H., eds., The Permian Basin: preserving our past—securing our future: West Texas Geological Society, Publication No. 02-111, p. 71–87.
- Ruppel, S. C., 1992, Styles of deposition and diagenesis in Leonardian carbonate reservoirs in West Texas: implications for improved reservoir characterization: Society of Petroleum Engineers Annual Exhibition and Technical Conference, 24691, p. 313–320.
- Ruppel, S. C., 2002, Geological controls on reservoir development in a Leonardian (Lower Permian) carbonate platform reservoir, Monahans field, West Texas: The University of Texas at Austin, Bureau of Economic Geology Report of Investigations No. 266, 58 p.
- Ruppel, S. C., and Ariza, E. E., 2002, Cycle and sequence stratigraphy of the clear fork reservoir at South Wasson field: Gaines County, Texas, *in* Lucia, F. J. (editor), Integrated outcrop and subsurface studies of the interwell environment of carbonate reservoirs: Clear Fork (Leonardian-age) reservoirs, West Texas and New Mexico: Final technical report to the Department of Energy, Contract No. DE-AC26-98BC15105, p. 59-94.
- Ruppel, S. C., Ward, W. B., Ariza, E. E., and Jennings, J. W., Jr., 2000, Cycle and sequence stratigraphy of Clear Fork reservoir-equivalent outcrops: Victorio Peak Formation, Sierra Diablo, Texas, *in* Lindsay, R., Trentham, R., Ward, R. F., and Smith, A. H. (eds.), Classic Permian geology of West Texas and Southeastern New Mexico, 75 years of Permian Basin oil & gas exploration & development: West Texas Geological Society Publication 00-108, p. 109–130.
- Saller, A. H., and Henderson, N., 1998, Distribution of porosity and permeability in platform dolomites: insights from the Permian of West Texas: American Association of Petroleum Geologists Bulletin, v. 82, no. 8, p. 1528–1550.
- Shinn, E. A., 1983, Tidal flat, *in* Scholle, P. A., Bebout, D. G., and Moore, C. H., eds., Carbonate depositional environments: American Association of Petroleum Memoir 33, p. 171–210.
- Tyler, Noel, and Banta, N. J., 1989, Oil and gas resources remaining in the Permian Basin: targets for additional hydrocarbon recovery: The University of Texas at Austin, Bureau of Economic Geology Geological Circular 89-4, 20 p.

- Vogt, J. N., 1986, Dolomitization and anhydrite diagenesis of the San Andres (Permian) Formation, Gaines County, Texas: unpublished Master's thesis, The University of Texas at Austin, 202 p.
- Ye, Q., and Mazzullo, S. J. , 1993, Dolomitization of lower Permian platform facies, Wichita Formation, north platform, Midland Basin, Texas: *Carbonates and Evaporites* v. 8, no. 1, p. 55–70.
- Zeng, Hongliu, and Kerans, Charles, 2003, Seismic frequency control on carbonate seismic stratigraphy: a case study of the Kingdom Abo sequence, West Texas: *American Association of Petroleum Geologists Bulletin*, v. 87, no. 2, p. 273–293.

| SERIES | STAGE | SUBSURFACE | | | OUTCROP | | | | |
|---------------|------------|------------------------|------------|------------------|------------------------------------|------------------|---------------|-------------------|------------------|
| | | CENTRAL BASIN PLATFORM | | NORTHERN SHELF | GUADALUPE MOUNTAINS/ SIERRA DIABLO | | | | |
| | | NEW MEXICO | TEXAS | | PLATFORM | MARGIN | SEQUENCE | | |
| Lower Permian | LEONARDIAN | San Andres | San Andres | San Andres | San Andres | Cutoff | Guad 1 | | |
| | | Glorieta | Glorieta | Glorieta | Glorieta | | Victorio Peak | Leo 7-8 | |
| | | Yeso | Paddock | upper Clear Fork | Clear Fork Group | upper Clear Fork | Victorio Peak | Leo 6 | |
| | | | Blinebry | | | | | middle Clear Fork | Leo 5 |
| | | | Tubb | | | | | Tubb | Leo 4 |
| | | | Drinkard | | | | | lower Clear Fork | lower Clear Fork |
| | | Abo | Wichita | Wichita | Wichita | Bone Spring | Leo 2 | | |
| | | | | Abo | Abo | | Leo 1 | | |
| | | Wolfcamp | Wolfcamp | Wolfcamp | Hueco | Hueco | Wolf 3 | | |

Figure 1. Chart showing the Leonardian stratigraphic section in the Permian Basin including the Clear Fork Group and analogous units in New Mexico and in outcrop.

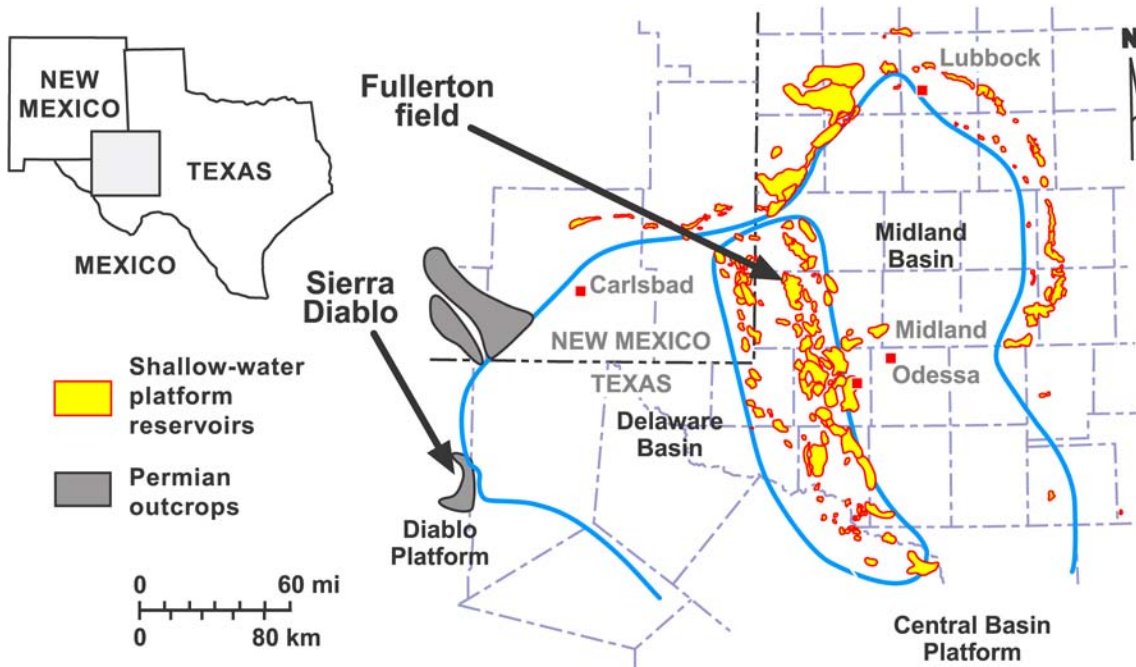


Figure 2. Regional map of the Permian Basin showing location of Fullerton field and analogous outcrops in the Sierra Diablo mountains.

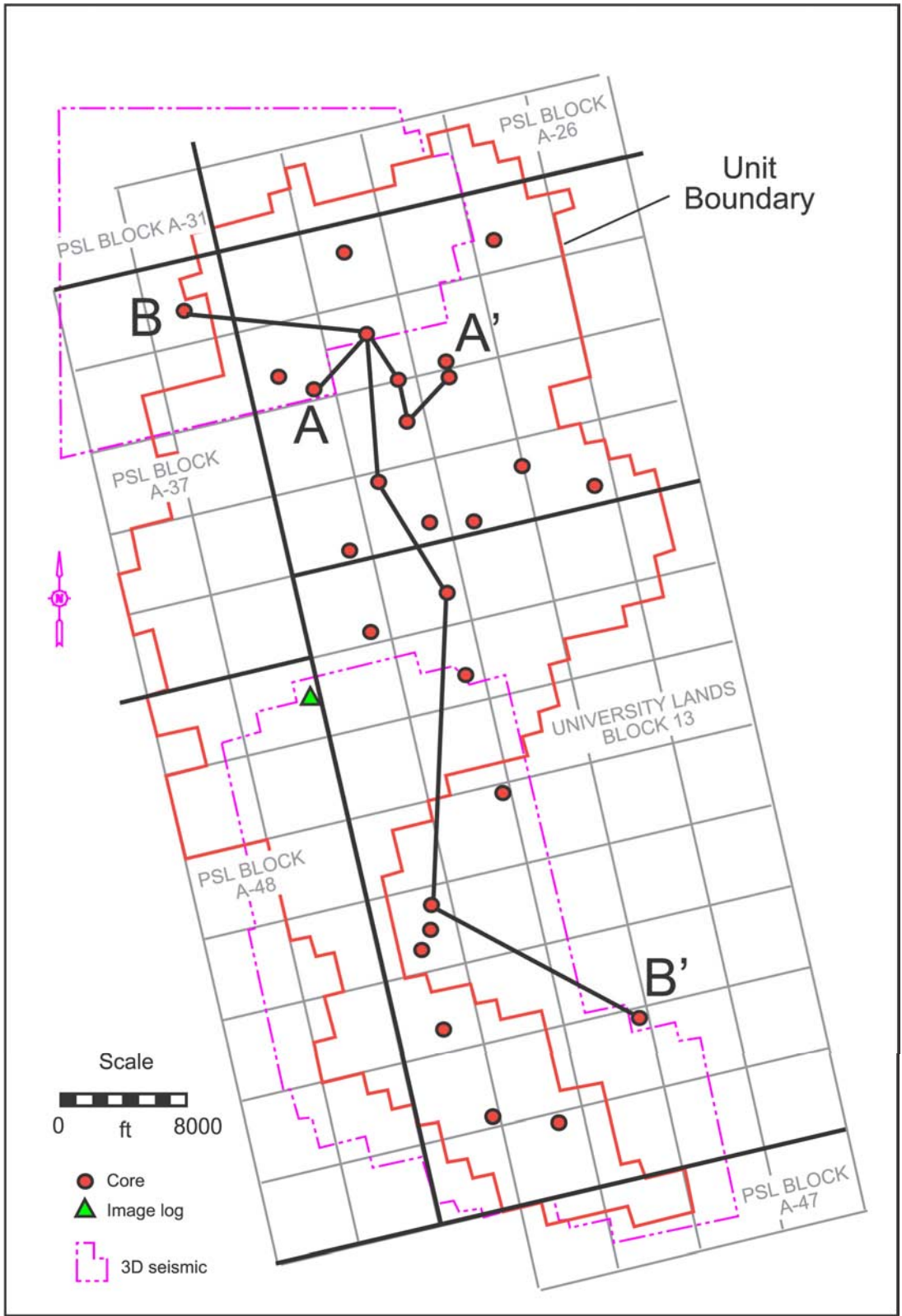


Figure 3. Map of Fullerton Clear Fork field showing location of focused study areas, cores, and 3-D seismic data.

TYPE LOG Fullerton Clear Fork Field

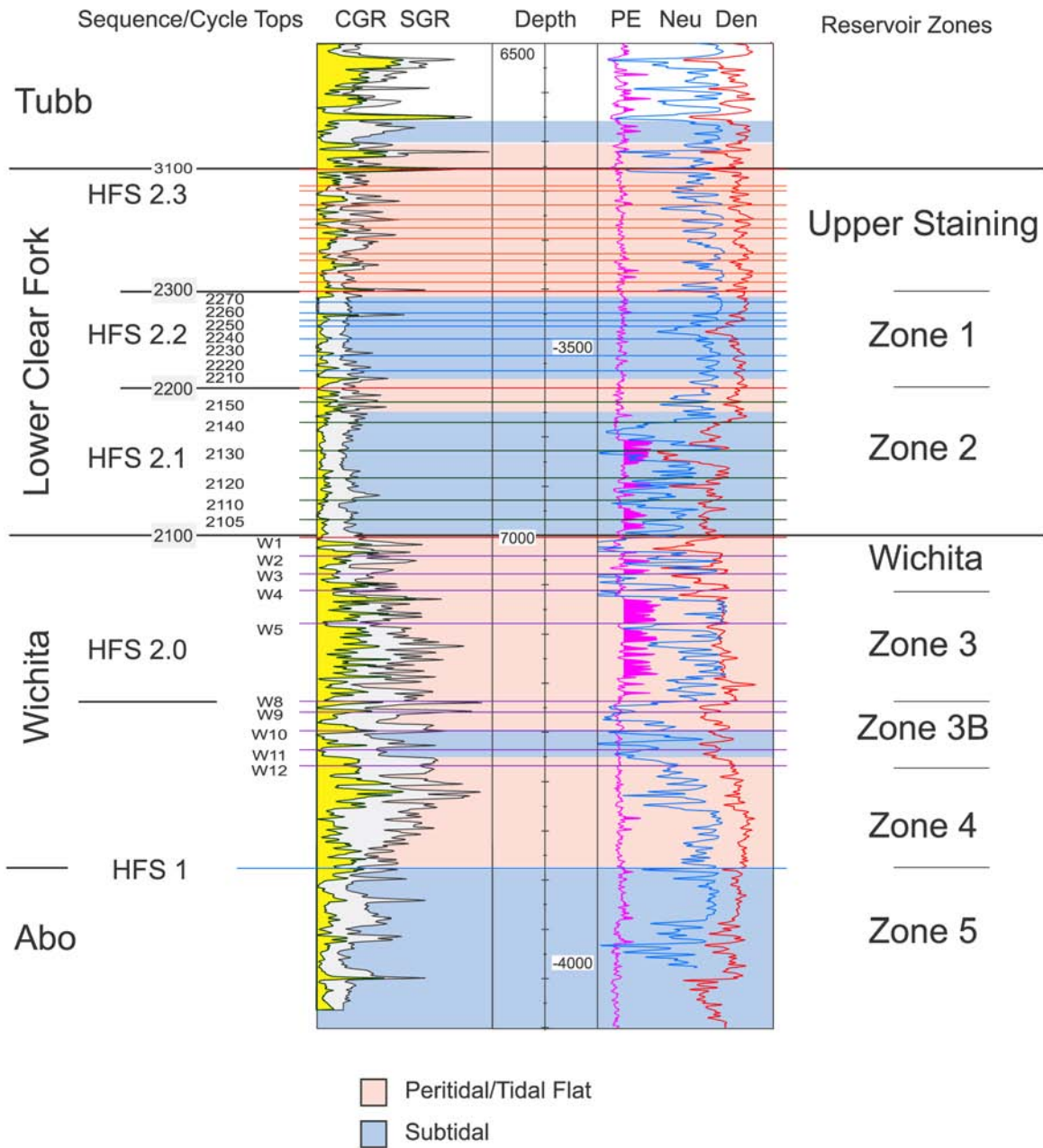


Figure 4. Type log of producing reservoir section at Fullerton Clear Fork field showing cyclicity and general facies patterns. Shaded areas of the PE log indicate the local presence of limestone in the dolomite-dominated section. Zones of elevated CGR log response indicate the presence of silt and clay.

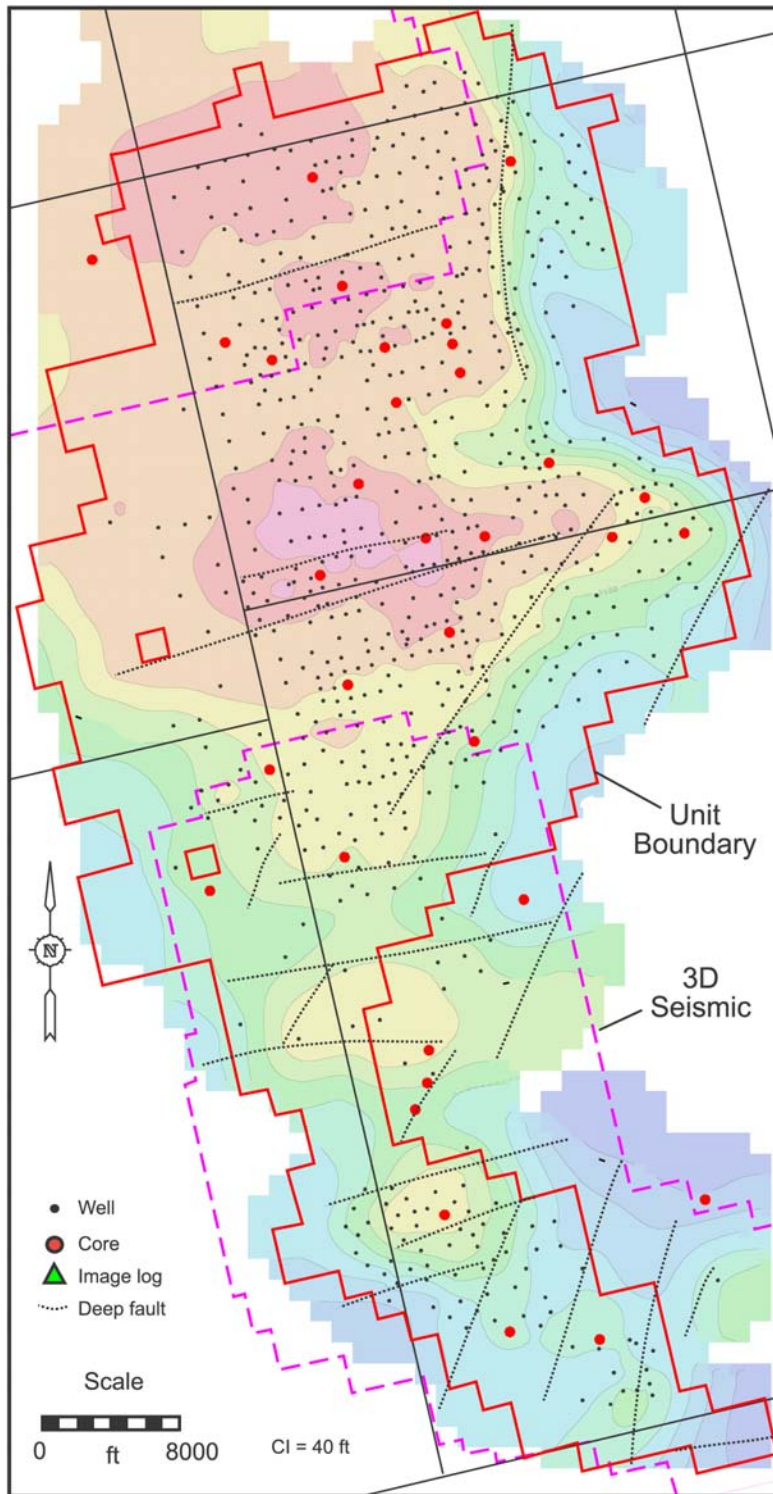


Figure 5. Structure of the Fullerton Clear Fork field. Datum is a prominent subtidal flooding event near the base of the Tubb Formation (see figures 4, 8).

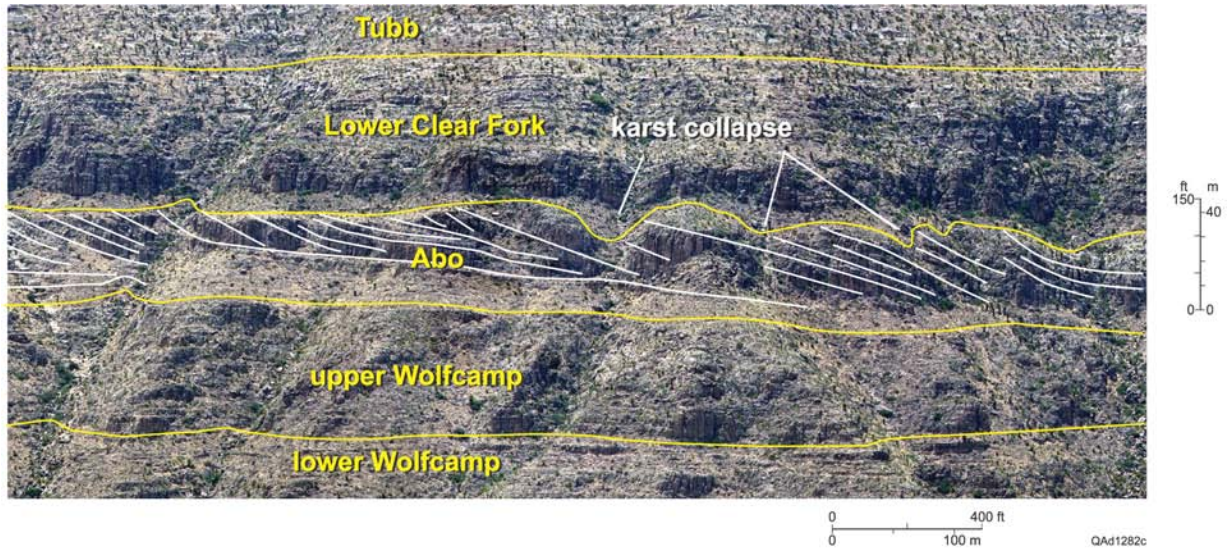


Figure 6. Outcrop photographs showing Abo–Lower Clear Fork section equivalent to producing reservoir interval at Fullerton field. Note top-lapping clinoformal geometry in the Abo and karst development at the Abo–Lower Clear Fork contact. Karst features are filled with locally collapsed peritidal tidal-flat deposits.

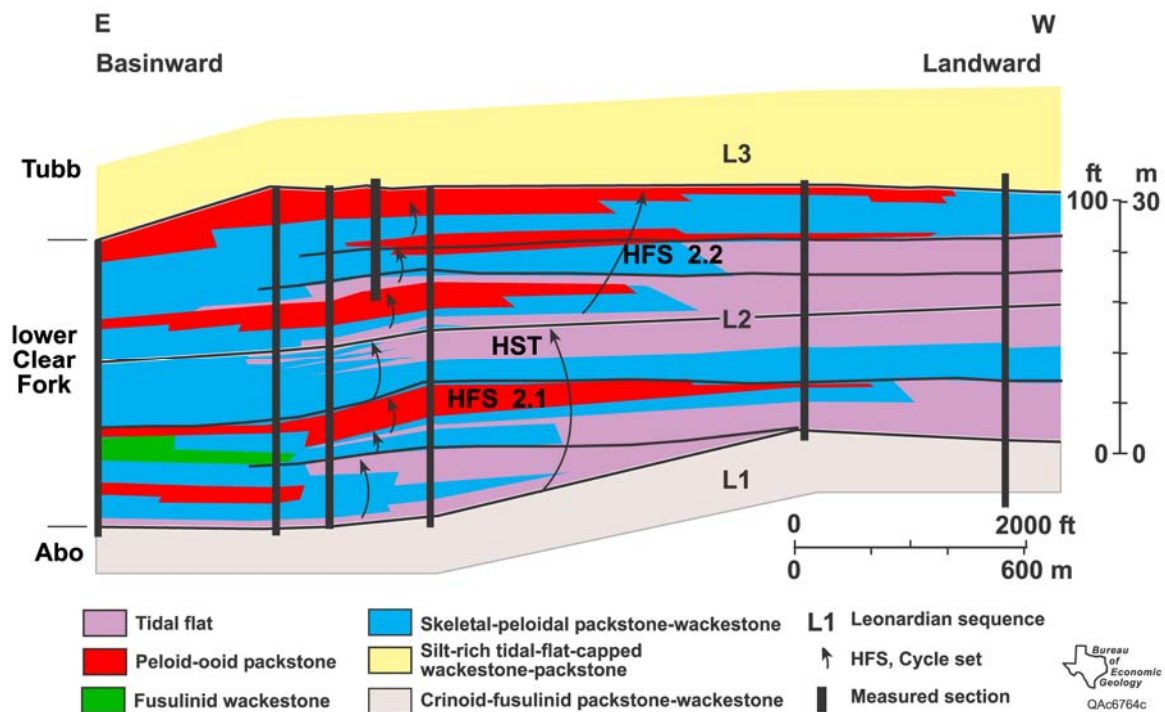


Figure 7. Cross section depicting lateral changes in facies and cyclicity in Sierra Diablo outcrops partly equivalent to Lower Clear Fork (sequence L2) reservoir rocks at Fullerton field. Note generally parallel, flat-lying contacts, and overall backstepping architecture.

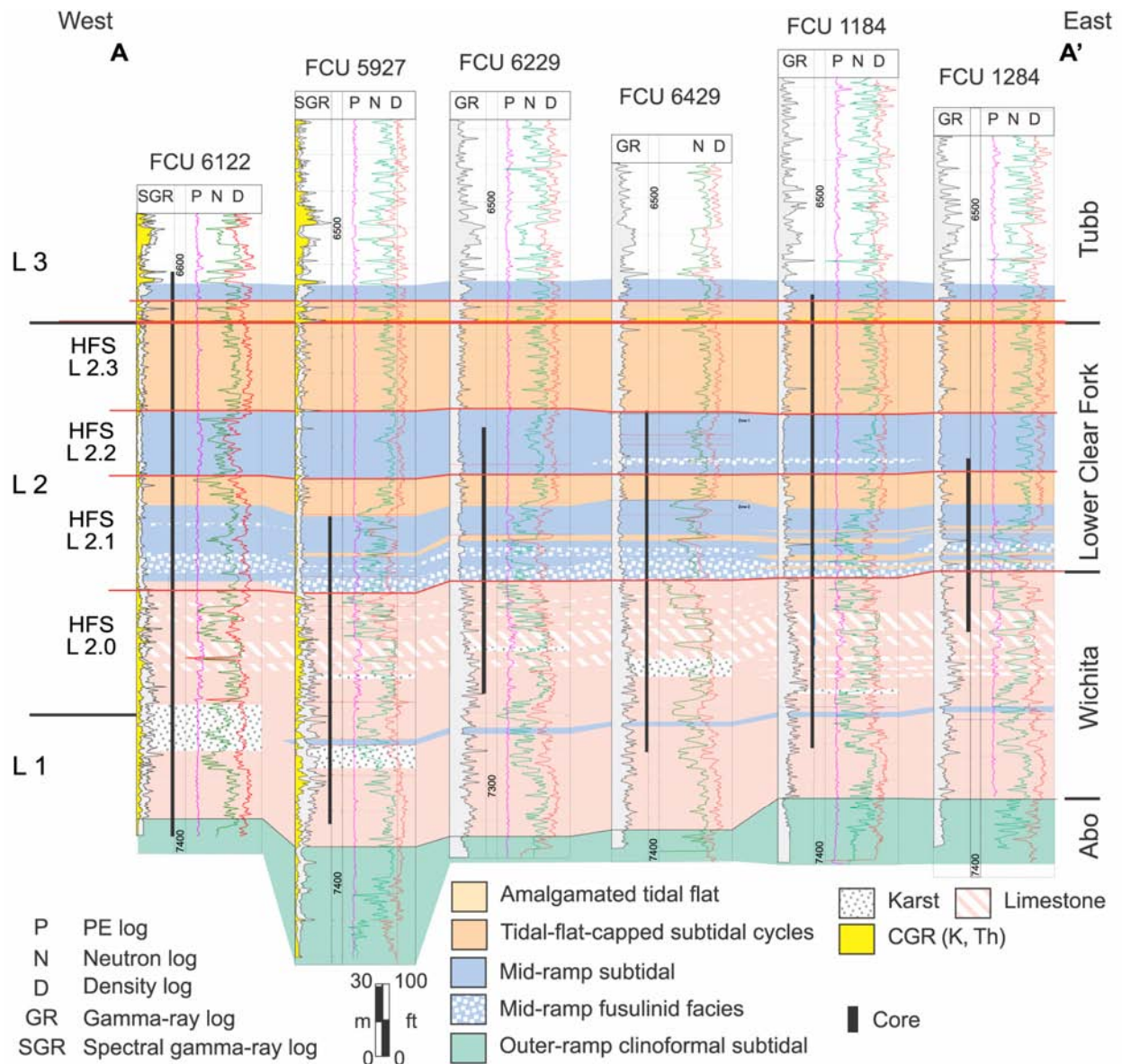


Figure 8. Cross section (A-A') illustrating sequence stratigraphy and facies in the central part of the Clear Fork reservoir at Fullerton field based on cores. The generally isopachous character of the reservoir section (Wichita–Lower Clear Fork) is consistent over most of the field area. Line of section shown in figure 3.

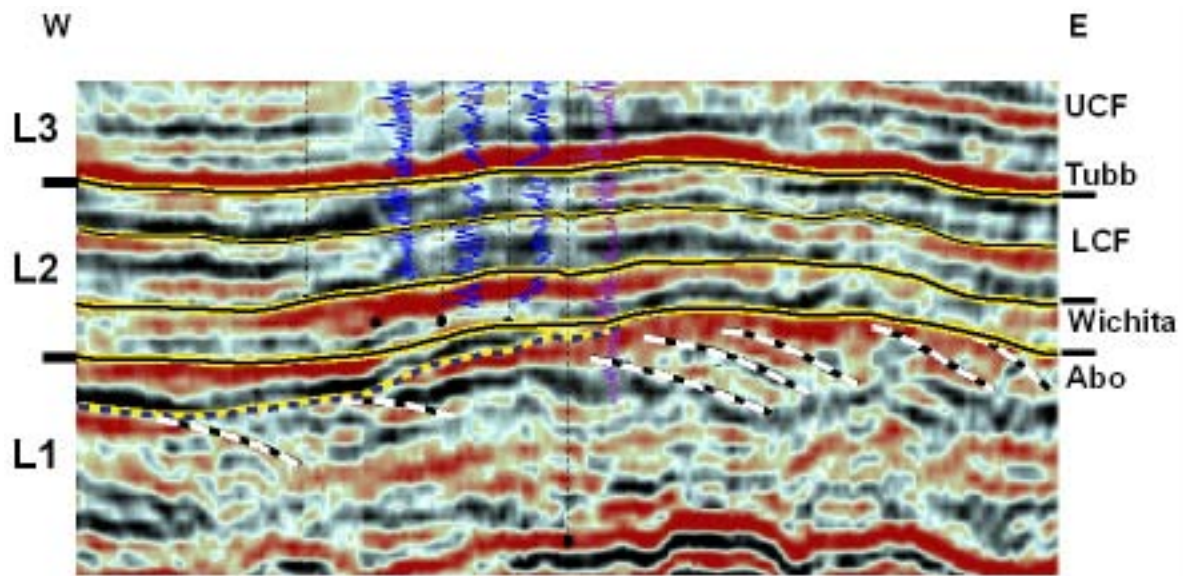


Figure 9. 3-D seismic section from southern part of Fullerton field showing seismic definition of the Clear Fork reservoir section. Yellow lines are time-line boundaries; dotted line defines the top of Abo Formation. Note that whereas the upper Wichita and Lower Clear Fork (LCF) intervals are essentially isopachous and continuous across the field, the lower Wichita and Abo display reciprocal thickness relationships. Blue lines define top-lapping Abo clinoforms. UCF = Upper Clear Fork.

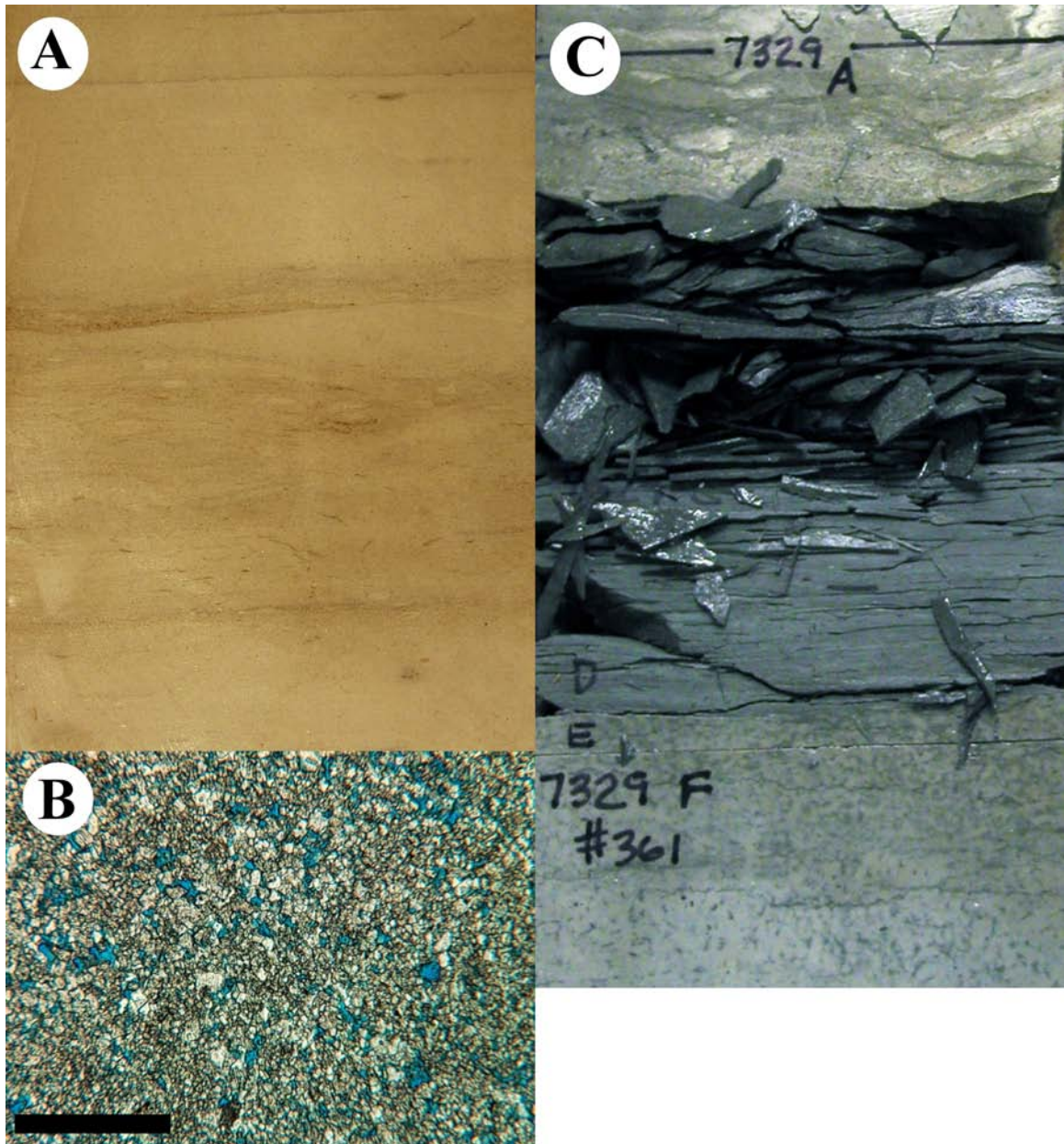


Figure 10. Core and thin-section photographs of typical Wichita tidal-flat facies. A. Slab photo of peritidal mudstone-wackestone showing weak laminations and local burrowing. Core is 4 inches wide. FCU 5927, depth: 7,021 ft. B. Photomicrograph of peritidal mudstone-wackestone facies showing abundant intercrystalline porosity. FCU 6122, depth: 7,092 ft; porosity: 13.8 percent; permeability: 1.6 md. Scale bar is 1 mm. C. Slab photo of clay-rich carbonate mudstone facies in the Wichita. Core is 4 inches wide. FM1 depth: 7,329 ft. Note underlying fenestral mudstone.

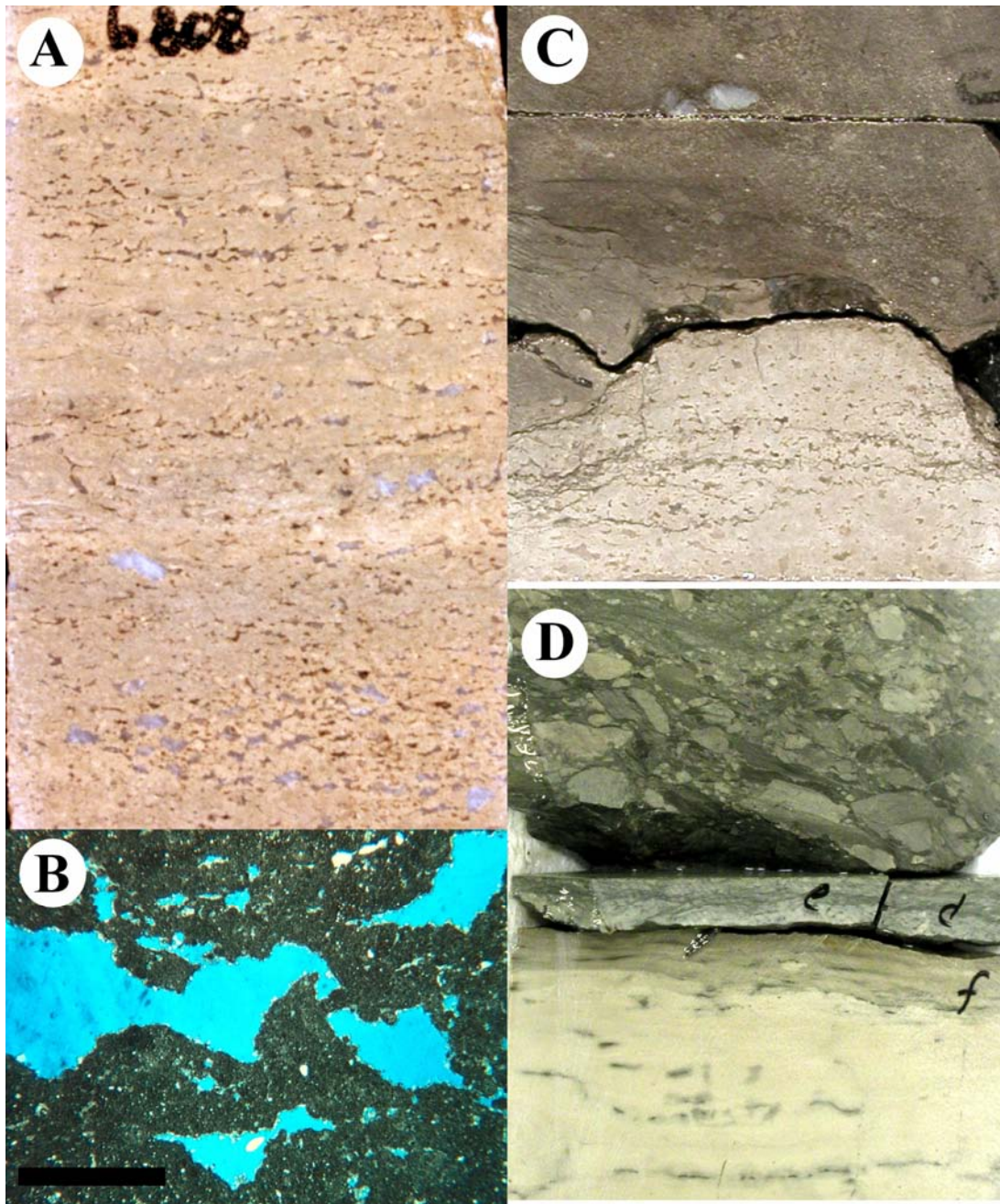


Figure 11. Core and thin-section photographs of typical tidal-flat facies and shallow subtidal facies in the Wichita and Lower Clear Fork. A. Slab photo of exposed tidal-flat facies showing typical parallel laminations and fenestral pores. Core is 4 inches wide. Lower Clear Fork FCU 7322, depth: 6,808 ft. Scale bar is 2 mm. B. Photomicrograph of exposed tidal-flat facies showing fenestral vuggy porosity. Lower Clear Fork FCU 6122, depth: 6,903 ft. Photo is 6 mm wide. C. Slab photo of cycle top showing fenestral exposed tidal-flat facies overlain by subtidal, burrowed peloid wackestone. Note small lithoclasts above cycle top. Lower Clear Fork, top HFS L 2.2. Core is 4 inches wide. FCU 7322, depth: 6,804 ft. D. Slab photo of large rip-up clasts overlying cycle top peritidal mudstone. Wichita FCU 7322, depth: 6,804 ft.

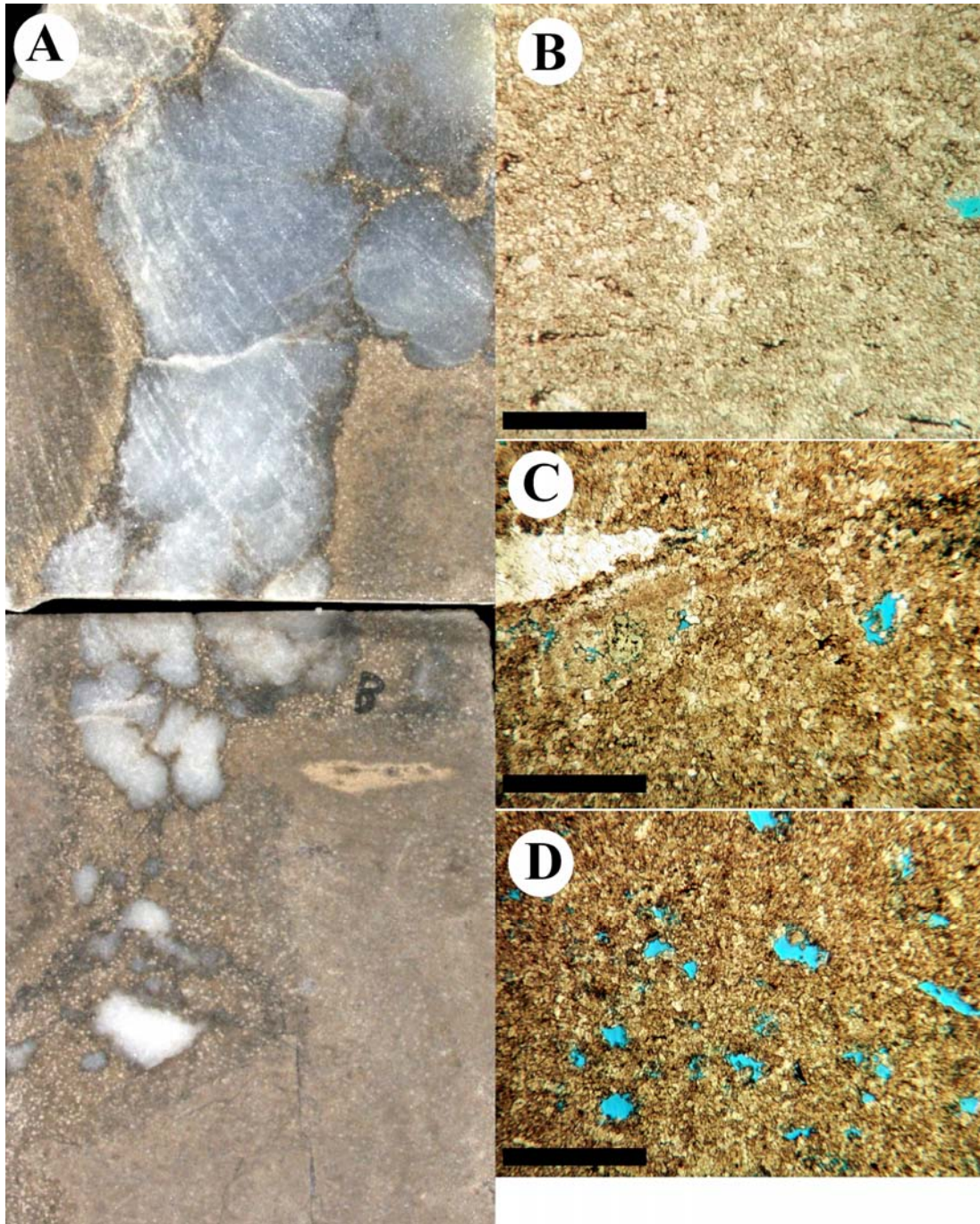


Figure 12. Core and thin-section photographs of typical peloid wackestone facies in the Lower Clear Fork. A. Slab photo of peloid wackestone with anhydrite-bearing, solution-widened vertical burrow. Lower Clear Fork, HFS L 2.2. Core is 4 inches wide. FCU 7322, depth: 6,874 ft. B. Thin-section photomicrograph of low-porosity burrowed, peloid wackestone. FCU 6429, depth: 6,817 ft. Scale bar is 1 mm. C. Thin-section photomicrograph of low-porosity burrowed, peloid wackestone. FCU 6229, depth: 6,820 ft. Scale bar is 1 mm. D. Thin-section photomicrograph of peloid wackestone with moldic pores. FCU 6229, depth: 6,841 ft. Scale bar is 1 mm.

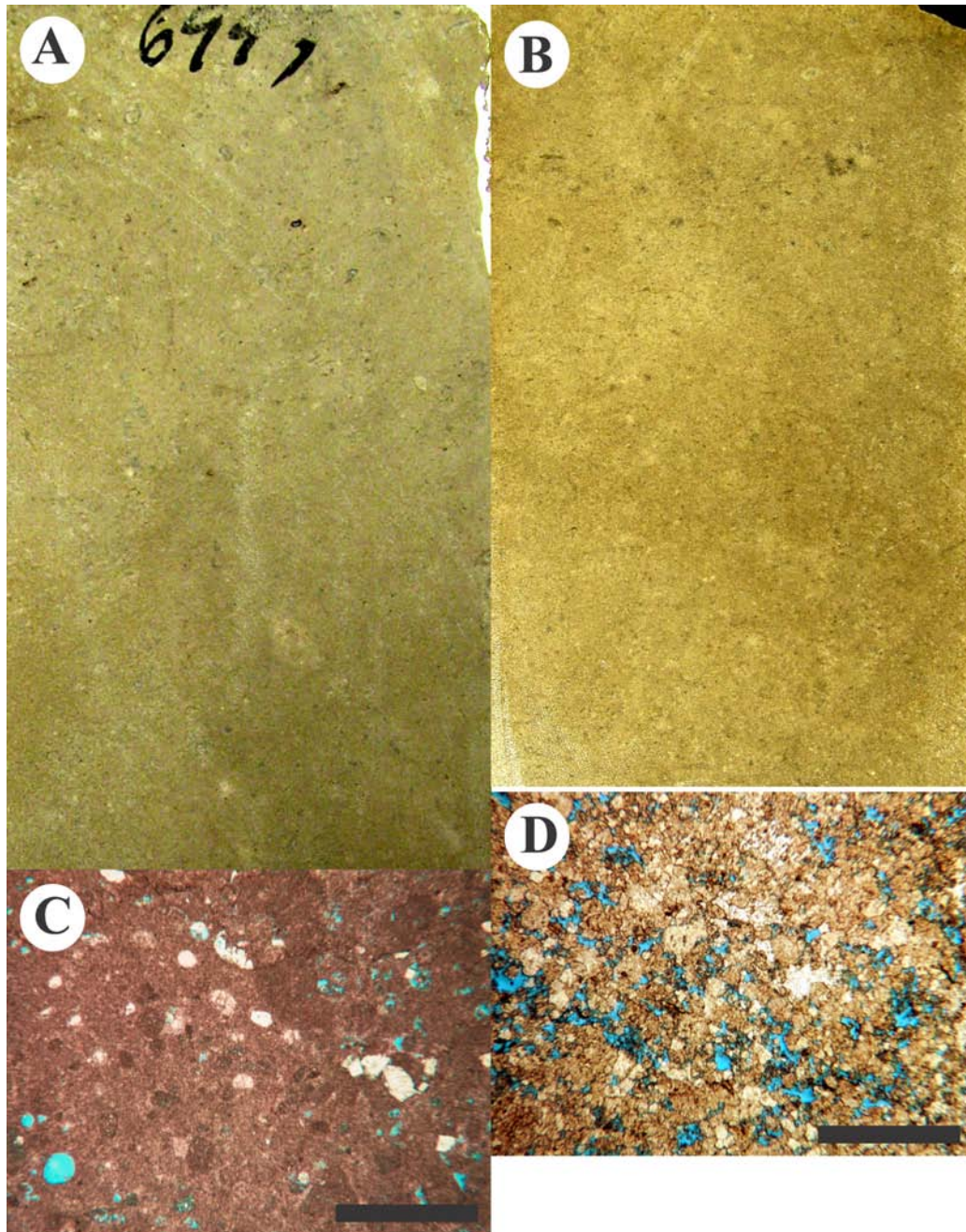


Figure 13. Core and thin-section photomicrographs of mud-rich peloid packstone-wackestone. A: Slab photo of burrowed Lower Clear Fork peloid packstone (dolostone). FCU 6229, depth: 6,997 ft. Core is 10 cm wide. B. Slab photo of Wichita peloid packstone (dolostone). FCU 5927, depth: 7,038 ft. Core is 10 cm wide. C. Photomicrograph of Lower Clear Fork peloid packstone (limestone) with moldic porosity. FCU 5927, depth: 6,903 ft. Scale bar is 1 mm. D. Photomicrograph of Lower Clear Fork peloid packstone (limestone) with moldic porosity. FCU 6229, depth: 6,817 ft. Scale bar is 1 mm.

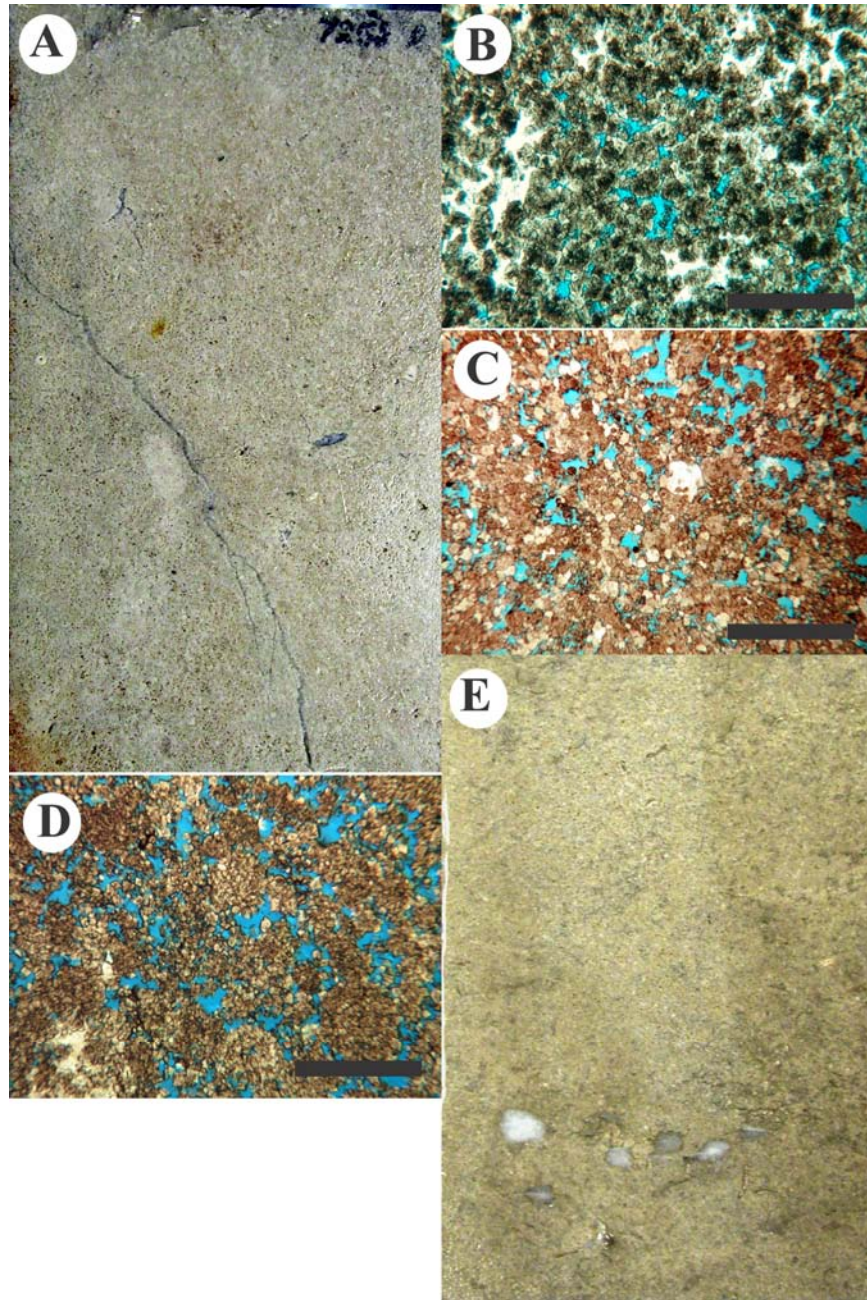


Figure 14. Core and thin-section photomicrographs of peloid, grain-rich packstones and grainstones. A. Slab photo of Abo peloid grain-dominated packstone. University Consolidated IV-25, depth: 7,252 ft. Core is 10 cm wide. B. Photomicrograph of Lower Clear Fork peloid dolostone grain-dominated packstone showing interparticle porosity. White areas are poikilotopic anhydrite. FCU 6122, depth: 6,976 ft. Scale bar is 1 mm. C. Photomicrograph of Lower Clear Fork peloid (oid?) dolostone grain-dominated packstone-grainstone with interparticle porosity. FCU 6946, depth: 6,835 ft. Scale bar is 1 mm. D. Photomicrograph of Lower Clear Fork peloid grain-dominated packstone dolostone showing interparticle porosity. FCU 6229, depth: 6,816 ft. Scale bar is 1 mm. E. Slab photo of Lower Clear Fork (L 2.2) peloid grain-dominated packstone (dolostone). FCU 6229, depth: 6,822 ft. Core is 10 cm wide.

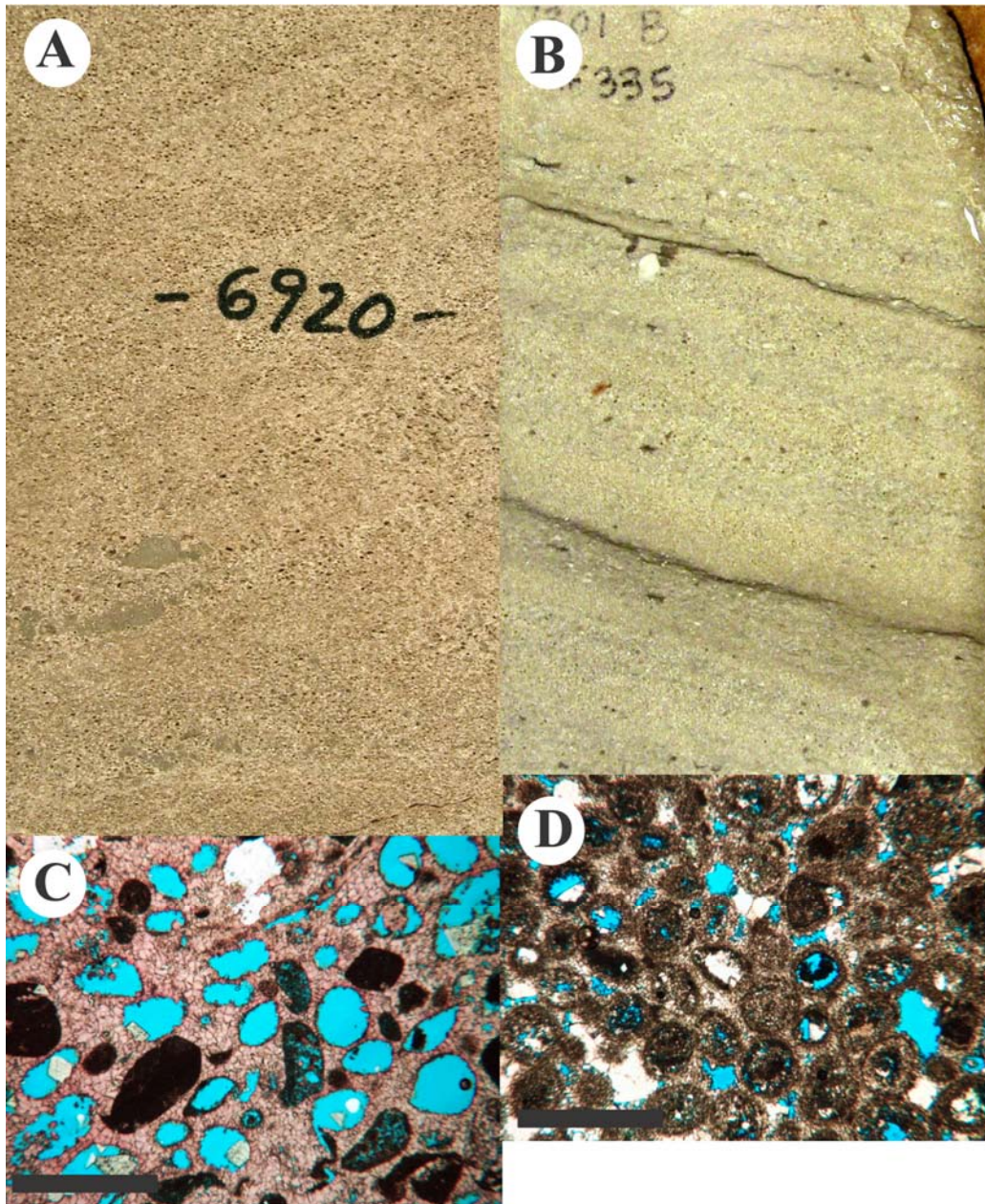


Figure 15. Core and thin-section photomicrographs of Lower Clear Fork and Abo grainstones. A. Slab photo of Lower Clear Fork ooid grainstone showing cross laminations. FCU 6122, depth: 6,920 ft. Core is 10 cm wide. B. Slab photo of Abo skeletal grainstone showing inclined laminations. FCU 7322, depth: 7,301 ft. Core is 10 cm wide. C. Photomicrograph of Lower Clear Fork ooid limestone grainstone showing oomoldic pores. FCU 5927, depth: 6,913 ft. Scale bar is 1 mm. D. Photomicrograph of Lower Clear Fork ooid dolostone grainstone wackestone showing interparticle and minor moldic pores. FCU 4828, depth: 7,137 ft. Scale bar is 1 mm.

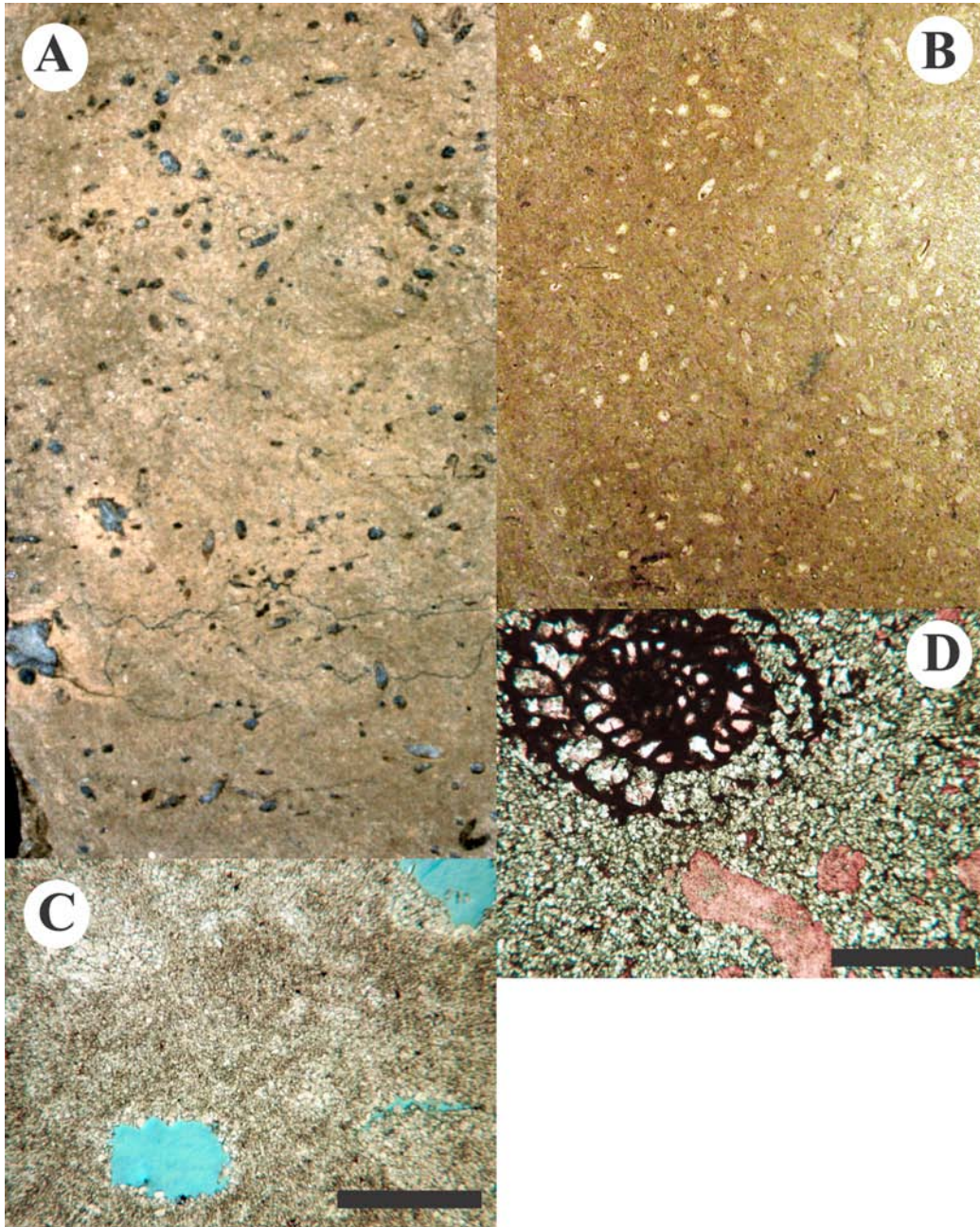


Figure 16. Core and thin-section photomicrographs of the fusulinid wackestone-packstone facies. A. Slab photo of fusulinid wackestone with open and anhydrite-filled fusu-moldic pores. FCU 7322, depth: 6,996 ft. Core is 10 cm wide. B. Slab photo of fusulinid wackestone with anhydrite-filled fusu-molds. FCU 7322, depth: 6,994 ft. Core is 10 cm wide. C. Photomicrograph of fusulinid wackestone showing open fusu-molds. FCU 7630, depth: 6,778 ft. Scale bar is 1 mm. D. Photomicrograph of fusulinid wackestone showing well-preserved fusulinids but little or no porosity. FCU 4828, depth: 7,018 ft. Scale bar is 1 mm.

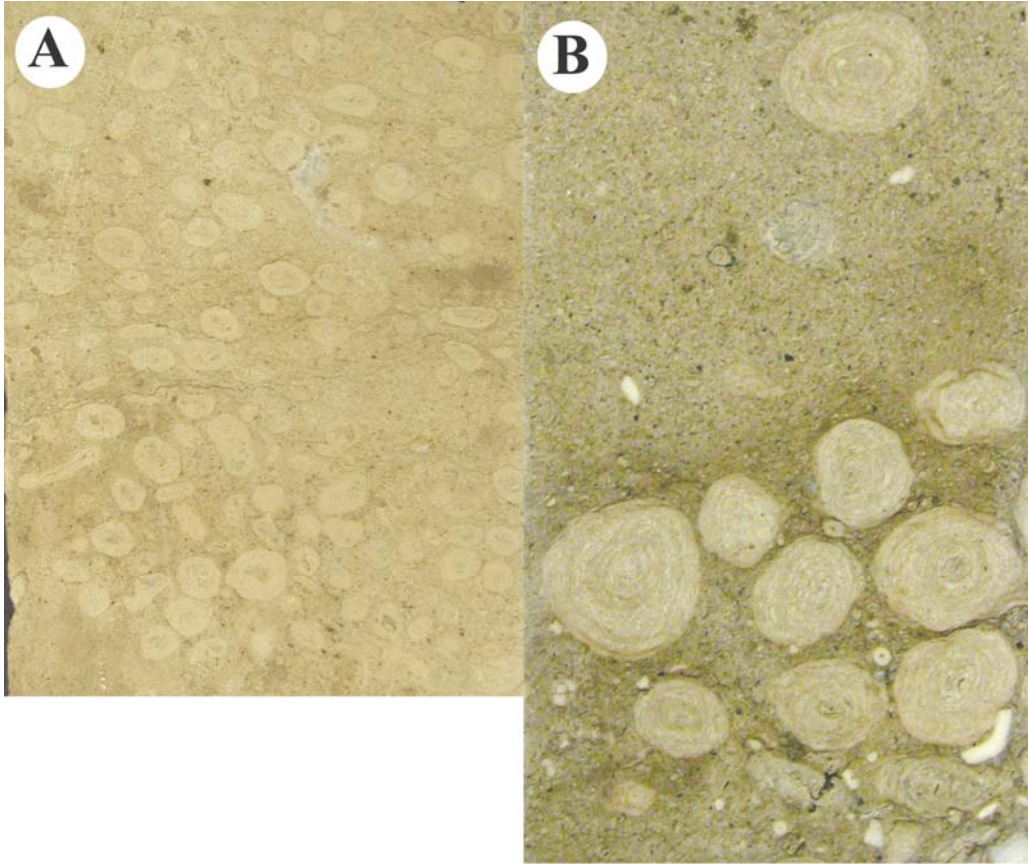


Figure 17. Core and thin-section photomicrographs of the oncooid, wackestone-packstone facies. A. Small, algally coated fusulinids. Lower Clear Fork, FCU 5927, depth: 6,980 ft. B. Large oncooids. Lower Clear Fork, FM-1 well, depth: 7,160 ft. Cores are 4 inches wide.

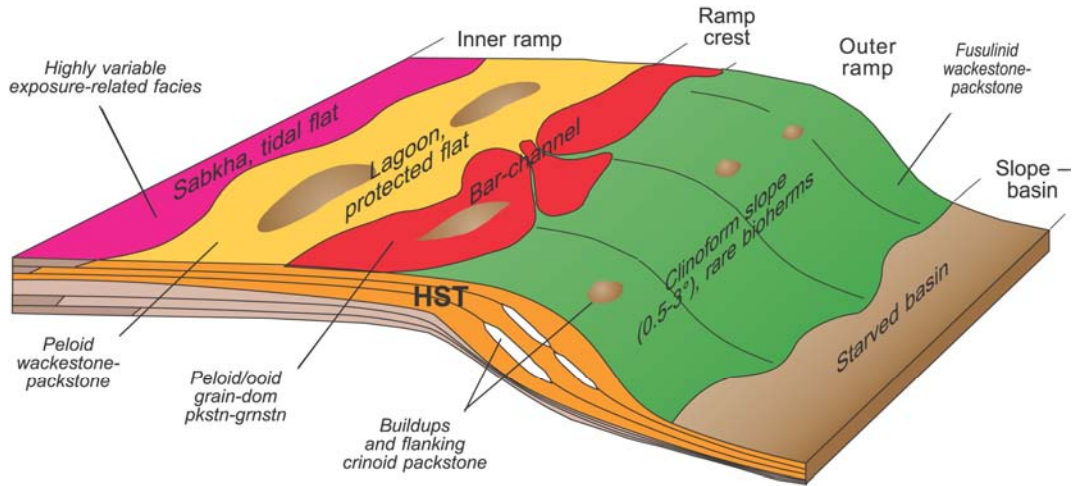


Figure 18. Depositional model for Permian shallow-water carbonate platforms in the Permian Basin. This model is applicable to most Leonardian and Guadalupian carbonate platform successions, including the reservoir succession at Fullerton field. After Kerans and Ruppel (1994).

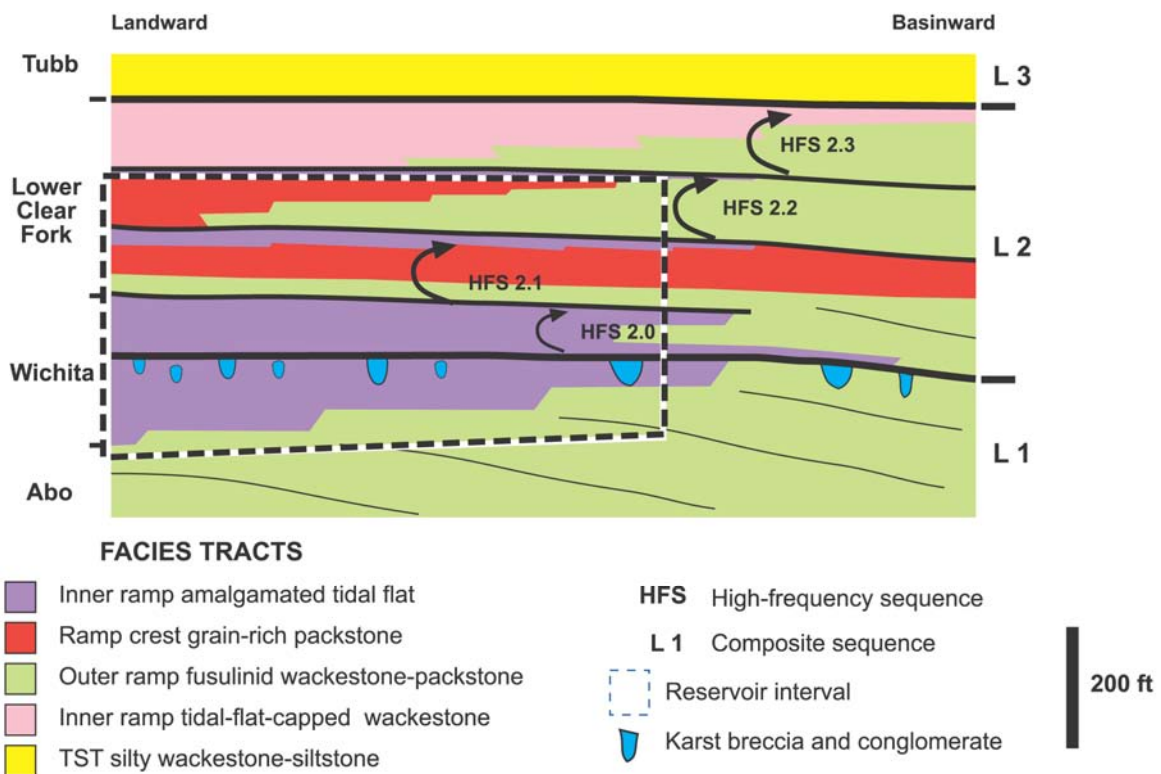


Figure 19. Generalized sequence-stratigraphic model of the lower Leonardian succession at Fullerton field showing primary facies tracts and stratigraphic nomenclature.

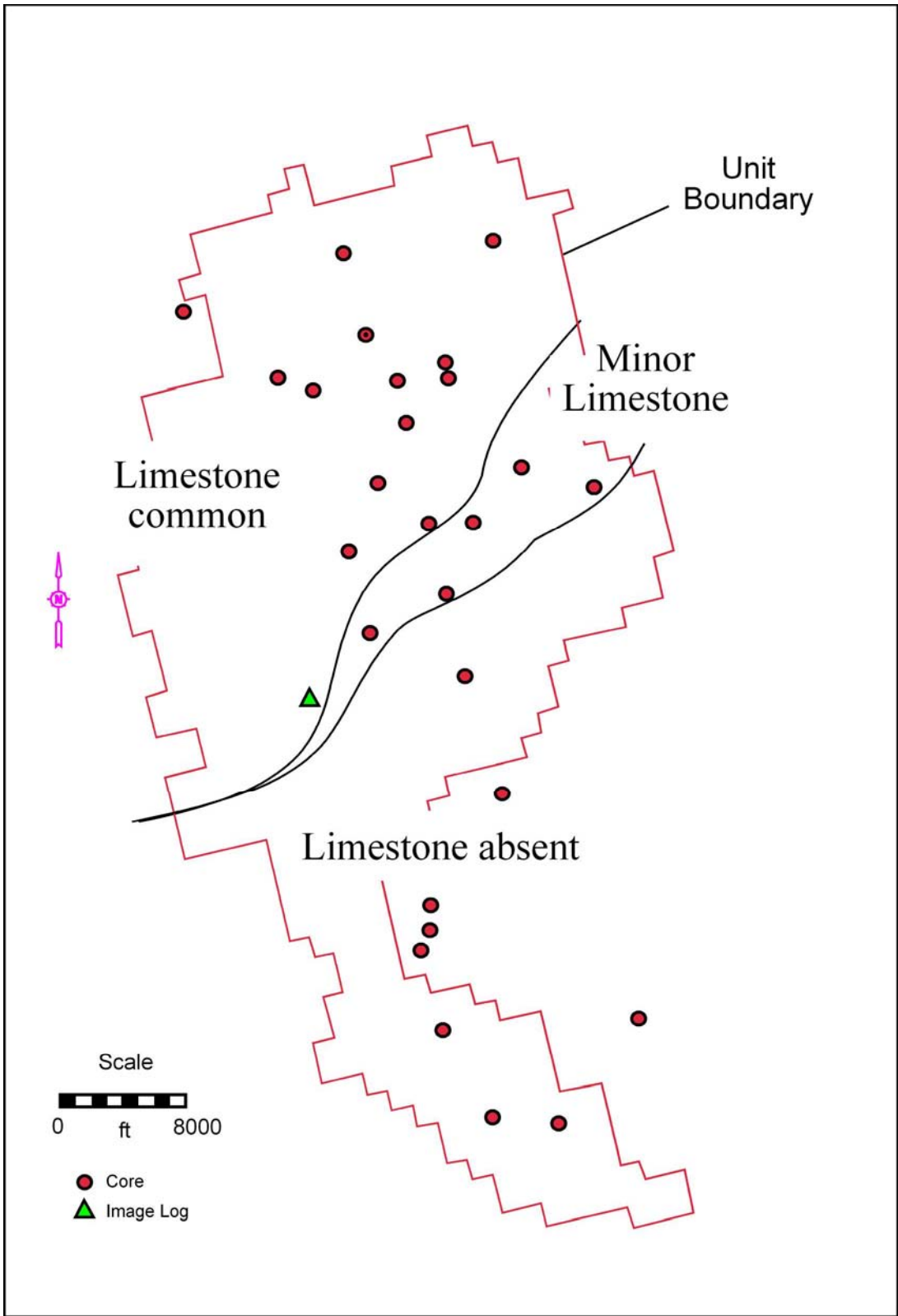


Figure 20. Map of limestone abundance in the Wichita Formation.

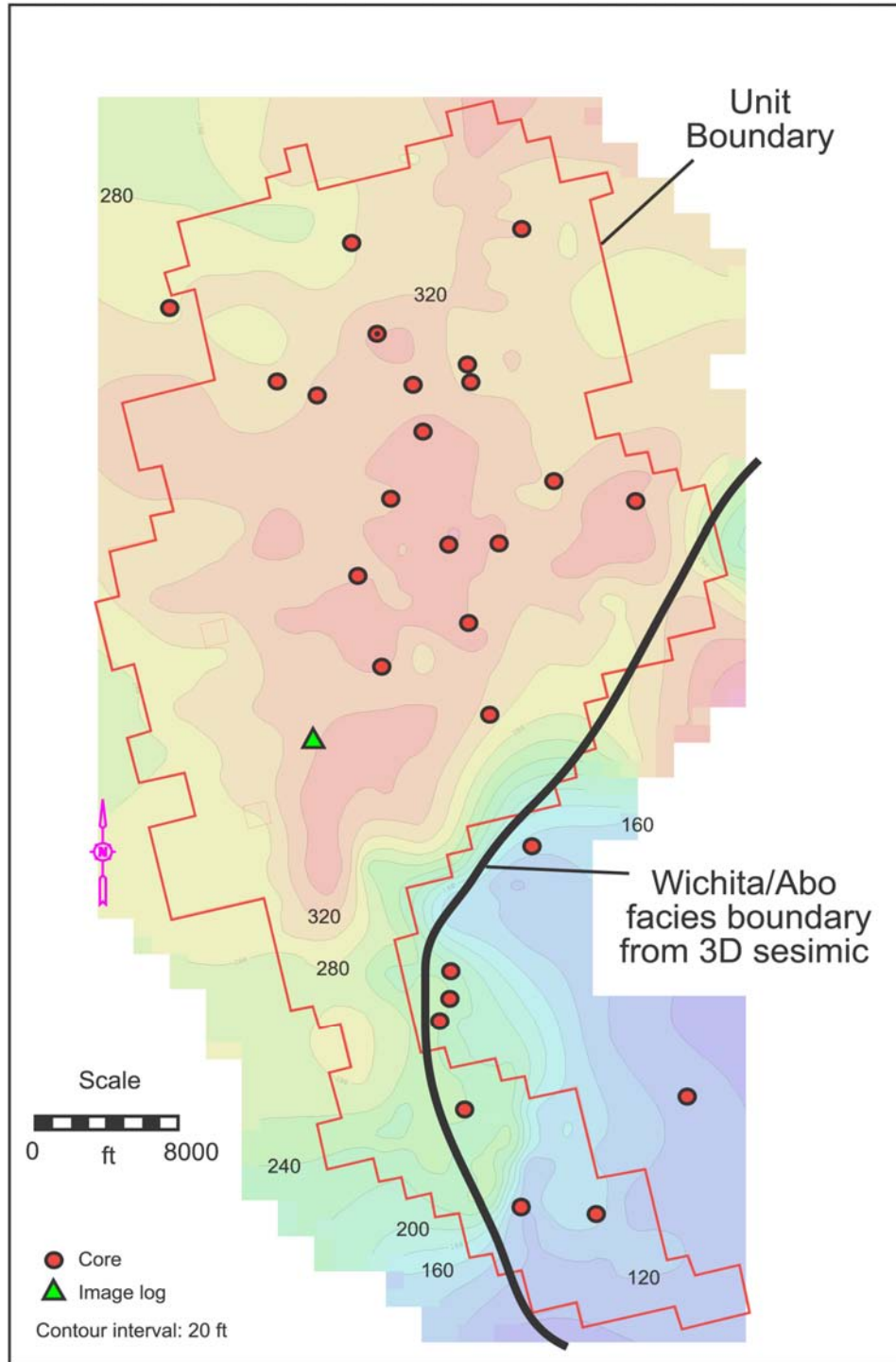


Figure 21. Thickness of the Wichita Formation in the Fullerton field area. The relatively sharp decrease in thickness in the southeastern part of the area is caused by the change in facies from Wichita tidal-flat facies to time-equivalent subtidal Abo facies.

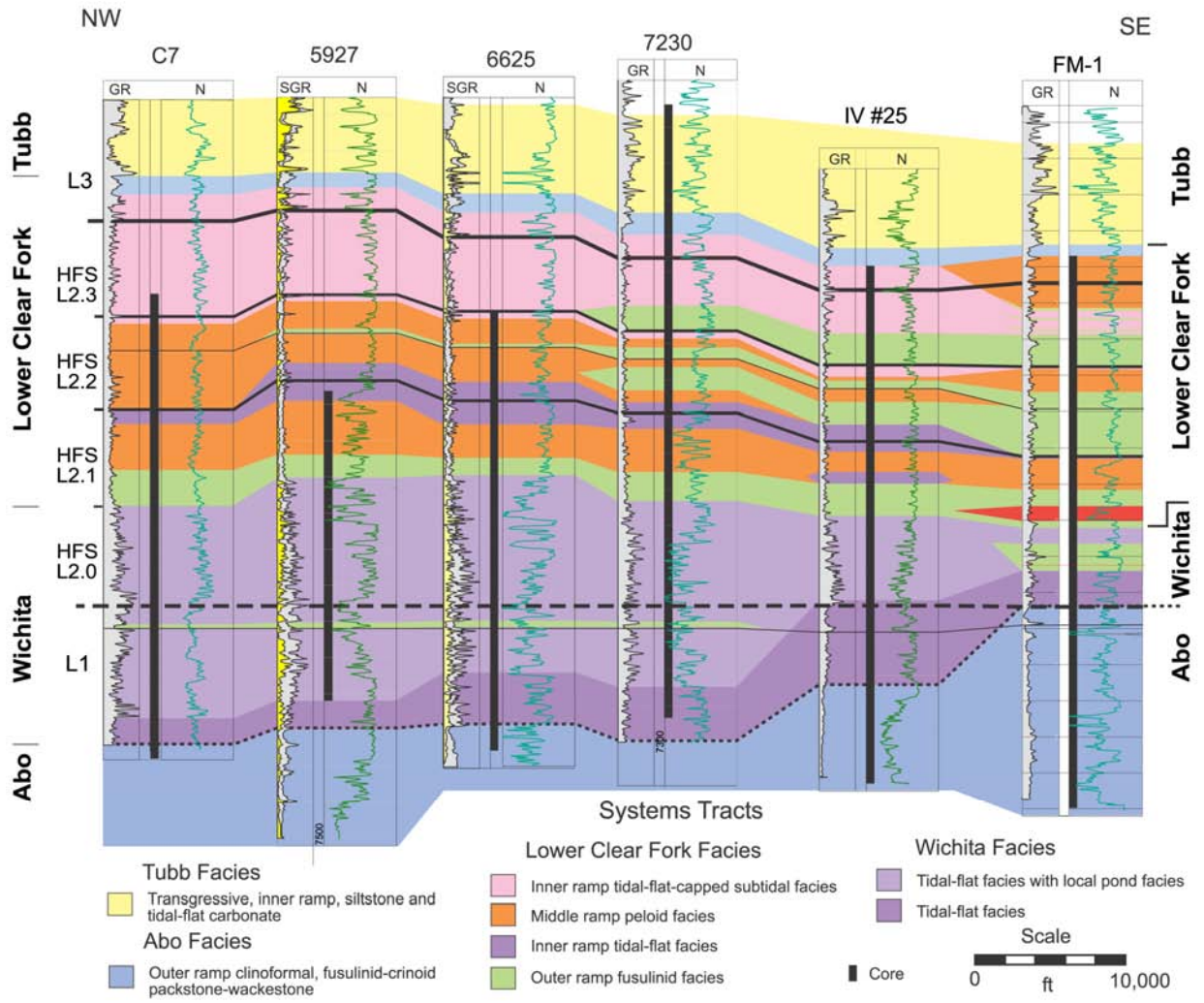


Figure 22. Northwest-southeast cross section (B-B') across the Fullerton field area showing the sequence architecture and general facies development based on cored well control. Line of section shown in figure 3.

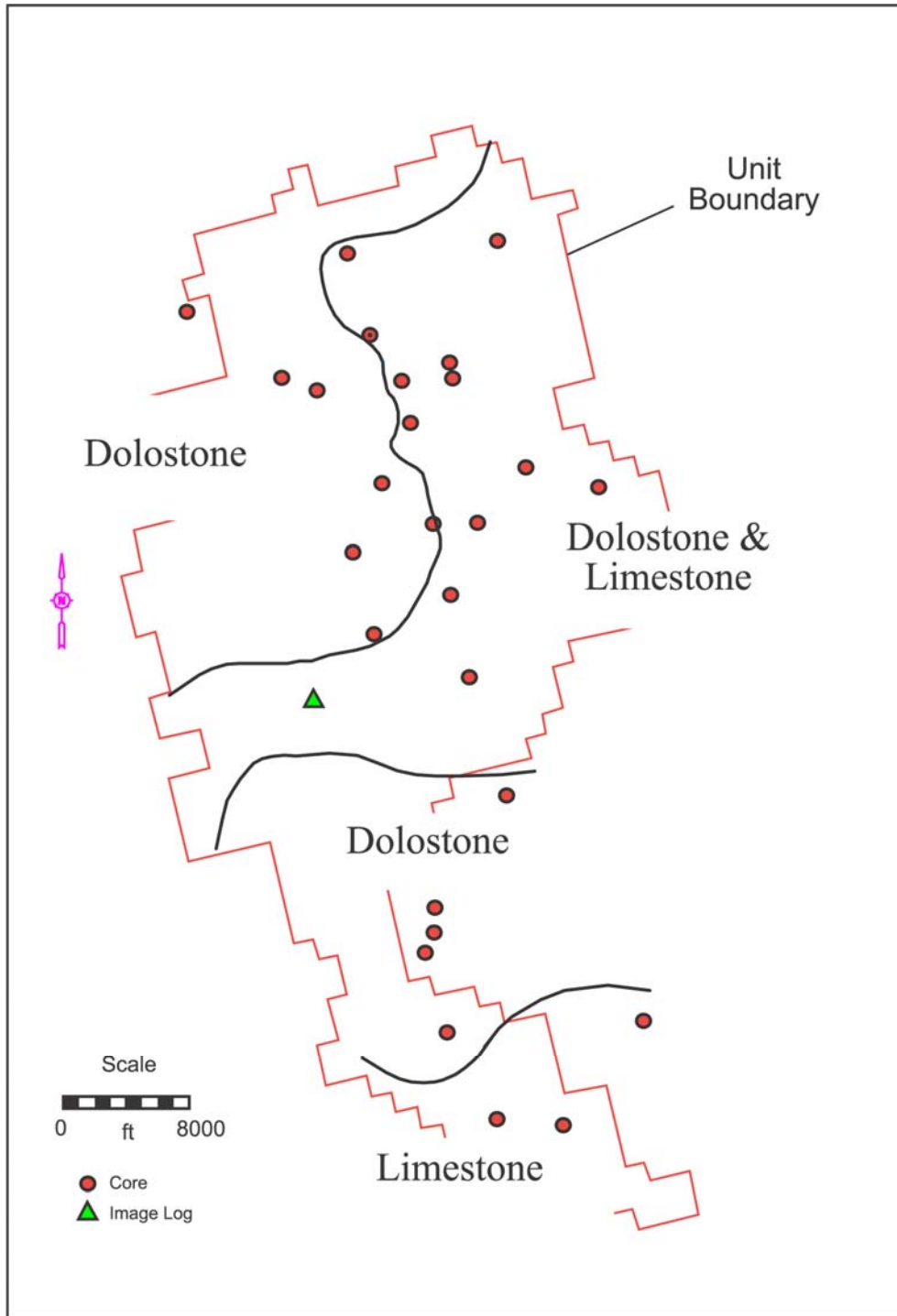


Figure 23. Map showing the distribution of limestone and dolostone in Lower Clear Fork HFS L 2.1 based on cores and wireline logs. Note: Most areas actually contain complexly interbedded limestone and dolostone. Limestone is generally more abundant in the south.

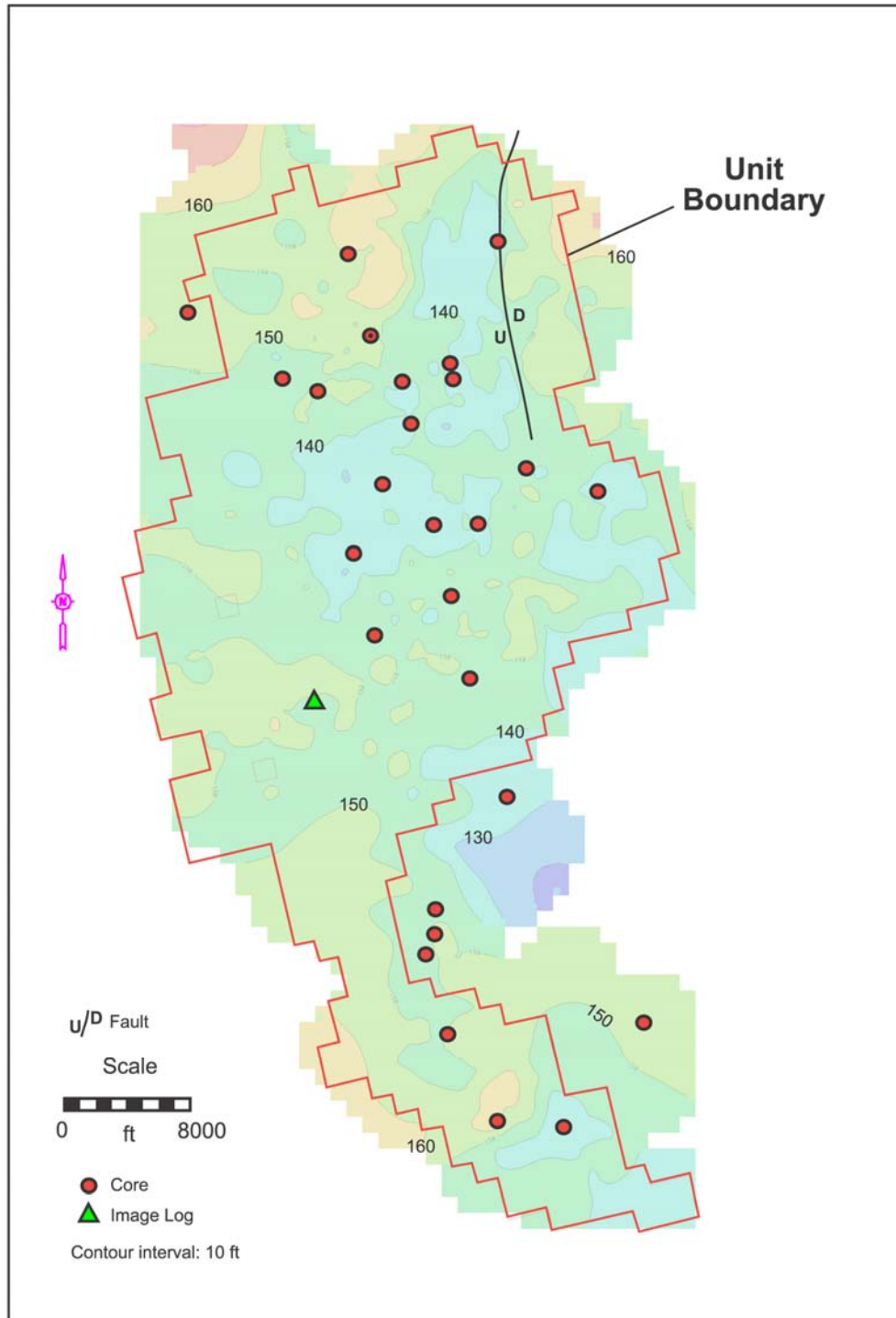


Figure 24. Map of the thickness of the Lower Clear Fork L 2.1 sequence at Fullerton field. Note the abrupt change in thickness along the north-trending fault in the northeastern part of the field.

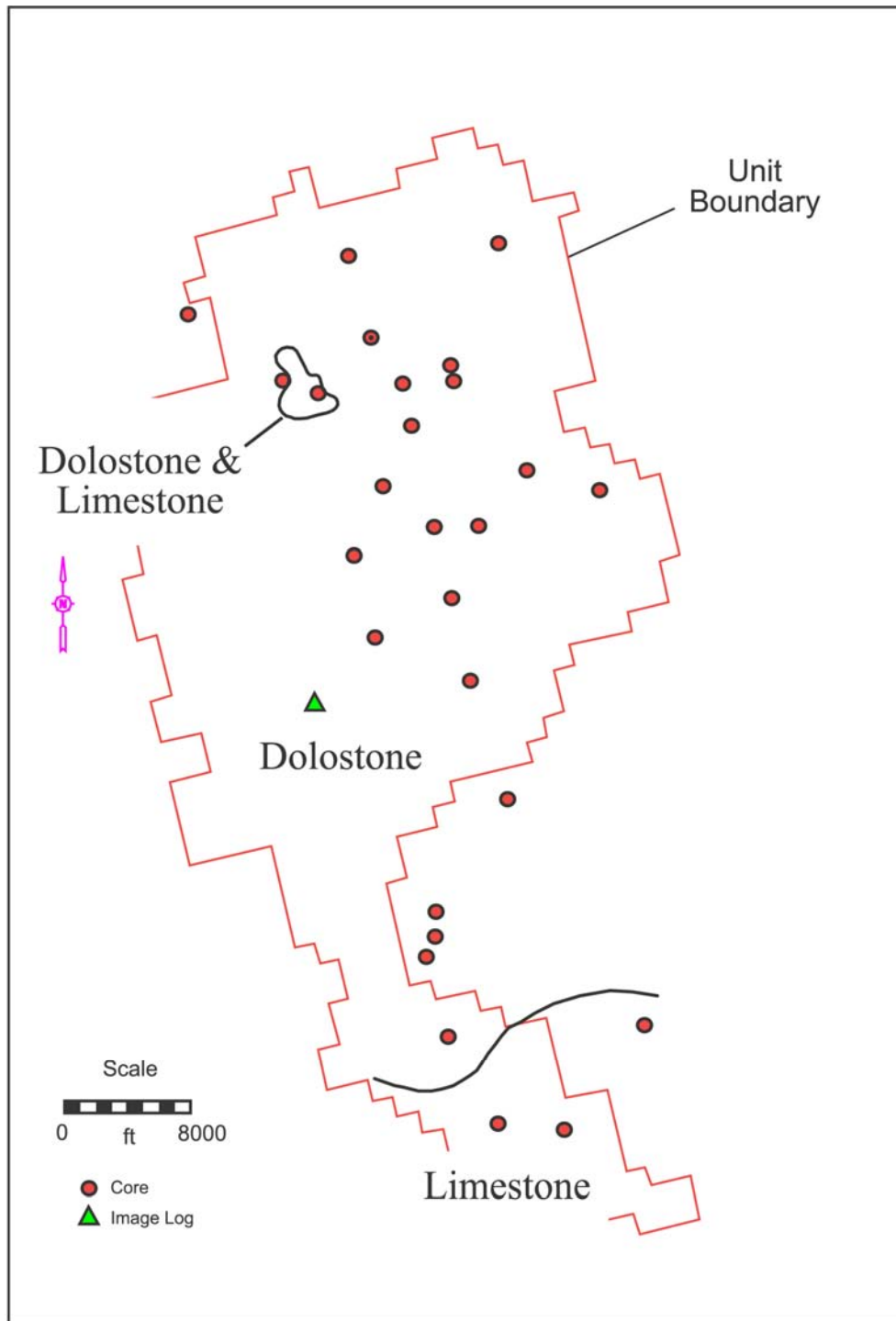


Figure 25. Map showing the distribution of limestone and dolostone in Lower Clear Fork HFS L 2.2 based on cores and wireline logs.

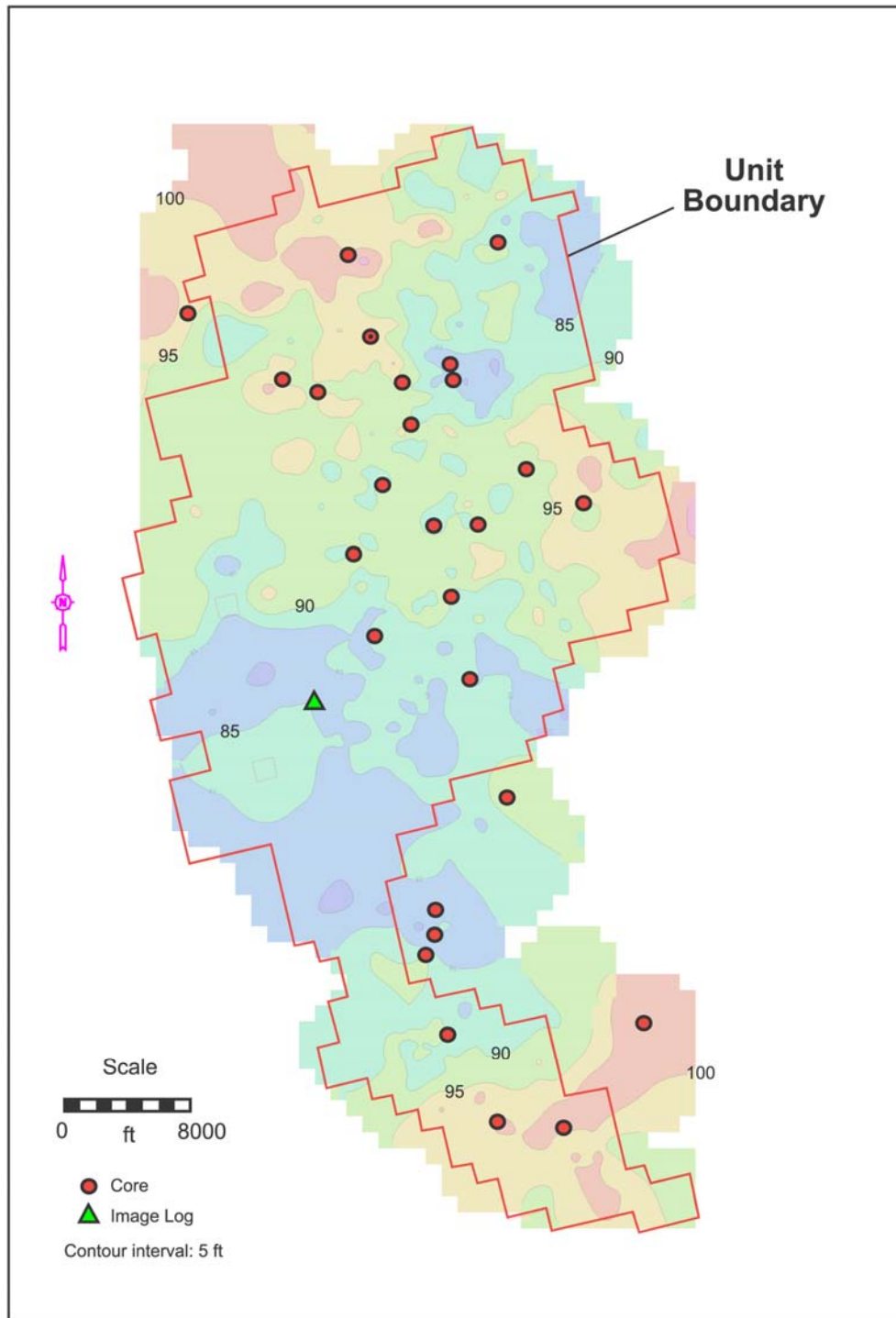


Figure 26. Map of the thickness of the Lower Clear Fork L 2.2 sequence at Fullerton field.

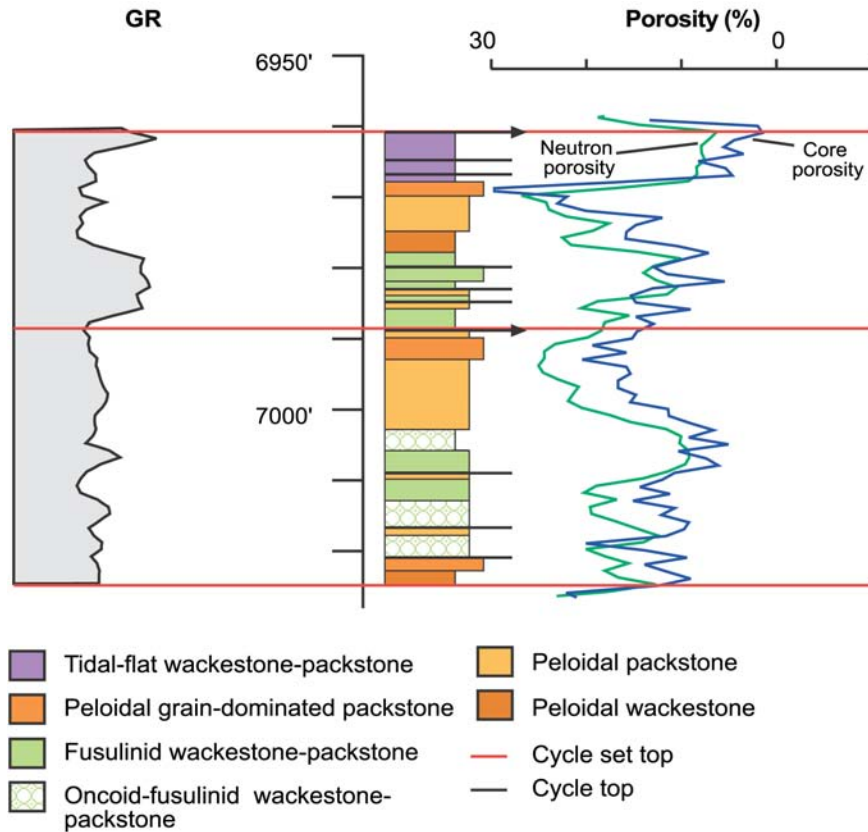


Figure 27. Facies stacking and cycle development in the fusulinid- and oncoïd-rich, transgressive systems tract (TST) of Lower Clear Fork HFS L 2.1. Note that porosity is typically developed at or near cycle tops. Note also the lack of any systematic relationship between gamma-ray log and facies or cyclicity.

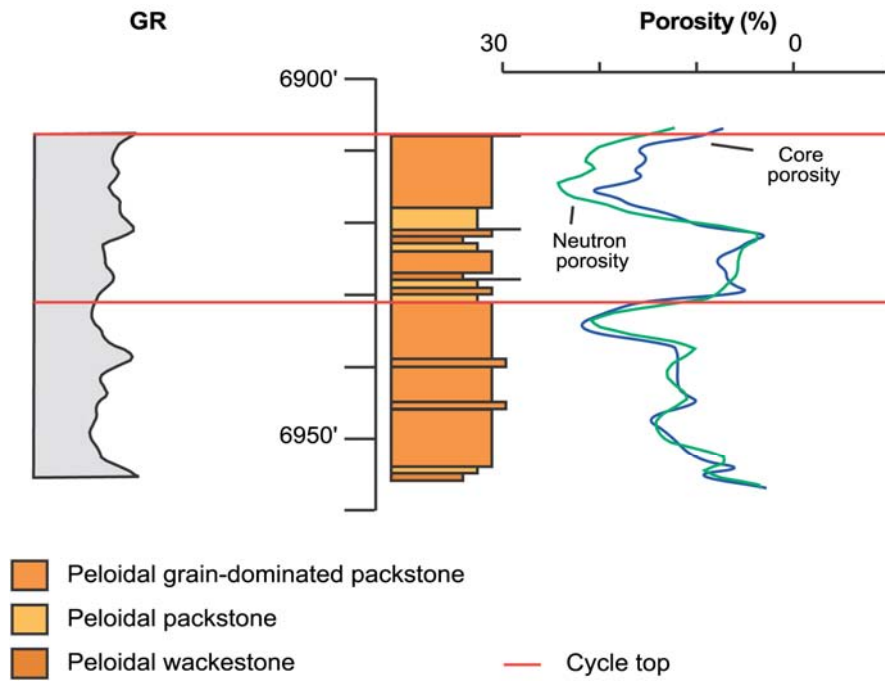


Figure 28. Facies stacking and cycle development in the grain-rich, highstand systems tract (HST) of Lower Clear Fork HFS L 2.1. Note that porosity is typically developed at or near cycle tops. As with other Lower Clear Fork successions, gamma-ray logs do not show a systematic response to facies or cyclicity.

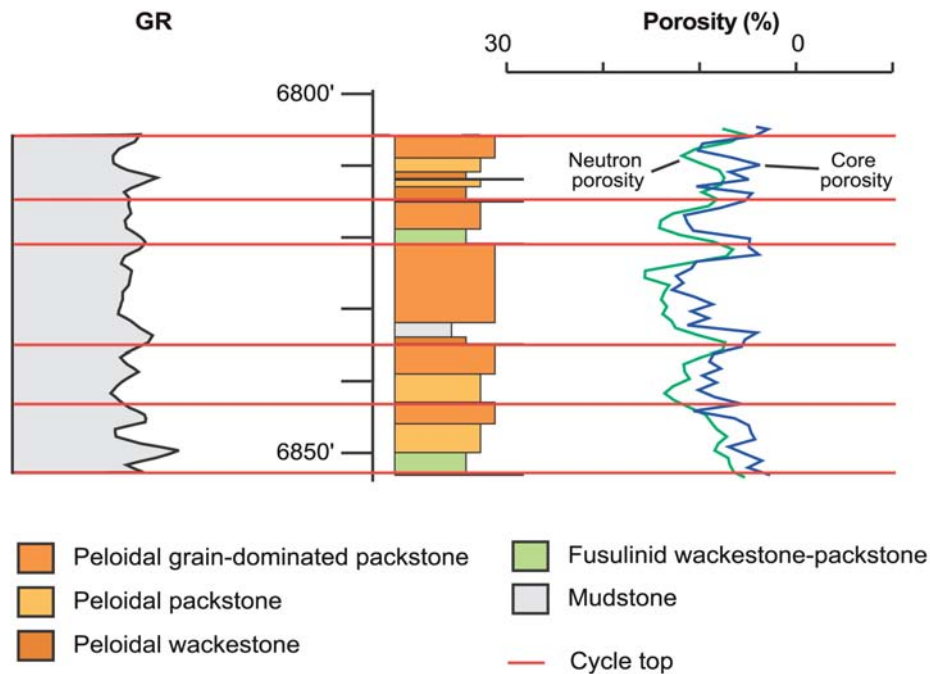


Figure 29. Facies stacking and cycle development in the grain-rich, late transgressive systems tract/early highstand systems tract of Lower Clear Fork HFS L 2.2. Note that porosity is typically developed at or near cycle tops. Note here again that gamma-ray logs do not display any relationship to facies or cycle development.

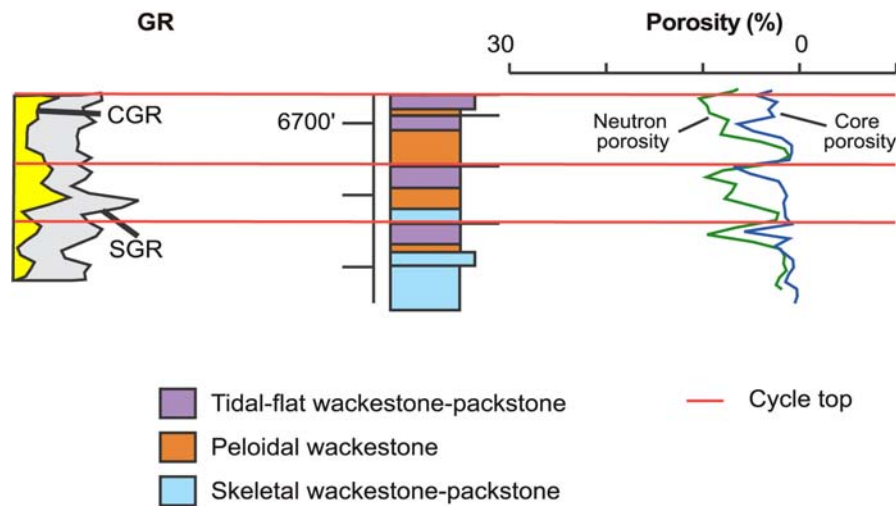


Figure 30. Facies stacking and cycle development in the nonreservoir Lower Clear Fork HFS L 2.3. Porosity is typically developed in cycle-capping tidal-flat facies at cycle tops, but little or no permeability is associated with the fenestral pores that dominate these caps.

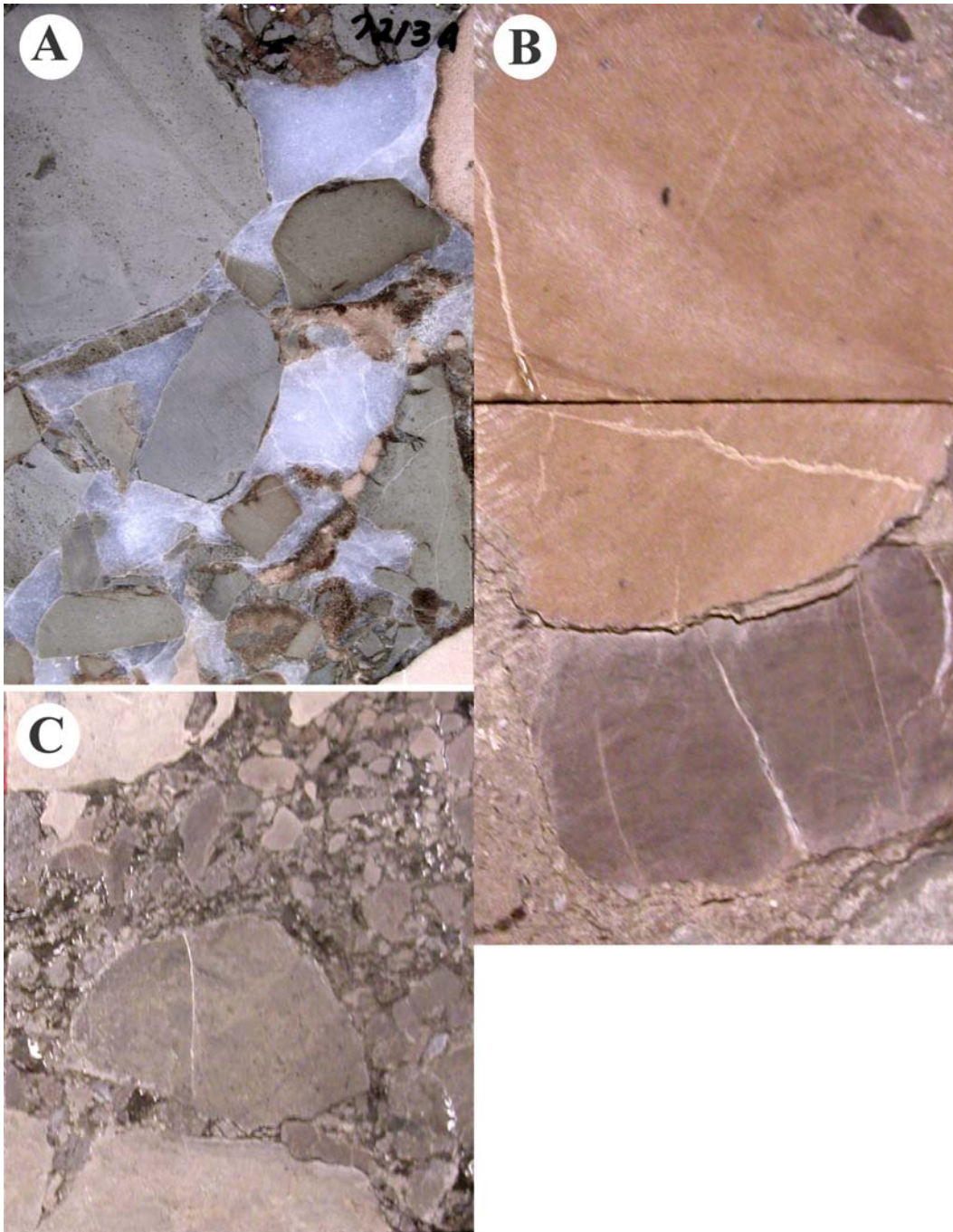


Figure 31. Core slab photos of polymict conglomerate in the Wichita Formation of probable karst origin. A. Amoco University Consolidated # IV-25, depth: 7,213 ft. B. FCU 6122, depth: 7,254 ft. C. FCU 6122, depth: 7,201 ft. All cores are 4 inches wide.



Figure 32. Core slab box photo of breccias developed at the Abo/Wichita contact in FM-1 core. Amoco University Consolidated # IV-25, depths: 7,211–7,228 ft. Core pieces are 4 inches wide.

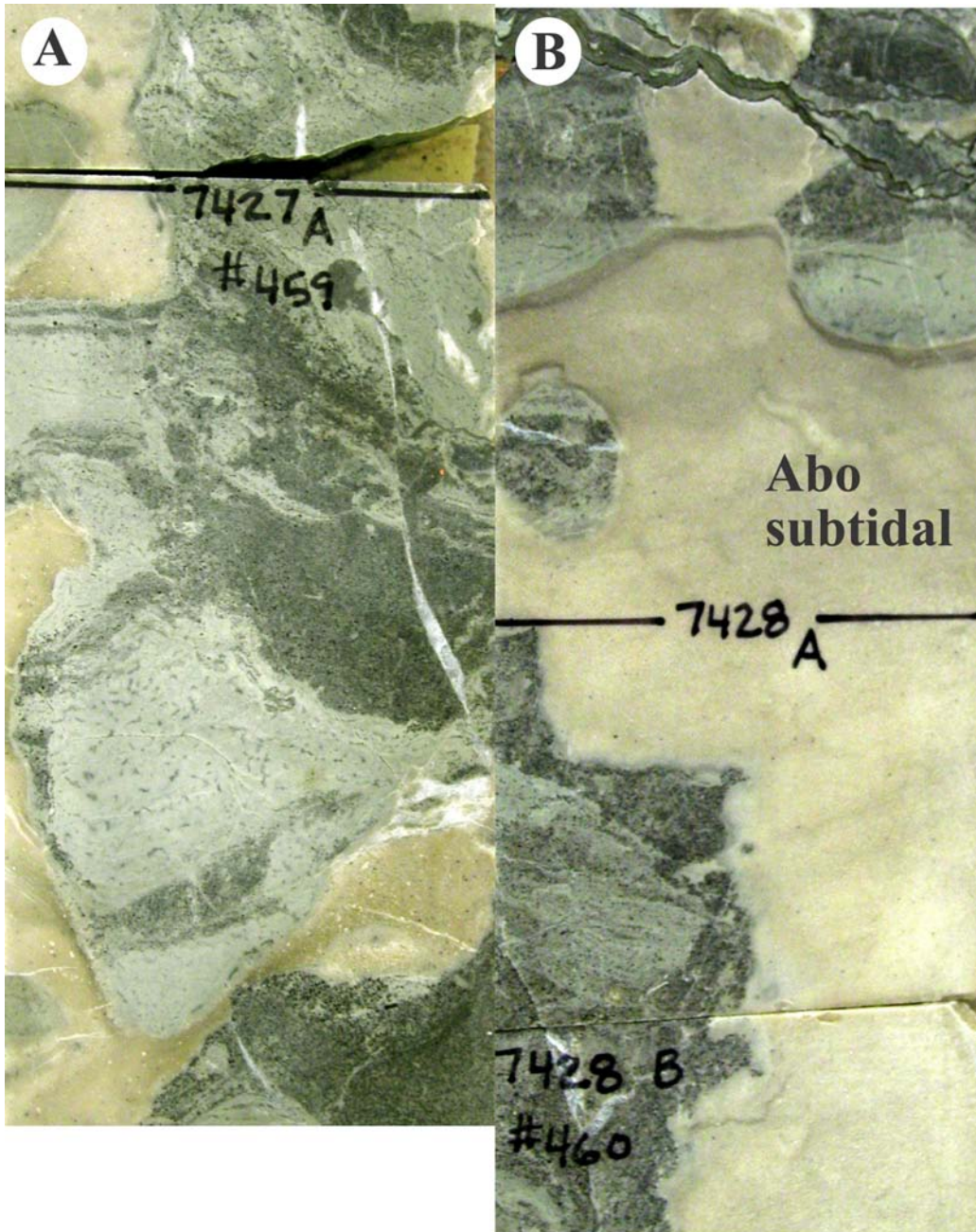


Figure 33. Core slab photos of contact zone of Abo/Wichita. Interrelationships between Abo subtidal facies (light-brown) and silty peritidal wackestones of the Wichita suggest that the contact represented a karsted locally collapsed interval.

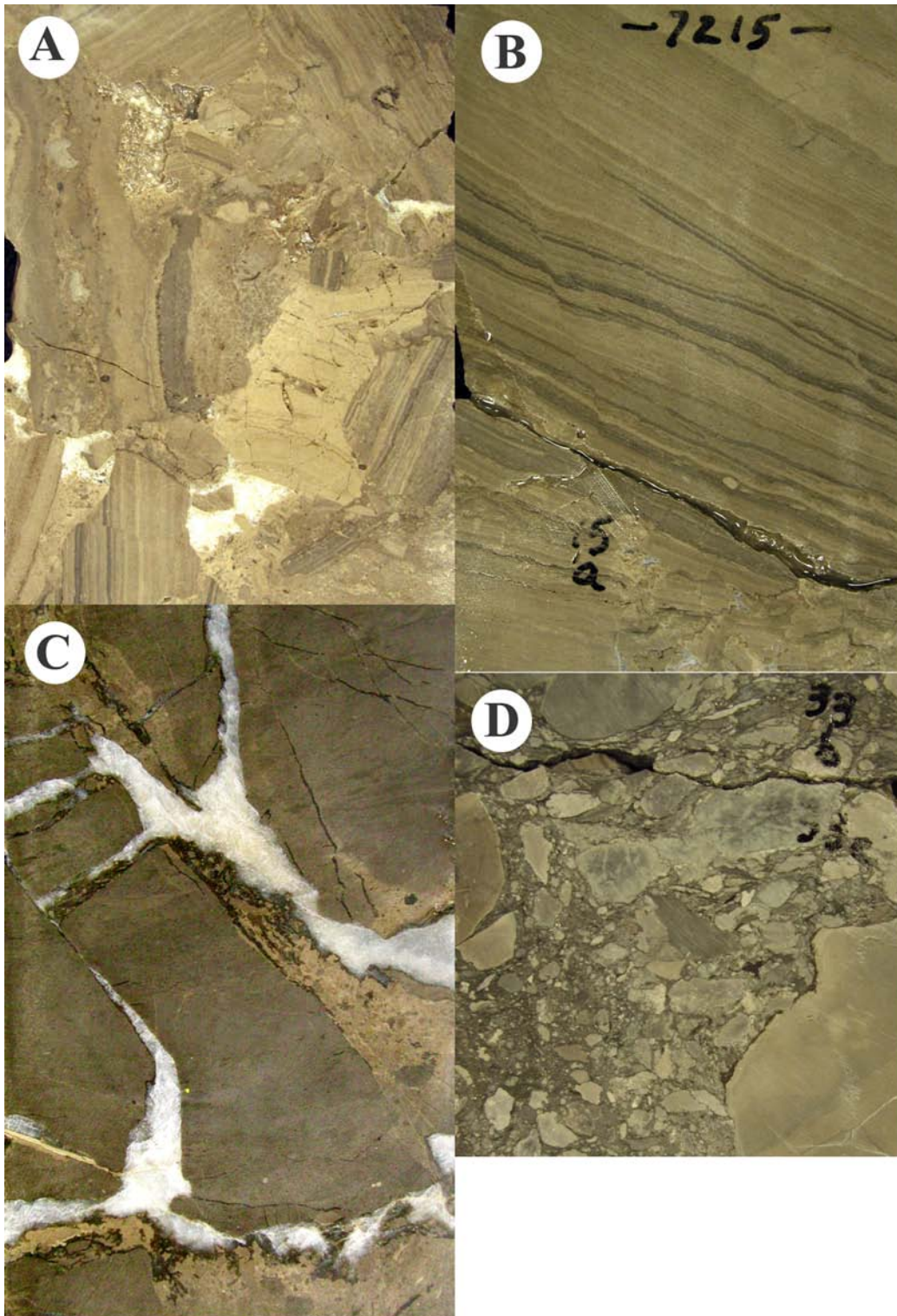


Figure 34. Core slab photos of monomict breccias from the Wichita. A. Rotated clasts of tidal-flat facies. B. Tilted blocks of laminated peritidal facies. Depth: 7,215 ft. C. Brecciated clasts of peloidal wackestone. University Consolidated V 15, depth: 6,899 ft. D. Clasts of peritidal mudstone-wackestone. All cores are 4 inches wide.

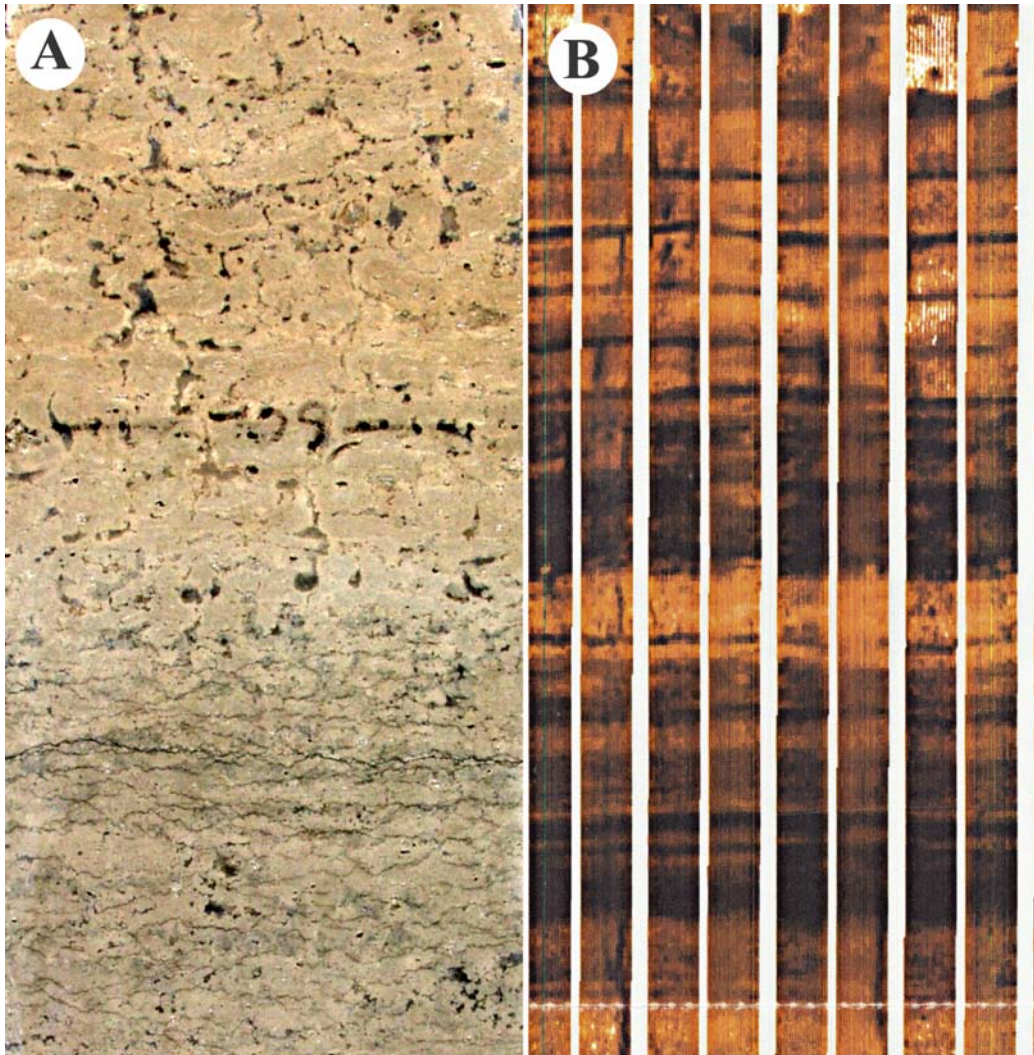


Figure 35. Image log and core photo images of laminated tidal-flat facies. Core: FCU 7322, depth: 6,909 ft. Image log: FCU 2564, depth: 6,900–6,904 ft. Core is 4 inches wide. Lower Clear Fork, HFS L 2.1.

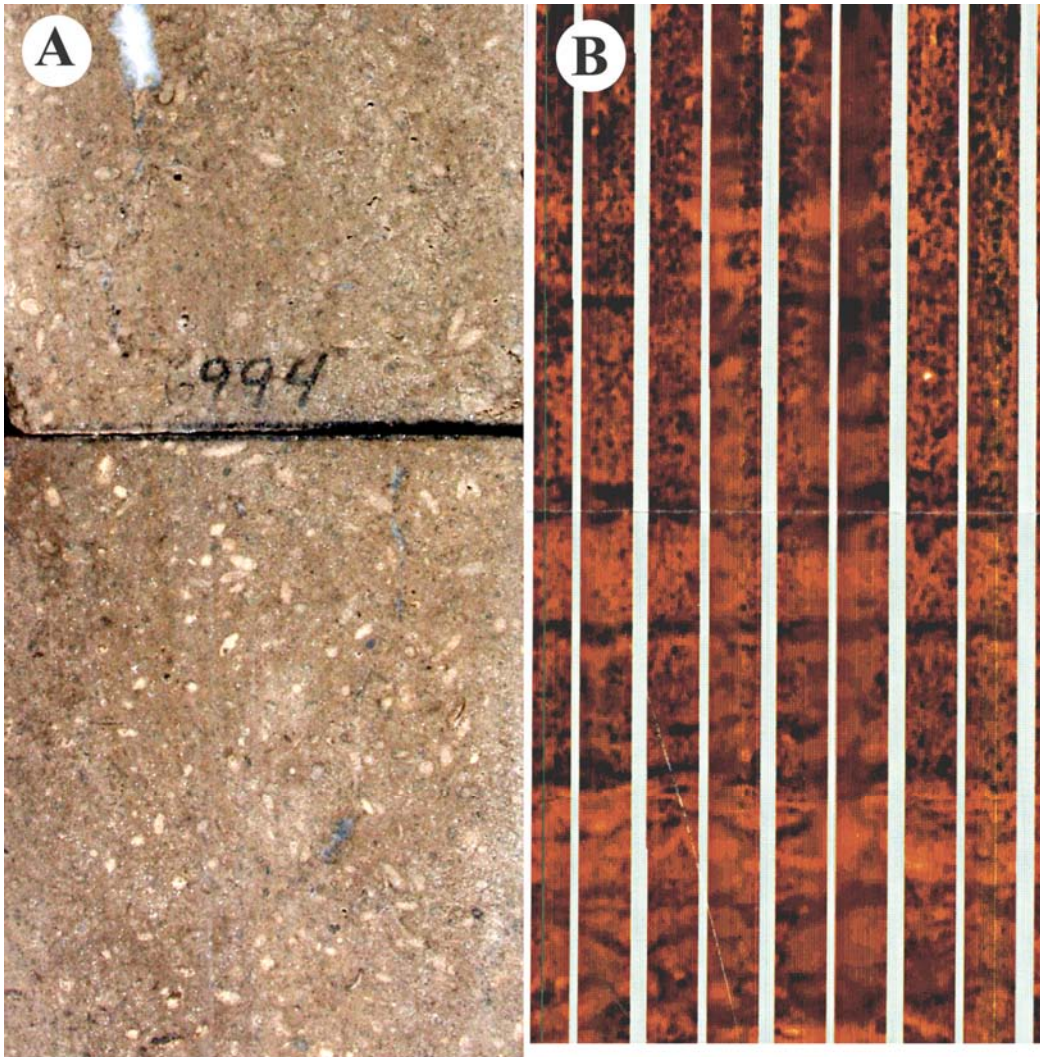


Figure 36. Image log and core photo images of fusulinid wackestone-packstone facies. Lower Clear Fork. Core: FCU 7322, depth: 6,994 ft. Image log: FCU 2564, depth: 6,990–6,994 ft. Core is 4 inches wide.

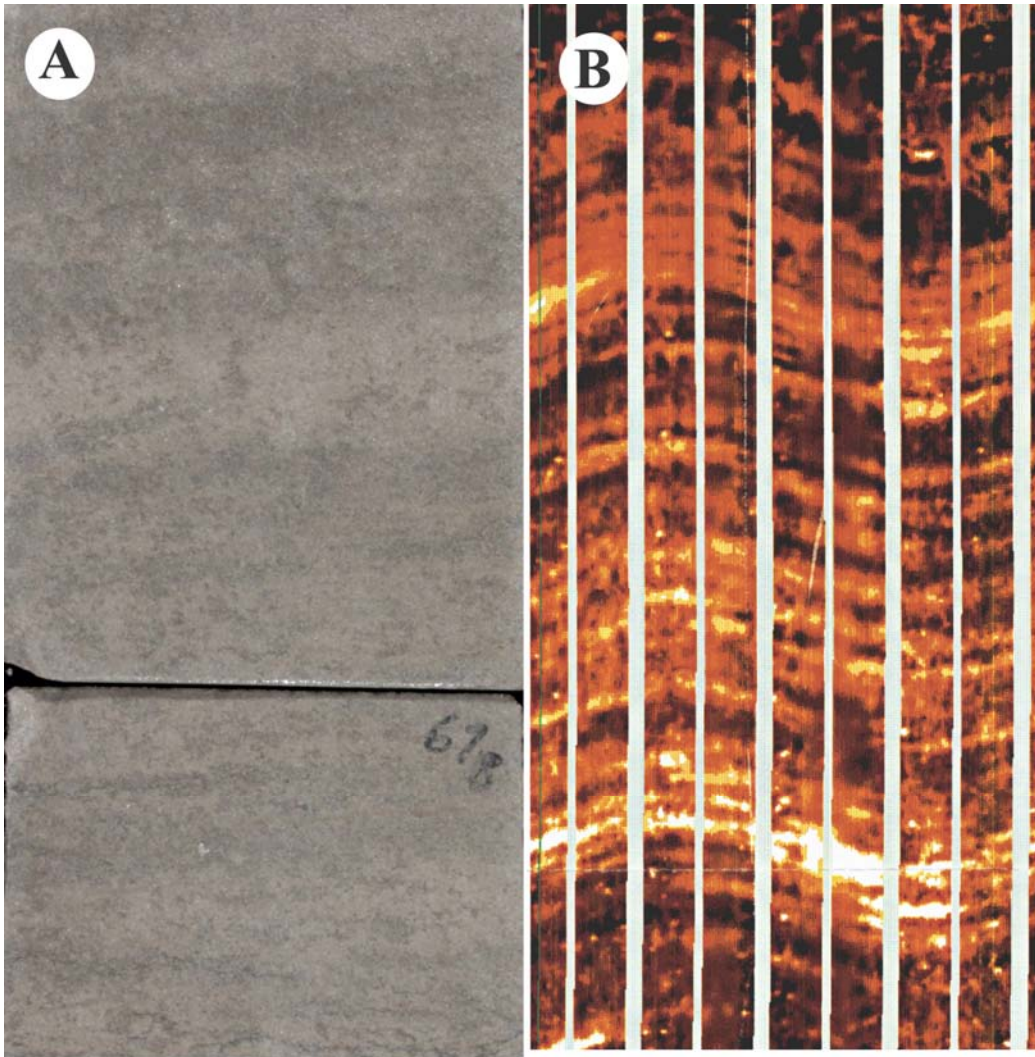


Figure 37. Image log and core photo images of crossbedded grainstone. Lower Clear Fork. Core: FCU 7322, depth: 6,967 ft. Image log: FCU 2564, depth: 7,002–7,005 ft. Core is 4 inches wide.

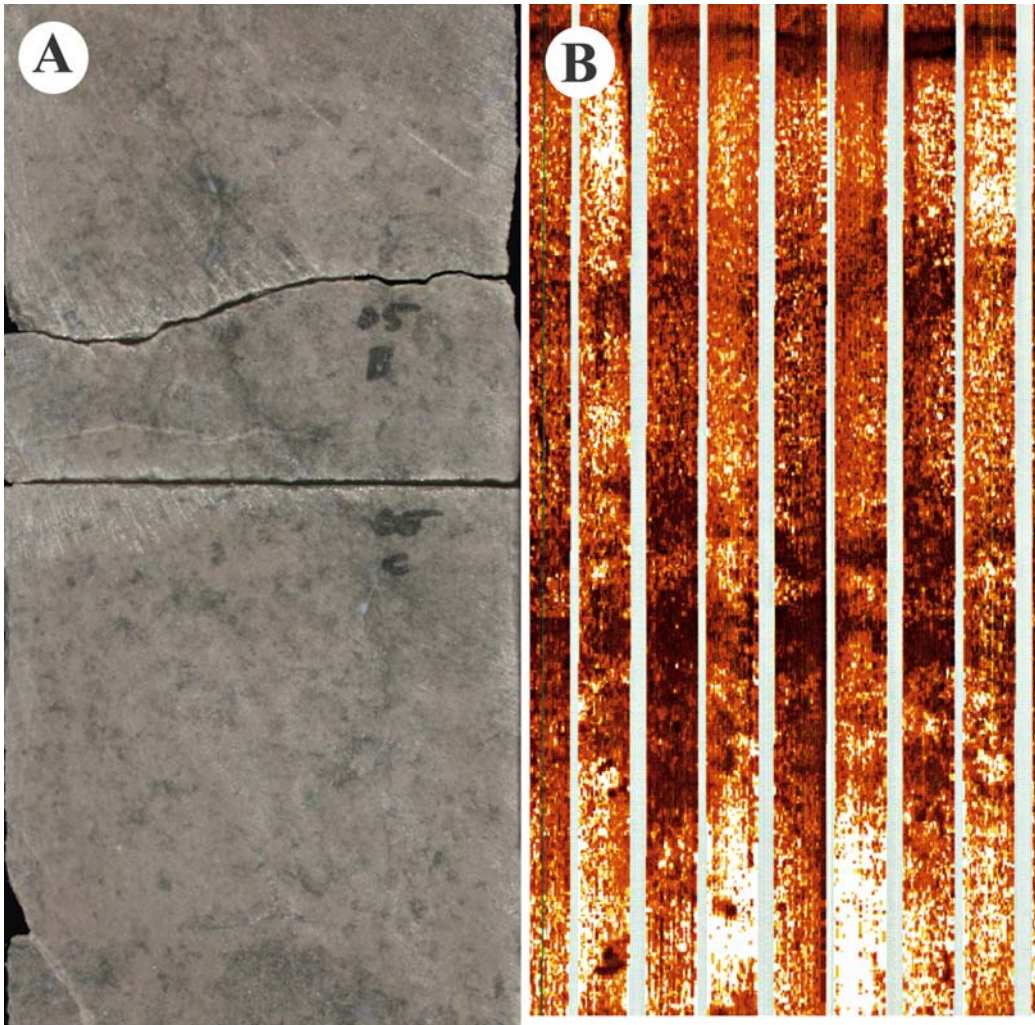


Figure 38. Image log and core photo images of peloid wackestone-packstone facies. Core: FCU 7322, depth: 6,905 ft. Image log: FCU 2564, depth: 6,905–6,909 ft. Core is 4 inches wide. Lower Clear Fork, HFS L 2.2.

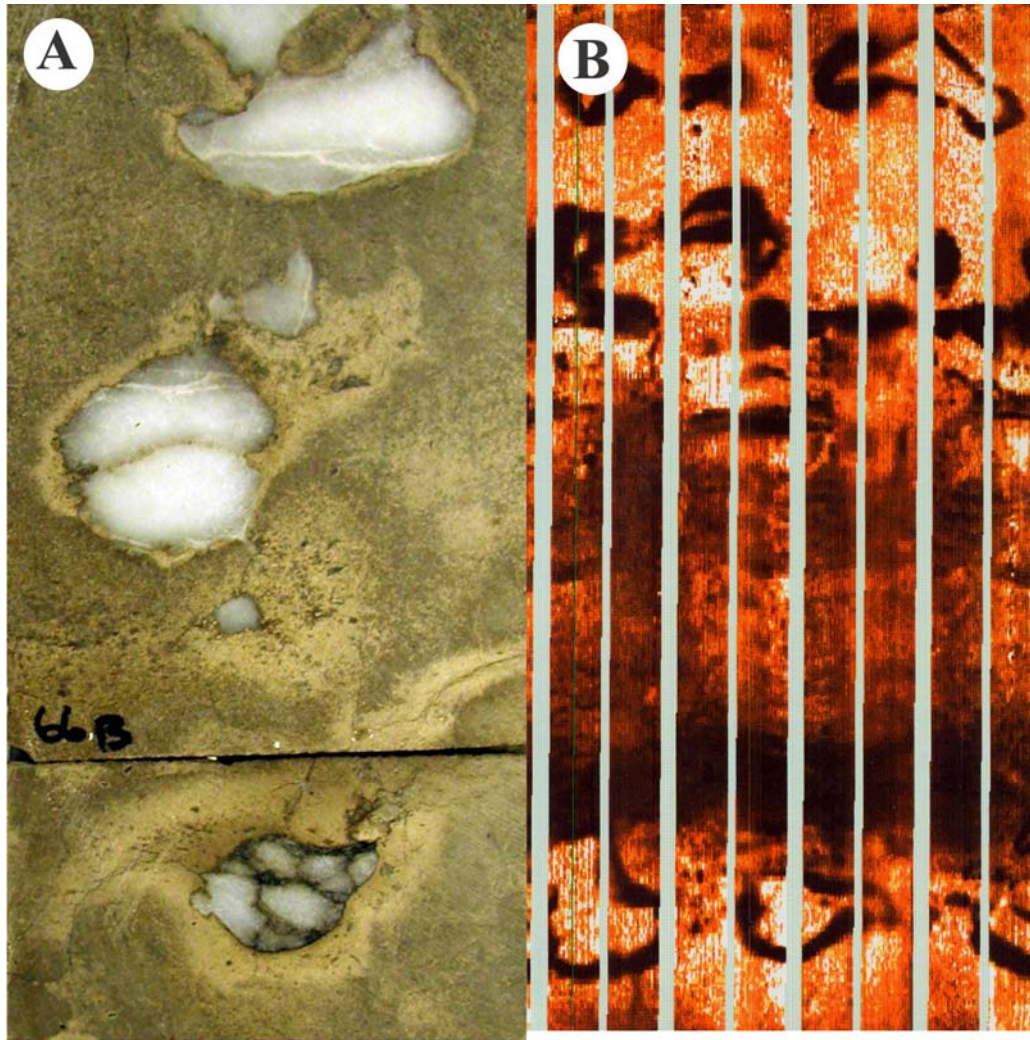


Figure 39. Image log and core photo images of nodular peloid wackestone typical of the Lower Clear Fork HFS L 2.2. Core photo shows anhydrite nodules surrounded by light-colored haloes of higher porosity. Image log displays the same features as white (high-resistivity) masses surrounded by black (low-resistivity owing to the fluid-filled pore space) rims. Core: FCU 6739, depth: 6,989 ft. Image log: FCU 2564, depth: 6,879–6,883 ft. Core is 4 inches wide.

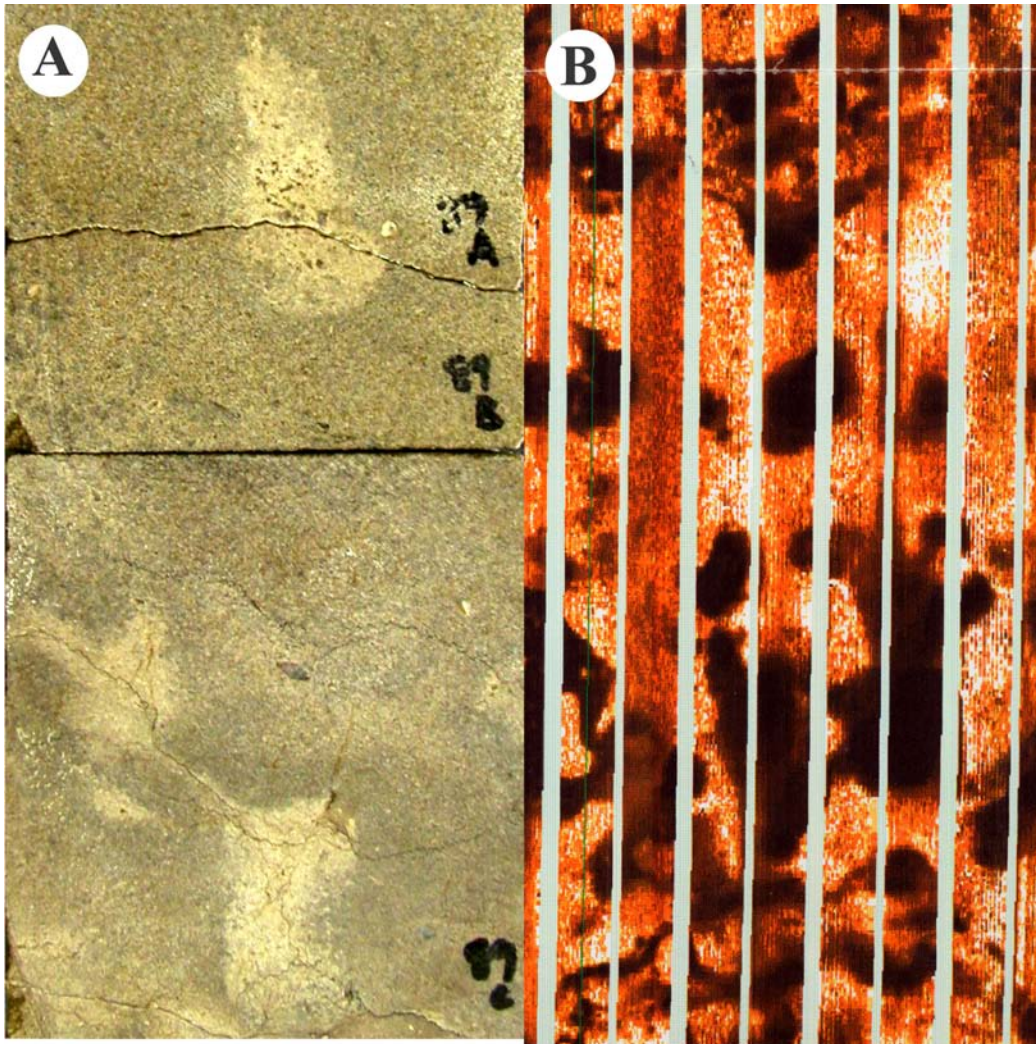


Figure 40. Image log and core photo images of “vuggy” fabric. Image log shows low-resistivity (black) features commonly interpreted to be open vugs. Core photo reveals that “vugs” are actually burrow fills (light-colored) of higher porosity. Lower Clear Fork. Core: FCU 6739, depth: 6,966 ft. Image log: FCU 2564, depth: 6,873–6,877 ft. Core is 4 inches wide.

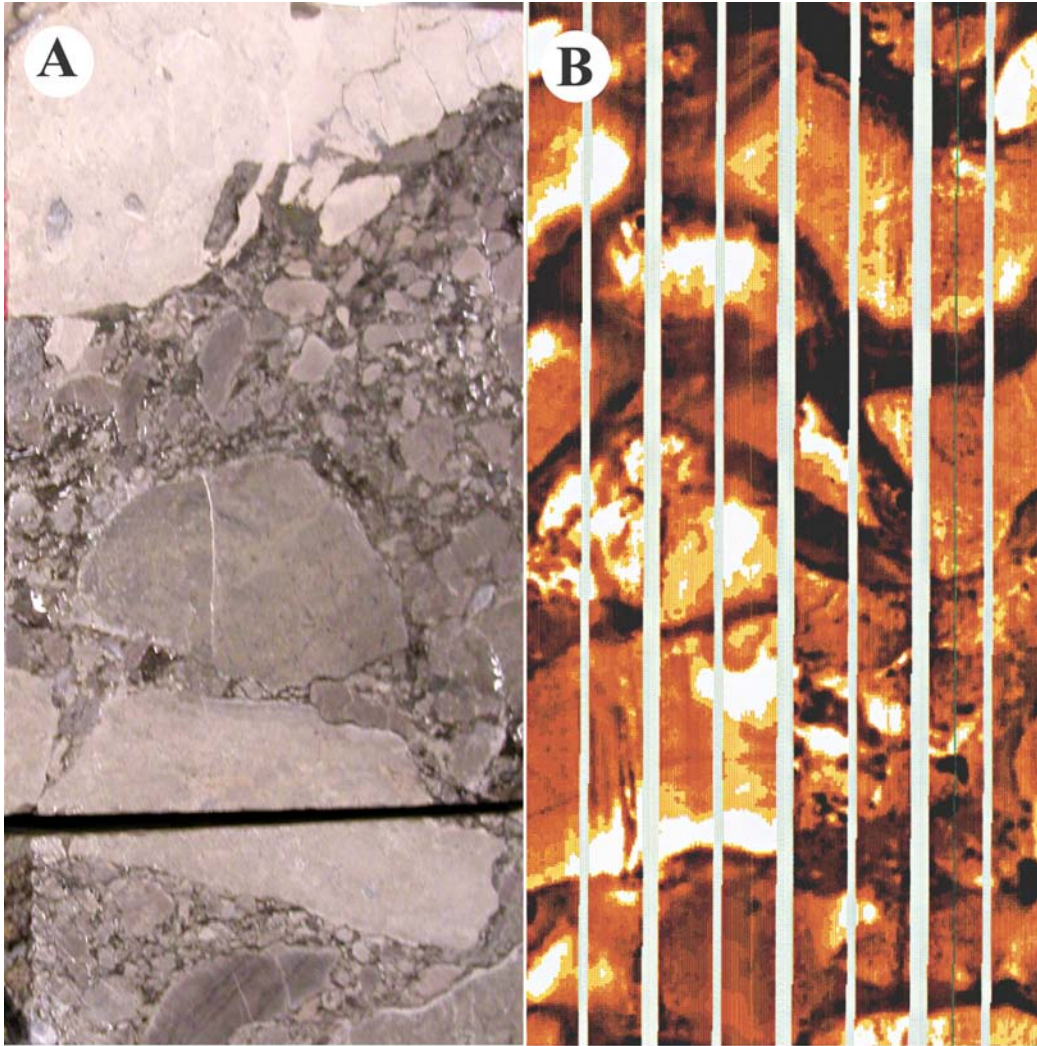


Figure 41. Image log and core photo images of polymict karst conglomerate. Wichita. Core: FCU 6122, depth: 7,201 ft. Image log: FCU 2564, depth: 7,171–7,182 ft. Core is 4 inches wide.

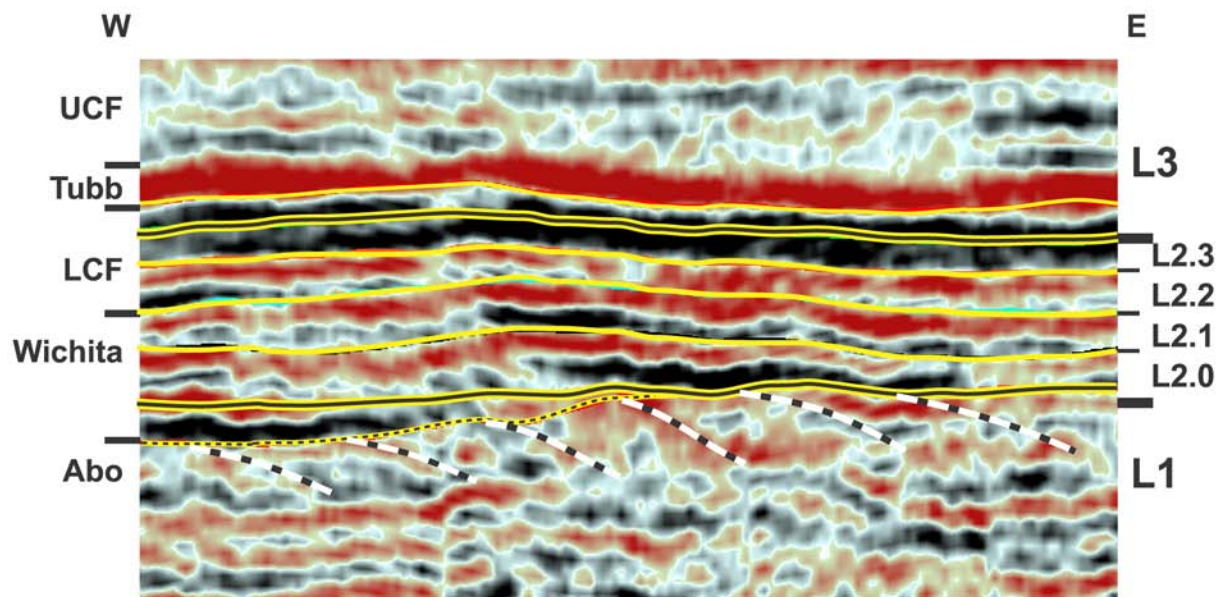


Figure 42. 3-D seismic section from Fullerton field showing general continuity and isopachous nature of Lower Clear Fork and Wichita reservoir intervals. Yellow lines are time lines; dotted line defines the top of Abo Formation.

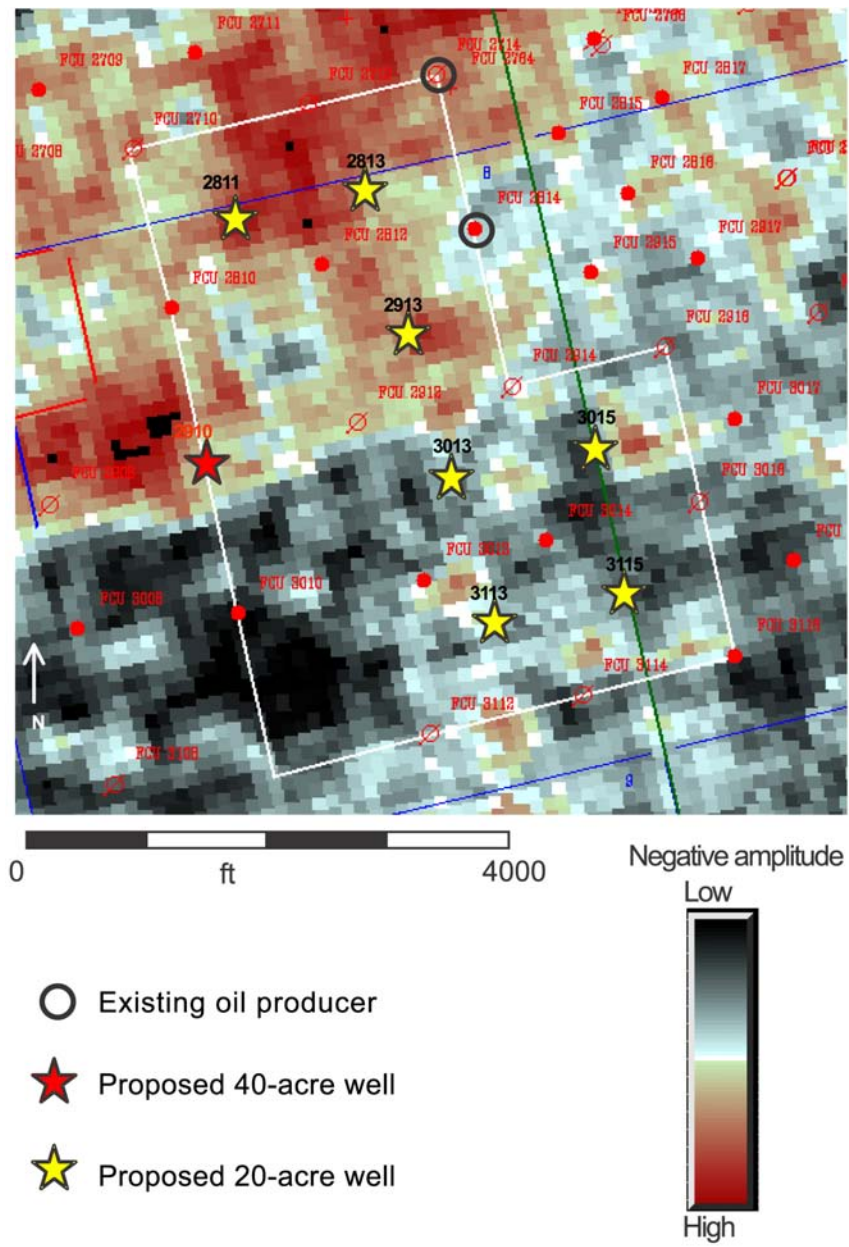


Figure 43. Map of negative amplitude data extracted from Fullerton 3-D data. The data show that proposed wells in the northern half of the area will encounter reservoir porosity, whereas those in the southern half will not.

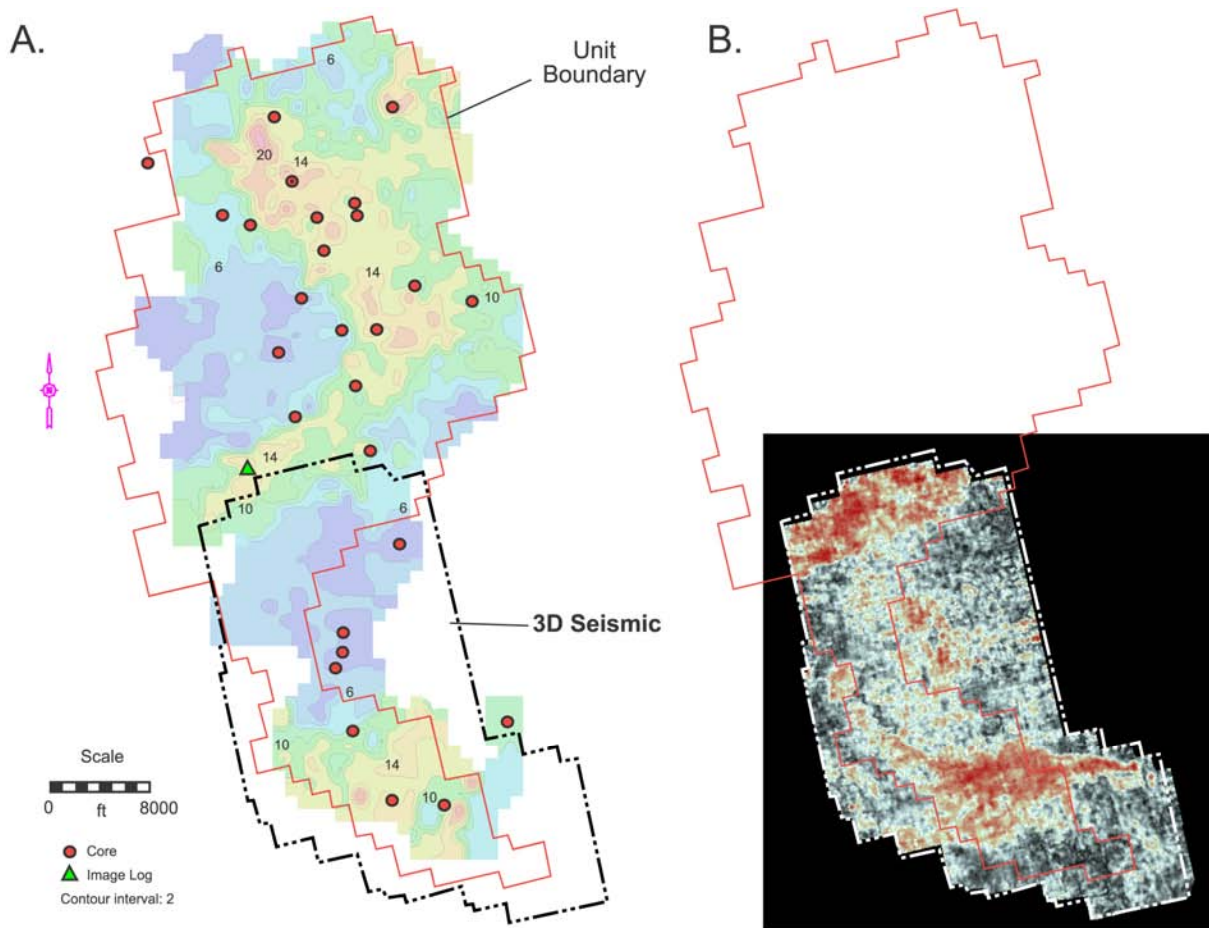


Figure 44. Porosity development in HFS 2.1. A. Map of porosity derived from well-log calculations. B. Map of negative amplitude data extracted from Fullerton 3-D seismic data. Note that the east-west-trending area of negative amplitude in the southern part of the field is not well imaged by wireline log data despite the close spacing of wells.

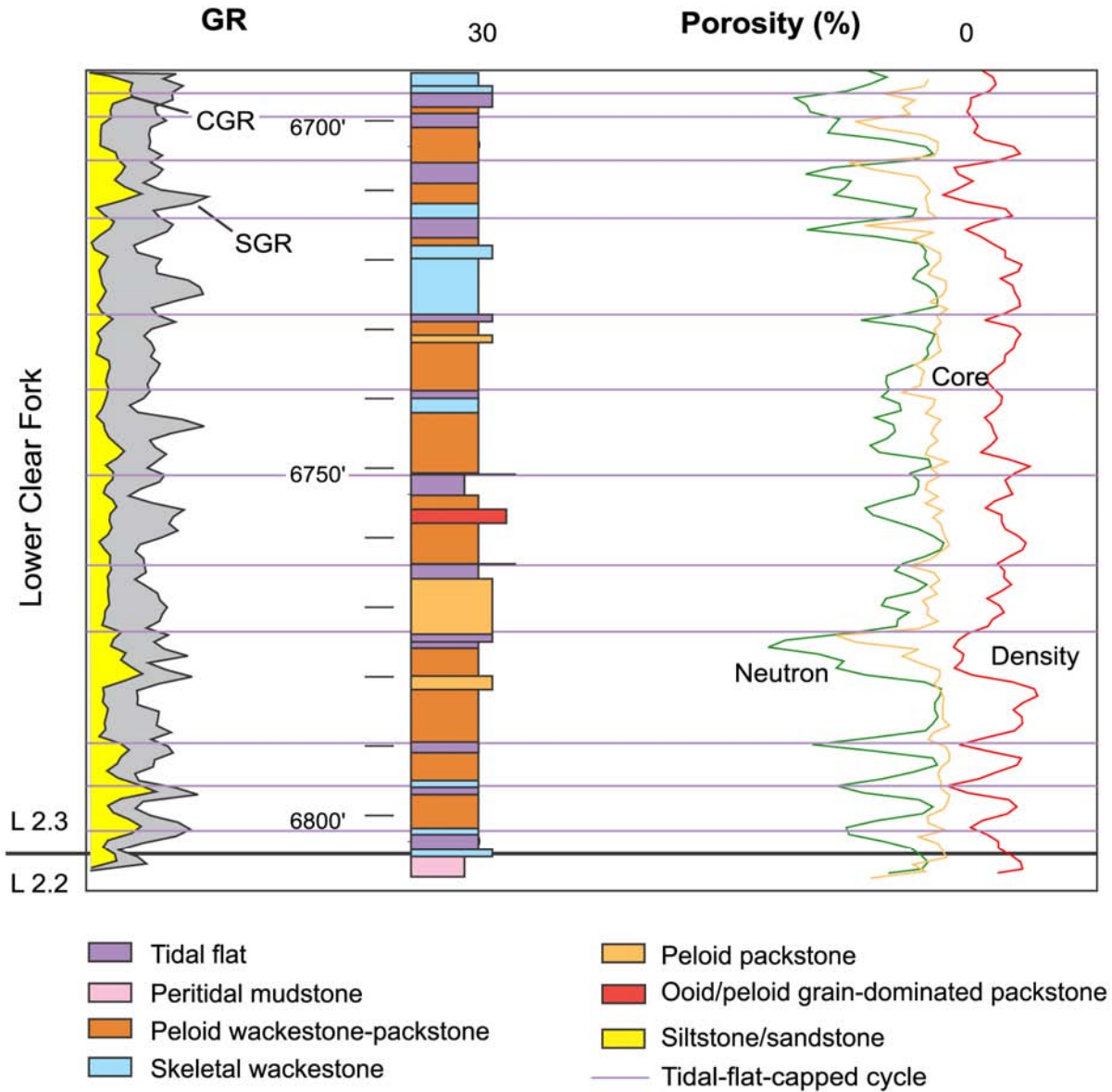


Figure 45. Comparison of core-defined facies and cyclicity with porosity logs in tidal-flat-capped cycles of HFS L 2.3. FCU 6122.

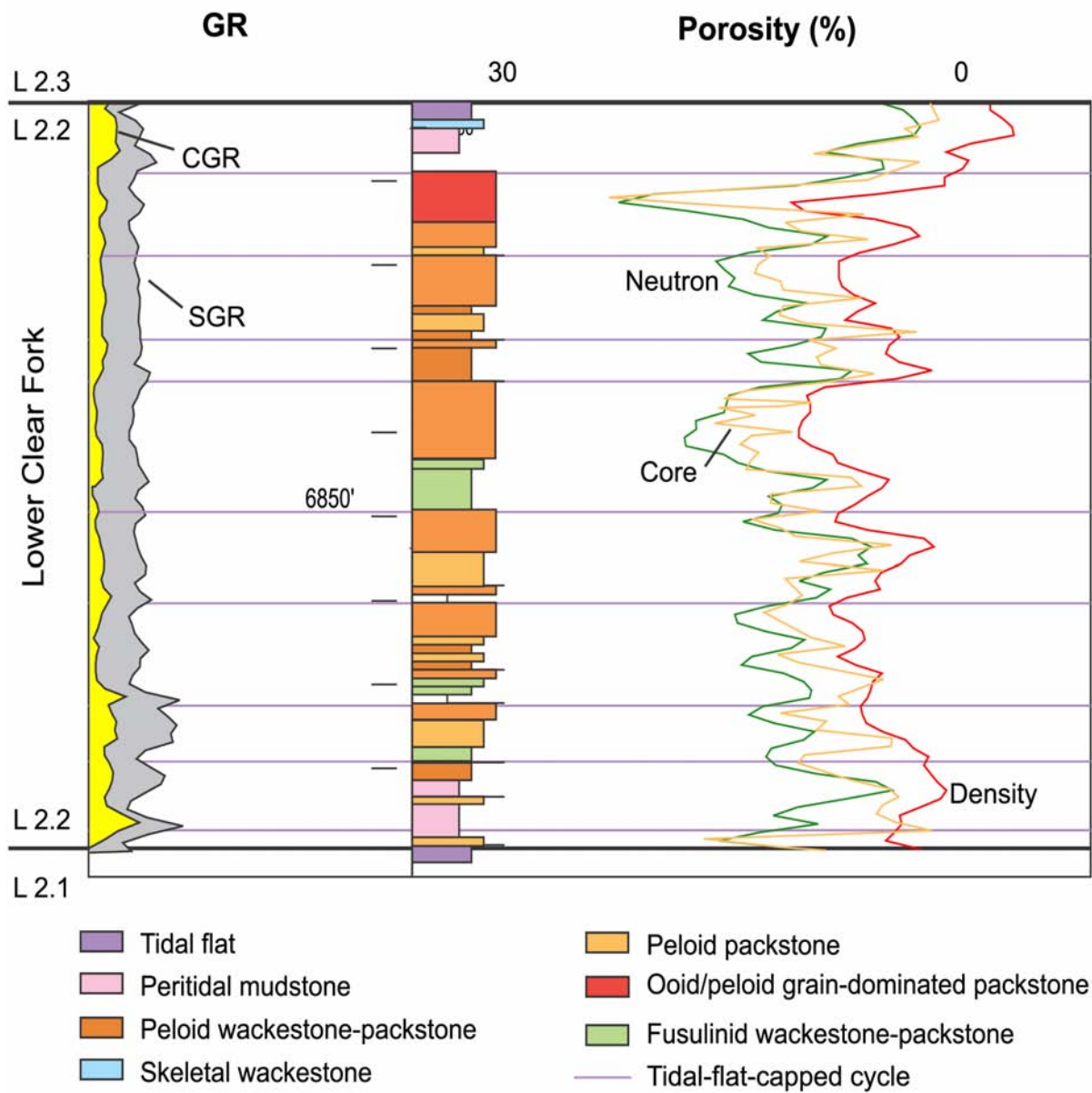


Figure 46. Comparison of core-defined facies and cyclicity with porosity logs in subtidal cycles of HFS L 2.2. FCU 6122.

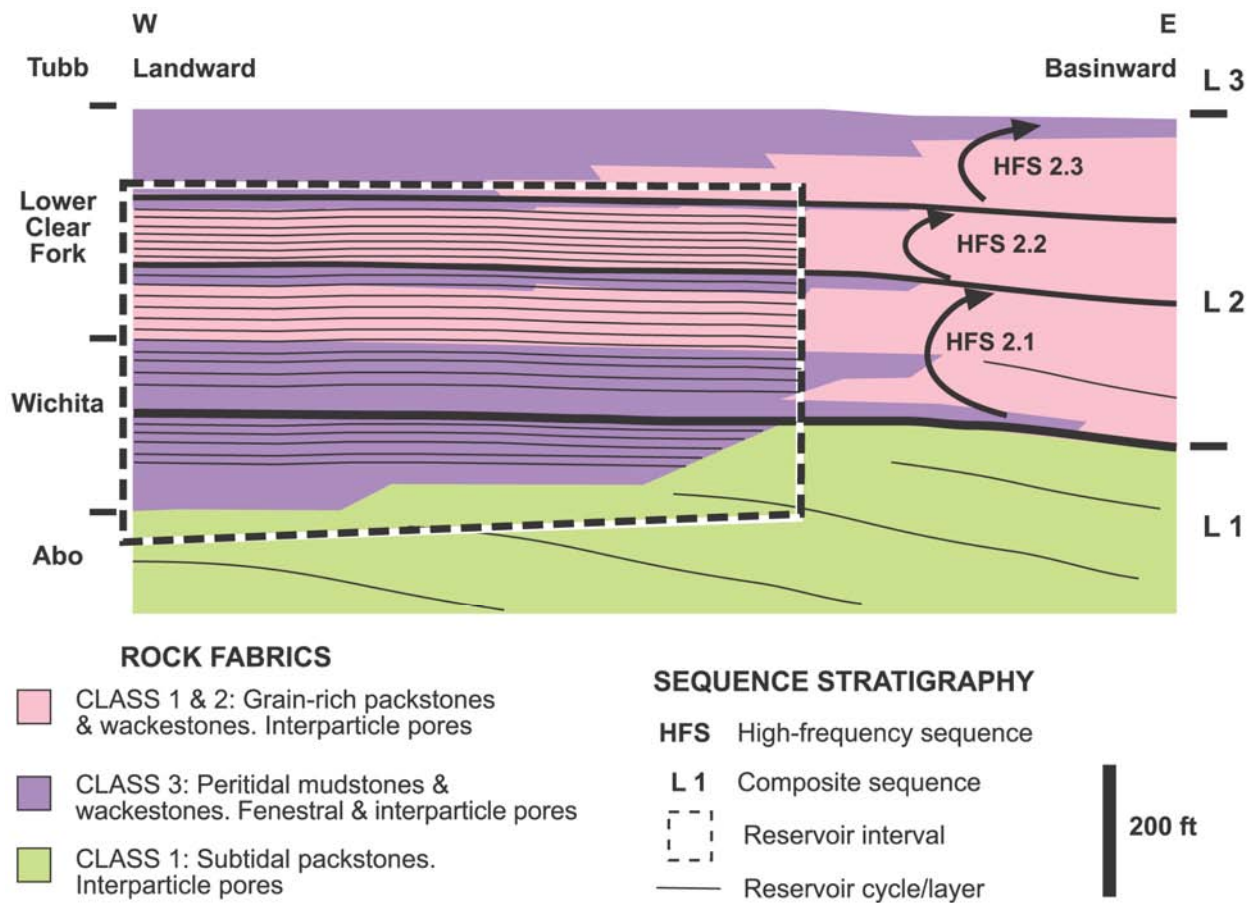


Figure 47. Schematic depiction of reservoir framework used for model construction at the Fullerton Clear Fork reservoir.

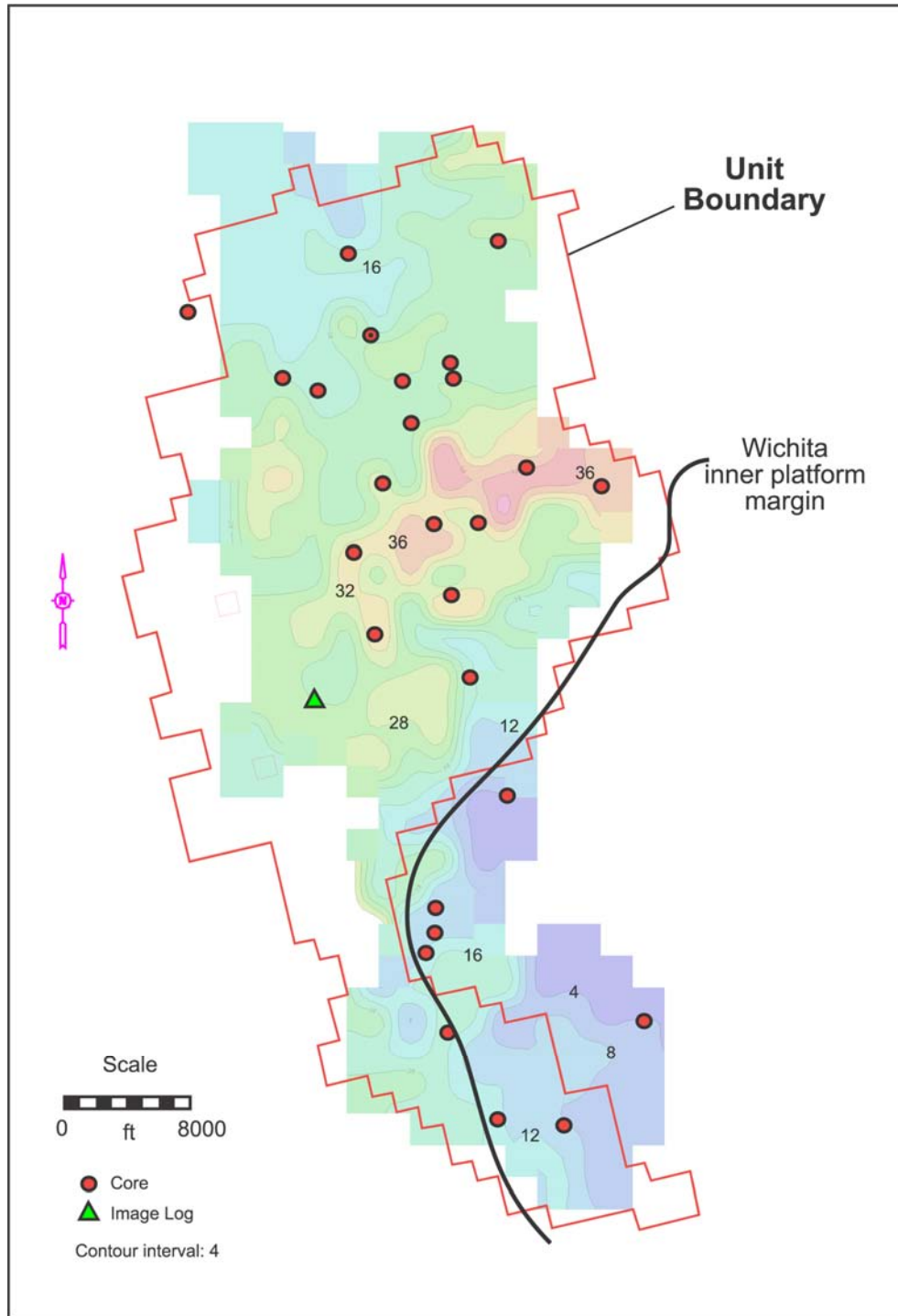


Figure 48. Map of total phih in the Wichita. Low values in the southeastern corner of the field are largely due to the facies change from Wichita tidal-flat facies to Abo facies in that area.

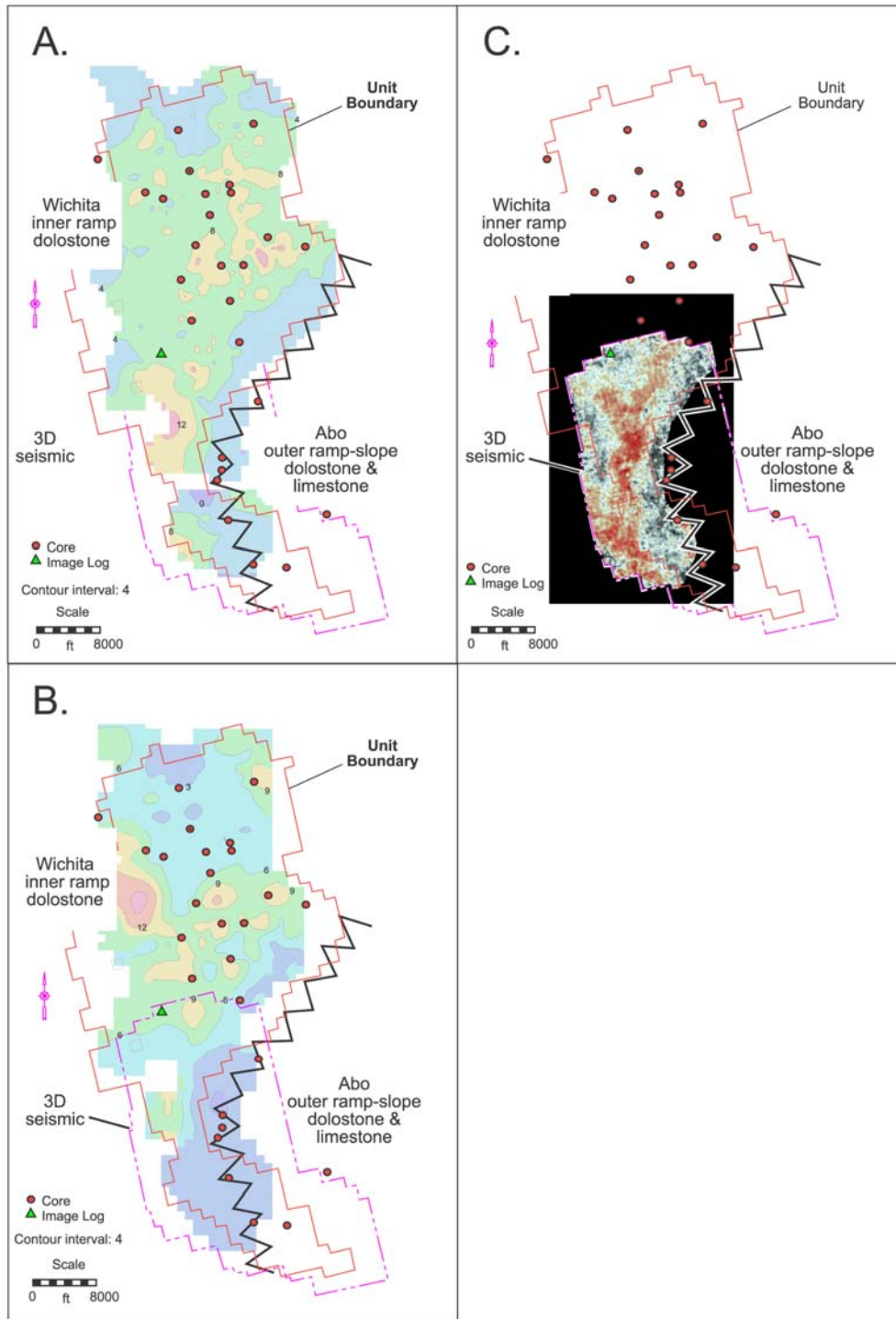


Figure 49. Maps of porosity distribution in the lower and upper parts of the lower Wichita (Sequence L 1). A. Phih map from wireline logs of the upper part of the lower Wichita (reservoir cycle/layers W8–W11). B. Phih map from wireline logs of the base of the lower Wichita (reservoir cycle/layer W12). C. Amplitude extraction from 3-D seismic volume for combined lower Wichita section. High negative amplitude equals high porosity. Zigzag line represents Wichita-Abo facies transition. Lower Wichita rocks are absent east of this line.

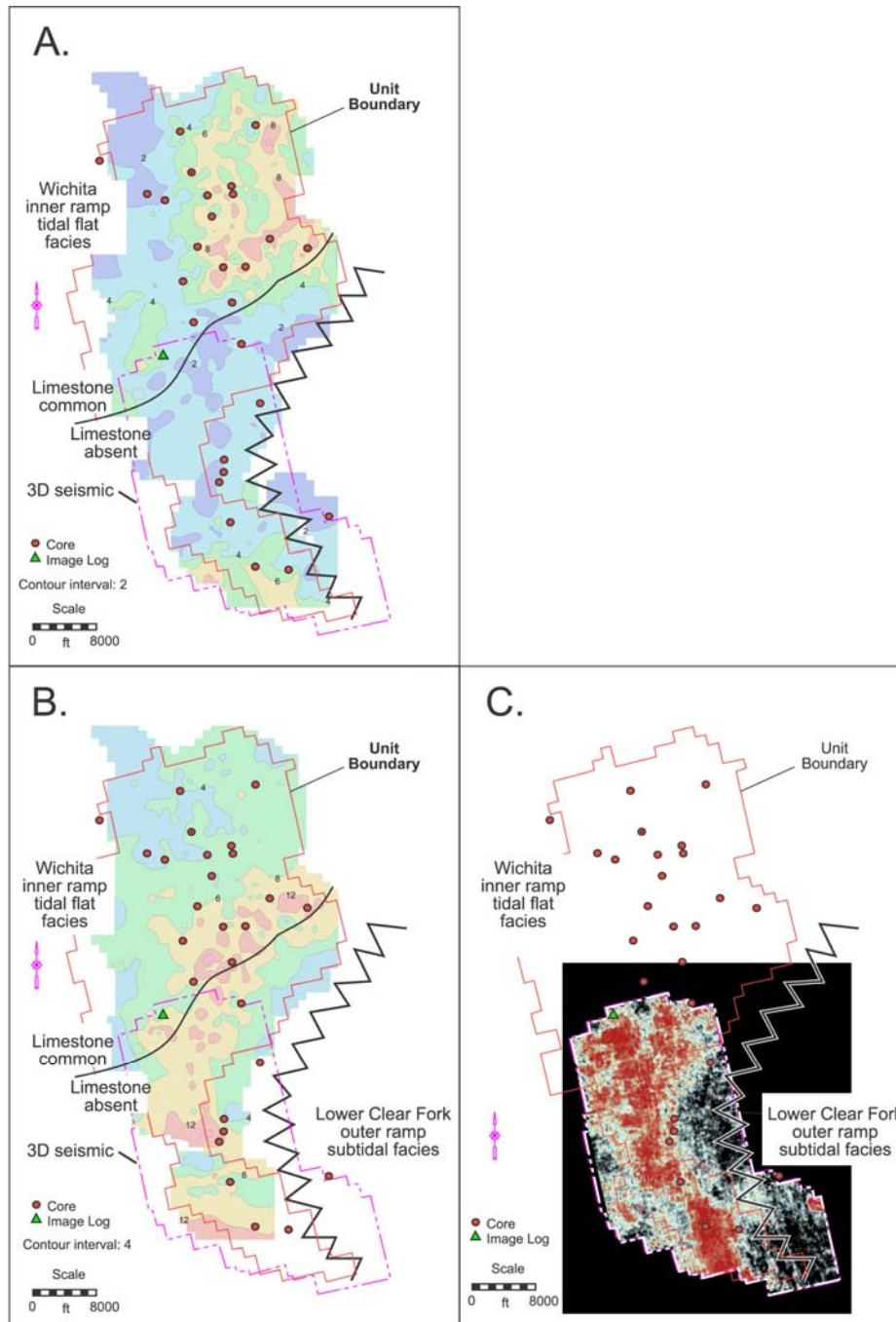


Figure 50. Maps of porosity distribution in the lower and upper parts of the upper Wichita (Sequence L 2.0). A. Phih map from wireline logs of the upper part of the upper Wichita (reservoir cycle/layers W1–W4). B. Phih map from wireline logs of the base of the upper Wichita (reservoir cycle/layers W4–W5). C. Amplitude extraction from 3-D seismic volume for combined upper Wichita section. High negative amplitude equals high porosity. Zigzag line represents Wichita–Lower Clear Fork facies transition. Upper Wichita rocks are absent east of this line. Note that porosity is concentrated along an arcuate belt that follows the outer edge of the Wichita inner platform tidal-flat complex.

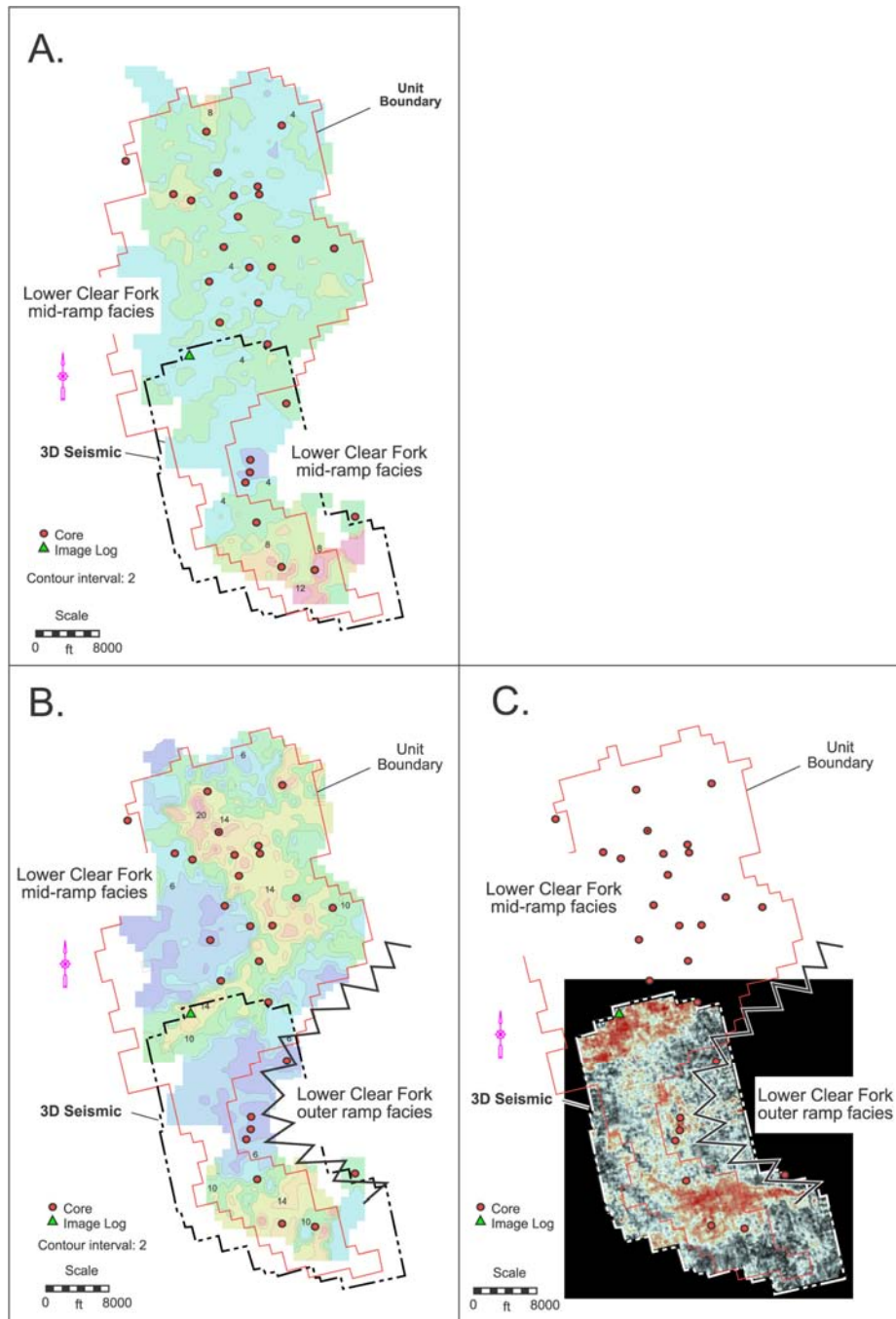


Figure 51. Maps of porosity distribution in the Lower Clear Fork. A. Phih map of HFS 2.2 from wireline logs. B. Phih map of HFS L 2.1. C. Amplitude extraction from 3-D seismic volume for HFS L 2.1 interval. High negative amplitude equals high porosity. Areas of high porosity in HFS L 2.1 and HFS L 2.2 correlate with areas of abundant limestone. Compare with figures 23 and 25.

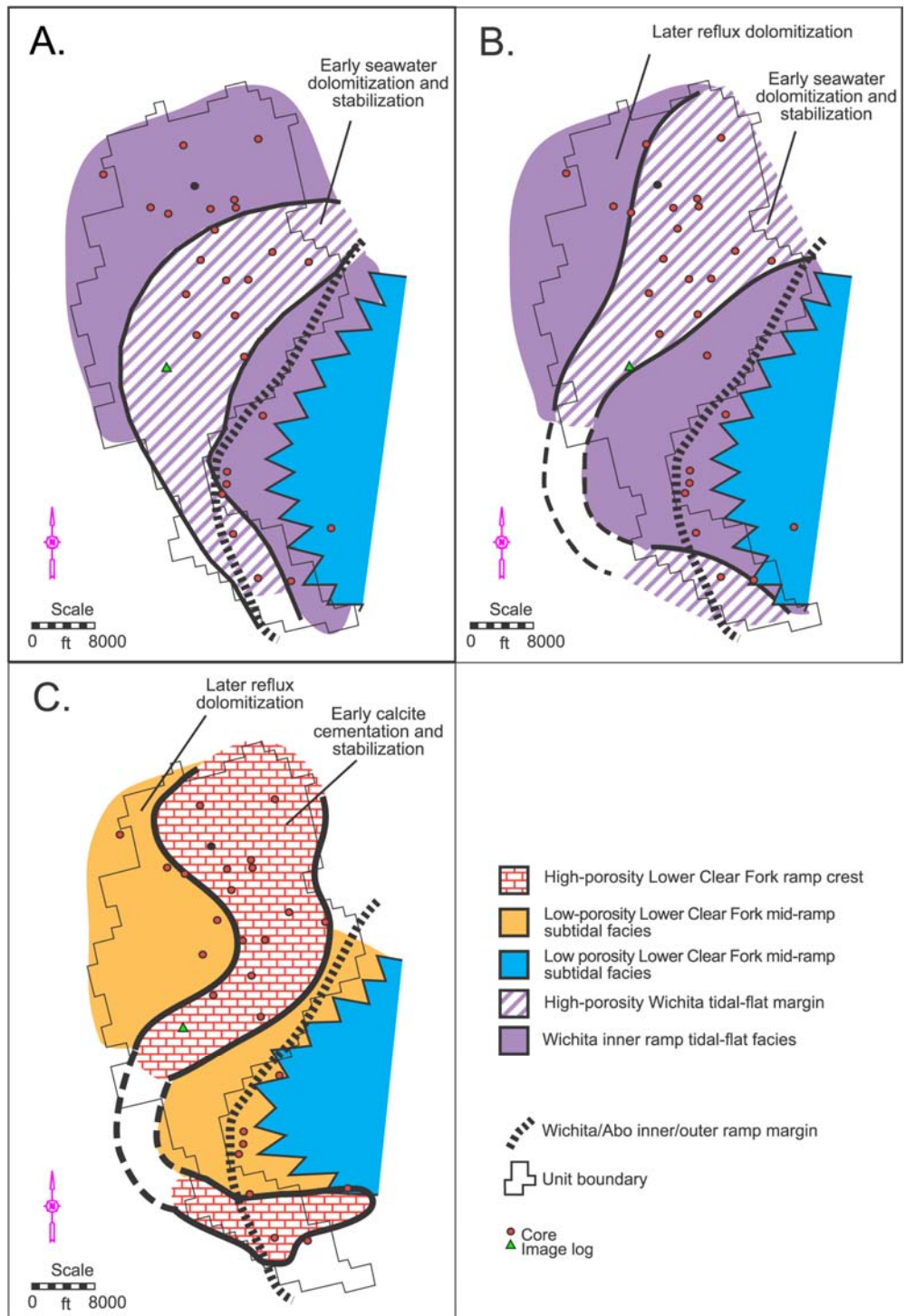


Figure 52. Models of porosity formation in the upper Wichita and the Lower Clear Fork (L2 sequence).

INTEGRATION OF ROCK FABRIC, PETROPHYSICAL CLASS,
AND STRATIGRAPHY FOR PETROPHYSICAL QUANTIFICATION OF
SEQUENCE-STRATIGRAPHIC FRAMEWORK,
FULLERTON CLEAR FORK FIELD, TEXAS

Rebecca H. Jones and F. Jerry Lucia

Bureau of Economic Geology
Scott W. Tinker, Director
John A. and Katherine G. Jackson School of Geosciences
The University of Texas at Austin
Austin, Texas 78713-8924

| | |
|---|-----|
| ABSTRACT..... | 125 |
| INTRODUCTION | 126 |
| METHODS | 128 |
| RESULTS | 129 |
| Abo Formation..... | 130 |
| Wichita Formation | 130 |
| Lower Clear Fork Formation | 131 |
| Lower Clear Fork L2.0 | 131 |
| Lower Clear Fork L2.1 | 132 |
| Lower Clear Fork L2.2 | 133 |
| Lower Clear Fork L2.3 | 134 |
| DISCUSSION..... | 135 |
| Limitations Due to Petrophysical Data Distribution..... | 135 |
| CONCLUSIONS..... | 137 |
| ACKNOWLEDGMENTS | 138 |
| REFERENCES | 139 |
| APPENDIX I: ROCK-FABRIC INSTRUCTIONS: Classifying Carbonate Pore Space from Thin Sections..... | 157 |

Figures

| | |
|--|-----|
| 1. Diagram showing fabrics composing petrophysical classes 1, 2, and 3 and a cross plot showing interparticle porosity vs. permeability, petrophysical class fields, and associated transforms | 141 |
| 2. Photomicrographs of class 1 fabrics observed in this study | 142 |
| 3. Photomicrographs of class 2 fabrics observed in this study | 143 |
| 4. Photomicrographs of class 3 fabrics observed in this study | 144 |
| 5. Location and boundaries of Fullerton field, Andrews County, Texas..... | 145 |

| | |
|---|-----|
| 6. Type log showing nomenclature used in this study and general vertical stacking of petrophysical classes..... | 146 |
| 7. Porosity-permeability plot of old Abo interval core analysis from wells throughout the field with core described in this study | 147 |
| 8. Photomicrographs of tidal-flat, class 3 fabrics observed in this study | 148 |
| 9. Distribution of limestone, dolostone, and petrophysical classes in the Wichita..... | 149 |
| 10. Wichita facies core analysis porosity-permeability plot and petrophysical class 3 transform used to calculate permeability | 150 |
| 11. Plot and histogram for Lower Clear Fork L2.1 subtidal unit high-resolution samples from wells FCU 5927 and 6429..... | 151 |
| 12. Porosity-permeability plot of core analysis from wells with core displaying dominantly class 1 fabrics in the subtidal portion of high-frequency sequence L2.1 | 152 |
| 13. Regions of different petrophysical classes and mineralogy in the subtidal portion of HFS L2.1 | 153 |
| 14. Regions of different petrophysical classes and mineralogy in HFS L2.2..... | 154 |
| 15. Porosity-permeability plot of Lower Clear Fork L2.2 showing that most samples plot in the class 1 field and photomicrograph example of poikilotopic anhydrite in a class 2 medium-crystalline dolostone | 155 |
| 16. Typical preexisting core analysis data vs. core analysis data resulting from unbiased sampling and careful cleaning of plugs | 156 |

Integration of Rock Fabric, Petrophysical Class, and Stratigraphy for Petrophysical Quantification of Sequence-Stratigraphic Framework, Fullerton Clear Fork Field, Texas

Rebecca H. Jones and F. Jerry Lucia

ABSTRACT

A major task in building a reservoir model is quantifying the geologic framework with petrophysical properties. Porosity and water saturation values can be obtained from wireline logs, but permeability is a rock property that cannot be obtained directly from logs. The traditional approach is to construct a single porosity-permeability transform to estimate permeability from porosity logs. In this study rock-fabric-specific porosity-permeability transforms are used together with the porosity log to estimate permeability. The numerous rock fabrics described from this field are grouped into three petrophysical classes, each having its unique transform, and the petrophysical classes are linked to stratigraphy through the study of high-resolution thin sections and core descriptions. The lowest stratigraphic unit studied in detail is the Wichita, which is composed dominantly of peritidal facies. It contains mostly fine-crystalline mud-dominated dolostones and mud-dominated limestones, all of which plot in the petrophysical class 3 field. Sequence L2.1 of the Lower Clear Fork contains an upper tidal-flat unit and a lower subtidal unit. The upper tidal-flat unit is composed of class 3 fine-crystalline mud-dominated fabrics similar to the Wichita. This unit extends over the entire field. The lower subtidal unit contains both limestone and dolostone. The dolostones are mostly medium-crystalline, subtidal grain-dominated dolopackstones and medium-crystalline mud-dominated dolostones that plot in the petrophysical class 2 field. Less common are intervals of oomoldic lime grainstone that also tend to plot in the petrophysical class 2 field on a porosity-permeability

cross plot. Grainstone is a class 1 rock fabric that plots in the class 2 field because total porosity—not interparticle porosity—is used. Interparticle porosity could not be calculated because of the lack of acoustic logs, and a class 2 transform was assigned to the limestones. In some areas old core analysis data suggest the presence of class 1 coarse-crystalline dolostones and anhydritic medium-crystalline dolostones. All other areas in the lower portion of sequence L2.1 are characterized by petrophysical class 2. The Lower Clear Fork sequence L2.2 is a class 2 medium-crystalline dolostone fabric that plots in the class 1 field because of the presence of large volumes of poikilotopic anhydrite. The sequence is characterized by a class 1 transform with the exception of a few areas of oomoldic limestone, which are characterized by a class 2 transform. The uppermost sequence in the Lower Clear Fork, L2.3, is composed of fine-crystalline dolostone class 3 peritidal facies and is characterized by a class 3 transform.

INTRODUCTION

The theory and development of the rock-fabric approach for quantifying geologic models was first described by Bureau of Economic Geology researchers Kerans, Lucia, and Senger (1994), Lucia (1995, 1999), and Jennings and Lucia (2001). This approach has been used successfully in a number of studies characterizing other Permian Basin carbonate reservoirs, including the San Andres at Seminole field (Lucia et al., 1995; Wang et al., 1998); the Clear Fork at South Wasson field (Lucia and Jennings, 2002), and the Grayburg at South Cowden field (Lucia and Ruppel, 1996; Ruppel and Lucia, 1996; Lucia, 2000).

The goal of the rock-fabric approach is to better understand permeability and original water saturation distribution in carbonate reservoirs. However, unlike porosity and water saturation, permeability cannot be measured by wireline tools and therefore is not easily obtainable. Research at the Bureau of Economic Geology has shown that permeability and water

saturation are a function of rock fabric and interparticle porosity. The three basic rock fabrics are (1) grainstone or dolograins, (2) grain-dominated packstone or dolopackstone, and (3) mud-dominated fabrics composed of mud-dominated packstone, wackestone, and mudstone and modified by dolomite crystal size. These fabrics are grouped into three petrophysical classes and given rock-fabric-specific porosity-permeability transforms (fig. 1), assuming that only interparticle pore space is present. Petrophysical class 1 rock fabrics include grainstones, dolograins, and coarse-crystalline ($>100\ \mu\text{m}$) dolostones (fig. 2); class 2 fabrics include grain-dominated packstones, grain-dominated dolopackstones, and medium-crystalline (20 to $100\ \mu\text{m}$) dolostones (fig. 3); and class 3 fabrics include mud-dominated packstones, wackestones, and mudstones and their fine-crystalline ($<20\ \mu\text{m}$) dolomitized counterparts (fig. 4).

Previous studies have shown that each petrophysical class has a respective porosity-permeability transform (fig. 1), which can be used to estimate permeability when interparticle porosity and petrophysical class can be determined from wireline logs. A complete suite of wireline logs is necessary to identify the rock-fabric petrophysical class. In the Fullerton Clear Fork field, however, there are few complete suites of wireline logs and the reservoir has been under waterflood for over 40 years. Therefore, this study was restricted to using gamma-ray logs and various types of porosity logs (Kane, this report). Consequently, separate-vug porosity, and thus interparticle porosity, could not be determined from logs, and relationships between total porosity and permeability had to be established. Likewise, petrophysical class could not be determined from porosity logs.

In this study, a new approach to determining petrophysical class was developed using the relationship between stratigraphy and petrophysical class. This approach is based on the concept

that petrophysical class is a product of rock fabrics and their dolomitization overprint and that this link between geologic description and petrophysical properties should result in a predictable relationship between petrophysical properties and stratigraphy. This report details the development of this relationship.

METHODS

Initial rock-fabric descriptions were done in the flow simulation area located in the north-central part of the field, where data quality and quantity are greatest (fig. 5). Two cores were resampled throughout the productive interval; 384 plugs were drilled from FCU 5927 and 111 samples from FCU 6429. New plugs were cut from every foot of core and analyzed for porosity and permeability. Thin sections were made from a wafer sliced from the end of each plug. Later, matching thin sections and core analyses were obtained in a similar manner from 210 samples of a core from FCU 7630 (fig. 5). New thin sections (245) were obtained from several other cores in the north-central part of the field (FCU 6429, FCU 6229, FCU 6122) and in the southern part of the field (FCU 4828, Univ. Cons. IV-25) as a check on rock-fabric interpretations.

Existing petrophysical data sets and thin sections were used to fill in the areas between the control wells. Data from 787 existing thin sections from 14 wells and whole core analyses from 63 wells were used. Neutron/density and PEF logs from 108 wells were used to determine mineralogy for mapping lithology.

Thin sections were described at the Bureau of Economic Geology on a polarizing microscope. Visual mineralogy estimates were made of percent calcite, dolomite, and anhydrite. Trace amounts of pyrite and quartz were also observed. Dolostones were defined as containing 80% or more dolomite and limestones as containing less than 80% dolomite as a percentage of the carbonate fraction. Dolomite crystal size (μm) was measured by selecting an average-sized

crystal and measuring the distance between its opposing crystal points. Fabrics were described using the Lucia classification (Lucia, 1995). These fabrics include grainstone, grain-dominated packstone, mud-dominated packstone, wackestone, and mudstone. Tidal-flat facies were described as grain dominated or mud dominated and brecciated. Separate-vug porosity was estimated and the presence of fractures noted. Point counts (300) were performed as necessary using a mechanical stage in areas of complex lithology or pore-type distribution to obtain more accurate estimates.

Appendix I contains detailed instructions for describing thin sections using the rock-fabric approach.

RESULTS

Rock-fabric variations were observed on many scales in the high-resolution data sets acquired in the north-central part of the field. Within a typical Lower Clear Fork cycle, mud-dominated facies compose the cycle base and the grain-dominated facies compose the cycle top. However, the petrophysical class is commonly constant throughout the cycle because the mud-dominated fabrics have been converted to a class 2 medium crystal mud-dominated fabric similar to the class 2 grain-dominated dolopackstone. Wichita cycles are typically composed of mud-dominated fabrics capped by tidal-flat facies. These peritidal fabrics have been converted to class 3 fine-crystalline mud-dominated dolostones. This pattern has been observed for peritidal intervals in the Lower Clear Fork as well. Therefore, it was initially thought that petrophysical properties in the Wichita could be characterized using porosity and a class 3 transform, whereas the Lower Clear Fork could be characterized using porosity and a class 2 transform. Figure 6 depicts the generalized stacking of petrophysical classes in a 1-D vertical profile for the Wichita and Lower Clear Fork Formations. However, several interesting variations were uncovered by

the detailed study, as shown by the characterization of sequence L2.2 as class 1 (fig. 6). Other lateral variations will be discussed in the following sections.

Abo Formation

The Abo Formation was not extensively studied because it is not part of the main reservoir. However, there are sufficient cores and core analysis data in the field to suggest that this formation can be characterized as a class 1 coarse-crystalline dolostone. No new core analysis or thin sections were made of the Abo, but there is marked consistency for the old data to plot in the class 1 field (fig. 7). Although a more detailed study of the Abo would most likely reveal complications, a petrophysical class 1 transform was assigned to the Abo Formation throughout the field for estimating permeability and initial water saturation.

Wichita Formation

The Wichita Formation consists of peritidal deposits that represent an updip, proximal facies equivalent of both the Abo outer platform succession and the lower portion of the Lower Clear Fork. As described in Ruppel and Jones (this report) core and outcrop data suggest that the Wichita composes parts of two depositional sequences: the highstand leg of sequence L1 and the transgressive leg of Leonardian sequence 2 (L2). The lower Wichita represents the updip, tidal-flat facies tract equivalent of the downdip, outer platform facies tract of the Abo in sequence L1, whereas the upper Wichita represents the updip tidal-flat facies equivalent of the basal Lower Clear Fork subtidal facies in high-frequency sequence L2.0, the earliest component of sequence L2.

The Wichita consists of mud-dominated fabrics including mudstones, wackestones, mud-dominated packstones, and tidal-flat fabrics. Typical tidal-flat features include pisolites, fenestrae, fine laminations, and desiccation cracks (fig. 8). Fenestrae are commonly lined with dolomite crystals and

filled with anhydrite or, less commonly, calcite. Fractures are locally present and typically filled with anhydrite or calcite. Very low porosity (<3%) limestones are interbedded with porous dolostones in the north-central part of the field (fig. 9) and may act locally as baffles to fluid flow. The rest of the Wichita contains primarily fine-crystalline dolostones. Both the limestones and the dolostones are dominantly petrophysical class 3, owing to the mud content and fine crystal size (fig. 10). Some class 2 grain-dominated dolopackstones and medium-crystalline mud-dominated dolostones are locally present but are uncommon in most of the field. Therefore, the formation was assigned petrophysical class 3, and a class 3 transform was used to estimate permeability and initial water saturation.

Lower Clear Fork Formation

The Lower Clear Fork sequences L2.0, L2.1, and L2.2 are composed primarily of subtidal facies with minor tidal-flat facies. The subtidal facies contain skeletal debris, including fusulinids, peloidal material, and ooids. Rock fabrics include wackestone, mud-dominated packstone, grain-dominated packstone, and grainstone. Both limestones and dolostones are present. Limestones in the Lower Clear Fork are grain dominated (figs. 2a and 3a) and often more porous than the dolostones, with most porosity values ranging from 5 to 15%, and some as high as 30%. The petrophysical classes are dominantly class 1 and 2, owing to the more grain-rich textures of the limestones and the medium and coarse dolomite crystal size in the dolostones.

Lower Clear Fork L2.0

In most of the field area, high-frequency sequence (HFS) 2.0 consists of amalgamated tidal-flat deposits of the upper Wichita, which are assigned to petrophysical class 3. However, subtidal Lower Clear Fork deposits of L 2.0 were deposited during the latter part of this HFS at the margins (downdip) of the field, as evidenced by core description of the most distal

southeastern well, but are not penetrated by other wells in the field. There is very little data from this facies, and it was assigned a petrophysical class of 2 because the limited data suggest that it is a medium-crystalline dolostone.

Lower Clear Fork L2.1

As described in Ruppel and Jones (this report), L 2.1 consists of a basal section of transgressive to early highstand subtidal platform facies and an upper section of highstand tidal-flat facies. In the lower subtidal interval, cycles shallow upward from lower energy wackestones and mud-dominated packstones to higher energy grain-dominated packstones and grainstones. The class 3 mud-dominated fabrics have been converted to a class 2 medium-crystalline dolostone similar to the class 2 grain-dominated dolopackstone. (fig. 11). Lime grainstones and grain-dominated packstones are interbedded with dolostones in some areas. Although the limestones are class 1 and 2 fabrics, respectively, they plot in the class 2 and 3 field on the porosity-permeability cross plot, most falling in the class 2 field, as shown by a histogram illustrated in figure 11. The limestones plot in the class 2 and 3 field because they contain considerable amounts of moldic porosity (a type of separate vug), and total porosity, not interparticle porosity, is used in the cross plot. Ideally, moldic porosity would be subtracted from total porosity and a class 1 transform and interparticle porosity would be used to estimate permeability. However, without acoustic logs, estimates of moldic porosity could not be made. In addition, the lime grainstones are interbedded with dolostones and cannot be mapped separately. Therefore, the moldic grain-dominated limestones are assumed to be class 2 because most of the data fall in the class 2 field. Accordingly, the subtidal portion of HFS L2.1 was characterized by a class 2 transform.

Class 1 dolostone fabrics are interpreted as dominant in two areas of the field on the basis of old core data (fig. 12). The class 1 dolostones appear to be coarse-crystalline dolostones and anhydritic medium-crystalline dolostones. The effect of patchy anhydrite on petrophysical class will be discussed more fully in the section HFS L2.2. The distribution of lithology and petrophysical class is shown in figure 13.

The upper highstand leg of HFS L2.1 consists of peritidal deposit fabrics, including mudstones, wackestones, and some mud-dominated packstones, many of which display exposure features, similar to the Wichita peritidal section. Dolostones are mud-dominated and fine-crystalline class 3 fabrics (fig. 6), and petrophysical class 3 is used to characterize this unit throughout the field.

Lower Clear Fork L2.2

HFS L 2.2 is composed dominantly of dolostone. Limestone is dominant in some areas of the field: in the south and in a small area in the northwestern part of the field (fig.14). Most samples studied are class 2 grain-dominated dolopackstones and medium-crystalline mud-dominated fabrics. However, many samples plot in the class 1 field rather than the class 2 field as expected (fig. 15a). The samples that plot in the class 1 field do not appear to have any consistent stratigraphic position. Most of these medium-crystalline dolostones contain $\geq 10\%$ poikilotopic anhydrite (fig. 15b), and their petrophysical class 1 behavior can be explained by the patchy distribution of anhydrite as discussed below. These rocks are consistently present throughout the field (except where limestone is present) and are best fit by a class 1 transform for estimating permeability and initial water saturation.

The shift of medium-crystalline class 2 dolostones into the class 1 field coincides with an increase in poikilotopic anhydrite, as explained by the fact that discrete patches of pore-filling

anhydrite will decrease porosity without decreasing pore-throat radius. Because permeability is controlled by the pore-throat radius, this reduction in porosity does not result in a corresponding decrease in permeability. This effect was first observed in the South Wason Clear Fork reservoir by Lucia and Jennings (2002) and was discussed by Lucia et al. (2004).

Limestone is interbedded with dolostone over most of the southern part of the field and locally in the northwest (fig. 14). HFS L2.2 in these areas is composed of a mix of low-porosity medium-crystalline mud-dominated dolostones (fusulinid wackestones) and high-porosity grain-dominated limestones (grain-dominated packstones and grainstones). The grainstones tend to contain mostly separate-vug porosity, and the grain-dominated packstones tend to have mixed separate-vug and interparticle porosity. These moldic limestones typically plot in the petrophysical class 2 and 3 field, as illustrated in figure 11. As a result, a class 2 transform was used in these areas to estimate permeability and initial water saturation.

Lower Clear Fork L2.3

Tidal-flat-capped restricted subtidal cycles compose the uppermost Lower Clear Fork high-frequency sequence (L 2.3) throughout most of the field area. Tidal flat caps are typically fine-crystalline mud-dominated fabrics with fenestrae, and the underlying cycle-base subtidal rocks are dominantly fine-crystalline mud-dominated dolostones. Whereas these cycle-capping tidal-flat facies are porous and nearly continuous across the field, they are very thin and contain little if any reservoir permeability. Both the thin tidal-flat caps and the fine-crystalline subtidal dolostones are petrophysical class 3. A possible exception to this classification occurs along the outer margins of the field where grain-rich peloidal packstones of the middle ramp become more common. A detailed study of this facies found a predominance of class 3 fabrics. Thus, a class 3 transform was used for L2.3 permeability and initial water saturation calculations throughout the field.

DISCUSSION

Limitations Due to Petrophysical Data Distribution

The detailed rock-fabric data available in the three wells studied in detail were extrapolated throughout the field using preexisting data sets. These detailed data sets are necessary in order to judge the quality of preexisting data sets and to determine the usefulness of the data. Preexisting data sets are variable in their quality, quantity, and distribution throughout the different stratigraphic intervals and must be used judiciously. Figure 16 shows the difference between the new data obtained in this study and preexisting whole core analysis on a porosity-permeability plot. The low-porosity, highly variable permeability data in the old analyses were eliminated because the data are most likely the result of biased samples or poor analysis procedures.

In addition to basic data quality issues, existing thin sections were often too widely spaced or biased toward a particular feature to yield an adequate description of the vertical variation in rock fabrics and petrophysical classes. More thorough sampling of many of the cores would have been useful. For example, vertical variations between class 3 and 2 dolostone fabrics occur on a scale smaller than that at which most cores are sampled, and these variations have been smoothed over in order to arrive at a usable approach. In particular, the rich variability in limestone fabrics has been overlooked and averaged out into an oversimplified petrophysical characterization. The impact of both data limitations and rock-fabric smoothing is discussed in the following section by stratigraphic unit.

The Abo subtidal facies (L1) is poorly known because of the lack of well penetration. Our class 1 rock-fabric assignment for this interval is based on the porosity-permeability plot of all available core analysis data (Fig. 7) from wells with core and confirmed by thin sections

examined in this study. However, there is considerable room within the data for areas and intervals that contain class 2 and 3 fabrics.

In the Wichita (L1 and L2), most fabrics are class 3, and the entire interval was modeled as class 3. However, thin sections and core descriptions indicate local and laterally discontinuous deposition of class 2 dolostone fabrics, particularly during the initial flooding of the platform during early L2 transgression. We were unable to establish any continuity of these fabrics across the field, which eliminated the possibility of including them in the model. Where present, their permeability is probably underestimated because class 3, rather than class 2, was applied. In addition, core descriptions show intervals of collapse breccia, suggesting the possibility of a touching-vug pore system composed of fractures and vugs that have not been included in this rock-fabric model. Indeed, the flow simulation required an increase in permeability by a factor of 15 to match injection volumes in the lower Wichita.

In the Lower Clear Fork, major changes in petrophysical class are mapped in both L2.1 and L2.2. In both HFS L2.1 and L2.2, distinct regions of petrophysical class 2 and class 1 dolostones are mapped. Regions of interbedded limestone and dolostone were mapped using new and existing thin sections, core analysis, grain density information, and wireline logs. The limestones have different rock fabrics from the dolostones. In most cases, the limestones are highly porous, are grain dominated, and contain separate-vug (often oomoldic) porosity. The interbedded dolostones are typically lower porosity, are more mud dominated, and have fine to medium dolomite crystals. As described in the results section, both the limestones and dolostones plot in the class 2 and 3 fields, with a majority of points in the class 2 field. Because most of the data plot in the class 2 field, a class 2 was assigned to the areas of interbedded limestone and dolostone. A more accurate petrophysical model would have resulted if dolostones

and limestones could have been mapped separately. However, the lack of adequate logs precluded mapping lithology at this scale.

CONCLUSIONS

At Fullerton field, we have linked rock fabrics and petrophysical-class transforms, depositional facies, diagenetic overprints, and stratigraphic position. Three basic porosity-permeability transforms are used: class 1, 2, and 3. Dolomitized tidal-flat facies are fine-crystalline dolostones and mud-dominated limestones that fall in the class 3 field. Subtidal facies in the Lower Clear Fork tend to be medium- to coarse-crystalline dolostones occasionally containing large amounts of poikilotopic anhydrite. Limestones tend to be class 1 and 2 grain-dominated fabrics having large volumes of separate vugs causing them to plot in the class 2 and 3 fields. This link between rock fabric, petrophysical class, and petrophysical properties allows the use of the three basic transforms and results in a reasonable petrophysical model. The use of multiple transforms keyed to stratigraphy represents a big improvement over single-transform techniques, which would have drastically overestimated permeability in some intervals and underestimated permeability in others.

Changes in petrophysical classes and thereby porosity-permeability transforms are the most significant between intervals composed primarily of subtidal facies and intervals composed primarily of peritidal facies. Core analysis demonstrates at least 12% porosity is required in the Wichita to provide 1 md of permeability, whereas only ~8% porosity is required to provide the same permeability in the Lower Clear Fork, owing to the significant differences in rock fabric and petrophysical class between these formations.

Finer scale changes in petrophysical class are present within and between cycles, within and between high-frequency sequences, between systems tracts, and between regions of the field.

The ability to incorporate subtle changes in petrophysical class at the field scale is highly dependent upon petrophysical data quality and quantity and degree of homogeneity in geologic and petrophysical parameters across the field. Refinements of our rock-fabric model would certainly be possible with additional high-resolution data. However, the results we achieved utilizing high-resolution data acquired in this study, in conjunction with preexisting data in a sequence-stratigraphic context, are very satisfactory, as measured by the excellent match between rock-fabric-modeled permeability and core-analysis-derived permeability throughout the reservoir (Lucia, Kane, and Jones, this report)

ACKNOWLEDGMENTS

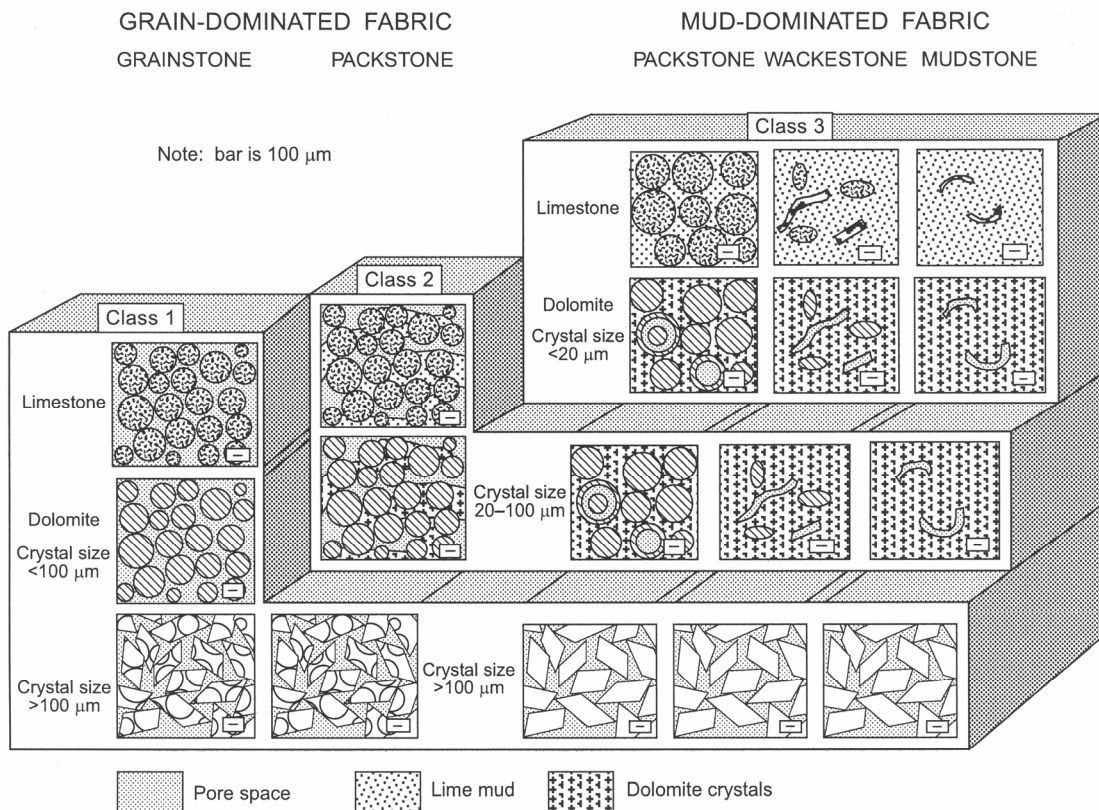
This research was funded by ExxonMobil Production Company, The University of Texas System, and the U.S. Department of Energy under contract DE-FC26-01BC15351. The Bureau of Economic Geology acknowledges support of this research by Landmark Graphics Corporation via the Landmark University Grant Program.

REFERENCES

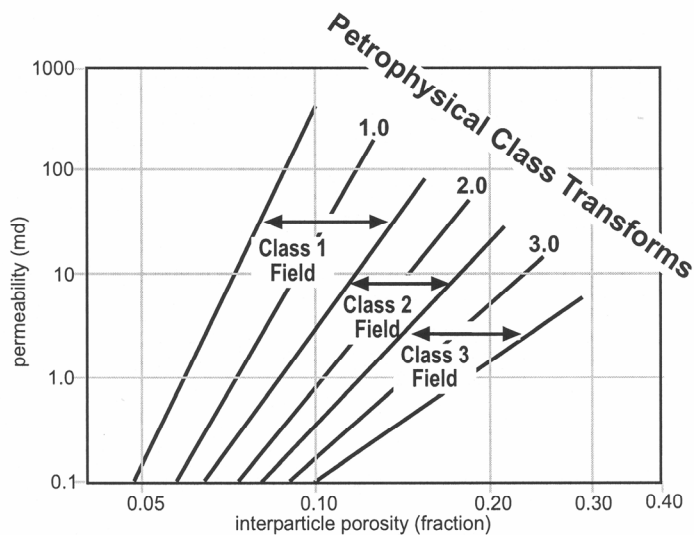
- Jennings, J. W., Jr., and Lucia, F. J., 2001, Predicting permeability from well logs in carbonates with a link to geology for interwell permeability mapping: Proceedings 2001 SPE Annual Technical Conference and Exhibition, Society of Petroleum Engineers, SPE 71336, p.1–16.
- Kerans, Charles, Lucia, F. J., and Senger, R. K., 1994, Integrated characterization of carbonate ramp reservoirs using Permian San Andres Formation outcrop analogs: American Association of Petroleum Geologists Bulletin, v. 78, no. 2, p. 181–216.
- Lucia, F. J., 1995, Rock-fabric/petrophysical classification of carbonate pore space for reservoir characterization: American Association of Petroleum Geologists Bulletin, v. 79, no. 9, p. 1275–1300.
- Lucia, F. J., 1999, Carbonate reservoir characterization: Berlin, Springer-Verlag, 226 p.
- Lucia, F. J., 2000, Petrophysical characterization and distribution of remaining mobile oil: South Cowden Grayburg reservoir, Ector County, Texas: The University of Texas at Austin, Bureau of Economic Geology, Report of Investigations No. 260, 54 p.
- Lucia, F. J., and Jennings, J. W., Jr., 2002, Calculation and distribution of petrophysical properties in the South Wasson Clear Fork field, *in* Lucia, F. J., ed., Integrated outcrop and subsurface studies of the interwell environment of carbonate reservoirs: Clear Fork (Leonardian-age) reservoirs, West Texas and New Mexico: The University of Texas at Austin, Bureau of Economic Geology, Final Technical Report prepared for U.S. Department of Energy under Contract No. DE-AC26-98BC15105, p. 95–142, <http://www.osti.gov/dublincore/ecd/servlets/purl/811895-4EHgbz/native/811895.pdf>.
- Lucia, F. J., Jones, R. H., and Jennings, J. W., 2004, Poikilotopic anhydrite enhances reservoir quality (abs.): American Association of Petroleum Geologists Annual Convention Abstracts Volume, v. 13, p. A88.
- Lucia, F. J., Kerans, C., and Wang, F. P., 1995, Fluid-flow characterization of dolomitized carbonate-ramp reservoirs: San Andres Formation (Permian) of Seminole field and Algerita Escarpment, Permian Basin, Texas and New Mexico, *in* Stouidt, E. L., and Harris, P. M., eds., Hydrocarbon reservoir characterization: geologic framework and flow unit modeling: SEPM (Society for Sedimentary Geology), SEPM Short Course No. 34, p.129–153.
- Lucia, F. J., and Ruppel, S. C., 1996, Characterization of diagenetically altered carbonate reservoirs, South Cowden Grayburg reservoir, West Texas: Proceedings, 1996 SPE Annual Technical Conference and Exhibition, Society of Petroleum Engineers, SPE 36650, p. 883–893.

- Ruppel, S. C., and Lucia, F. J., 1996, Diagenetic control of permeability development in a highly cyclic, shallow-water carbonate reservoir: South Cowden Grayburg field, Ector County, Texas: West Texas Geological Society Fall Symposium, p. 7–22.
- Wang, F. P., Lucia, F. J., and Kerans, C., 1998, Modeling dolomitized carbonate-ramp reservoirs: A case study of the Seminole San Andres Unit—Part I, Petrophysical and geologic characterizations: *Geophysics*, v. 63, no. 6, p. 1866–1875.

PETROPHYSICAL CLASSES



QA 15772c



QAd2746c

Figure 1. Diagram showing fabrics composing petrophysical classes 1, 2, and 3 and a cross plot showing interparticle porosity vs. permeability, petrophysical class fields, and associated transforms.

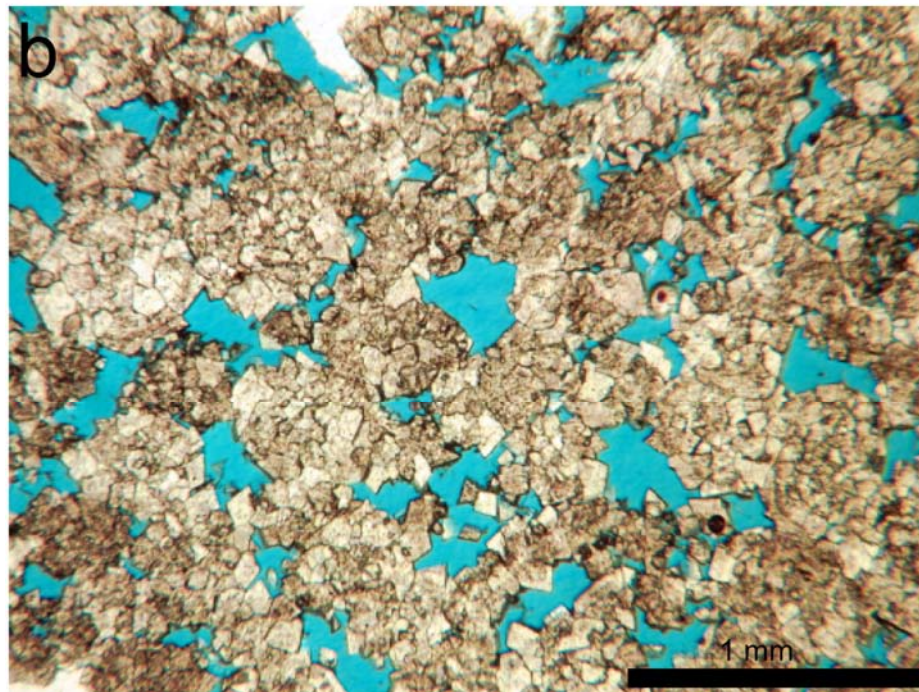
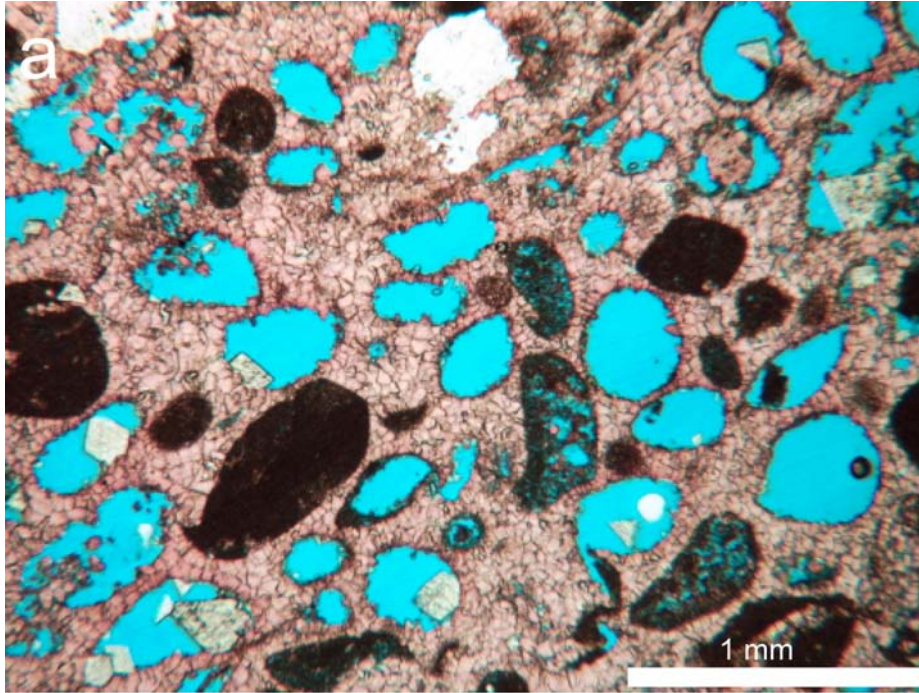


Figure 2. Photomicrographs of class 1 fabrics observed in this study: (a) Lime grainstone with separate-vug pore space: FCU 5927, 6913', $\phi = 22.0\%$, $k = 2.69$ md. (b) Coarse-crystalline dolograins: FCU 7630, 6997', $\phi = 11.7\%$, $k = 112.56$ md, dolomite crystal size 120 μm .

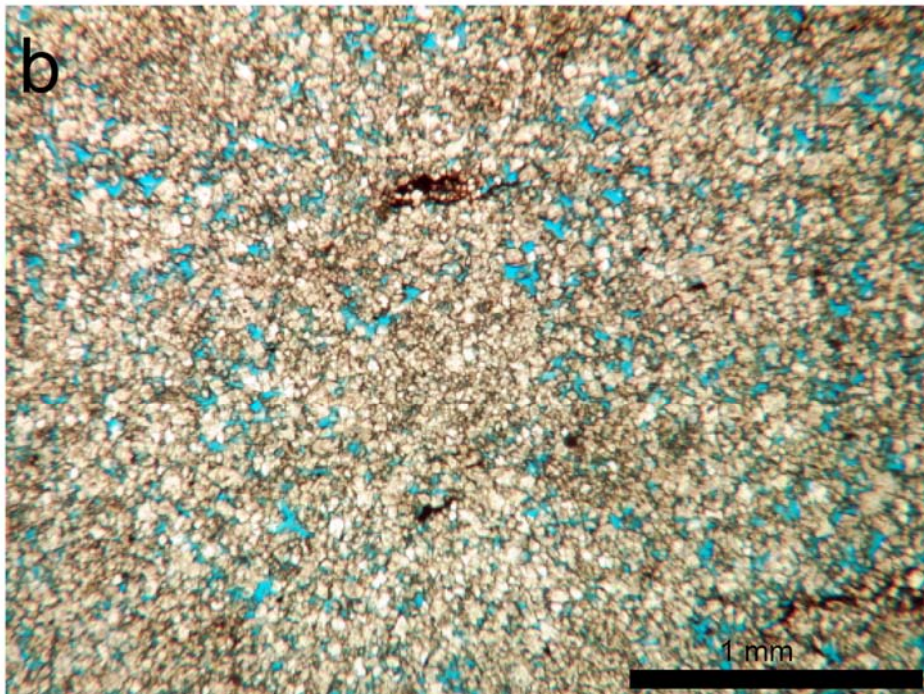
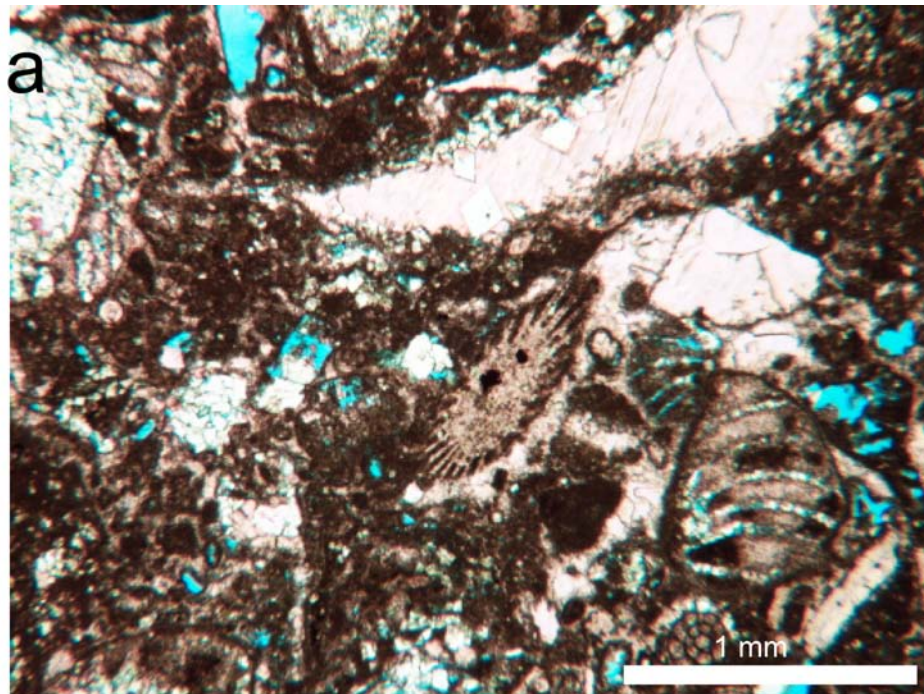


Figure 3. Photomicrographs of class 2 fabrics observed in this study: (a) Grain-dominated packstone with separate-vug pore space: FCU 5927, 6987', $\phi = 8.8\%$, $k = 0.04$ md. (b) Medium-crystalline grain-dominated dolopackstone: FCU 6429, 6914', $\phi = 18.1\%$, $k = 27.2$ md, dolomite crystal size $55 \mu\text{m}$.

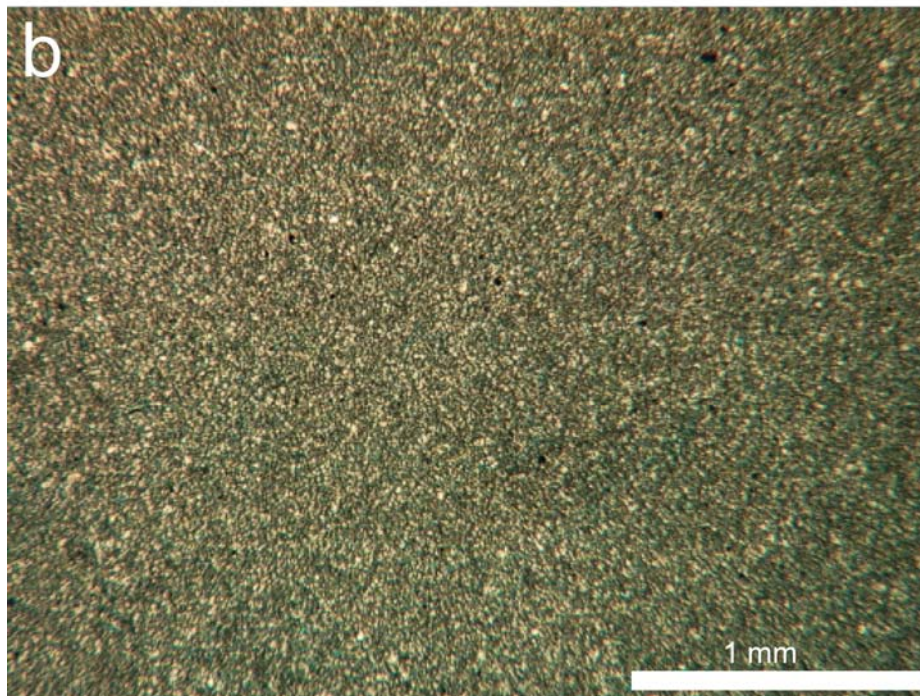
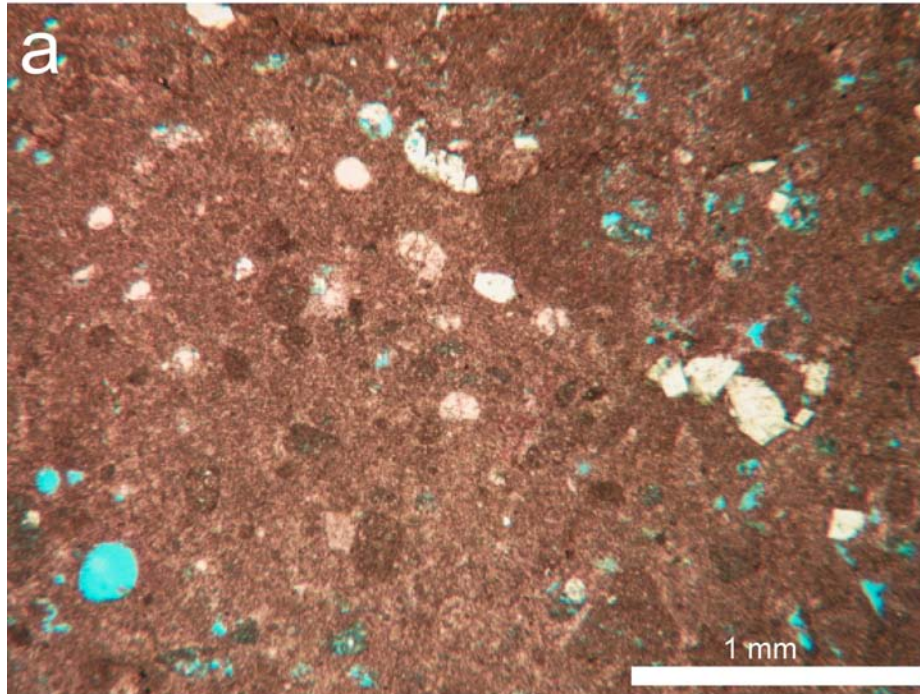
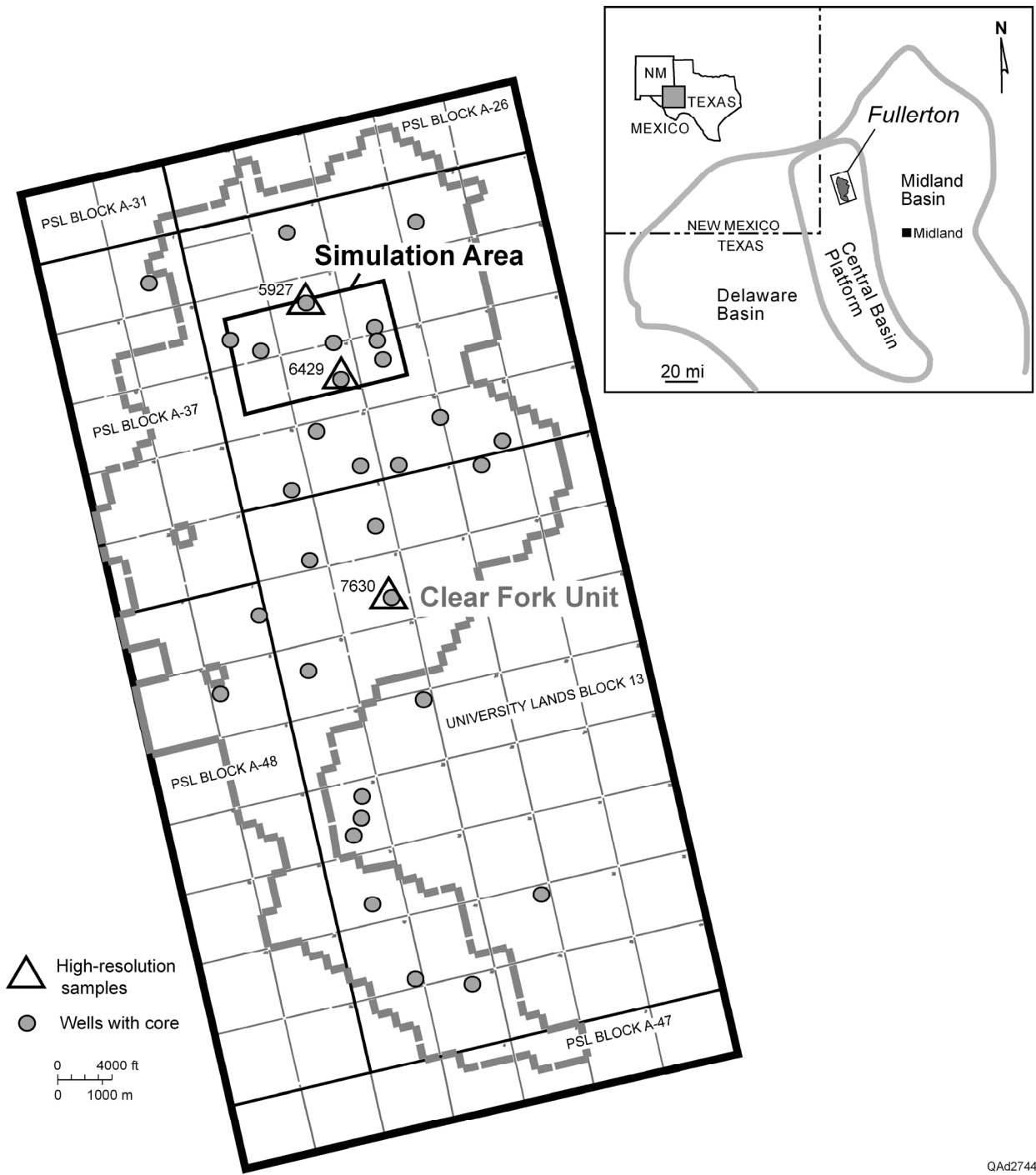
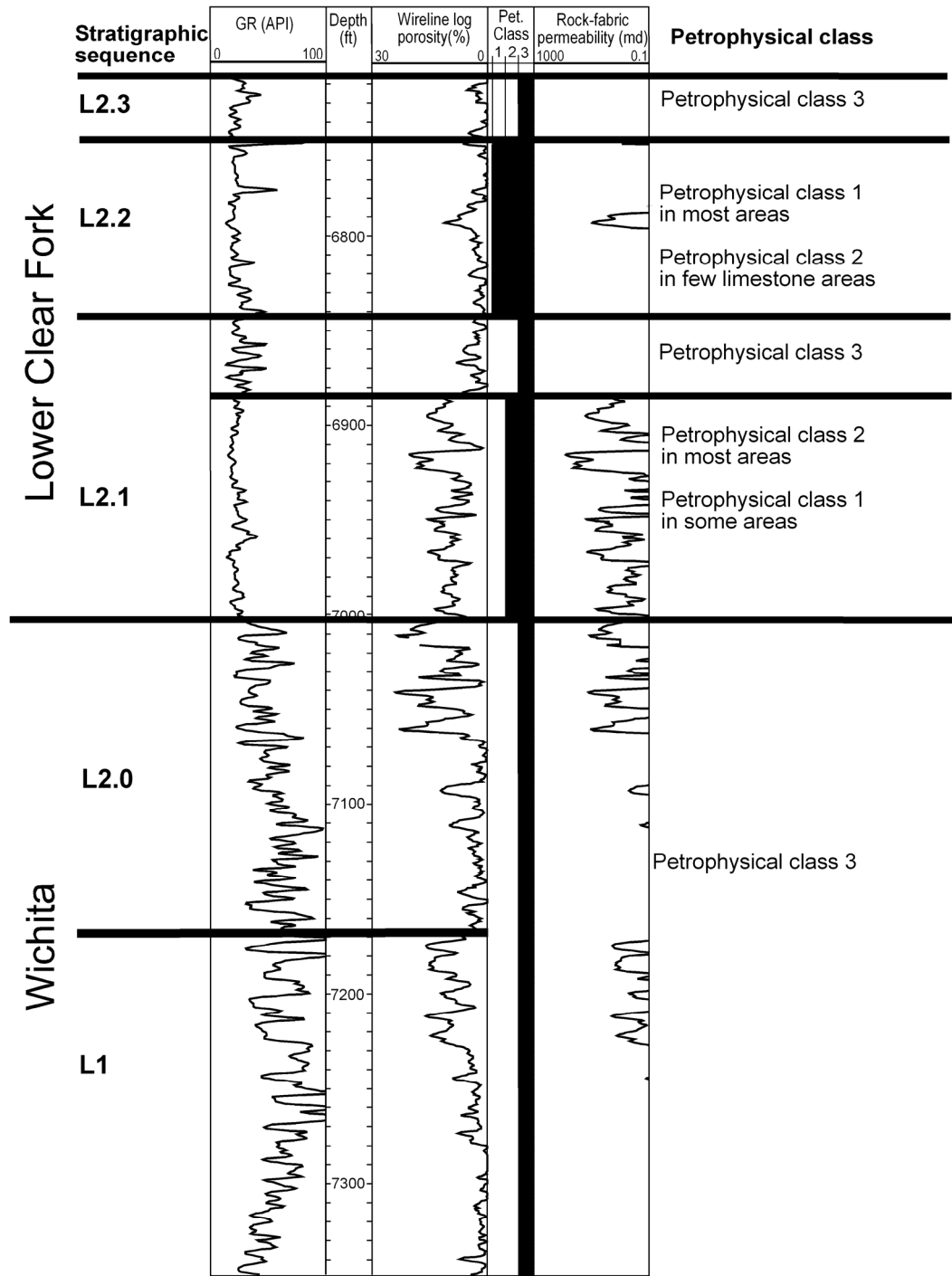


Figure 4. Photomicrographs of class 3 fabrics observed in this study: (a) Wackestone: FCU 5927, 6903', $\phi = 11.2\%$, $k = 0.74$ md. (b) Fine-crystalline dolomudstone with microporosity: FCU 5927, 7009', $\phi = 15.7\%$ porosity, $k = 0.86$ md, dolomite crystal size <10 μm .



QAd2744c

Figure 5. Location and boundaries of Fullerton field, Andrews County, Texas. Boundaries include the Clear Fork Unit and the flow simulation area of this study. Also shown are the location of cored wells and detailed study cores.



QA2754c

Figure 6. Type log showing nomenclature used in this study and general vertical stacking of petrophysical classes. Formations and Leonardian stratigraphy displayed on the left side of logs. Wireline logs are from FCU 5927 and are gamma-ray, wireline-log porosity, and rock-fabric-calculated permeability.

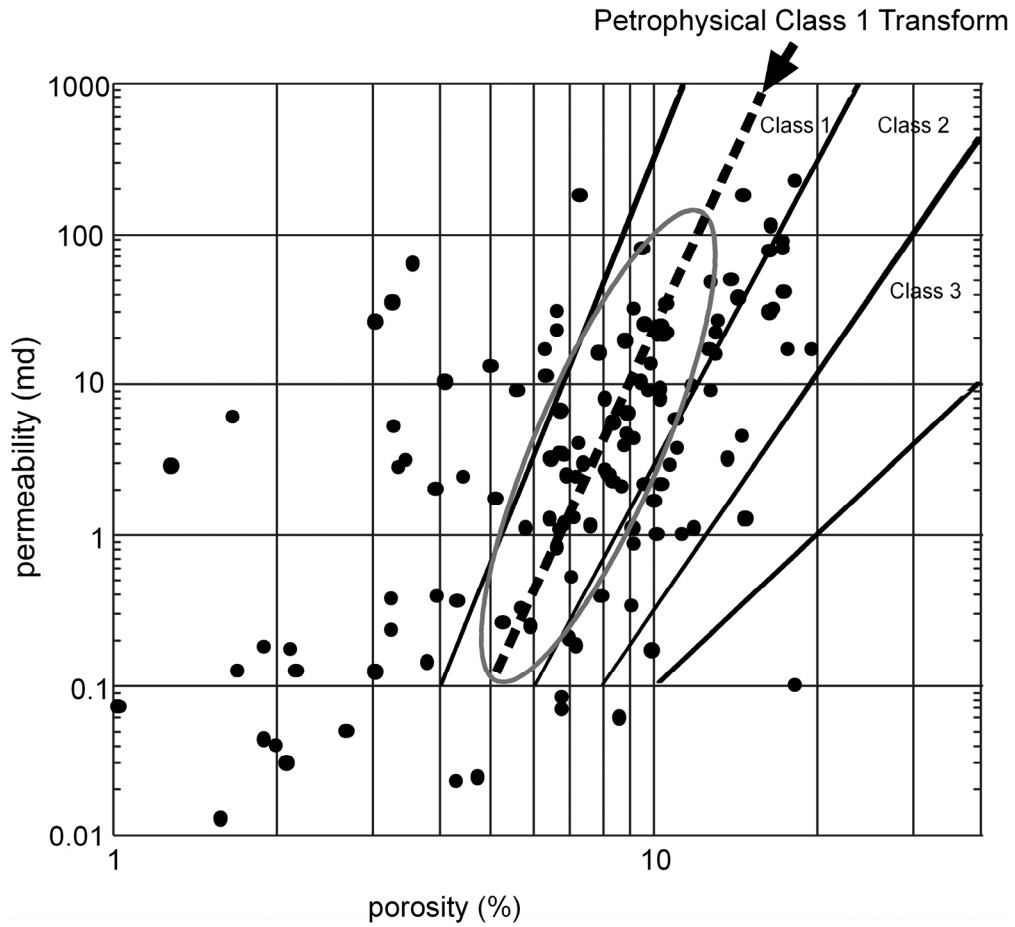


Figure 7. Porosity-permeability plot of old Abo interval core analysis from wells throughout the field with core described in this study.

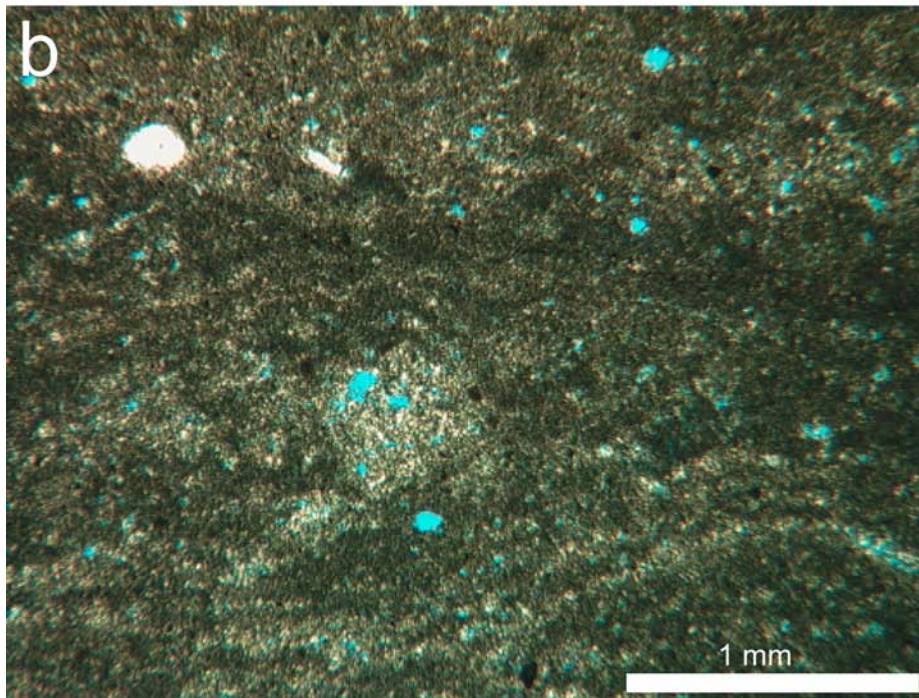
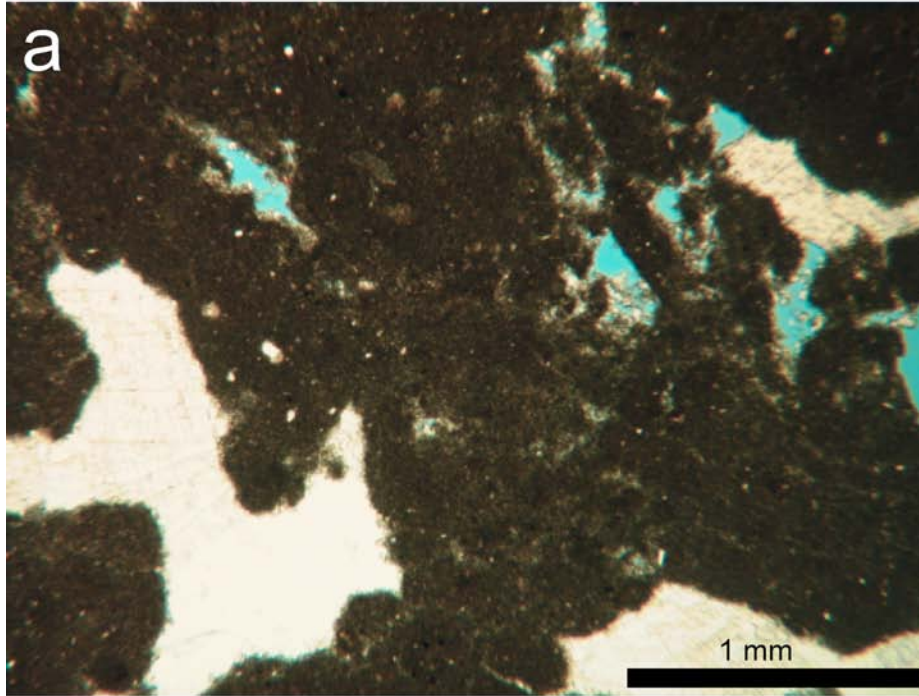


Figure 8. Photomicrographs of tidal-flat, class 3 fabrics observed in this study: (a) Tidal-flat facies with fenestral pores nearly completely filled with anhydrite (white): FCU 5927, 6999', $\phi = 10.2\%$, $k = 0.08$ md. (b) Tidal-flat facies with separate-vug porosity and microporosity: FCU 5927, 7001', $\phi = 17.7\%$, $k = 1.26$ md, dolomite crystal size $<10 \mu\text{m}$.

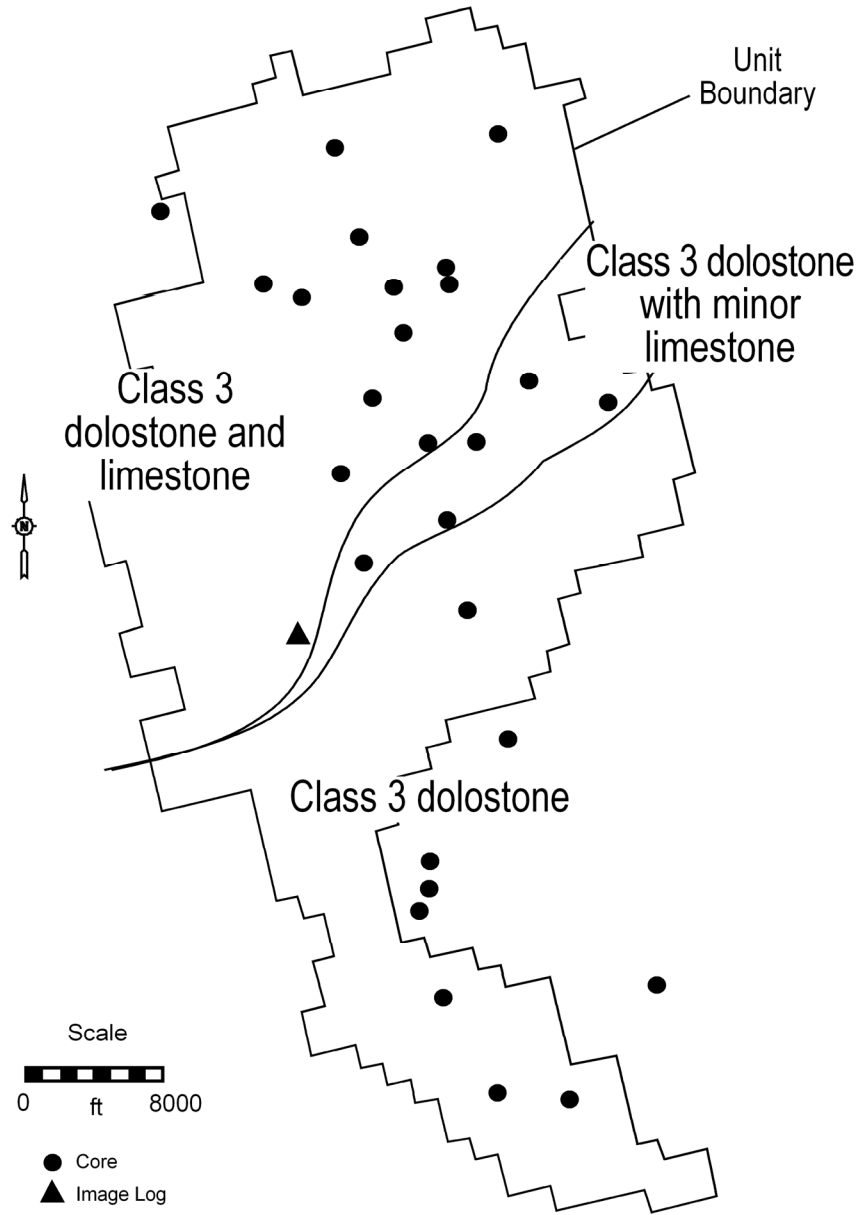


Figure 9. Distribution of limestone, dolostone, and petrophysical classes in the Wichita.

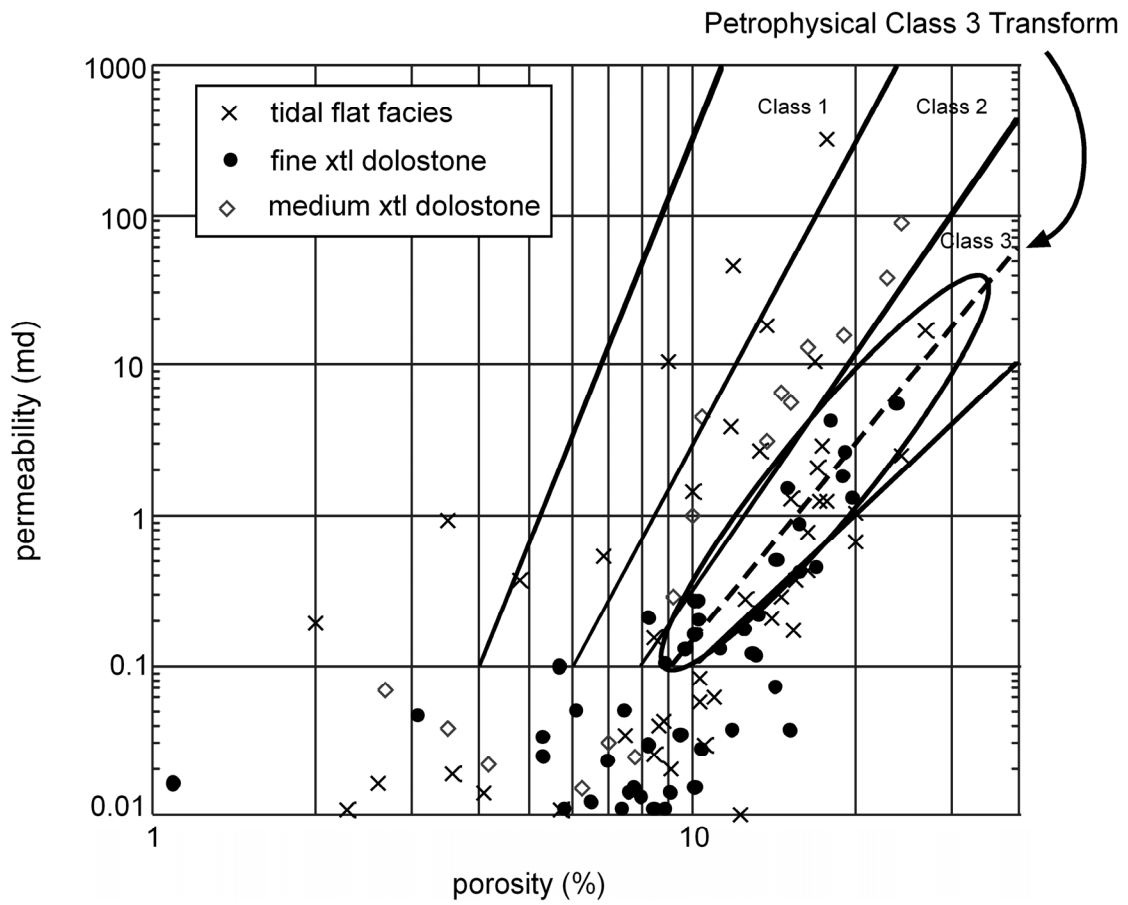


Figure 10. Wichita facies core analysis porosity-permeability plot and petrophysical class 3 transform (heavy dashed line) used to calculate permeability. Ellipse shows that the majority of data plots in the class 3 field.

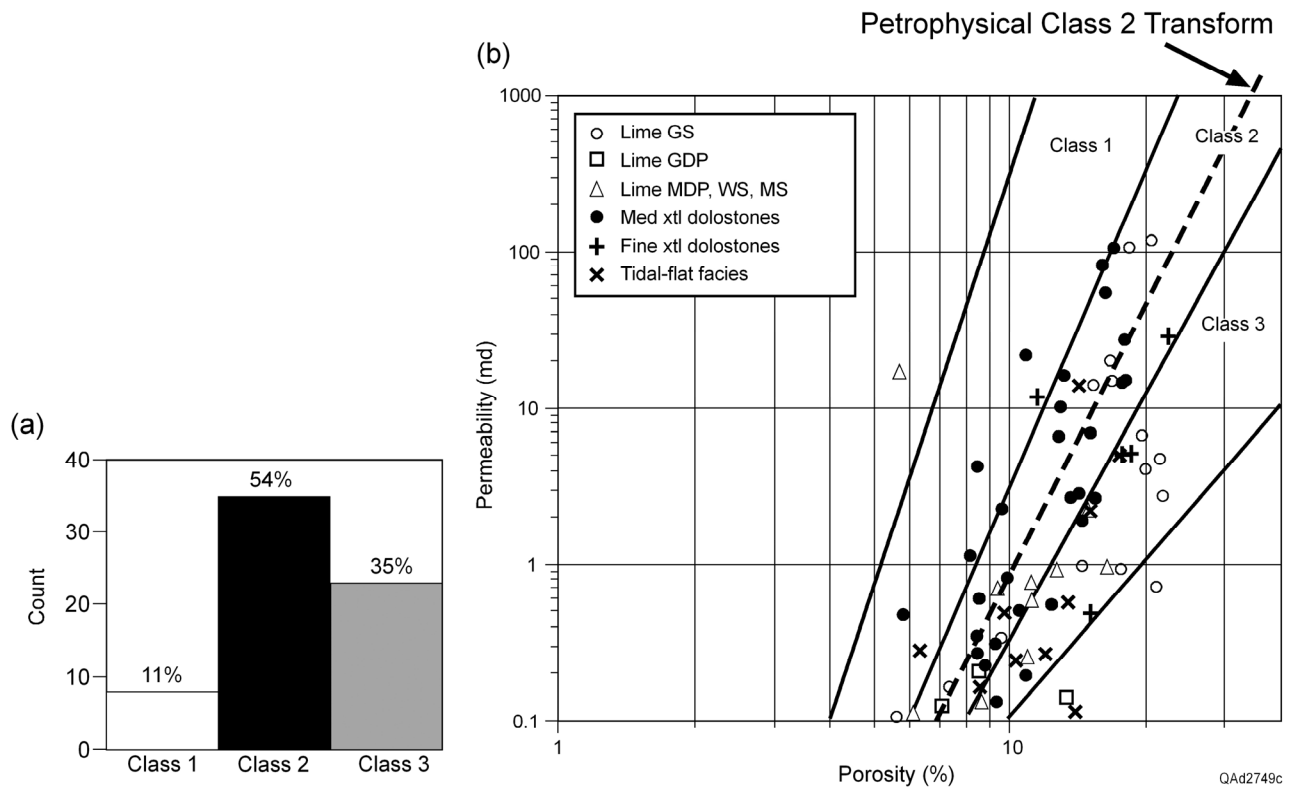


Figure 11. Plot and histogram for Lower Clear Fork L2.1 subtidal unit high-resolution samples from wells FCU 5927 and 6429. (a) Total core porosity vs. permeability plot of these rock fabrics showing that class 2 dolostones and the higher permeability class 1 moldic limestones both plot in the class 2 field. The petrophysical class 2 transform was used for permeability calculations. (b) Histogram showing sample populations from this plot showing that more than 50% of the samples plot in the class 2 field. Those that plot in the class 3 field are moldic grain-dominated limestones and class 3 limestones and dolostones.

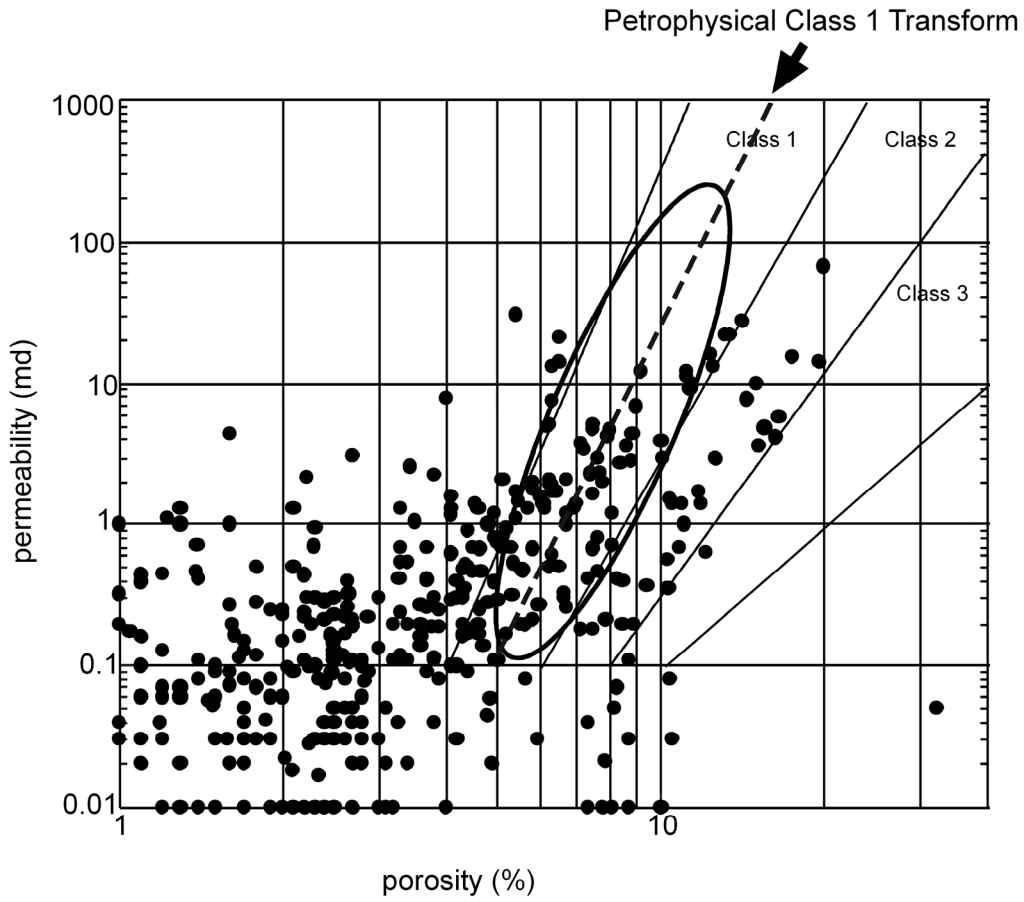


Figure 12. Porosity-permeability plot of core analysis from wells with core displaying dominantly class 1 fabrics in the subtidal portion of high-frequency sequence L2.1.

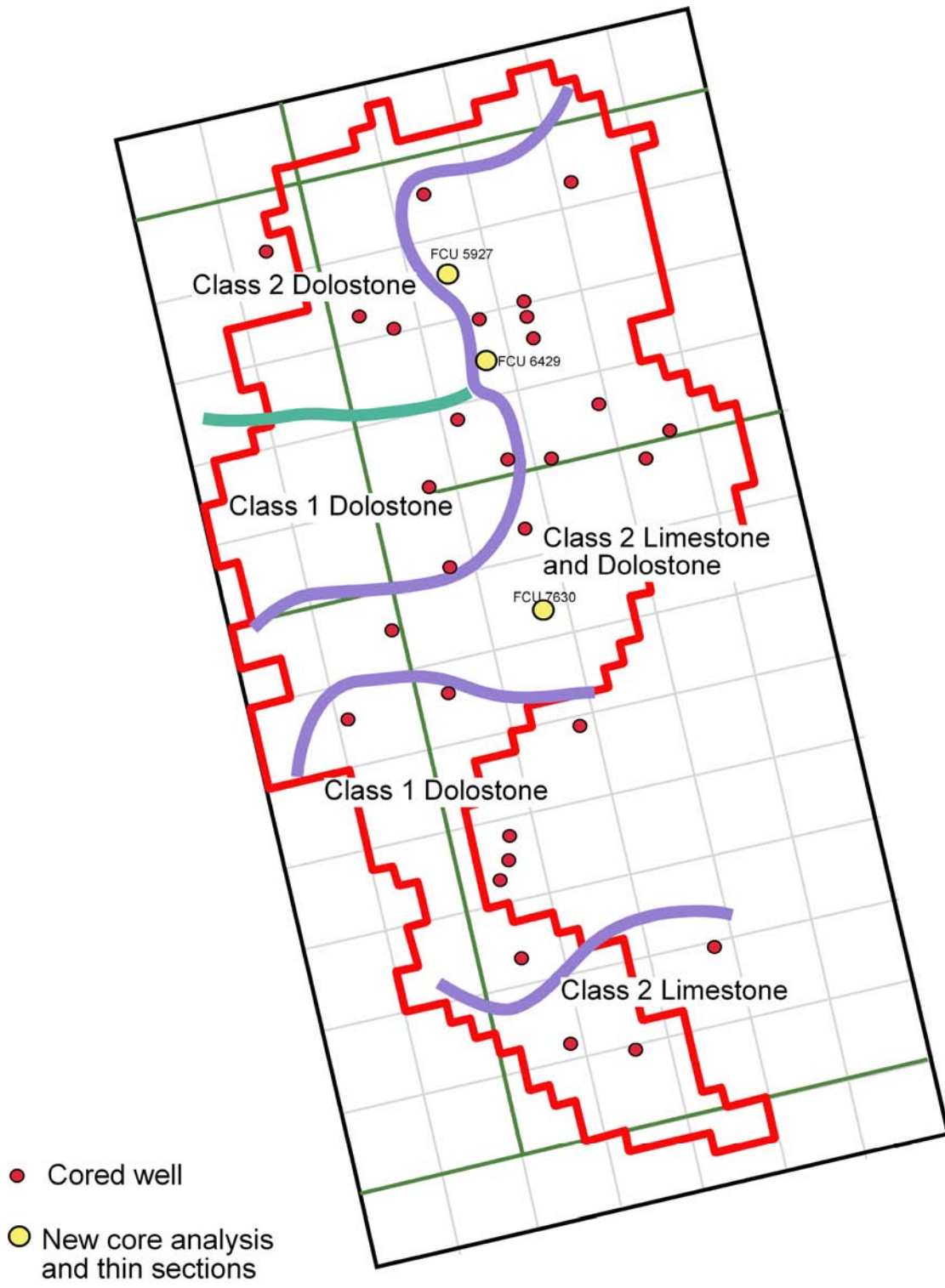


Figure 13. Regions of different petrophysical classes and mineralogy in the subtidal portion of HFS L2.1.

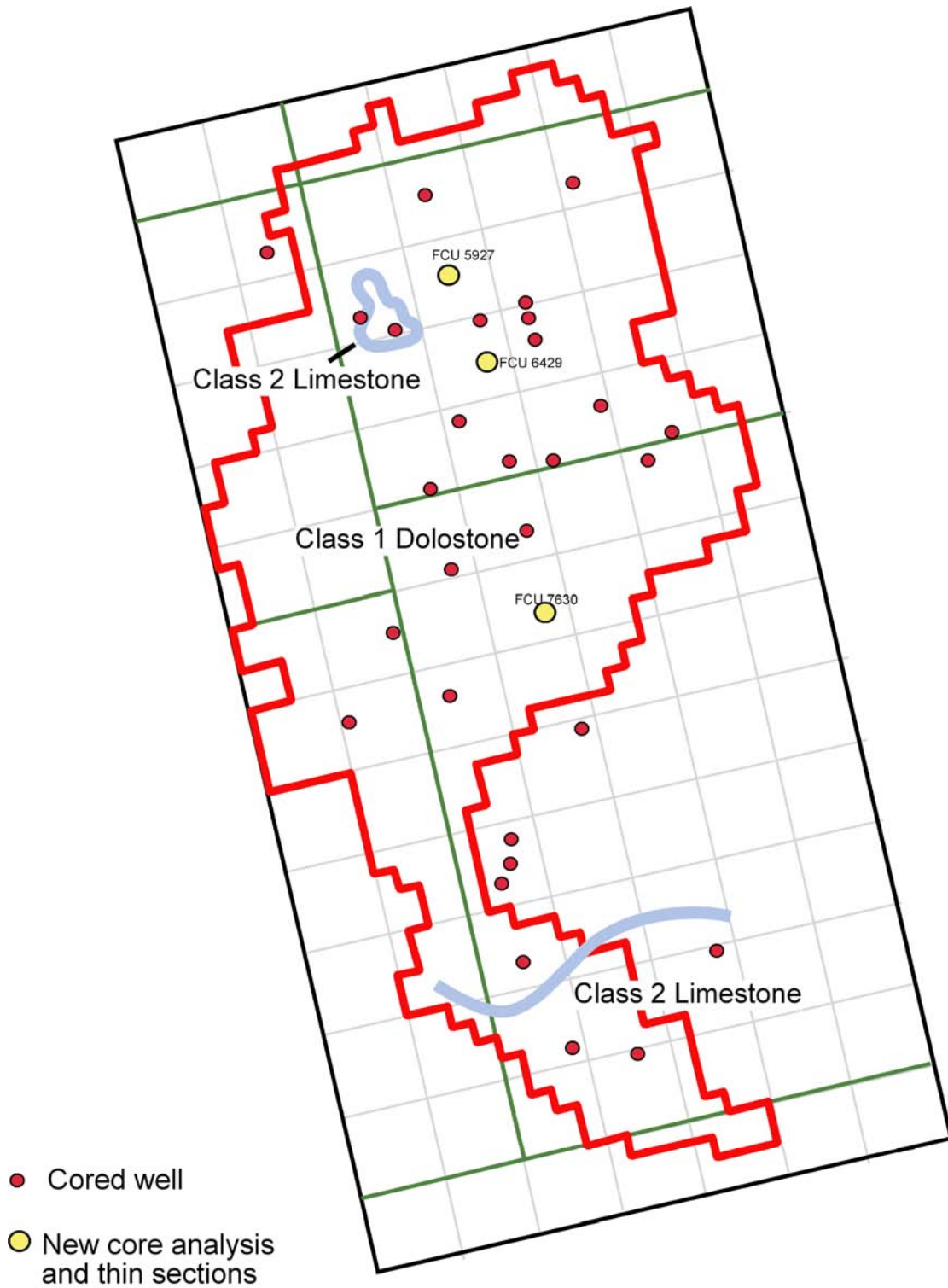
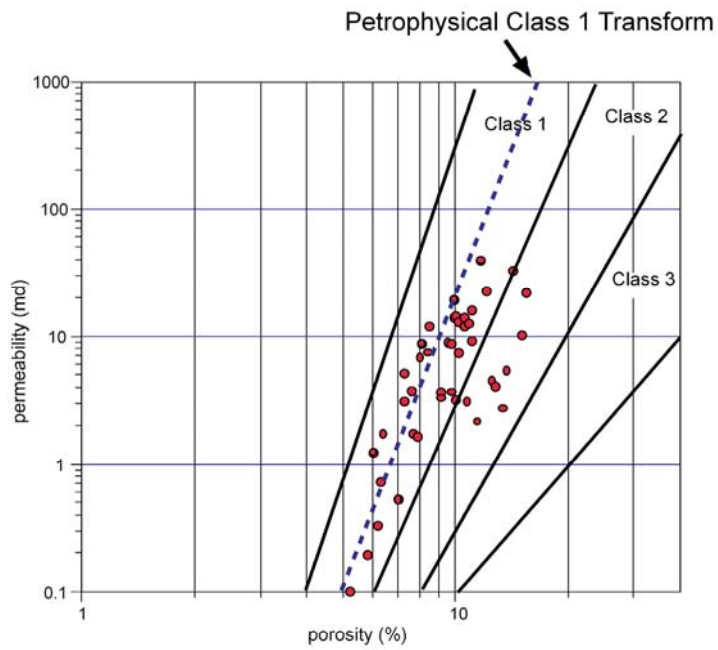


Figure 14. Regions of different petrophysical classes and mineralogy in HFS L2.2.

(a)



(b)

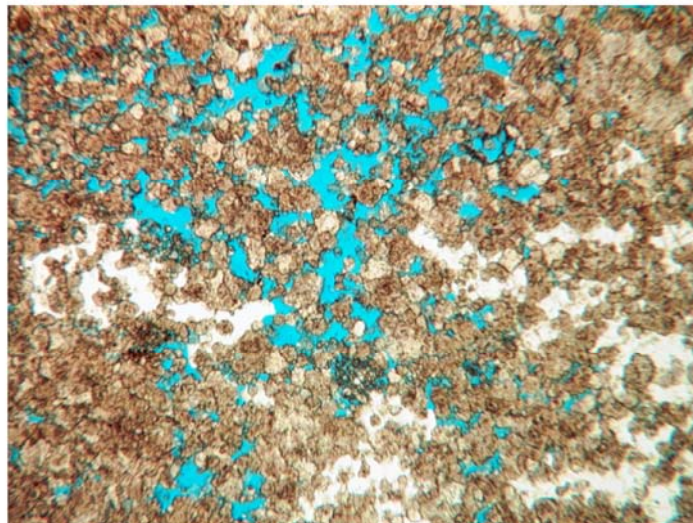


Figure 15. (a) Porosity-permeability plot of Lower Clear Fork L2.2 showing that most samples plot in the class 1 field although they are mostly class 2 medium-crystalline dolostones. (b) Photomicrograph example of poikilotopic anhydrite in a class 2 medium-crystalline dolostone having $\phi = 8.1\%$, $k = 9.02$ md, and 30% anhydrite. The presence of a large volume of anhydrite shifts the sample into the class 1 field.

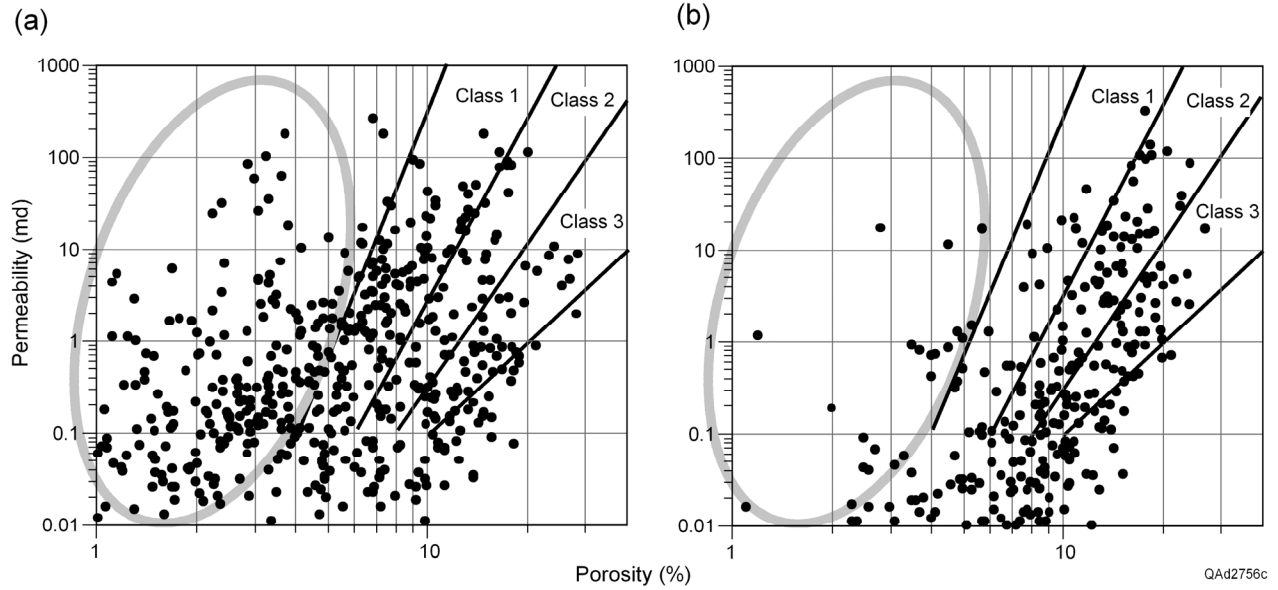


Figure 16. Typical preexisting core analysis data (a) vs. core analysis data resulting from unbiased sampling and careful cleaning of plugs (b). Note the large low-porosity data cloud denoted by the gray ellipse in (a) is not present in (b). Data in (a) are from FCU 6921 (just south of flow simulation area); data in (b) are the new samples of FCU 5927 and 6429 obtained for this study.

APPENDIX I: ROCK-FABRIC INSTRUCTIONS

Classifying Carbonate Pore Space from Thin Sections

Procedure

The following comments outline the general procedure for describing pore space for petrophysical characterization.

1. Identify grains.

Easily done in most limestones and fine crystalline dolostones, more difficult but usually possible in medium crystalline dolostone, and often highly interpretive in large crystalline dolostone.

2. Look between grains and at grain sorting (figs. 1, 2).

Limestones

If intergrain volume contains only pore space (no mud-size material) or pore filling minerals (Calcite, dolomite, sulfate) and is well sorted, the rock is a grainstone: petrophysical class 1

If intergrain volume contains pore space or pore filling minerals, mud-sized sediment, and if the grains are poorly sorted, the rock is a grain-dominated packstone: petrophysical class 2.

If intergrain volume contains only mud-sized sediment and no intergrain porosity, the rock is a mud-dominated fabric: petrophysical class 3. If the fabric is grain supported it is classified as a mud-dominated packstone, if not grain supported and more than about 10 percent grains, wackestone, and if less than 10 percent grains, mudstone.

The boundary between grain-dominated and mud-dominated packstone is gradational, and some judgment is required in selecting the correct classification.

Dolostones

The above comments can be applied to fine crystalline dolostones and medium crystalline grain-dominated fabrics without modification. However, the dolomite crystal size is important in large crystalline dolostones and in medium crystalline mud-dominated fabrics. All large crystalline dolostones are petrophysical class 1 without regard to precursor fabric, and medium crystalline mud-dominated dolostones are class 2, not class 3.

3. Look within grains or crystals (fig. 3).

Pore space located within grains of crystals is referred to as intraparticle pore space, a type of separate-vug porosity.

The size of the intraparticle pore space has a large effect on the petrophysical properties. If the separate-vug porosity is clearly visible (moldic, intrafossil, etc.), the pores will be oil saturated. However, if the intraparticle pore space is microporosity (faintly visible), the pores may be filled with oil and capillary held water.

4. Look for pore space significantly larger (>2X) than the particle (grains or crystals) size (fig. 3).

Pores that are significantly larger than the particle size may be separate vugs or touching vugs, and it is difficult to tell the difference in thin section. If the large vugs are fabric selective they are probably separate vugs. However, if they are connected by microfractures they may form a touching-vug pore system. If the large vugs are not fabric selective, they may form an interconnected pore system.

Documentation

The following comments outline the procedures for completing the attached thin-section description form (fig. 4).

Lithology

Dolomite crystal size is most important because it controls pore size in mud-dominated dolostones.

Types of anhydrite include poikilotopic, pore filling, and nodular. This may have important implications as to pore-size distribution. Gypsum is important in log analysis.

Texture

Enter the rock-fabric name. Grainstone, grain-dominated packstone, mud-dominated, mud-dominated packstone, wackestone, mudstone. Alternatively, show percent mud vs grains graphically. May indicate grain types by name or by symbol.

Petrophysical Fabric

Estimation of interparticle porosity (Ippor). Interparticle porosity is estimated by subtracting vuggy porosity from core analysis porosity, if available. May be estimated from thin sections if core analysis is not available.

Size of particles, grains or crystals, is given in microns. If the fabric is a grain-dominated packstone, the size of the particles and the interparticle fabric (mud of crystals) is given as a fraction.

Separate-vug porosity (Svug) from thin section description. Types in include grain molds, intrafossil, intragrain microporosity, etc.

The presence of touching vugs (Tvug) should be indicated by type (fracture, vug, etc.).

One of three petrophysical classes is normally recorded. However, because there is a range of classes from 0.5 to 4, any value within this range is acceptable. See attachment for explanation of class range to rock fabrics.

Core Analysis

The data entered here is normally from the thin-section sample. If not, it should be so noted.

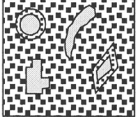
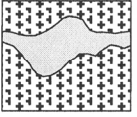
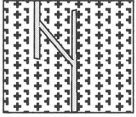
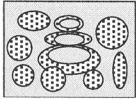
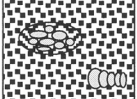
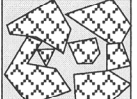
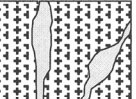
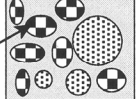
| VUGGY PORE SPACE | | | | |
|---|--|---|--|--|
| SEPARATE-VUG PORES (VUG-TO-MATRIX-TO-VUG CONNECTION) | | | TOUCHING-VUG PORES (VUG-TO-VUG CONNECTION) | |
| PERCENT SEPARATE-VUG POROSITY | GRAIN-DOMINATED FABRIC | MUD-DOMINATED FABRIC | GRAIN- AND MUD-DOMINATED FABRICS | |
| | EXAMPLE TYPES | EXAMPLE TYPES | EXAMPLE TYPES | |
| | Moldic pores  | Moldic pores  | Cavernous  | Fractures  |
| | Intrafossil pores  | Intrafossil pores  | Breccia  | Solution enlarged fractures  |
| | Intragrain microporosity  | Shelter pores  | Fenestral  | Microfractures connecting moldic pores  |

Figure 3

DEVELOPMENT OF THE WIRELINE-LOG DATABASE AND DETERMINATION OF
POROSITY USING WIRELINE LOGS

Jeffrey A. Kane and James W. Jennings, Jr.

Bureau of Economic Geology
Scott W. Tinker, Director
John A. and Katherine G. Jackson School of Geosciences
The University of Texas at Austin
Austin, Texas 78713-8924

| | |
|--|-----|
| ABSTRACT..... | 167 |
| INTRODUCTION | 167 |
| OVERVIEW OF WIRELINE-LOG DATABASE..... | 168 |
| DATABASE ASSEMBLY PROCEDURES..... | 170 |
| QUALITY CONTROL..... | 170 |
| POROSITY-LOG NORMALIZATION..... | 172 |
| MOVING AVERAGE COMPUTATION..... | 175 |
| CORE CALIBRATION..... | 175 |
| CONCLUSIONS..... | 177 |
| REFERENCE..... | 178 |

Figures

| | |
|---|-----|
| 1. Map showing 316 wells with Sidewall neutron logs (SNP) used to calculate porosity for Fullerton Clear Fork field..... | 179 |
| 2. Map showing 437 wells with compensated neutron logs (NPHI) used to calculate porosity for Fullerton Clear Fork field..... | 180 |
| 3. Map showing all 733 wells used in porosity calculation for Fullerton Clear Fork field | 181 |
| 4. An example of the Gaussian weighting function using various scale factors..... | 182 |
| 5. Examples of average SNP porosity areally averaged with different scale factors | 183 |
| 6. Plot of layer averaged core porosity (y-axis) as a function of layer averaged normalized compensated neutron porosity (x-axis) showing the calibration line for dolomites..... | 184 |
| 7. Plot of layer averaged core porosity (y-axis) as a function of layer averaged normalized sidewall neutron porosity (x-axis) showing the calibration line for dolomites | 185 |
| 8. Plot of core porosity (y-axis) as a function of normalized compensated neutron porosity (x-axis) showing the calibration line for limestone | 186 |
| 9. Plot of core porosity (y-axis) as a function of normalized sidewall neutron porosity (x-axis) showing the calibration line for limestone | 187 |

Development of the Wireline-Log Database and Determination of Porosity Using Wireline Logs

Jeffrey A. Kane and James W. Jennings, Jr.

ABSTRACT

This paper reviews development of the wireline-log database used in the Fullerton Clear Fork field reservoir characterization project. A review of the field's logging history is followed by a discussion that covers the assembling and quality checking of the log data and normalization of neutron-porosity logs, along with their subsequent calibration to core porosity. This study deviated slightly from the norm in that assembly of the database and quality control of data were concurrent with interpretation of the data. Because of the nature of the reservoir, traditional log normalization methods were not adequate. A method of normalization is described herein that is a modification of traditional methods, which overcomes these problems.

INTRODUCTION

This report describes procedures used to assemble, quality check, and interpret wireline logs from Fullerton Clear Fork field, which is located in northwestern Andrews County, Texas. The field is dominantly dolomite with an average core porosity of slightly more than 6 percent and a maximum core porosity of about 33 percent. Discovered in the 1940's, the field has logs that span 6 decades of technology.

Assembling and quality checking the log data were complicated as new and redigitized log data were received throughout the study period. The constant influx of data throughout the project required specialized updating processes to keep the database current. With such a large field, data normalization became an issue. Several common normalization methods were tried

but found to be inadequate. The final normalization method employed is different from traditional methods in that the mean and standard deviation of the data at each well are estimated from other wells nearby using a weighted moving average. The logs being normalized are then shifted to these new local values. Finally, the normalized data are calibrated to available core-porosity information. Only porosity was calculated in this study. Because of the long life of the field, modern log data used were not representative of original field-water saturations. Correlations of porosity to water saturation were therefore used to estimate original saturation conditions. These correlations are discussed elsewhere (Jones and Lucia, this report).

OVERVIEW OF WIRELINE-LOG DATABASE

Fullerton Clear Fork field contains log suites that span logging history. Because the field was discovered in the mid-1940's, earliest log suites are the electric logs common to that period. And because the field has had several periods of development throughout its history, log suites range from these original electric logs to modern suites available today. This long time span created numerous difficulties for log quality control and analysis.

Log suites in Fullerton Clear Fork field can be divided into four general groupings. The first grouping is composed of those logs associated with initial field development in the mid- to late 1940's and includes early electric logs. The second grouping differs from the first group by the addition of a gamma-ray neutron log to the early electric log suite and is characteristic of the 1950's. The third grouping consists essentially of a sidewall neutron log and a modern resistivity log, either a dual laterolog or a dual induction. This log suite was common throughout the 1960's and was the first suite to contain a log calibrated in porosity units. During the 1970's the use of the compensated neutron log was introduced, commonly without resistivity logs. Use of this suite has continued through the present.

The oldest electric logs (or e-logs) commonly comprised three tools, a long lateral of varying spacing length; a short normal, again of varying spacing; and a limestone lateral curve. The long laterals had spacings of 13, 18, and 24 ft generally; however, some other lengths occasionally used. The short normal typically had 10-inch spacing; however, 12-, 16-, and 18-inch spacings were also used. Limestone laterals were essentially all 32-inch laterals, along with a few 34-inch laterals. For the most part, these log suites were not used for evaluation in the field, except in some specialized circumstances, in which attempts to evaluate original-oil-saturation profiles were made.

The second group, which includes those wells that contain some form of gamma-ray neutron log, comprises wells that were logged through the 1950's to early 1960's. Unfortunately, these logs vary considerably in tool design, measurement type, and overall quality. Numerous problems properly defining the logging environment and a lack of core information for calibrating these data to porosity precluded using this group of wells in field analysis.

The third group of wells, as stated earlier, comprises sidewall neutron logs (SNP), typically run with a dual laterolog. This is the oldest suite of logs with calibrated porosity curves and core sufficient to provide a calibration to core-measured porosities. This set of data comprises 320 wells, 316 of which have data acceptable for normalization. Locations of these 316 well are displayed in figure 1. The actual process of porosity normalization will be discussed in a subsequent section.

The fourth group is essentially all modern-day logs. The dominant porosity log in this group is the compensated neutron log (CNL). The dataset is made up of 471 wells, 437 of which were of sufficient quality to use for normalization (figure 2).

Twenty wells are common to groups three and four. Because of this overlap the total number of wells used for the quantitative part of the full field study is 733, not 753. Locations of these wells are shown in figure 3. As can be seen from this figure, well coverage is good over most of the field; however, the west edge and some of the south part lacks coverage sufficient for detailed characterization.

DATABASE ASSEMBLY PROCEDURES

The software chosen to build and maintain the log database was Geolog, which is marketed by Paradigm Geophysical Software. This software has two advantages for a project this size. It can handle large numbers of wells in its database, and, more important, it can process large numbers of wells in batches relatively quickly. The ability to run a batch efficiently greatly facilitated keeping the log database current. It also has a robust programming language, allowing user-defined extensions of almost any complexity.

QUALITY CONTROL

The initial database included approximately 1,150 wells. Because of concerns over quality of the original database, the operator, ExxonMobil began a complete redigitization of all logs in the field soon after the reservoir characterization project began. Ultimately 1,206 wells were redigitized. The digitization contractor, IHS Energy, provided all initial quality control (QC) with respect to the actual digitization project. Data were then sent to ExxonMobil, and ExxonMobil forwarded the data to the Bureau of Economic Geology (BEG) for inclusion in the characterization project. During the initial phase of the project, detailed quality control was performed on approximately 275 wells after these data were received from ExxonMobil. The wells included examples from all log-suite types. This level of quality control allowed team

members to provide feedback to the digitizing company and ExxonMobil to resolve some issues early on that may have caused significant problems later. During the remainder of the project, all well data received were reviewed prior to loading for completeness of digitization, and detailed QC was performed randomly.

For quality control of digitized log data to be properly maintained, copies of original paper logs are critical. Visual verification of the quality of digitization, verification of proper log-header transcription, and review of paper logs for well-bore-environment specifics affecting proper log analysis can be done only with access to copies of original paper logs. A well-bore environment issue can serve as an example. After review of numerous gamma-ray neutron logs, it was noted that at least half were run during well-deepening events, meaning that logs had both open-hole and cased-hole components. These logs needed to be broken into open-hole and cased-hole sections and normalized independently. This situation would not have been recognized, however, without copies of the paper logs available for review. Further investigation showed that a lack of core data associated with these wells and a broad spectrum of gamma-ray neutron tool types that were run in this group made normalization of these data unfeasible for this project.

Well logs for a given well in an update could have several files associated with it, and each of these files would contain log data at different levels of correction. Not all log types were included in the correction process nor in all levels of the correction process, so the loading of all files was necessary to capture all the data. Because of differences in data quality by file, the data had to be loaded in a specific order to ensure that the most recent, most completely edited curve was primary. For a few wells this process could be done interactively, but the large number of wells in this project made interactive loading unrealistic, requiring that an automated or semiautomated process be developed instead. Each file was ordered on the basis of level of

correction and date received. Once this ordering was done, all data were copied into a file from oldest, unedited data, to oldest edited data, to most recent unedited data, and finally to most recent edited data. At the conclusion of this process, a single file existed that contained all log data for a given well in a single table. The process culminated in 17,200 logs in the final update. Each time new data were acquired, the entire database was completely rebuilt to guarantee a complete dataset.

Each time the database was rebuilt, available log curves were reviewed. The digitization provider was often inconsistent in the naming conventions used, so curve mnemonics referring to the same data type varied throughout the digitization process. A total of 525 different log mnemonics were found in this review at the end of the project. Rectifying the differences was beyond the scope of this project and was performed only on an as-needed basis.

POROSITY-LOG NORMALIZATION

The first step in determining basic petrophysical parameters in this study was normalization of usable data. For this study, because a primary goal was accurate assessment of porosity, the normalization process focused exclusively on porosity logs, specifically compensated neutron logs (CNL) and sidewall neutron logs (SNP). Two different normalization methods were employed. A traditional normalization method was used in the early stages in a small area of the field selected for detailed study, modeling, and simulation. In later, full-field studies, this method of normalization was not adequate without modification.

Traditional normalization methods fall into two general categories. The first category of normalization methods requires stratigraphic intervals of constant properties over the area to be considered. For instance, in normalizing a porosity log, a low-porosity interval, such as an anhydrite, and a high porosity interval, such as shale, would be determined in each well, and

values of each log (CNL, SNP) for these intervals would be averaged for the area of interest. Each well log would then be shifted so that its average value across those intervals would be the same as the global average for that log in the respective stratigraphic interval. Fullerton field has no such intervals that can be used, however, making this approach inappropriate.

The second category of normalization methods commonly employed requires assumption that a distribution of some statistical parameter(s), i.e., minimum and maximum values, or the average and standard deviation of the porosity, is constant over some thick interval. The assumption of constant average and standard deviation of porosity was used in the initial study area. The approach was reasonable given the small (approximately two square mile) size of the initial study area. When this approach was applied to the full-field normalization of the neutron-porosity logs, it was found that these parameters are not constant across the entire field (approximately 45 square miles), so a variation of this method was employed.

The method in cases with areally varying statistics follows the work of Jennings and others (2002). First CNL or SNP porosity values were vertically averaged separately over genetic intervals. In Fullerton, stratigraphic cycles were the genetic intervals used. Using a number of intervals, a vertical average CNL or SNP porosity value is determined for all cycles under consideration by well. The vertical standard deviations of these cycle averages were also computed by well. In the Fullerton study, 19 such cycles were used, including cycles for the Lower Clear Fork to upper Wichita interval.

This computation by genetic intervals minimizes random errors such as measurement noise while preserving geologically relevant information. This phase of the process does not correct for systematic errors such as those generated by incorrect calibration of the logging tool. Such systematic errors are uniform over a single log at a single well location. As such, the error

will be reflected in the mean and standard deviation computed for a given well. Combining the means and standard deviations over a number of wells as would be done in computing a moving average, suppresses the systematic error associated with a single well.

Areally averaging the vertically averaged porosities and standard deviations of the averaged porosities over a subset area will provide a way of estimating a slowly laterally varying average and standard deviation of the CNL or SNP porosity. This use of a moving average can be thought of as a low-pass filter removing high-frequency local variability to enhance larger scale trends. The values of mean and standard deviation predicted via this method are now taken to be correct values at the well. To correct the neutron-porosity log curve to this new value for mean and standard deviation, each data value (CNL or SNP) is adjusted with this equation

$$\Phi_{corr} = (\Phi_{orig} - \mu_{orig}) \frac{\sigma_{pred}}{\sigma_{orig}} + \mu_{pred}$$

where Φ_{corr} is the corrected or normalized CNL or SNP data value, σ_{pred} is the new or predicted standard deviation, σ_{orig} is the standard deviation calculated from the original log data, Φ_{orig} is the original CNL or SNP data value, μ_{pred} is the new or predicted mean, and μ_{orig} is the mean calculated from the original data.

CNL and SNP logs were handled separately because their lithology response in dolomite is substantially different. Typically, CNL and SNP logs are run according to the assumption that the matrix being logged is limestone. If the actual matrix is not limestone then the calculated porosity will be in error. For SNP logs, this porosity difference is about 2 porosity units too high in dolomite. CNL variations in dolomite are not constant; however, in the porosity range encountered in Fullerton reservoir rock the difference is about 6 porosity units too high for dolomite. Because of this difference in dolomite response, the two different tools were handled separately and combined into a single dataset after calibration to available core porosity.

MOVING-AVERAGE COMPUTATION

Many different weighting functions can be used to compute a moving average. For this study, a Gaussian weighting function was used:

$$w_i = e^{-\left(\left(\frac{x-x_i}{s}\right)^2 + \left(\frac{y-y_i}{s}\right)^2\right)}$$

where w_i is the weight computed at the location x_i, y_i , x and y are the x and y locations of the well and s is the scale factor.

This function decays toward zero as the distance increases from the point where estimation is occurring but never goes to zero. In other words, all data are always used, although the weight of each point decreases with increasing distance from the estimation point (figure 4). The fundamental parameter controlling the Gaussian weighting function is the scale factor, which influences the decay rate of the weighting value computed by the Gaussian function with respect to distance. An optimal scale factor would suppress local variation without unduly suppressing the larger scale variations. In Fullerton field this parameter is chosen by inspection. A number of maps were made with varying scale factors (figure 5). After inspection a scale factor of 3,000 ft was used because visually it suppressed local variations in porosity without over-smoothing.

CORE CALIBRATION

Once data are normalized, they must be corrected to represent porosity, commonly done by calibration to available whole-core data. All available core data were used in this calibration process. For each curve used, two different calibration lines were derived, one for dolomite and one for limestone. Plots showing calibration lines for both compensated neutron logs and sidewall neutron logs are provided in figures 6 through 9.

The method used to determine calibration lines differed slightly between limestone and dolomite. Because dolomite is most prevalent throughout the reservoir interval, the approach for generating dolomite calibration lines was consistent with the averaging scheme used to determine normalization estimators. That is, core data were averaged over the same stratigraphic cycles as those for normalized neutron-porosity logs. The goal was to eliminate, as much as possible, the difference in vertical resolution between the two measurements. In addition, vertical averaging reduces random noise associated with the measurements.

The limestone calibration had to be handled somewhat differently. Because limestones are not as pervasive as the dolomites in this reservoir, the aforementioned method would not work. The averaging used to generate dolomite porosity calibrations suppresses the limestone response of the logs because of the relative percentage of limestone being much less than that of dolomite in this reservoir. Limestone calibration was therefore computed by comparing neutron porosity data with core data in the limestone intervals. Which data points corresponded to limestone was determined by selective filtering of the photoelectric factor (PEF) curve. Because calcite has a PEF value of five and dolomite has a PEF value of three, if a limit of accepting only a PEF value greater than four is set, limestones would be the prevalent lithology used to create the calibration line in this case. Porosity calibration lines for the four different groups are

Compensated neutron – dolomite

$$\Phi_{\text{core}} = -0.0231 + 0.82296 \times \Phi_{\text{NPHInorm}}$$

Compensated neutron – limestone

$$\Phi_{\text{core}} = -0.0358 + 1.1709 \times \Phi_{\text{NPHInorm}}$$

Sidewall neutron – dolomite

$$\Phi_{\text{core}} = -0.0178 + 1.0781 \times \Phi_{\text{SNPnorm}}$$

Sidewall neutron – limestone

$$\Phi_{\text{core}} = -0.0238 + 1.248 \times \Phi_{\text{SNPnorm}}$$

where Φ_{core} is the core-calibrated log porosity, Φ_{NPHInorm} is the normalized compensated neutron porosity, and Φ_{SNPnorm} is the normalized sidewall neutron porosity.

CONCLUSIONS

Porosity evaluation in large fields requires detailed attention to data quality control, but the level of quality control needed in a digital database can be acquired only through access to the original paper logs used to generate the digital data. Transcription and digitization errors can occur and, in some cases, well-bore information present on the paper logs is never captured.

Owing to the timing of log digitization, methods had to be developed for updating the database as new and re-edited log data was received to guarantee the logs being used were the most current, most edited versions. In the case of Fullerton Clear Fork, the sheer volume of data necessitated automating many of the processes.

Proper normalization is necessary to allow correct calibration to core porosity fieldwide. Traditional porosity log normalization methods failed to provide acceptable results. A novel normalization method was therefore applied that overcomes shortcomings of the other methods tried. This method, which involves both vertical averaging of log data by genetic interval and areal moving averages to extract trends in the local mean and standard deviation of target log

data is general in nature and should have wide applicability. The dual averaging, vertically and areally, has the effect of minimizing the effects of both random errors such as measurement noise and systematic errors associated with logging tool miscalibration. The normalization method outlined has advantages over other normalization methods in that any reasonably thick interval can be used to normalize the log, even the reservoir interval itself.

REFERENCE

Jennings, J. W., Jr., Lucia, F. J., and Ruppel, S. C., 2002, 3D modeling of stratigraphically controlled petrophysical variability in South Wason Clear Fork Reservoir: Society of Petroleum Engineers SPE Paper No. 77592, 15 p.

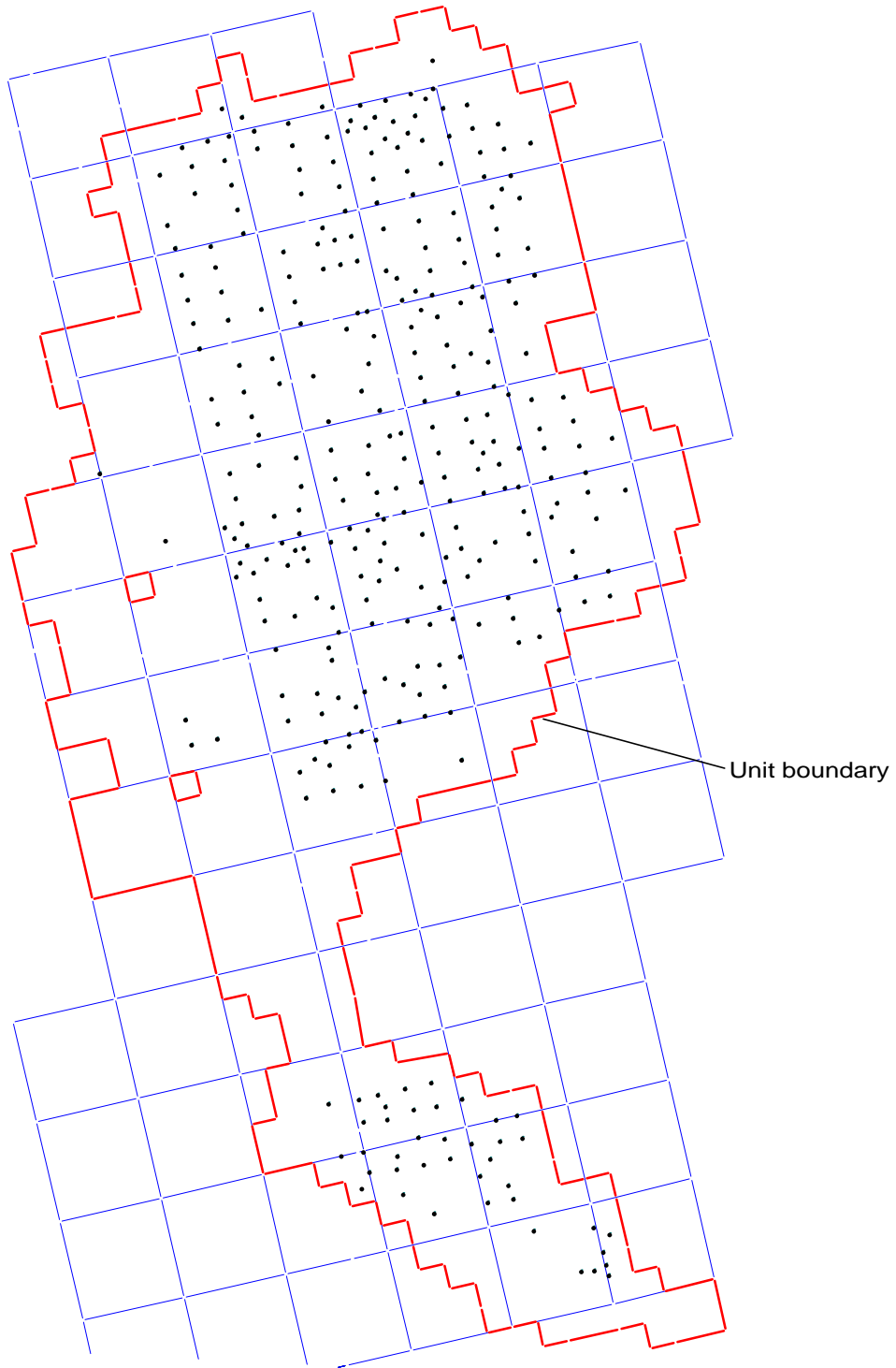


Figure 1. Map showing 316 wells with Sidewall neutron logs (SNP) used to calculate porosity for Fullerton Clear Fork field.

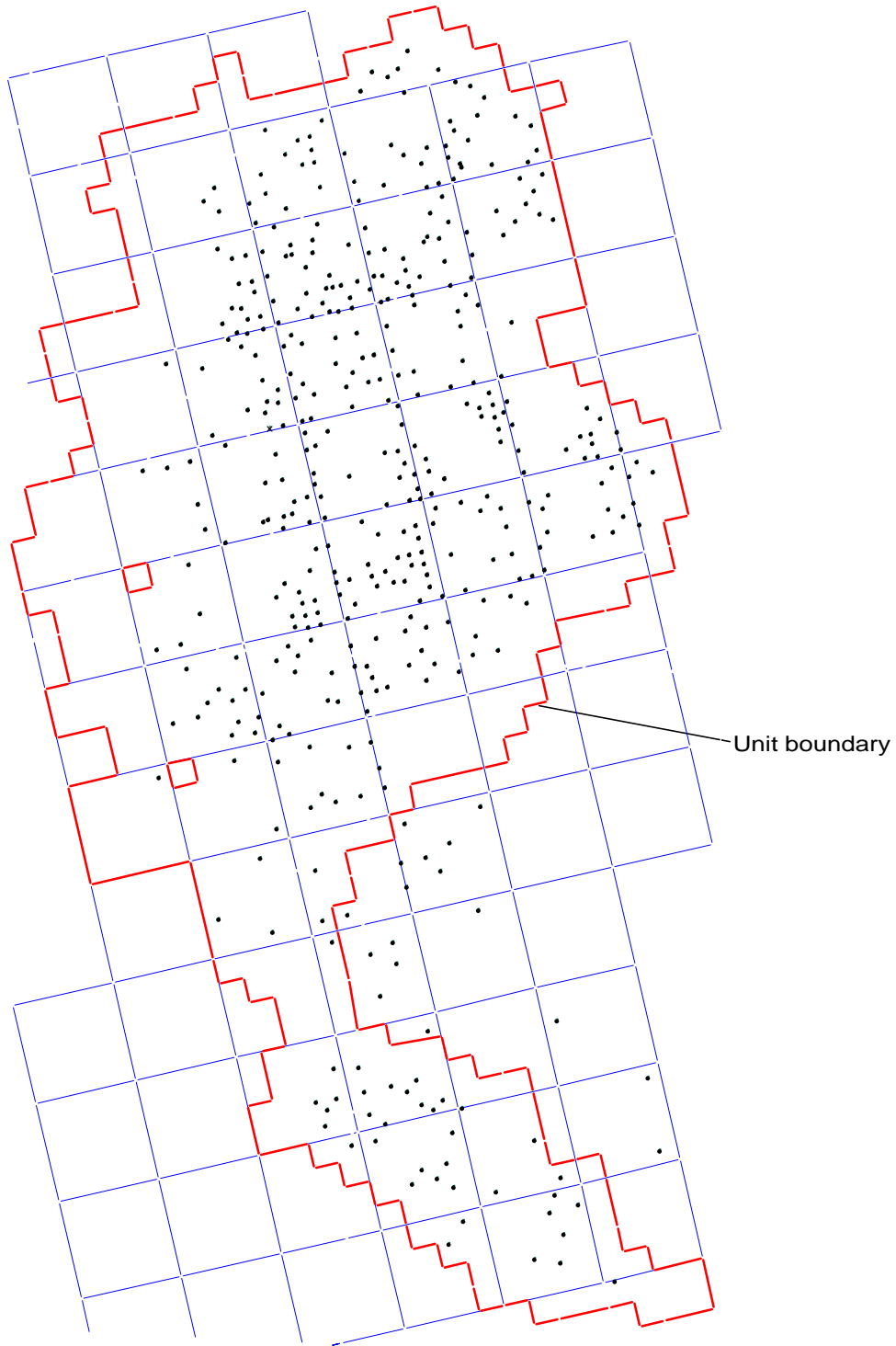


Figure 2. Map showing 437 wells with compensated neutron logs (NPHI) used to calculate porosity for Fullerton Clear Fork field.

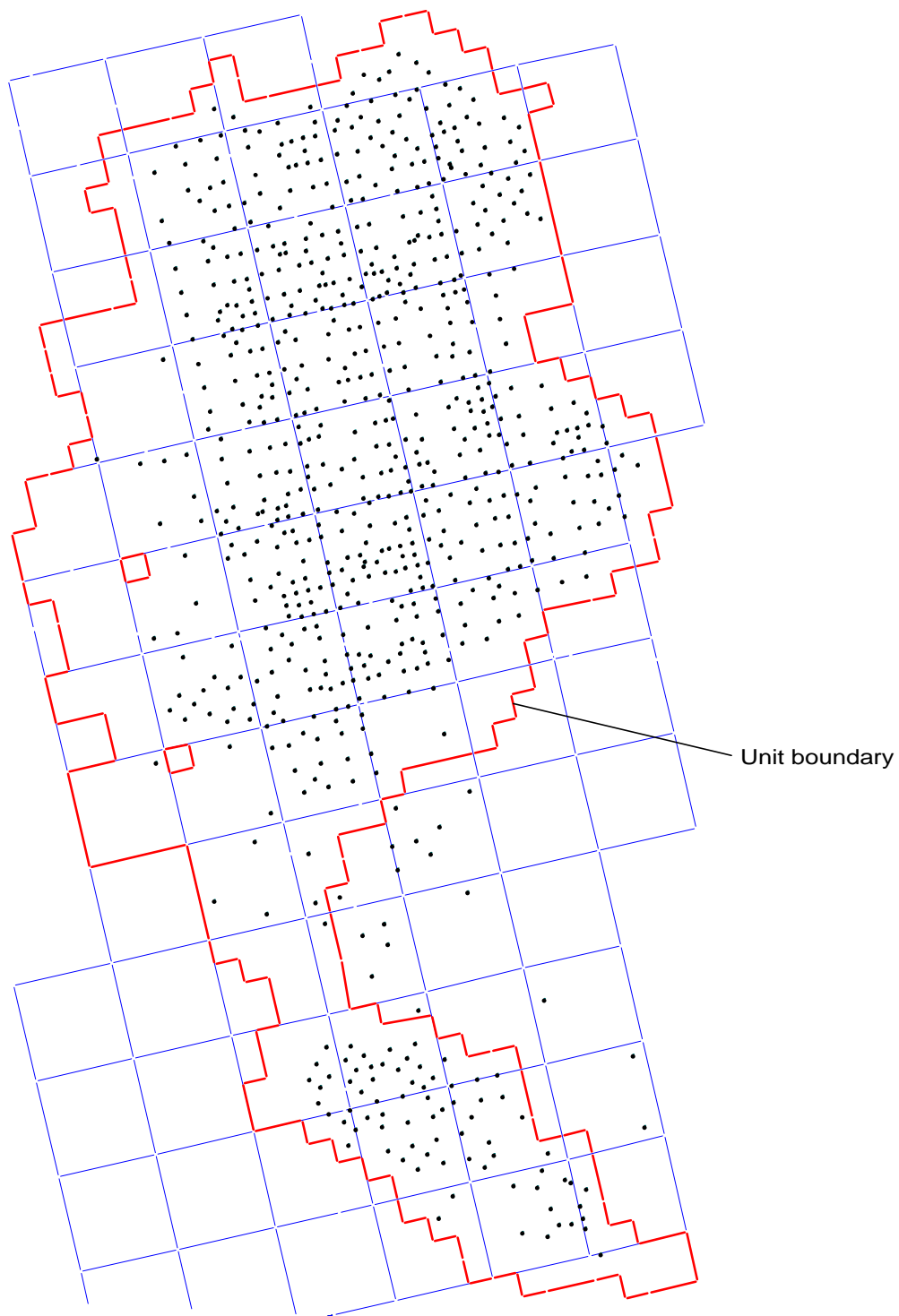


Figure 3. Map showing all 733 wells used in porosity calculation for Fullerton Clear Fork field.

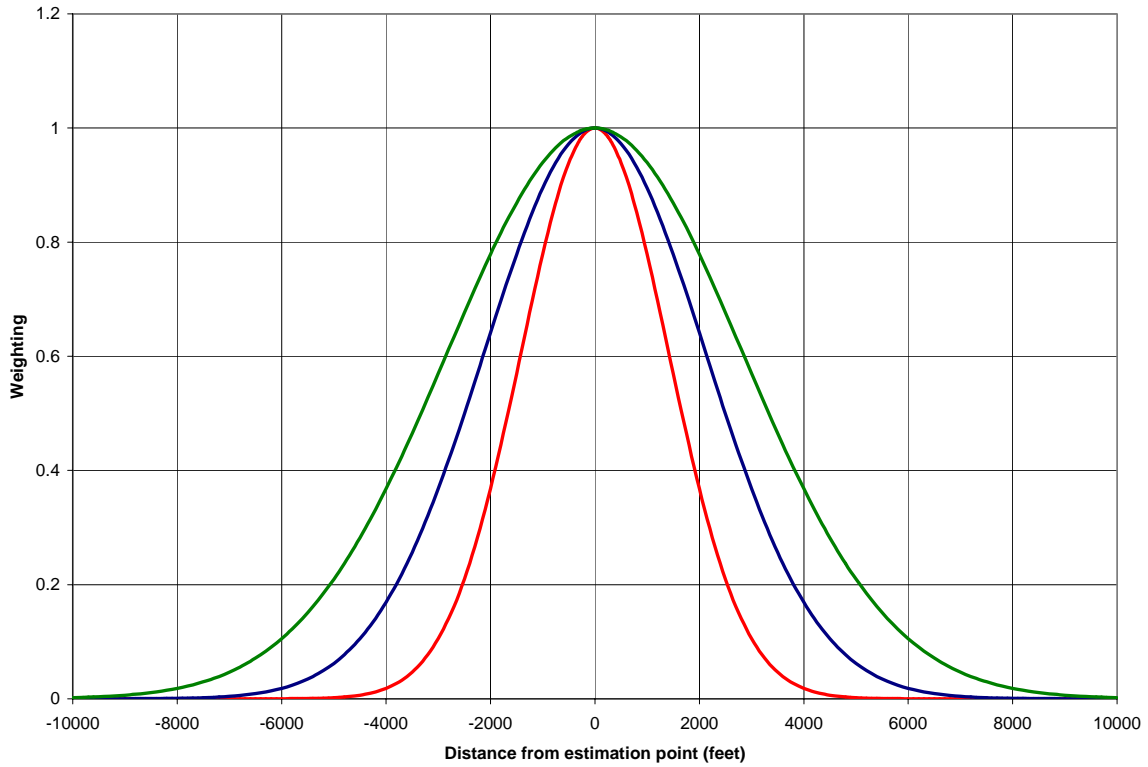


Figure 4. An example of the Gaussian weighting function using various scale factors. The red curve represents a scale factor of 2000 ft, blue 3000 ft and green 4000 ft. A scale factor of 3000 ft was used for porosity log normalization in the Fullerton field study.

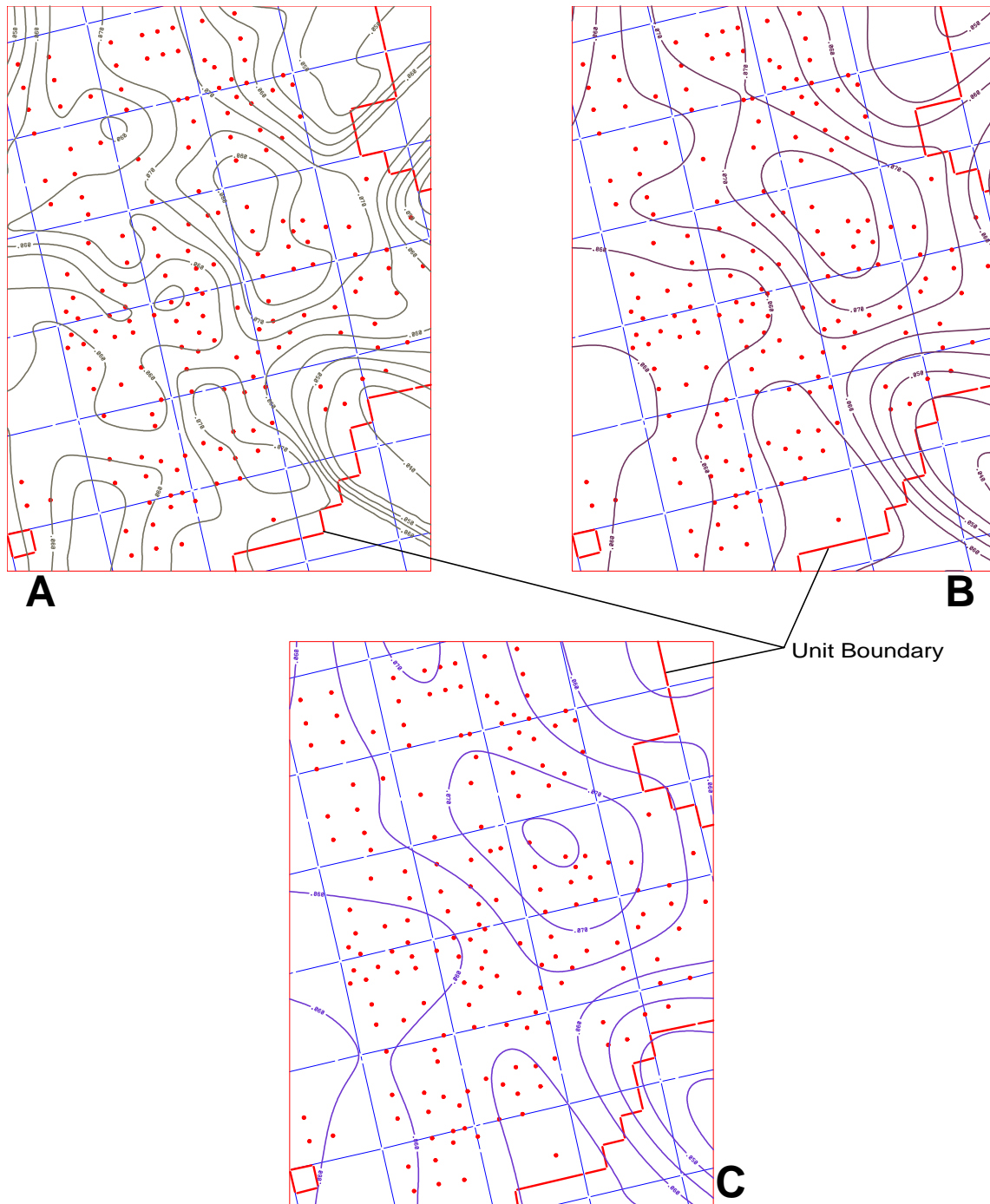


Figure 5. Examples of average SNP porosity areally averaged with different scale factors. Map A was generated using a 2000 foot scale factor, map B with a 3000 foot scale factor and map C, a 4000 foot scale factor. Red circles represent well control. Map A still contains “bull’s-eyes”, contours controlled by a single data point. Map C shows a lack of local variability, completely dominated by larger scale trends. Map B represents a reasonable compromise between local variability and larger scale trends. A scale factor of 3000 ft (map B) was used for porosity normalization in Fullerton Clear Fork field.

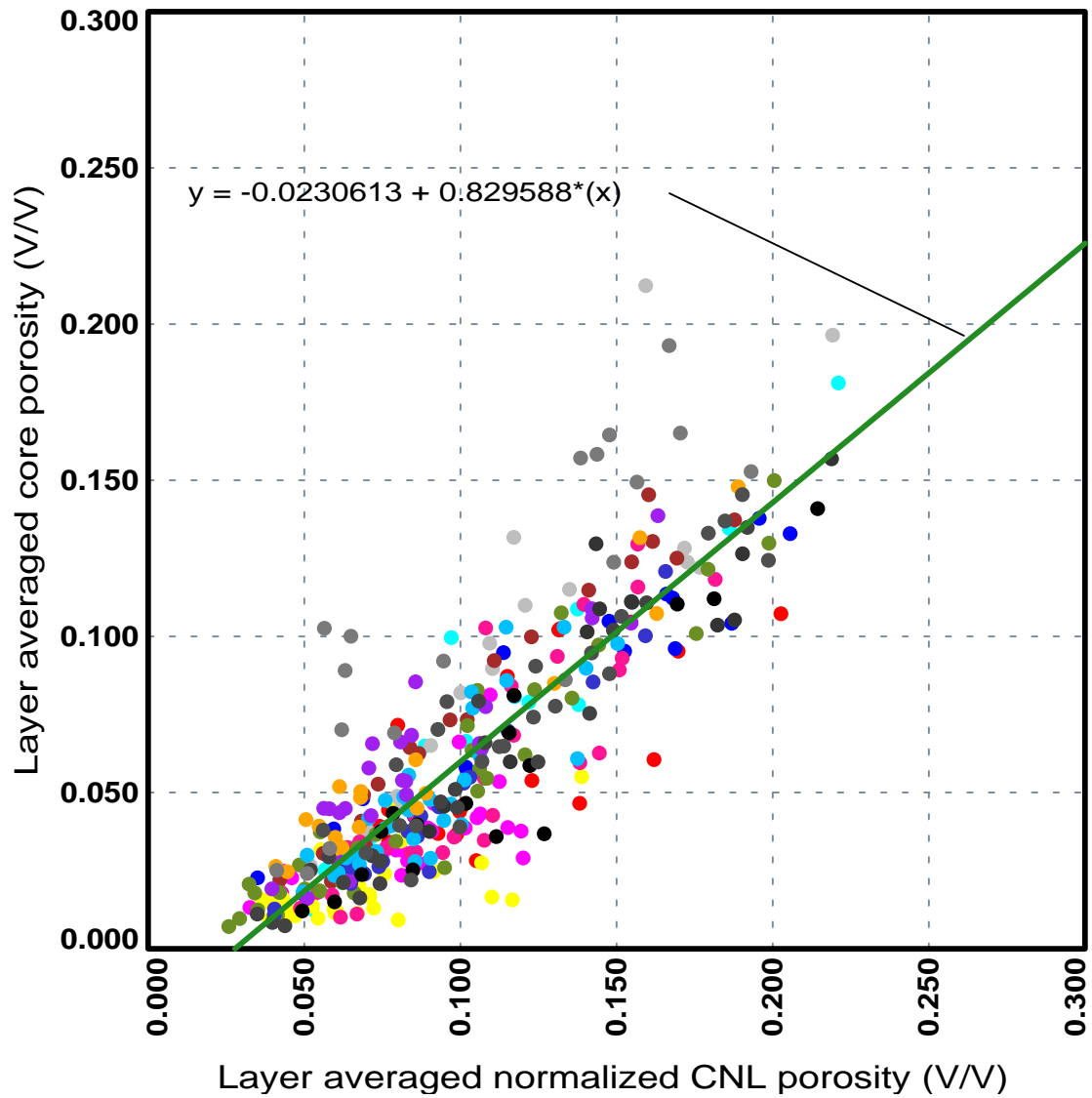


Figure 6. Plot of layer averaged core porosity (y-axis) as a function of layer averaged normalized compensated neutron porosity (x-axis) showing the calibration line for dolomites. Each point represents data that have been vertically averaged over a single cycle. Like colors represent data from the same well. Calibration is based on 21 wells.

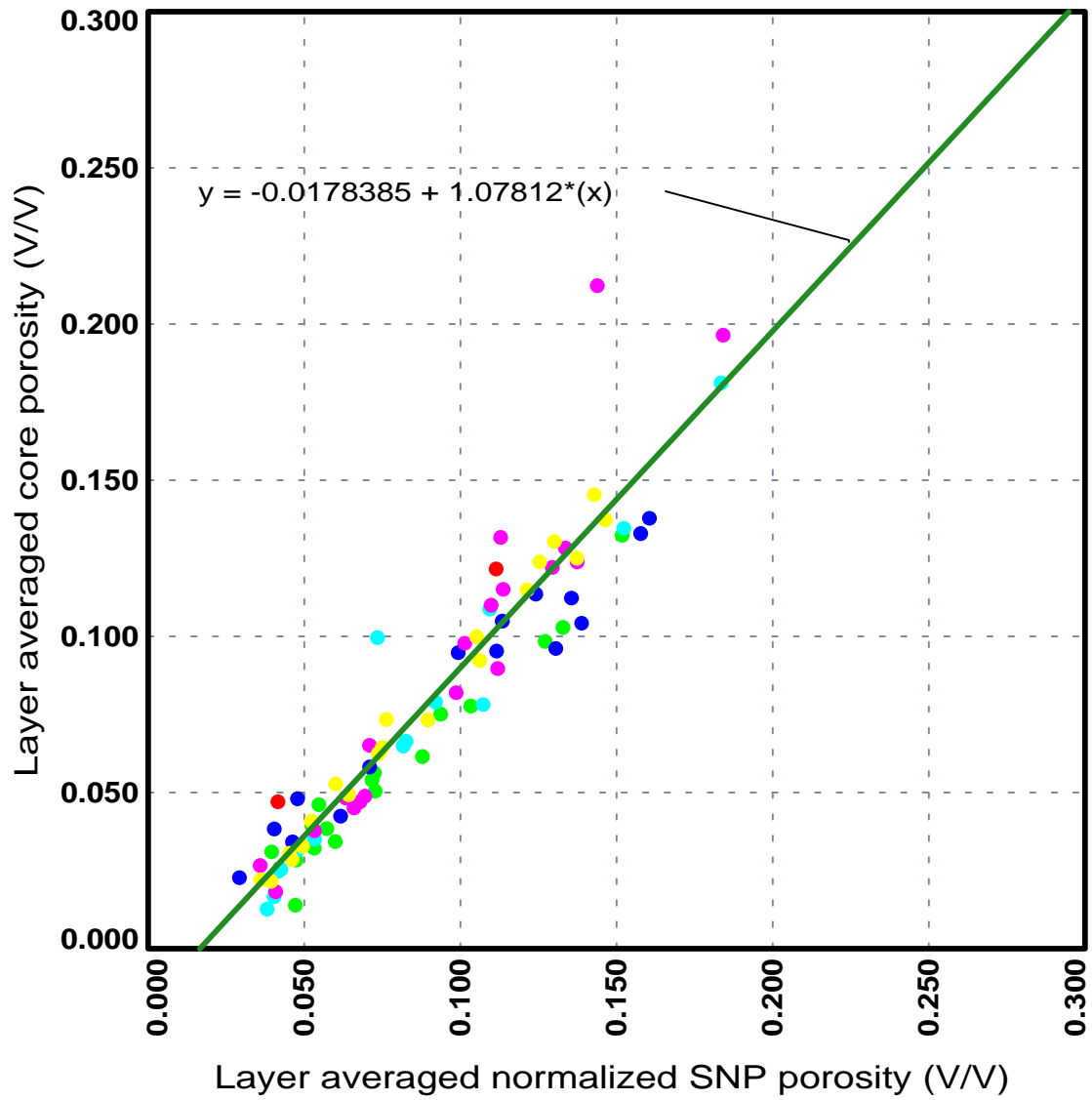


Figure 7. Plot of layer averaged core porosity (y-axis) as a function of layer averaged normalized sidewall neutron porosity (x-axis) showing the calibration line for dolomites. Each point represents data that have been vertically averaged over a single cycle. Like colors represent data from the same well. Calibration is based on six wells.

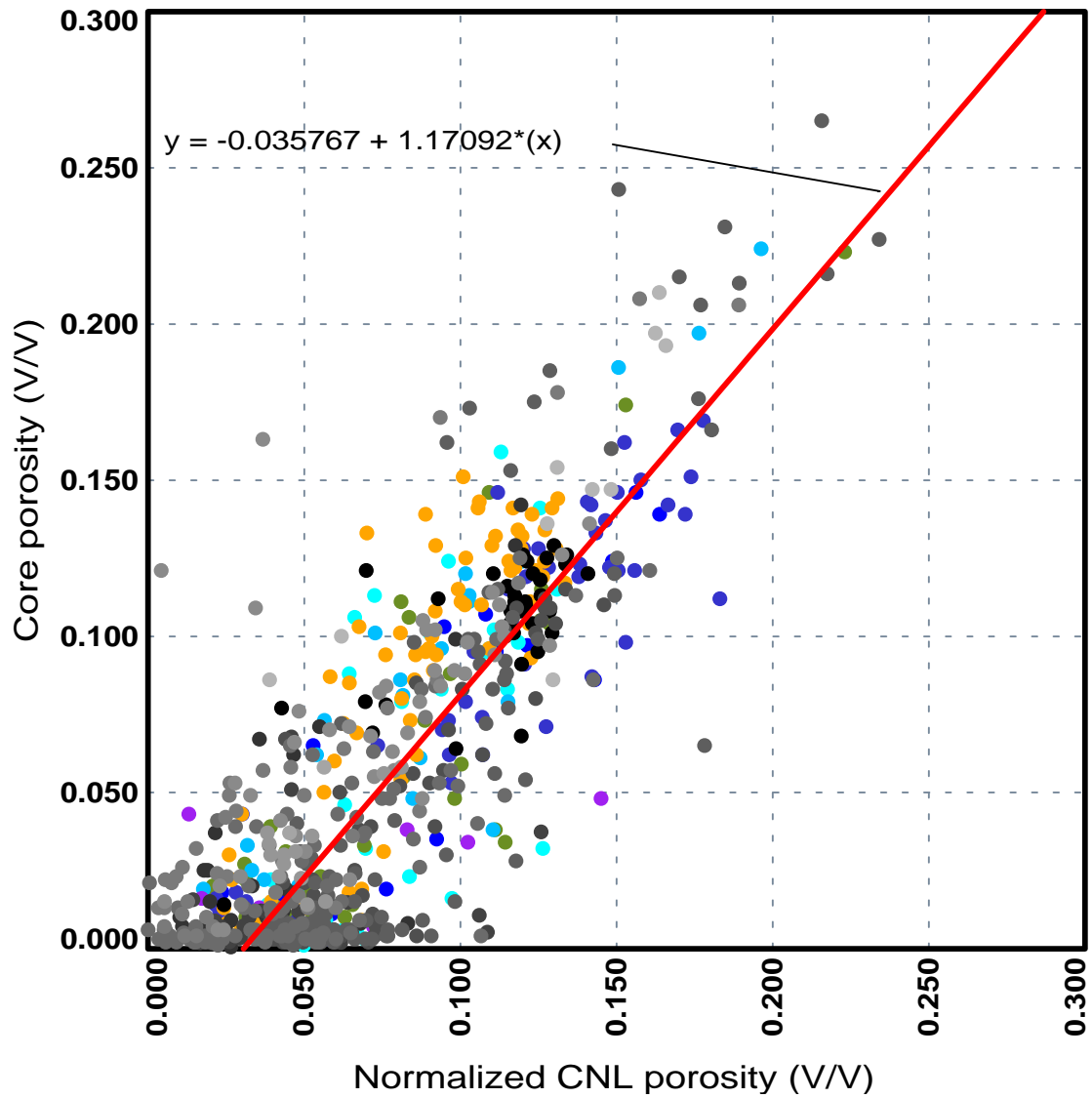


Figure 8. Plot of core porosity (y-axis) as a function of normalized compensated neutron porosity (x-axis) showing the calibration line for limestone. Each point represents an individual core sample. Only data where the photo-electric factor was greater than four was used in the generating the calibration. Like colors represent data from the same well. Calibration is based on 21 wells.

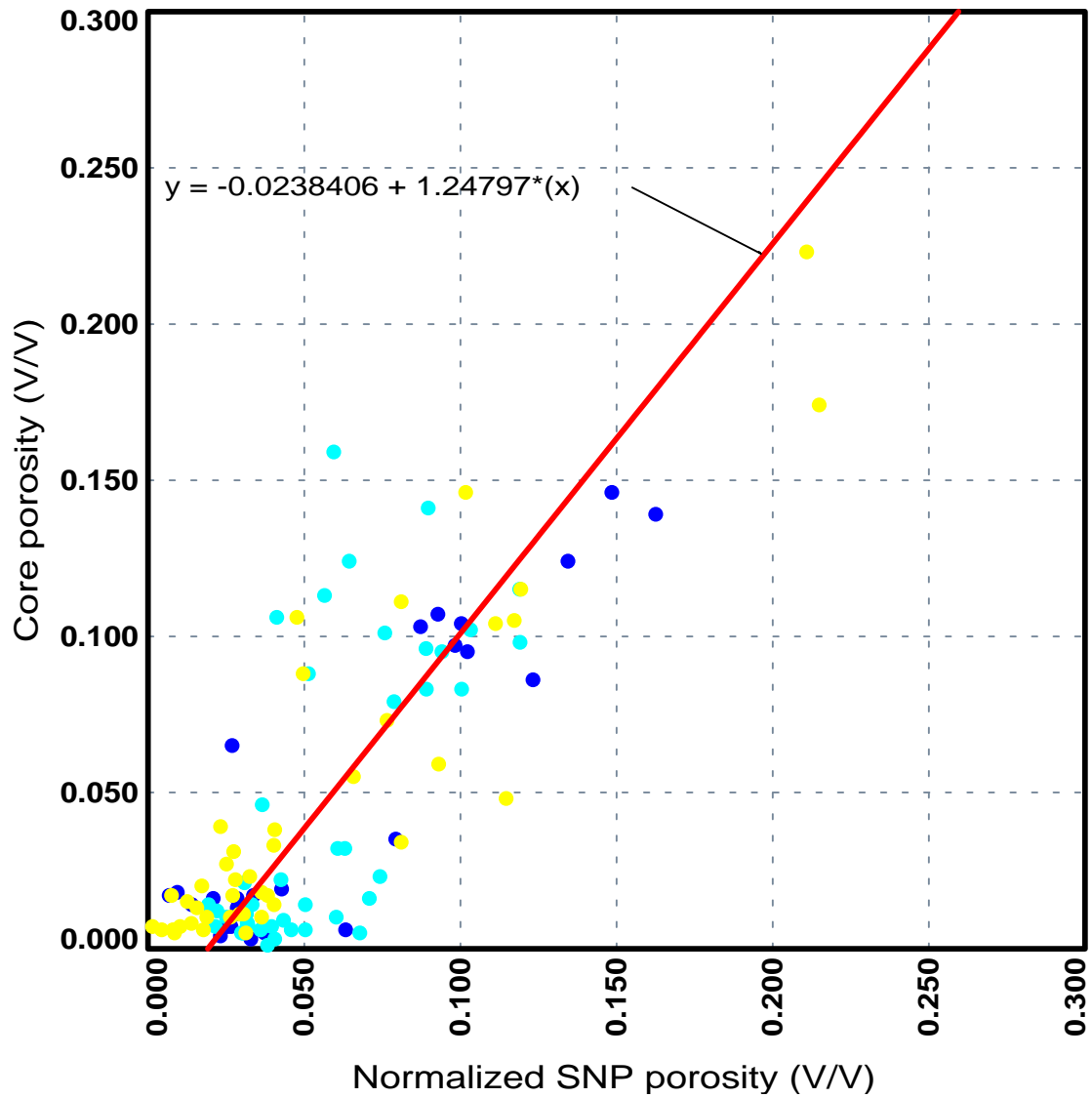


Figure 9. Plot of core porosity (y-axis) as a function of normalized sidewall neutron porosity (x-axis) showing the calibration line for limestone. Each point represents an individual core sample. Only data where the photo-electric factor was greater than four was used in the generating the calibration line. Like colors represent data from the same well. Calibration is based on five wells.

CALCULATIONS OF PERMEABILITY AND INITIAL WATER SATURATIONS
FROM WIRELINE LOGS

F. Jerry Lucia and Jeffrey A. Kane

Bureau of Economic Geology
Scott W. Tinker, Director
John A. and Katherine G. Jackson School of Geosciences
The University of Texas at Austin
Austin, Texas 78713-8924

| | |
|--|-----|
| ABSTRACT..... | 193 |
| PERMEABILITY CALCULATIONS FROM WIRELINE LOGS | 194 |
| ESTIMATION OF ORIGINAL WATER SATURATION..... | 196 |
| COMPARISON OF MODEL S_w WITH ARCHIE S_w | 200 |
| DISCUSSION..... | 201 |
| REFERENCES | 202 |

Tables

| | |
|---|-----|
| 1. Thomeer and core analysis values for class 2 samples | 203 |
| 2. Thomeer and core analysis values for class 3 samples | 203 |
| 3. List of electrical measurements from the Lower Clear Fork..... | 204 |

Figures

| | |
|--|-----|
| 1. Map showing location of calibration wells in the simulation area | 205 |
| 2. Cross plots showing development of permeability transforms for dolostone in sequence L2.2 | 206 |
| 3. Comparison of core and calculated permeability in sequence L2.2 | 207 |
| 4. Porosity-permeability cross plot for moldic limestone in sequence L2.2..... | 208 |
| 5. Comparison of core and calculated permeability in sequence L2.1 | 208 |
| 6. Comparison of core and calculated permeability in the Wichita peritidal facies | 209 |
| 7. An example of fitting Thomeer parameters to a class 2 medium crystalline dolostone | 210 |
| 8. Cross plots of Thomeer G factor and porosity for class 3 fabrics and class 2 fabrics showing little relationship between porosity and G factor | 211 |
| 9. Cross plots of extrapolated entry pressures and porosity for class 3 fabrics and class 2 fabrics showing statistical relationships between entry pressure and porosity | 212 |
| 10. Comparison of class 3 curves with curves calculated using the Thomeer model..... | 213 |
| 11. Comparison of Thomeer class 3 capillary pressure model with generic class 3 model | 214 |
| 12. Comparison of class 2 curves with curves calculated using the Thomeer model..... | 215 |

| | |
|--|-----|
| 13. Comparison of Thomeer class 2 capillary pressure model with generic class 2 model | 216 |
| 14. Capillary pressure curves from moldic limestone | 217 |
| 15. Comparison of capillary pressure curves from class 1 anhydritic dolostones with curves using the generic class 1 model | 217 |
| 16. Example of model and Archie S_w from well FCU 5727..... | 218 |

Calculations of Permeability and Initial Water Saturations from Wireline Logs

F. Jerry Lucia and Jeffrey A. Kane

ABSTRACT

Permeability is calculated from wireline logs using total porosity from wireline logs and apparent-rock-fabric number for stratigraphic relationships. Total porosity was used instead of interparticle porosity because the appropriate wireline logs needed to calculate interparticle porosity were not available. The use of total porosity required the use of an apparent-rock-fabric number, which was taken from stratigraphic relationships presented by Jones and others as part of this report. Permeability profiles were calculated using the global transform and compare reasonably well with core permeability values. The exception is in the lower section of the Wichita where karst fabrics are present suggesting a touching-vug pore system.

Initial water saturations were calculated using capillary pressure models. A generic model for class 1 fabrics was used and new models were developed for class 2 and 3 fabrics. The new models were developed using the Thomeer approach. Because most of the original wells had poor log suites and new wells were drilled after the advent of water flooding, calculation of initial water saturation from wireline logs was not feasible. However, calculations from capillary models appeared to match log calculations in intervals believed to be unflooded.

PERMEABILITY CALCULATIONS FROM WIRELINE LOGS

Permeability is calculated from wireline logs using the global porosity-permeability transform (eq. 1, 2). This equation was derived from a database of rock-fabric descriptions, interparticle porosity, permeability, and petrophysical-class values (Lucia, 1999; Lucia and others, 2001; Jennings and Lucia, 2003).

$$\text{LOG}(k)=((a-b*\text{LOG}10(\text{rfn})) + (c - d*\text{LOG}10(\text{rfn}))*\text{LOG}10(\text{ippor})) \quad (1)$$

or

$$\text{LOG}(k)=((a-b*\text{LOG}10(\text{arfn})) + (c - d*\text{LOG}10(\text{arfn}))*\text{LOG}10(\text{phi})) \quad (2)$$

where

rfn = rock-fabric number,

arfn = apparent rock-fabric number,

ippor = interparticle porosity,

phi = total porosity,

a = 9.7982,

b = 12.0838,

c = 8.6711, and

d = 8.2965.

Interparticle porosity and rock-fabric number are inserted into equation 1 to calculate permeability. However, as discussed by Jones and Lucia (this report), total porosity is used in the study because the abbreviated log suite available throughout the field does not allow for the calculation of interparticle porosity. Therefore, apparent rock-fabric number (ARFN) rather than rock-fabric number is used in equation 2, along with total porosity. The ARFN is provided by the relationship between rock-fabric petrophysical class and stratigraphy, as discussed by Jones and Lucia (this report), and total porosity is from porosity logs (Kane, this report).

The method was tested on six cored wells in the simulation area (fig. 1) with good to excellent results. Sequence L2.2 is composed of anhydritic dolostone with a small area of limestone. Whereas an ARFN of 1 was used throughout the full field, a more rigorous approach to assigning ARFN's was applied in the simulation area. In the dolostone area a statistical transform was developed that used multiple ARFN's. The porosity-permeability cross plot (fig. 2a) shows that most of the data fall within the class 1 field. However, the statistical line trends into the class 2 field. The statistical line could have been used to calculate permeability in the dolostone facies. However, an ARFN is required to use the global transform. Therefore, a relationship between porosity and ARFN was developed (fig. 2b), and ARFN's calculated from the porosity log were used in the global transform. This method could not be applied throughout the field and was replaced with an ARFN of 1. As shown in figure 3a the match between core and calculated permeability values is quite good using an ARFN of 1.

A small area of limestone is present in sequence L2.2, and the porosity and permeability data plot along the class 2-3 boundary, indicating an ARFN of 2.5 (fig. 4). The data plot along the class 2-3 boundary using total porosity because the porous limestone is dominated by moldic class 1 grainstone and class 2 grain-dominated packstone, and grain molds do not add significantly to permeability. The data would plot in the appropriate class field if moldic porosity were subtracted from total porosity. As shown in figure 3b the match between core and calculated permeability values is quite good using an ARNF of 2.5 except for 5 to 10 ft of high permeability toward the top. This interval contains a large crystalline dolostone, which is an anomalous fabric in this area.

The upper interval of sequence L2.1 is composed of peritidal facies characterized by an ARFN of 3. The lower interval is composed of subtidal dolostones and limestones that could not

be mapped separately. An ARFN of 2 was used to calculate permeability because the porous limestones are moldic grain-dominated fabrics that tend to plot in the class 2 field and, in general, the dolostones are class 2 medium crystalline grain-dominated dolopackstones and wackestones (see Jones and Lucia, this report). As illustrated in figure 5, there is a good match between core and calculated permeability.

The Wichita is dominated by peritidal facies characterized by an ARFN of 3, and the comparison illustrated in figure 6 shows a good correlation between core and calculated permeability in sequence L2, except for a few permeability spikes that are assumed to be sample bias. In sequence L1 the log calculations tend to underestimate permeability. A few core descriptions and one image log show collapse breccia in this interval (fig. 6b), suggesting the presence of fracturing due to karsting and collapse that may account for higher than predicted permeability in this area. As discussed by Wang (this volume), in conjunction with building the simulation model the matrix permeability estimates were increased about 20 times in order to match injection.

ESTIMATION OF ORIGINAL WATER SATURATION

Estimates of initial water saturation (S_w) were made using a capillary pressure model. There are several methods for doing this, the most popular being the Leverett J junction, which relates saturation to reservoir height and the ratio of permeability and porosity (k/ϕ), where k/ϕ is a measure of pore size. The difficulty with this method is that a permeability value is required. Permeability is often obtained from a single porosity-permeability transform, which results in S_w being a function of porosity only and not pore size. However, it is well known that S_w is a function of pore size as well as reservoir height. Lucia (1995) showed that the combination of rock fabric and interparticle porosity is a measure of pore size and that S_w is a

function of rock-fabric petrophysical class, porosity, and reservoir height. The difficulty with this method is the requirement for a petrophysical-class value. In this study, initial water saturation was calculated using petrophysical class obtained from rock-fabric stratigraphy, as described by Jones and Lucia (this report), porosity from wireline logs, and reservoir height assuming a zero capillary pressure level at -4,100 ft. The presence of multiple oil-water contacts suggested in past field studies was not investigated. However, the evidence presented for multiple oil-water contacts is thought to be equivocal.

Initially we used the generic relationships derived by Lucia (1995):

$$\text{Class 1 } S_w = 0.02219 \times H^{-0.316} \times \phi^{-1.745} \quad (3)$$

$$\text{Class 2 } S_w = 0.1404 \times H^{-0.407} \times \phi^{-1.440} \quad (4)$$

$$\text{Class 3 } S_w = 0.6110 \times H^{-0.505} \times \phi^{-1.210} \quad (5)$$

where

S_w = water saturation in fraction,

H = reservoir height in feet, and

ϕ = porosity in fraction (assuming that little vuggy porosity is present).

During the progress of the field study new capillary pressure data were obtained. The samples were selected on the basis of rock-fabric descriptions and porosity. Comparing the generic models with the new capillary pressure data indicated that the class 2 and 3 generic models overestimate water saturation, suggesting the need for a new saturation model.

The new models were developed using the Thomeer (1960) method for characterizing capillary pressure curves. The Thomeer method estimates the irreducible water saturation, entry

pressure, and shape of the capillary pressure curve (the G factor) from a cross plot of percent bulk-volume of mercury occupied and entry pressure corrected for surface effects.

$$(BV_{occ}/BV_{inf}) = 2.71828^{(-G/(\text{LOG}(P_c/P_d)))}$$

where

BV_{occ} = fraction of bulk volume occupied by mercury in fraction,

BV_{inf} = fraction of bulk volume occupied by mercury extrapolated to infinite pressure,

G = Thomeer parameter related to shape of capillary pressure curve,

P_c = capillary pressure in psi, and

P_d = entry capillary pressure corrected for surface effects in psi.

Using a spreadsheet program developed by Ed Clerke of Aramco Petroleum Company, parameters were selected until a reasonable match was made between the data and the model (fig. 7). In several cases a bimodal fit was required and the fit to the lowest pressure data was used in the model. In all cases the BV_{inf} approximated the total porosity because injection pressures of greater than 50,000 psi were used in the measurements. Therefore, BV_{occ}/BV_{inf} is assumed to be S_w. The samples were grouped by petrophysical class, and porosity was correlated to the G factor and to the extrapolated entry pressure. The data are presented in tables 1 and 2. There is little correlation between porosity and G factor for class 2 and class 3 (fig. 8). The average value for class 2 was 0.2, and the average value for class 3 was 0.1, suggesting that there may be a relationship between rock fabric and G. Extrapolated entry pressure correlated quite well with porosity for both class 2 and class 3 rocks, although the correlation was different in each case (fig. 9).

The resulting saturation models for class 2 and 3 are given below:

$$S_{hg} = (BV_{occ}/BV_{inf}) = 2.71828^{(-G/(\text{LOG}(P_c/P_d)))},$$

assuming total porosity filled with mercury at infinite pressure.

or

$$S_w = 1 - [2^{-G / (\text{LOG}(P_c / P_d))}]$$

$$P_c = 1.191H \text{ (based on field data)}$$

Class 2

$$G = 0.2$$

$$P_d = 0.0768067 * \Phi^{-2.8394}$$

$$S_w(\text{Class 2}) = 1 - [2.71828^{-0.2 / (\text{LOG}(P_c / (0.0768067 * \Phi^{-2.8394})))}]$$

or in terms of H,

$$S_w(\text{Class 2}) = 1 - [2.71828^{-0.2 / (\text{LOG}(15.5064 * H / \Phi^{-2.8394})))}]$$

Class 3

$$G = 0.1$$

$$\text{Class 3 } P_d = 3.1117 * \Phi^{-1.9717}$$

$$S_w(\text{Class 3}) = 1 - [2.71828^{-0.1 / (\text{LOG}(P_c / (3.1117 * \Phi^{-1.9717})))}]$$

or in terms of H,

$$S_w(\text{Class 3}) = 1 - [2.71828^{-0.1 / (\text{LOG}(0.3827 * H / (\Phi^{-1.9717})))}]$$

The new capillary pressure models were compared with capillary pressure data and with the original generic models by visual inspection. The new class 3 model compares well with the original data but provides somewhat high S_w values at high capillary pressures (figs. 10a, 10b). This may be due to using only data from the lower curve of the dual-porosity curves to develop the S_w equations. The new model calculates significantly lower S_w values than the generic model (fig. 11a, 11b). The new class 2 model compares well with the original data in the low-porosity and high-porosity ranges (figs. 12a and 12c) but provides somewhat low S_w values in the mid-porosity range (fig. 12b). It calculates significantly lower S_w values than the generic model (fig 13a, 13b).

Class 1 oomoldic grainstone capillary pressure curves, illustrated in figure 14, are similar to class 3 curves (fig. 11). Oomoldic grainstones are found interbedded with class 2 dolostone, and an ARFN of 2 was used to estimate initial S_w . This results in underestimating initial S_w for the oomoldic grainstones interbedded with class 2 dolostones. In the limestone sector of the phase 1 area an ARFN of 2.5 was used to estimate permeability. However, only three capillary pressure models were used in this study, and the class 3 model was selected to estimate initial S_w in the limestone area.

Six capillary pressure curves from the anhydritic dolostone interval in sequence L2.2 were obtained and are illustrated in figure 15. The curves are comparable to the generic class 1 capillary pressure model. An ARFN of 1 was used to calculate initial S_w for the anhydritic dolostone, and no new model was needed.

COMPARISON OF MODEL S_w WITH ARCHIE S_w

An example comparison of water saturations calculated from capillary models and from Archie's equation is presented in figure 16. Two of the three principal inputs into the capillary pressure model are illustrated: porosity and petrophysical class. Archie water saturations were calculated using an m and n of 2, which is supported by laboratory measurements listed in table 3. Water resistivity was estimated at 0.04 ohmms. Waterflooding was initiated in 1961, and most of the field was under waterflood by 1973. As a result, capillary pressure S_w values are expected to be equal to or lower than Archie values.

Examination of figure 16 shows intervals of class 2 and 3 where model S_w and Archie S_w match closely. This suggests that the capillary pressure models give reasonable estimates of original water saturation. However, in many porous intervals Archie S_w is higher than model S_w . These intervals are considered to contain flood water. Because flood water is less saline and

more resistive than 0.04 ohmms, the Archie S_w is considered to underestimate S_w in the flooded intervals. The upper 20 ft shown in figure 16 illustrates the common observation that Archie S_w values are unreliable when porosity is less than 5 to 6 percent.

A calculation of original water saturation using the Archie equation could not be made because of the poor quality of the original wireline logs and the long history of waterflooding. An attempt was made to use the early resistivity logs and more modern porosity logs from adjacent wells to calculate Archie S_w . In addition, Archie S_w was calculated for wells having initial low water production that might not have been completely flooded at the time of logging. No robust conclusion could be drawn from these results because the effects of injection water could not be adequately accounted for.

DISCUSSION

The stratigraphic approach used to predict apparent rock-fabric number together with total porosity results in reasonable estimates of matrix permeability using the global transform equation. The estimates of matrix permeability are considered to be highly reliable in the simulation area. However, they are less reliable outside of the simulation area because no detailed calibration between apparent rock-fabric number and stratigraphy was made. Additional detailed studies should be done in areas of future simulation modeling.

These results are achieved despite the grouping of limestones and dolostones and grain-dominated and mud-dominated fabrics. The fabrics tend to group in the class 2 field because the presence of grain molds in the grainstone moves the plot-points into the class 2 field and the conversion of the limestone into a medium crystalline dolostone moves the mud-dominated dolostones into the class 2 field. The mud-dominated limestones are tight and are not an issue. The peritidal facies can be correlated and are typically class 3 fine crystalline dolostones. In

sequence L1, however, there appears to be a touching-vug pore system, and matrix porosity and the permeability values are understated.

The new capillary pressure models for calculating initial S_w in the class 2 and 3 fabrics fit the capillary pressure data better than the generic models. Limited comparisons with Archie S_w calculations suggest that the model saturations are reasonable. The zero capillary pressure level of -4,100 was used to minimize the transition zone effect at the base of the reservoir. We have no real data to support this but assume that the Wichita and Lower Clear Fork are one reservoir. We know of no conclusive evidence for multiple reservoirs.

REFERENCES

- Jennings, J. W., Jr., and Lucia, F. J., 2003, Predicting permeability from well logs in carbonates with a link to geology for interwell permeability mapping: Society of Petroleum Engineers Reservoir Evaluation & Engineering, v. 6, no. 4, p. 215–225.
- Lucia, F. J., 1995, Rock-fabric/petrophysical classification of carbonate pore space for reservoir characterization: American Association of Petroleum Geologists Bulletin, v. 79, no. 9, p. 1275–1300.
- Lucia, F. J., 1999, Carbonate reservoir characterization: New York, Springer-Verlag, 226 p.
- Lucia, F. J., Jennings, J. W., Jr., Rahnis, M. A., and Meyer, F. O., 2001, Permeability and rock fabric from wireline logs, Arab-D reservoir, Ghawar field, Saudi Arabia: GeoArabia, v. 6, no. 4, p. 619–646.
- Thomeer, J. H. M., 1960, Introduction of a pore geometrical factor defined by the capillary pressure curve: American Institute of Mining, Metallurgical, and Petroleum Engineers Transactions, v. 219, p. 354–358.

Table 1. Thomeer and core analysis values for class 2 samples (MxIMDDstn = Medium crystalline mud-dominated dolostone; GDDP = Grain-dominated dolopackstone).

| Depth | Sample No. | Well FCU | G factor | Pd (psi) | Bvinf | Phi (%) | Perm (md) | Rock Fabric | Pet. Class |
|-------|------------|----------|----------|----------|-------|---------|-----------|-------------|------------|
| 6822 | 10 | 6429 | 0.1 | 150 | 1.5 | 10.7 | 1.13 | MxIMDDstn | 2 |
| 6855 | 42 | 6429 | 0.1 | 100 | 2 | 14.4 | 5.6 | GDDP | 2 |
| 6907 | 94 | 6429 | 0.2 | 75 | 8 | 8.6 | 0.53 | MxIMDDstn | 2 |
| 6908 | 95 | 6429 | 0.5 | 50 | 10 | 10.1 | 8.3 | MxIMDDstn | 2 |
| 6991 | 98 | 5927 | 0.4 | 60 | 8 | 8.4 | 0.28 | MxIMDDstn | 2 |
| 6995 | 102 | 5927 | 0.2 | 25 | 12 | 12.8 | 9.76 | MxIMDDstn | 2 |
| 6813 | 1 | 6429 | 0.3 | 10 | 13 | 12.5 | 9.63 | GDDP | 2 |
| 6818 | 6 | 6429 | 0.25 | 80 | 9 | 11.6 | 2.38 | GDDP | 2 |
| 6914 | 101 | 6429 | 0.2 | 20 | 18 | 17.5 | 16.23 | GDDP | 2 |
| 6915 | 102a | 6429 | 0.3 | 40 | 18 | 18.5 | 16.3 | GDDP | 2 |
| 6938 | 57 | 5927 | 0.2 | 100 | 8 | 8.0 | 0.58 | MxIMDDstn | 2 |

Table 2. Thomeer and core analysis values for class 3 samples (FxIMDDstn = Fine crystalline mud-dominated dolostone).

| Depth | Sample No. | Well FCU | G factor | Pd (psi) | Bvinf | Phi (%) | Perm (md) | Rock Fabric | Pet. Class |
|-------|------------|----------|----------|----------|-------|---------|-----------|-------------|------------|
| 7001 | 108 | 5927 | 0.12 | 150 | 17 | 17.9 | 0.99 | FxIMDDstn | 3 |
| 7002 | 109 | 5927 | 0.15 | 56 | 23 | 23.6 | 5.66 | FxIMDDstn | 3 |
| 7003 | 110 | 5927 | 0.12 | 140 | 14 | 14.2 | 0.6 | FxIMDDstn | 3 |
| 7004 | 111 | 5927 | 0.13 | 300 | 3 | 20.1 | 0.88 | FxIMDDstn | 3 |
| 7007 | 114 | 5927 | 0.13 | 150 | 5 | 26.2 | 15.9 | FxIMDDstn | 3 |
| 7009 | 116 | 5927 | 0.15 | 120 | 15 | 15.7 | 0.95 | FxIMDDstn | 3 |
| 7044 | 147 | 5927 | 0.13 | 80 | 18 | 18.6 | 3.79 | FxIMDDstn | 3 |
| 7045 | 148 | 5927 | 0.13 | 100 | 19 | 19.1 | 2.64 | FxIMDDstn | 3 |
| 7054 | 157 | 5927 | 0.2 | 175 | 10 | 10.5 | 0.232 | FxIMDDstn | 3 |
| 7056 | 159 | 5927 | 0.13 | 100 | 19 | 19.5 | 1.93 | FxIMDDstn | 3 |
| 7059 | 162 | 5927 | 0.13 | 100 | 15 | 15.9 | 0.45 | FxIMDDstn | 3 |
| 7089 | 192 | 5927 | 0.15 | 200 | 13 | 13.3 | 0.267 | FxIMDDstn | 3 |

Table 3. List of electrical measurements from the Lower Clear Fork (GDDP = Grain-dominated dolopackstone; Gstn = Grainstone; MDDP = Mud-dominated dolopackstone).

| Well | Formation | Sp No. | Rock Fabric | Separate Vug (%) | Pet. Class | M | N |
|----------|-----------|--------|-------------|------------------|------------|------|------|
| FCU 6429 | LCF | 1 | GDDP | 2 | 2 | 2.05 | 2.04 |
| FCU 6429 | LCF | 6 | GDDP | 3 | 2 | 2.22 | 2.20 |
| FCU 6429 | LCF | 8 | GDDP | 2 | 1 | 1.86 | 1.97 |
| FCU 6429 | LCF | 2 | GDDP | 0 | 1 | 1.86 | 1.94 |
| FCU 5927 | LCF | 2 | Moldic Gstn | 12 | 1 | 2.04 | 2.10 |
| FCU 5927 | LCF | 3 | Moldic Gstn | 20 | 1 | 2.14 | 2.11 |
| FCU 5927 | LCF | 3 | Moldic Gstn | 15 | 1 | 2.13 | 2.02 |
| FCU 6429 | LCF | 32a | GDDP | 0 | 1 | 1.85 | 1.91 |
| FCU 5927 | LCF | 35 | Moldic Gstn | 7 | 1 | 2.05 | 1.95 |
| FCU 6429 | LCF | 35a | GDDP | 2 | 1 | 1.89 | 1.85 |
| FCU 5927 | LCF | 57 | MDDP | 1 | 2 | 1.83 | 1.87 |
| FCU 6429 | LCF | 100 | GDDP | 0 | 1 | 1.84 | 1.91 |
| FCU 6429 | LCF | 101 | GDDP | 1 | 2 | 1.89 | 1.94 |
| FCU 6429 | LCF | 102a | GDDP | 0 | 2 | 1.88 | 1.89 |
| Average | | | | | | 1.96 | 1.98 |

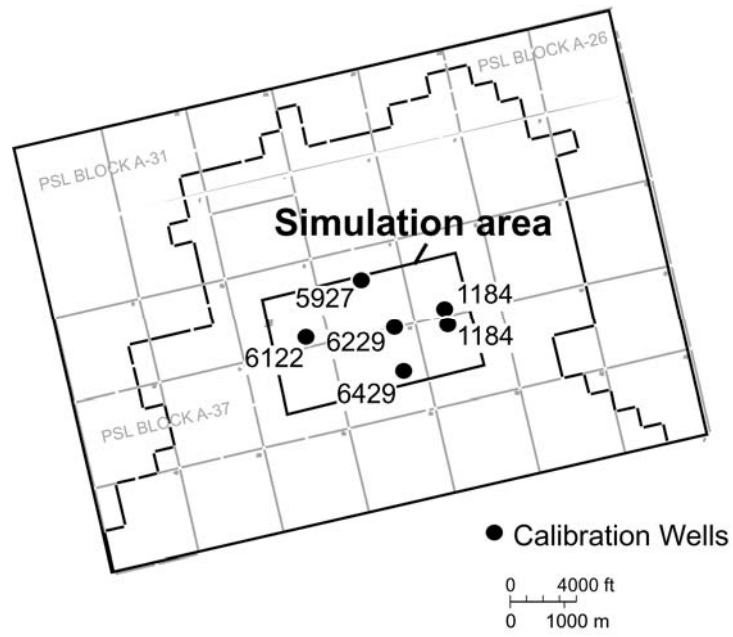


Figure 1. Map showing location of calibration wells in the simulation area.

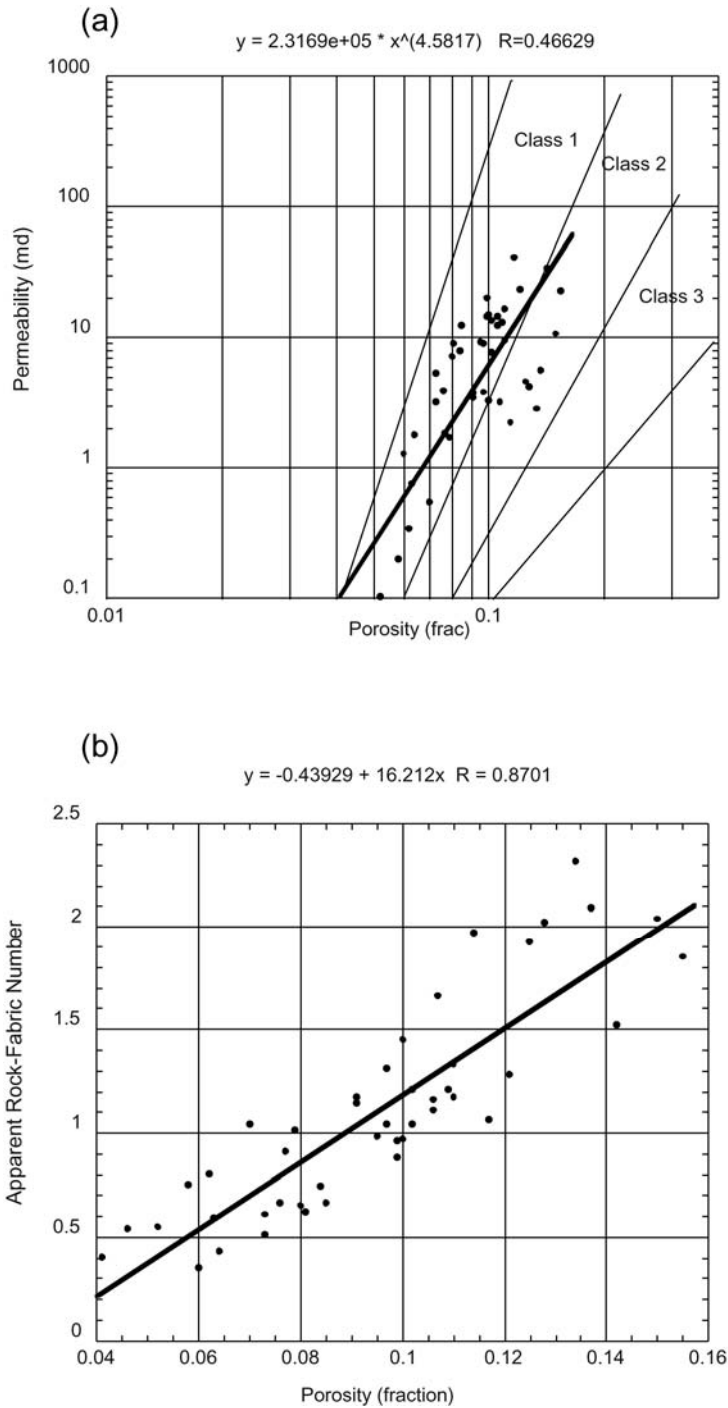
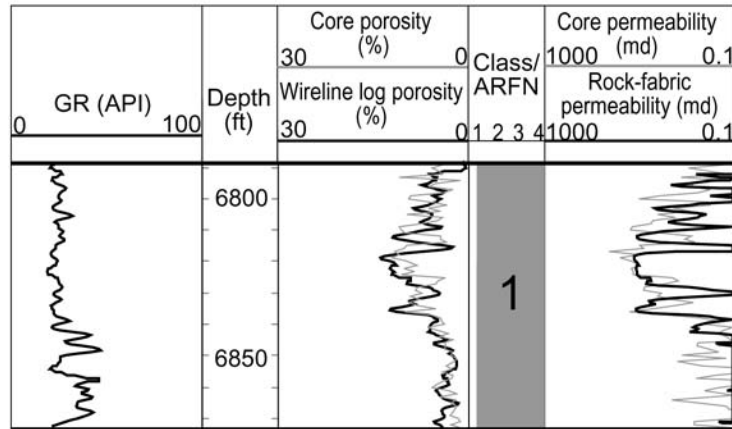


Figure 2. Cross plots showing development of permeability transforms for dolostone in sequence L2.2. (a) Porosity-permeability cross plot showing that most of the points fall in the class 1 field. A class 1 transform was used in the full field model. (b) Apparent rock-fabric number (ARFN) calculated from core data is plotted against porosity and the relationship used in uncored wells to calculate ARFN for use in the global transform equation.

(a)



(b)

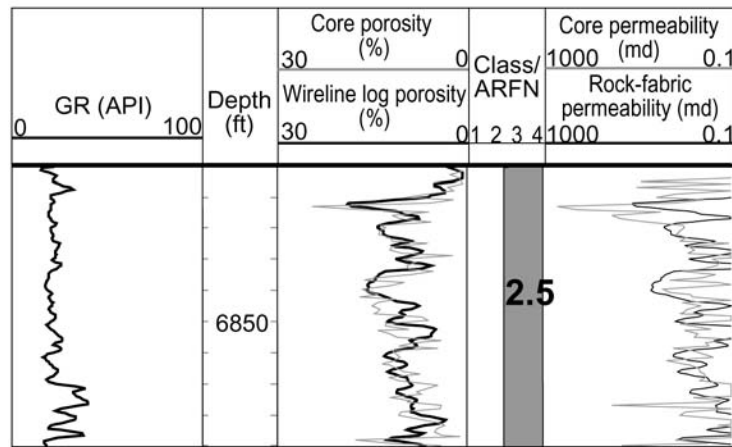


Figure 3. Comparison of core and calculated permeability in sequence L2.2. (a) Comparison in the dolostone intervals using a class 1 transform instead of the method outline line figure 2. (b) Comparison in the limestone area using the ARFN 2.5 transform. The high permeability in the upper 10 ft is a class 1 large crystalline dolostone.

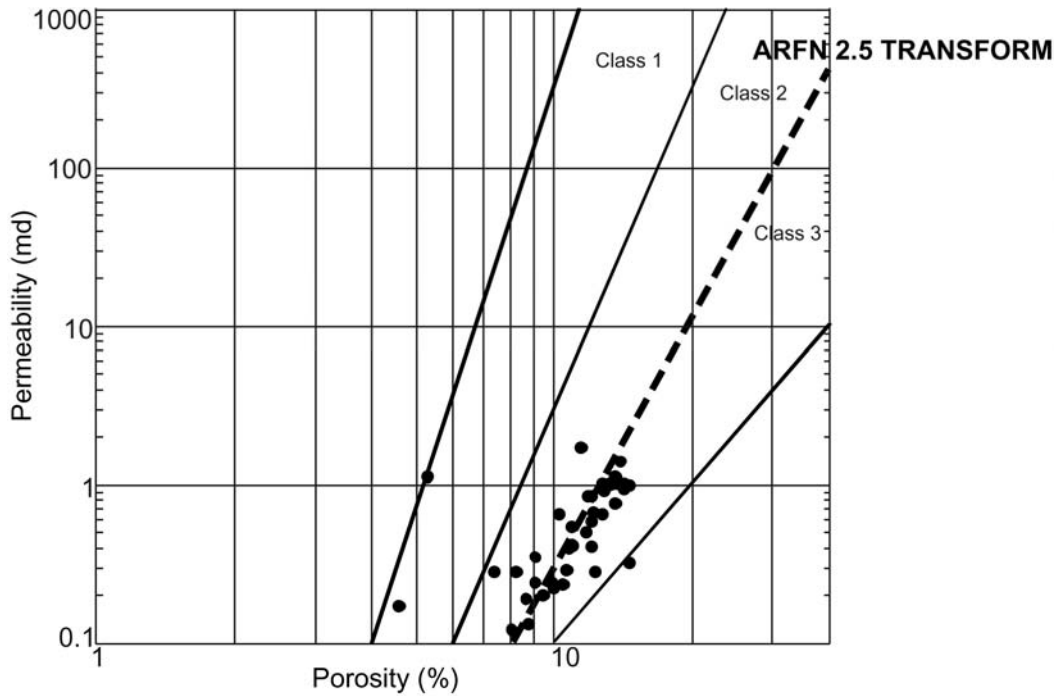


Figure 4. Porosity-permeability cross plot for moldic limestone in sequence L2.2. The data cluster along the class 2-3 boundary because moldic porosity adds little to permeability.

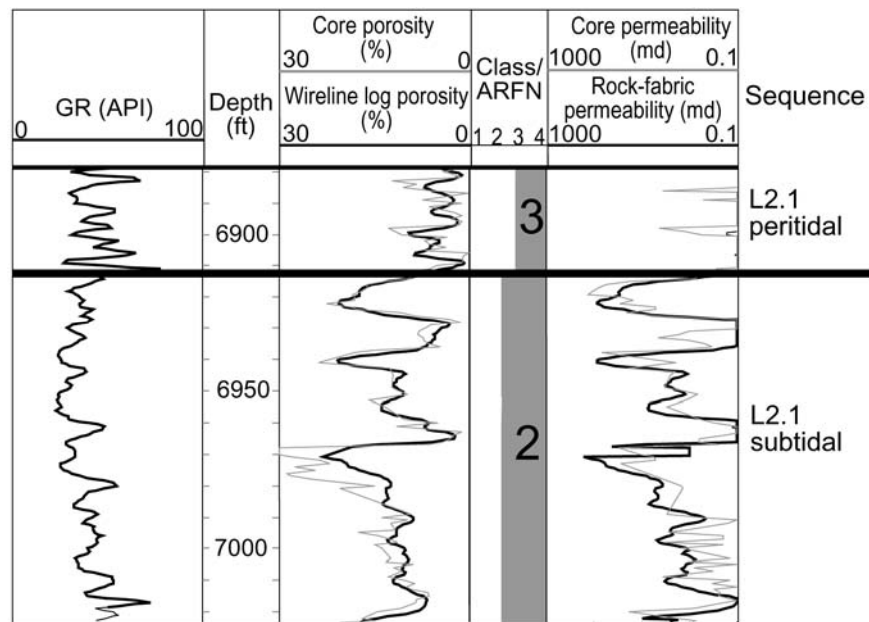


Figure 5. Comparison of core and calculated permeability in sequence L2.1. A class 3 transform is used in the upper peritidal interval and class 2 in the subtidal interval.

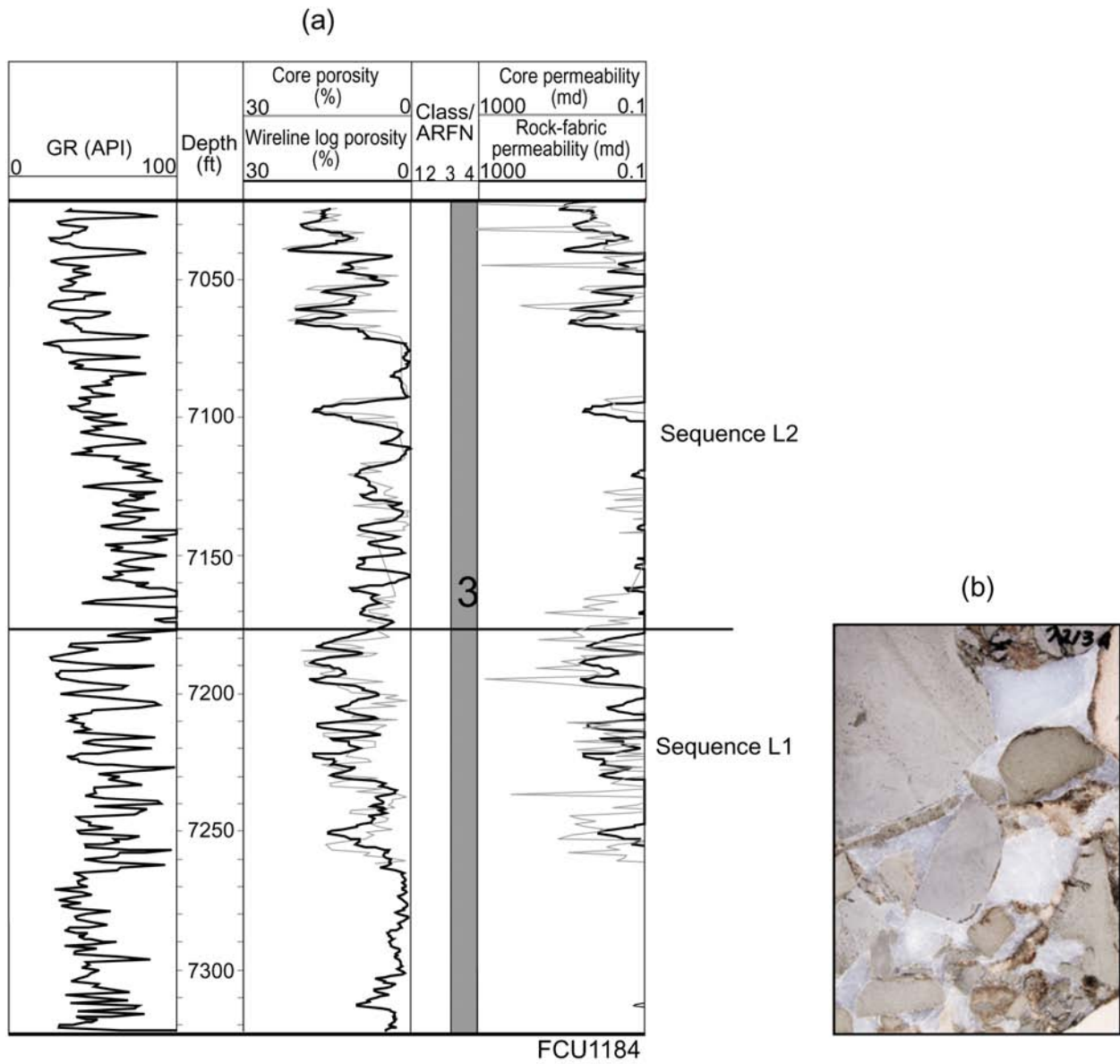


Figure 6. Comparison of core and calculated permeability in the Wichita peritidal facies. (a) A comparison of core and calculated permeability showing good correlation in sequence L2 and poor correlation in L1. (b) A core photograph of karst breccia found in L1 suggesting a touching-vug pore system.

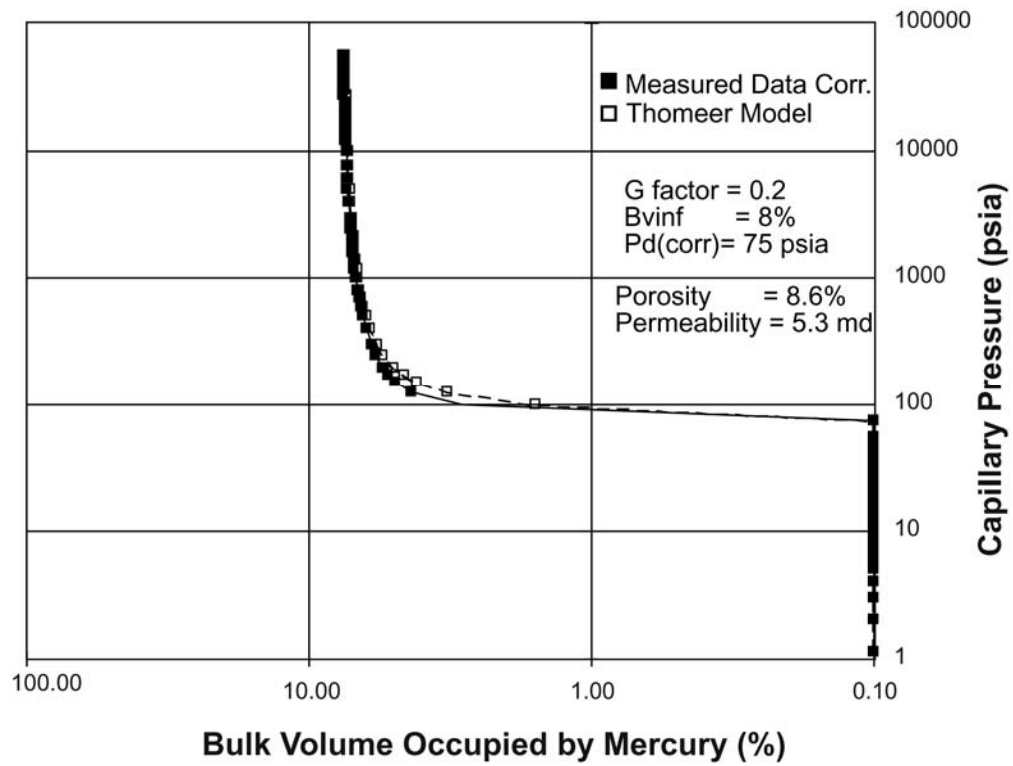


Figure 7. An example of fitting Thomeer parameters to a class 2 medium crystalline dolostone.

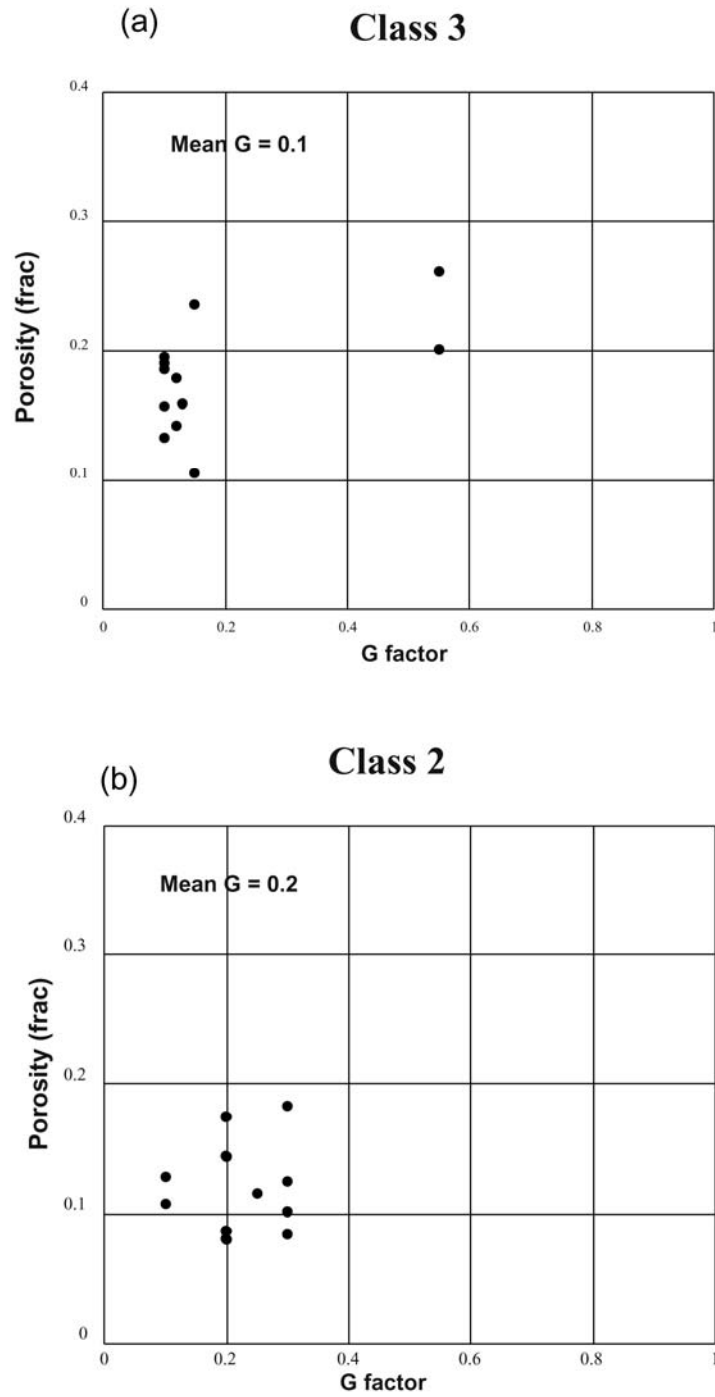
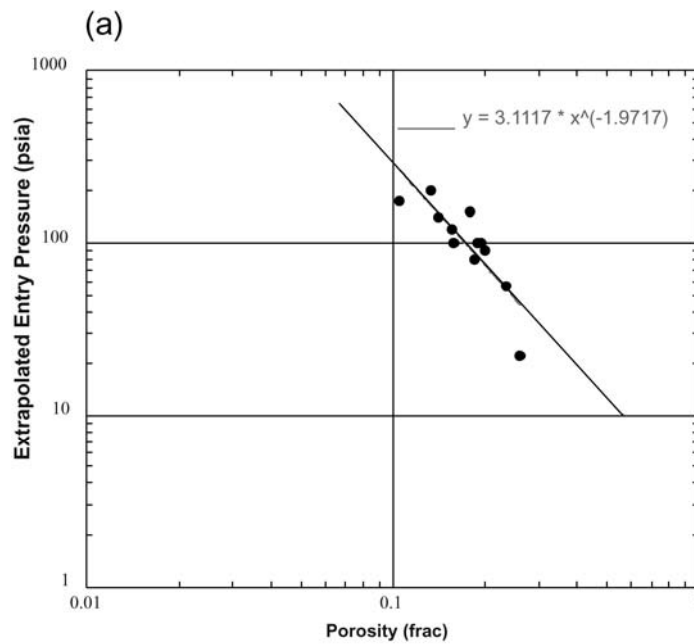


Figure 8. Cross plots of Thomeer G factor and porosity for (a) class 3 fabrics and (b) class 2 fabrics showing little relationship between porosity and G factor. Several of the class 3 samples are bimodal and require two curves to fit, and both G factors are presented in figure a.

Class 3



Class 2

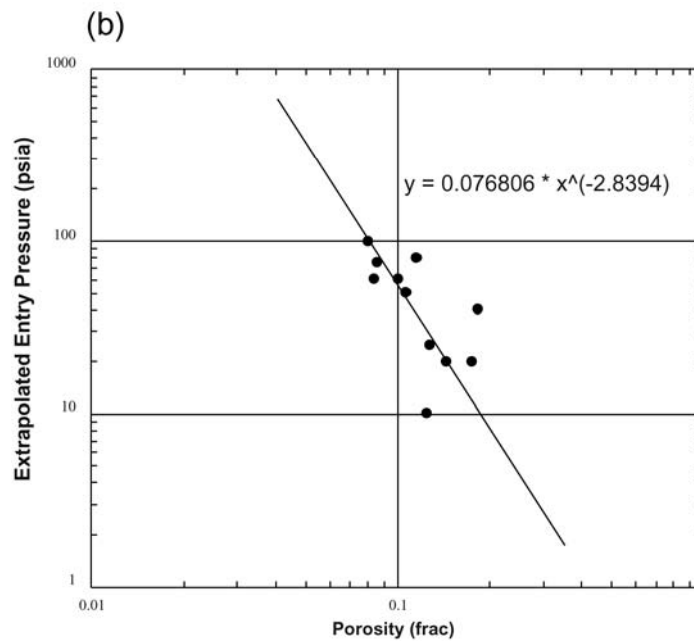


Figure 9. Cross plots of extrapolated entry pressures and porosity for (a) class 3 fabrics and (b) class 2 fabrics showing statistical relationships between entry pressure and porosity.

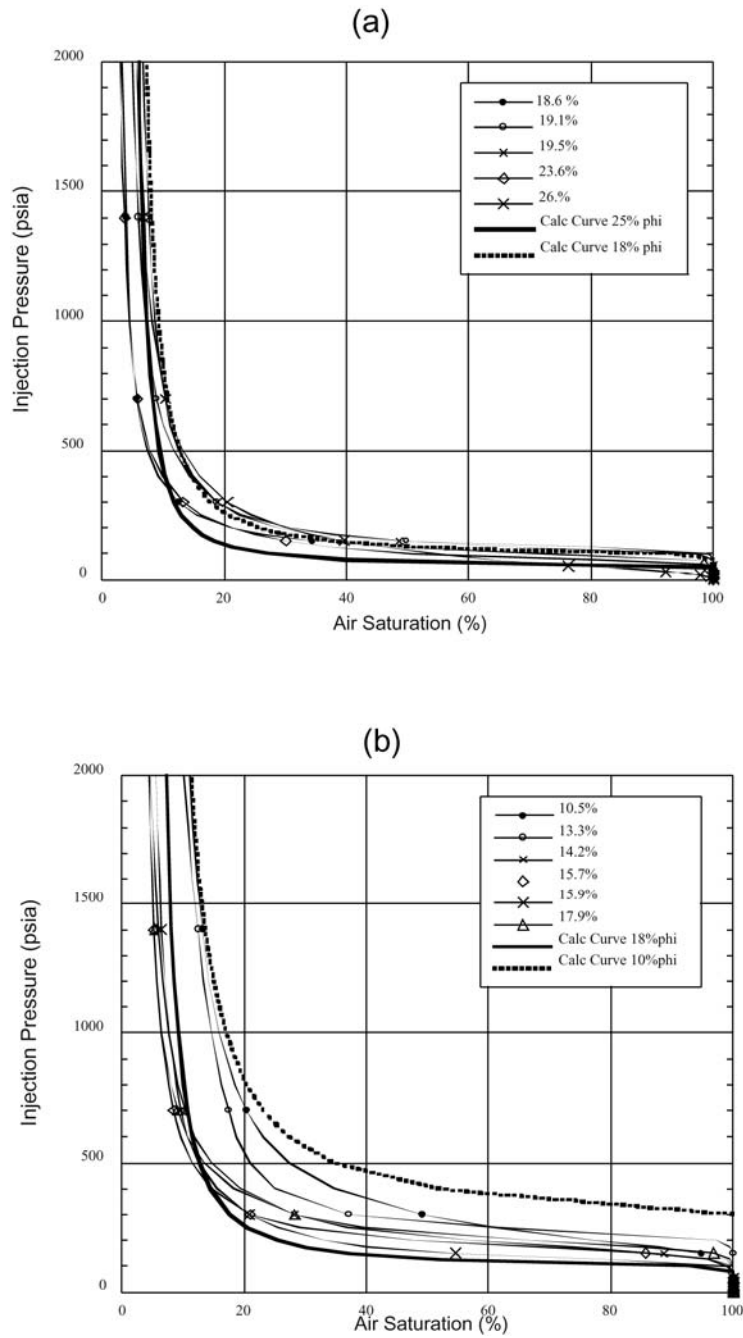


Figure 10. Comparison of class 3 curves with curves calculated using the Thomeer model. (a) Porosity less than 18 percent and (b) porosity greater than 18 percent.

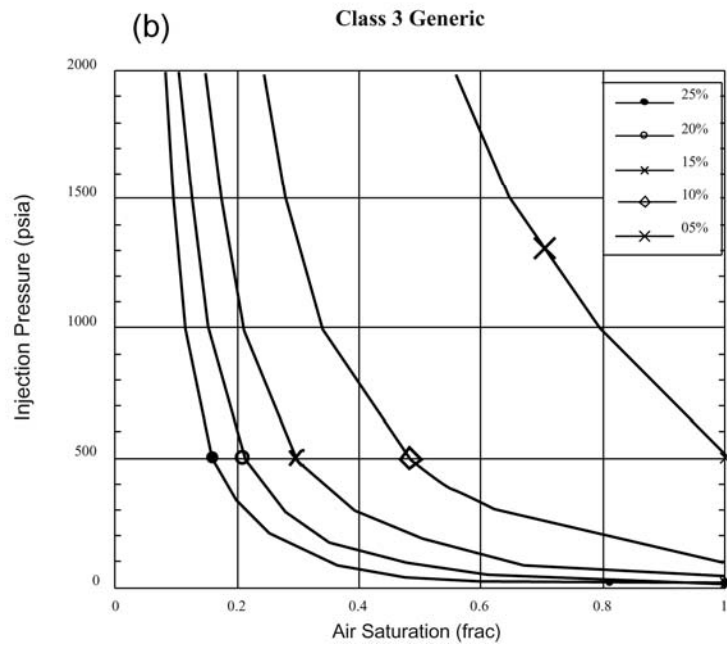
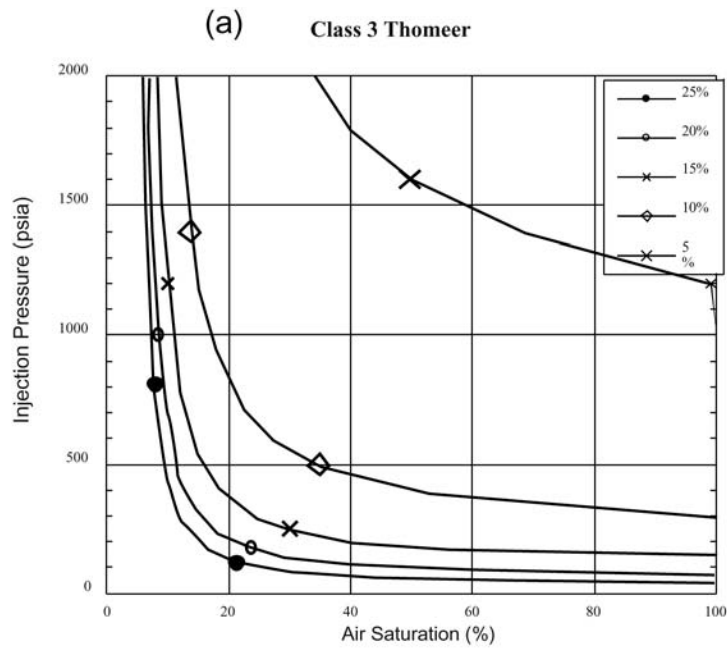


Figure 11. Comparison of (a) Thomeer class 3 capillary pressure model with (b) generic class 3 model.

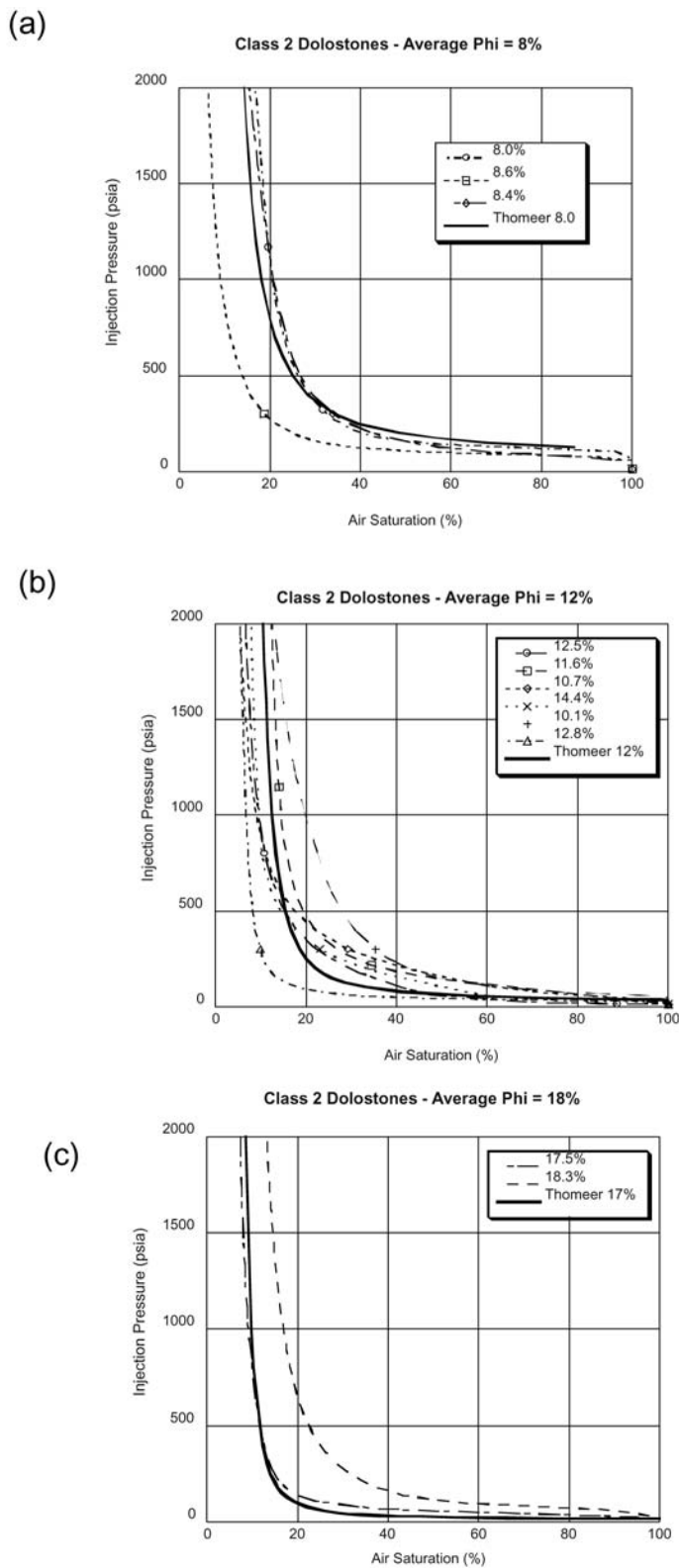


Figure 12. Comparison of class 2 curves with curves calculated using the Thomeer model. (a) Porosity average 8 percent, (b) porosity average 12 percent, (c) porosity average 18 percent.

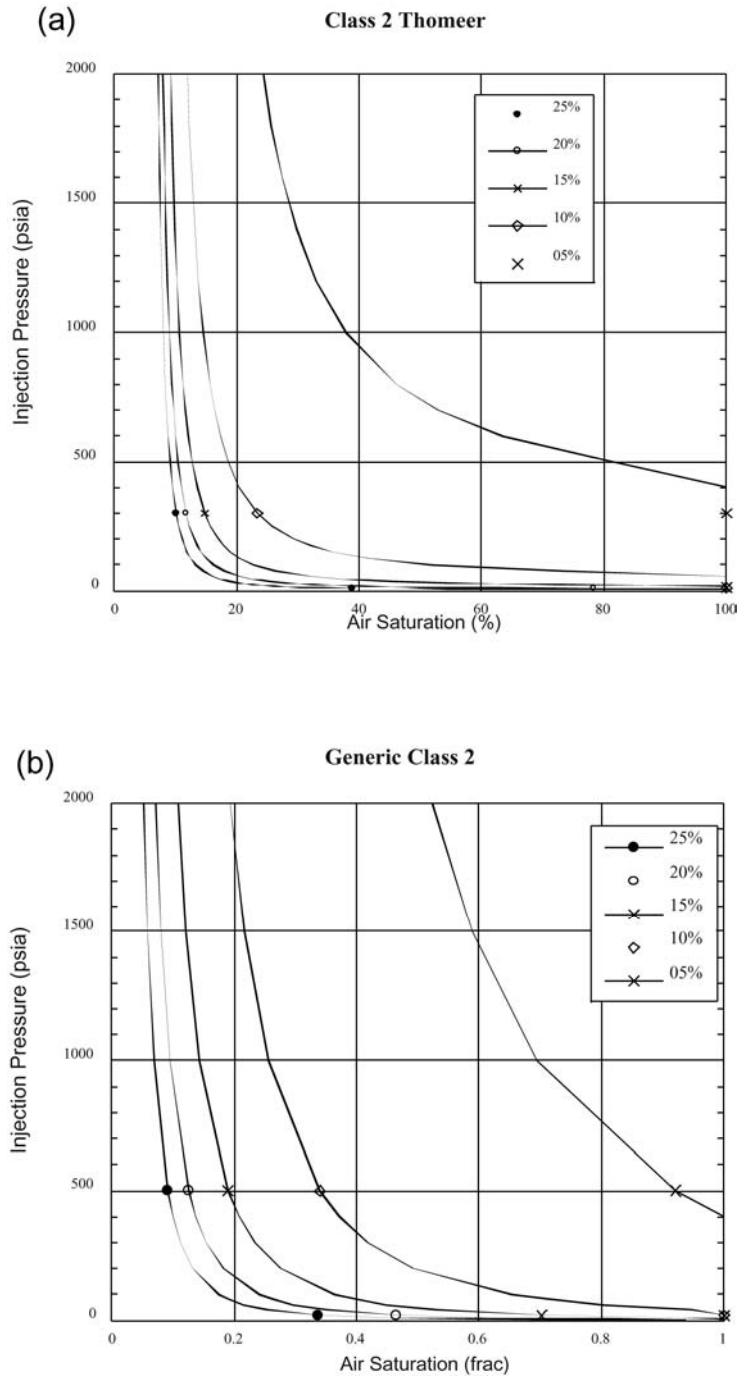


Figure 13. Comparison of (a) Thomeer class 2 capillary pressure model with (b) generic class 2 model.

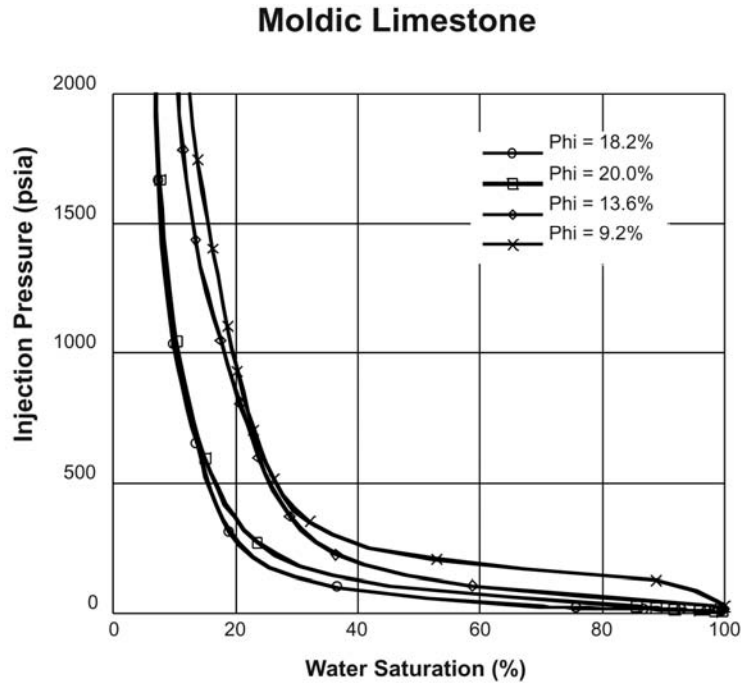


Figure 14. Capillary pressure curves from moldic limestone.

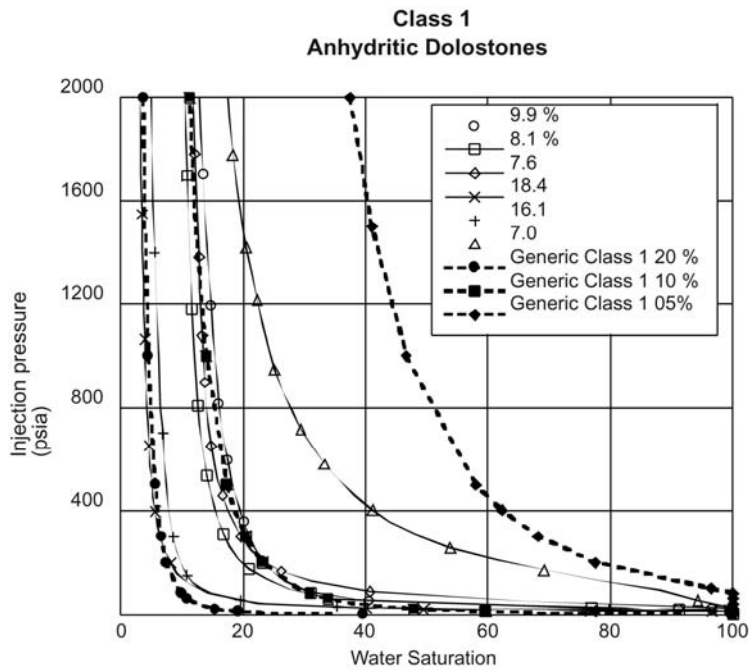


Figure 15. Comparison of capillary pressure curves from class 1 anhydritic dolostones with curves using the generic class 1 model.

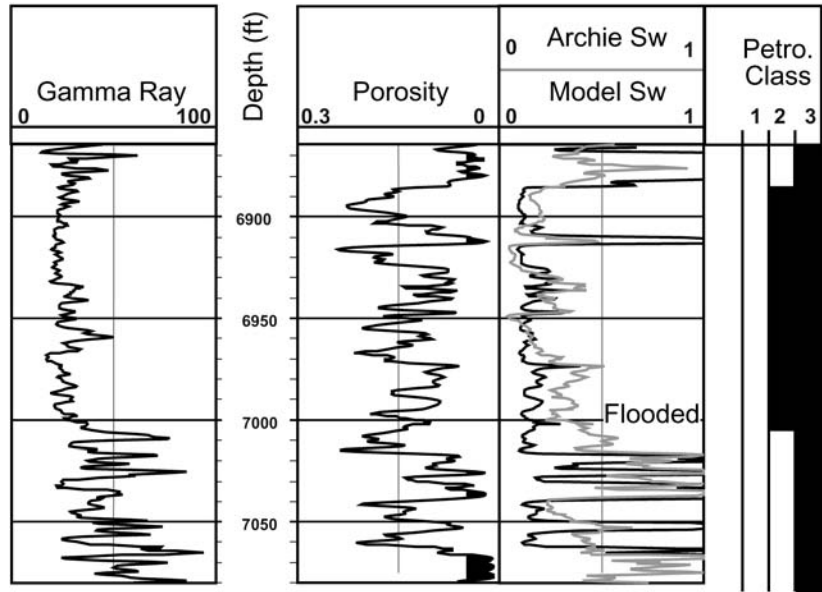


Figure 16. Example of model and Archie S_w from well FCU 5727.

RESERVOIR MODELING AND SIMULATION OF FULLERTON
CLEAR FORK FIELD, ANDREWS COUNTY, TEXAS

Fred Wang and F. Jerry Lucia

Bureau of Economic Geology
Scott W. Tinker, Director
John A. and Katherine G. Jackson School of Geosciences
The University of Texas at Austin
Austin, Texas 78713-8924

| | |
|---|-----|
| ABSTRACT..... | 225 |
| INTRODUCTION | 226 |
| 3-D RESERVOIR MODELING..... | 227 |
| Stratigraphic Modeling | 227 |
| Upscaling | 229 |
| Petrophysical Modeling | 230 |
| Porosity Distribution..... | 231 |
| Permeability (k) and kh Distribution | 232 |
| S _w and S _o φh Distribution..... | 234 |
| VOLUMETRICS | 235 |
| Sensitivity Analysis | 236 |
| Search Radius in Mapping..... | 236 |
| Grid Resolution..... | 237 |
| Water-Oil Contact..... | 237 |
| Porosity Cutoffs | 238 |
| Water Saturation Cutoffs | 239 |
| Permeability Cutoffs..... | 239 |
| Compound Effects of Vertical Resolution and Cutoff Values | 240 |
| PRODUCTION-TREND ANALYSIS | 242 |
| FLOW-UNIT MODEL AND RESERVOIR SIMULATION | 243 |
| Flow-unit Model..... | 243 |
| Flow Simulation | 249 |
| Sensitivity Study..... | 250 |
| SUMMARY | 253 |
| REFERENCES | 256 |
| APPENDIX A: UPSCALING | 295 |

Tables

| | |
|--|-----|
| 1. Geologic and reservoir parameters of Fullerton Clear Fork Unit..... | 257 |
| 2. Geologic frameworks used in 3-D reservoir models..... | 258 |
| 3. Dimensions of 3-D field models..... | 259 |
| 4. Formation volume factor, oil-gas ratio, and WOC used in OOIP estimates..... | 259 |
| 5. Effect of variable search radius on OOIP estimates of FCU..... | 259 |
| 6. Effect of water-oil contact on OOIP estimates of FCU..... | 260 |
| 7. Effect of cutoff values on OOIP..... | 260 |
| 8. Effect of cutoff values on OOIP in FCU for WOC at -3940 ft summarized by ExxonMobil zonation..... | 261 |
| 9. Effect of cutoff values on OOIP in Fullerton field for WOC at -3940 ft summarized by ExxonMobil zonation..... | 261 |
| 10. Effect of cutoff values on OOIP in FCU for WOC at -3940 ft summarized by high-frequency cycles..... | 262 |
| 11. Effect of cutoff values on OOIP in Fullerton Clear Fork field for WOC at -3940 ft summarized by high-frequency cycles..... | 263 |
| 12. Effect of vertical resolution on OOIP..... | 264 |
| 13. Summary of parameters affecting OOIP..... | 264 |
| 14. Dimensions of 3-D models of initial 2,000-acre model (simulation area)..... | 264 |

Figures

| | |
|---|-----|
| 1. Production history of waterflooding in Fullerton Clear Fork Unit..... | 265 |
| 2. Workflow of 3-D modeling..... | 265 |
| 3. Geologic framework used to build 3-D models of Fullerton Clear Fork field..... | 266 |
| 4. Effect of search radius of 2,500 ft and 5,000 ft on porosity mapping..... | 266 |
| 5. Porosity distribution in fine-grid model..... | 267 |
| 6. Average porosity distribution in Zone 1, Zone 2, Wichita, Zone 3, Zone 3B, and Zone 4..... | 267 |
| 7. ϕ_h distribution in reservoir Zone 1 (Lower Clear Fork HFS 2.2) by cycle..... | 268 |
| 8. Porosity distribution in reservoir Zone 1 (Lower Clear Fork. HFS 2.2) by cycle..... | 268 |

| | |
|---|-----|
| 9. Porosity distribution in reservoir Zone 2 (Lower Clear Fork. HFS 2.1) by cycle..... | 268 |
| 10. Porosity distribution in Zones Wichita, 3, 3B, and 4, in the Wichita Formation..... | 269 |
| 11. Permeability distribution in 3-D model..... | 269 |
| 12. Permeability distribution in reservoir zones 1, 2, Wichita, 3, 3B, and 4..... | 270 |
| 13. Kh distributions in Zone 1, Zone 2, Wichita, Zone 3, Zone 3B, and Zone 4..... | 270 |
| 14. Results of petrophysical analysis in FCU 5927, 1284, and 1435..... | 271 |
| 15. Water saturation distribution in 3-D model with oil-water contact at –3,940 ft..... | 271 |
| 16. Water saturation distributions in Zone 1, Zone 2, Wichita, Zone 3, Zone 3B, and Zone 4..... | 272 |
| 17. Hydrocarbon volume distributions in Zone 1, Zone 2, Wichita, Zone 3, Zone 3B, and Zone 4..... | 272 |
| 18. Hydrocarbon volume distribution in six reservoir zones..... | 273 |
| 19. Hydrocarbon volume distribution in Zone 1 (Lower Clear Fork HFS L 2.2)..... | 273 |
| 20. Hydrocarbon volume distribution in Zone 2 (Lower Clear Fork HFS 2 L 2.1)..... | 273 |
| 21. Hydrocarbon volume distribution in the Wichita Formation..... | 274 |
| 22. Formation volume factor and oil-gas ratio of two types of crude in FCU..... | 274 |
| 23. Effect of water-oil contact on vertical coverage in Zone 3B, Zone 4, and Zone 5 (Abo)..... | 275 |
| 24. Effect of water-oil contact on areal coverage in Zone 3, Zone 3B, Zone 4, and Zone 5 (Abo)..... | 275 |
| 25. Effect of water-oil contacts on OOIP estimate..... | 276 |
| 26. Effects of porosity cutoffs of 3%, 5% and 10%, and permeability cutoffs of 0.1, 0.5, and 1 mD on volumetrics..... | 276 |
| 27. Effects of cutoff values on OOIP estimate porosity, water saturation, and permeability..... | 277 |
| 28. Relationship between permeability and porosity cutoff values..... | 277 |
| 29. Effects of porosity cutoffs and grid vertical resolution on volumetrics, 3%, 5%, and 10% on fine-grid model, and 3%, 5% and 10% on cycle-based model..... | 278 |
| 30. Effects of porosity cutoffs and grid vertical resolution on volumetrics, 0.1, 0.5, and 1.0 mD on fine-grid model, and 0.1, 0.5, and 1.0 mD on cycle-based model..... | 279 |
| 31. Changes in OOIP between high-resolution and cycle-based models with respect to porosity cutoff, water saturation cutoff, and permeability cutoff values..... | 279 |

| | |
|---|-----|
| 32. Production data and trends in primary and waterflooding | 280 |
| 33. Initial 3:1 line-drive waterflooding pattern | 280 |
| 34. Porosity and $S_o\phi$ in Zone 2, Wichita, and Zone 3, overlaid with production trends..... | 281 |
| 35. Water-injection patterns in the initial reservoir model area in 2001 | 281 |
| 36. Production data and trends in primary and waterflooding in simulation area..... | 282 |
| 37. Lawyer Canyon cycle 1 flow-layer model | 283 |
| 38. Average porosity for various rock fabrics in sequences L2.1 and L2.2 | 284 |
| 39. Flow layers and cycles in sequence L2.1 | 285 |
| 40. Flow layers in sequence L2.2 | 286 |
| 41. Flow layers in the Wichita..... | 287 |
| 42. Lower Clear Fork and Wichita flow layers in cored wells of simulation area illustrating the use of porosity to build a flow model..... | 288 |
| 43. Porosity distribution in the simulation area..... | 288 |
| 44. Permeability distribution in the simulation area..... | 289 |
| 45. Water saturation distribution in the simulation area..... | 289 |
| 46. Porosity and $S_o\phi$ trends in the simulation area..... | 290 |
| 47. Porosity distribution in simulation model | 290 |
| 48. Initial oil saturation in simulation model..... | 291 |
| 49. Simulated oil saturation in 1960, 1970, 1980, and 2002, simulation area | 291 |
| 50. Simulated oil saturation in 2002, in Zone 1 | 292 |
| 51. Simulated oil saturation in 2002, in selected model layer slices of the Lower Clear Fork HFS L2.1 (reservoir Zone 2)..... | 292 |
| 52. Simulated oil saturation in 2002, in upper model layers of the Wichita | 293 |
| 53. Simulated oil saturation in 2002, in model layers of Wichita reservoir Zone 3B | 293 |
| 54. Corey correlations for relative permeability..... | 293 |
| 55. Effect of relative permeability on simulated oil rate, water rate, pressure, and oil recovery | 294 |
| 56. Effect of permeability multiplication on simulated water production..... | 294 |

Reservoir Modeling and Simulation of Fullerton Clear Fork Field, Andrews County, Texas

Fred Wang and F. Jerry Lucia

ABSTRACT

Fullerton Clear Fork field in Andrews County, West Texas, discovered in 1942, produces from lower Clear Fork, Wichita and Abo carbonates. The reservoir consists of tidal-flat to subtidal dolomite and limestone. The field was unitized in 1953, and waterflood began in 1960. Production peaked in 1986 at 15,000 bopd and declined sharply to 6,000 bopd in 2001 (fig. 1). Cumulative oil production from the field had reached 289 million barrels (MMbbl) as of July 2004.

3-D reservoir modeling and simulation studies were carried out in an integrated geologic, petrophysical, and geophysical study to address various issues on data, production, modeling, and simulation. Two 3-D reservoir models, a 2,000-acre window model, and a full-field model were built using a cycle-based geologic framework and rock-fabric-dependent petrophysical properties. Reservoir simulation was performed in a 1,600-acre area in a small-window model. A comprehensive sensitivity study on volumetrics was conducted using the full-field model.

Fullerton Clear Fork field is a highly heterogeneous reservoir with complex lithology and porosity controlled by diagenetic overprints. Porosity is better developed in the mud-dominated inner-ramp Wichita Formation than in the subtidal Lower Clear Fork Formation. Although ϕ_h is higher in the Wichita, k_h is greater in the Lower Clear Fork because of differing rock fabrics.

The simulation study was divided into two phases: (1) sensitivity analysis and (2) history matching. From the sensitivity study we could rank importance of reservoir parameters affecting production performance. In simulation, oil relative permeability for primary recovery has a strong effect on recovery from waterflooding. Because fractures and breccias are common in testing and core data, negative skin factors (or effective well-bore radii) were used to simulate near-well-bore fractures, and permeability values in the Lower Wichita were modified to simulate karst-related breccias. Through history matching, optimal fluid and rock properties were determined.

INTRODUCTION

Fullerton Clear Fork field in Andrews County, West Texas, discovered in 1942, produces 42° API crude from Lower Clear Fork and Wichita carbonates (table 1). The reservoir consists of tidal-flat to subtidal dolomite and limestone (see Ruppel and Jones, this volume, for a detailed description of the geology and mineralogy of the field). The field was unitized in 1953, and waterflood began in 1960. Production peaked in 1986 at 15,000 bopd and declined sharply to 6,000 bopd in 2001 (fig. 1). Cumulative oil production from the field had reached 289 million barrels (MMbbl) as of July 2004.

This report describes data and methodologies used in constructing geologic and flow models. Issues on geologic framework, petrophysical properties, water-oil contact, volumetrics, and upscaling are discussed. The objectives of 3-D modeling are to detect discrepancies among geologic, petrophysical, and engineering data; to build geologically realistic reservoir models; to establish criteria for volumetric estimations; to explore techniques of upscaling; to identify critical issues and parameters controlling production and injection fluid flow; and to develop strategies for reservoir management and

production enhancement. 3-D modeling is, therefore, an iterative process (fig. 2), which integrates geologic, petrophysical, and geophysical and engineering data and improves consistencies among these data.

3-D RESERVOIR MODELING

Geological, petrophysical, geophysical, and engineering data were used to build 3-D geologic and flow models. Two models were built for the field. The first encompasses an area of about 2,000 acres in the north-central part of the field (fig. 3a). This area, sometimes referred to as the Phase-I Study Area, was selected for initial detailed, integrated, geologic, petrophysical, and engineering characterization of the field because it includes the highest density of cores and best suites of wireline logs in the field. The second model includes the entire Fullerton Clear Fork Unit (fig. 3a). For both models, RMS software from Roxar and Gocad software from Earthscience Division were used for model construction. The 2,000-acre model includes 140 wells, whereas the full-field model includes a total of 730 wells out of the 1,250 wells in the unit.

Stratigraphic Modeling

Oil has been recovered from three formations—Lower Clear Fork, Wichita, and Abo. Core and outcrop data (see Ruppel and Jones, this report) show that the depositional setting changed from prograding subtidal during Abo deposition to aggradational peritidal during the Wichita deposition then to aggradation to progradation subtidal during Lower Clear Fork deposition. Ruppel and Jones (this report) discussed depositional and diagenetic history of the field, the controls over porosity development, and the methods used to construct the reservoir framework in detail.

The geologic framework used in the construction of the two 3-D models differed only slightly. For the initial 2,000-acre model, three high-frequency cycles (table 2) were defined and used to subdivide the Lower Clear Fork HFS 2.1 (Zone 1) reservoir section. Later, during full-field characterization, it was found that this part of the section was better characterized as having eight high-frequency cycles.

The full-field 3-D model was constructed using 36 stratigraphic horizons (table 2) and wireline-log data from 730 wells using good-quality data (fig. 3a). The horizons were correlated and mapped on the basis of well picks guided by the conceptual geological model and seismic data. Twenty-five high-frequency cycle tops (table 2) were identified in cores and correlated using wireline logs from the Lower Clear Fork (Zone 1) to the top of the Abo. Cycle tops were ultimately picked and correlated in a total of about 1,000 wells to improve layer interpolation and limit model boundary effects. Only 730 wells, however, were actually used to distribute petrophysical data.

From outcrop and seismic data, the Abo is recognized to be a west-east-prograding outer-ramp succession (Ruppel and Jones, this report). However, because only scattered core data are available and limited deep wells were drilled to the Abo Formation, detailed core and log correlations necessary to accurately model the true architecture of the Abo are unavailable. Instead, 11 horizons (table 2) were arbitrarily defined on the basis of the probable geological architecture of the Abo (according to outcrop and seismic data), mapped, and were then used to create a conceptual prograding-wedge model. Figure 2b shows 9 of the 11 horizons used to build the Abo unit.

Two 3-D-model software packages (RMS from ROXAR and GOCAD from Earthscience Division) were used to build the full-field geological model. Petrophysical properties of porosity, permeability, and initial water saturation were derived from wireline-log data for 730 selected wells. These data were converted from the standard LAS format into RMS well format to load into both packages. Two 3-D models, a high-resolution fine-grid model and a cycle-based model were built. The models contained grid cells of 242 (150 ft) in x direction, 432 (150 ft) in y direction, and 380 layers in fine-grid model and 35 layers in cycle-based model. Total numbers of cell in the full-field models are about 42 millions in the fine-grid model and 3.7 millions in the cycle-based model (table 3). The reservoir architecture built into the 3-D model (fig. 3c) shows prograding wedges in the Abo unit.

Upscaling

One of the most important and controversial issues in 3D petrophysical modeling is upscaling. Upscaling occurs in several levels during 3D modeling such as upscaling wireline log data to high-resolution grid and upscaling high-resolution grid into coarse grid for seismic-data guided modeling and reservoir simulation. Because upscaling has significant effects on volumetric estimates and permeability, the vertical resolution of 3D model and the method used for permeability scaleup need to be decided before petrophysical modeling.

Because the assumption of random distribution in porosity and permeability is only valid for limited reservoirs and geologic scales, meaning and utility of statistical averages can be confusing and sometimes misleading. This can be illustrated by the permeability average in vertical direction. Permeability average in vertical direction is

normally calculated by arithmetic average, geometric average and $k\text{-}\phi$ correlations. Because differences in these averages can be significant, especially when models are used for reservoir simulation, we conducted a detailed study on permeability upscaling using five two-layer models with seventy cases. The detailed petrophysical properties of two layer models and results are discussed in Appendix A.

Table A.1 lists the parameters used in fourteen cases of a two-layer model (figure A.1), layer 1 is a 2-ft layer with porosity (20%) and permeability (70.06 mD), and layer 2 is a 5-ft layer with varying porosities and permeabilities. According the theory of fluid flow through porous media, average permeability of these models are the arithmetic means. Results in table A.2 and fig. A.2 show that geometric means tend to underestimate average permeabilities, and difference between arithmetic mean and geometric mean increases with the permeability contrast between the two layers. This difference can be in an order of magnitude or higher in highly heterogeneous, stratified systems. Note that permeabilities in stratified systems do not follow $k\text{-}\phi$ correlations derived from core data. Permeabilities in most 3D models with vertical scales greater than scales of log and core data are commonly controlled by large-scale features such as stratifications, stacking patterns, permeability contrasts among strata, fractures, *etc.*, and are much higher than those calculated from geometric mean and $k\text{-}\phi$ correlations.

Petrophysical Modeling

Petrophysical properties of rock fabric, porosity, permeability, and water saturation from 730 selected wells were calculated (Kane, this report; Lucia and Kane, this report) and loaded into ROXAR and Gocad. Petrophysical properties were first upscaled to grid resolution of 3-D models and mapped using the inverse-distance

technique with search radii of 2,500 and 5,000 ft. Figure 4 shows porosity distributions in two layers, with search radii of 2,500 and 5,000 ft. Because in the west and south parts of the unit (circled areas in fig. 4) most wells are old with poor log quality, spacing of wells selected is sparse, and a search radius of 2,500 ft leaves many areas unmapped, we widened the search radius to 5,000 ft to increase mapping coverage.

Porosity Distribution

Porosity and ϕh distributions in Fullerton Clear Fork field (figs. 5, 6 and 7) are a complex function of facies, rock fabric, lithology, and diagenesis overprints. Figures 5 through 10 suggest that this reservoir is highly heterogeneous, both laterally and vertically. Porosity patterns and flow barriers can be recognized by cycle, zone, and area. The unit is conventionally divided into north- and south-dome areas and the north dome can be further divided into east and west sub-regions. Overall, porosity is best developed in the Lower Clear Fork (ExxonMobil Zone 2) and in the Wichita (ExxonMobil Zones Wichita [W] and 3B).

Figures 6a and 8 show that porosity in Zone 1 (Lower Clear Fork 1 2.2), a grain-rich subtidal interval, is higher in the south dome area than the north dome. In the north dome, porosity is better developed in two areas, a NW-SE-trending belt in the middle of the field and a narrow NS belt farther west (shown in fig. 8) in cycles L2220 to L2260. Porosity in Zone 1 is normally less than 10 percent.

Zone 2 reservoir (Lower Clear Fork HFS 2.1) is a grain-dominated subtidal unit. Porosity in Zone 2 (figs. 6b and 9) is higher than that in Zone 1. In the north dome, porosity is best developed in a NW-SE trend (outlined area), mostly in L2105 to 2140 cycles. Reservoir quality sharply decreases away from this high-porosity trend, and Zone-

2 porosity in most of the west part of the field is very low. Zone 2 is separated from Zone 1 by laterally extensive, low-permeability, tidal-flat cycles at the base of Zone 1 and the top of Zone 2 (between L2220 and L2150 in Figs. 8 and 9). No such continuous flow barriers exist between Zone 2 and the Wichita zone.

The Wichita at the Fullerton Clear Fork Unit (FCU), includes four operator-named zones: Wichita (Zone W), Zone 3, Zone 3B, and Zone 4. Essentially all of these rocks are mud-dominated, inner-ramp, tidal-flat facies. Generally speaking, porosity in the Wichita Zone-uppermost Wichita Formation (fig. 6) is significantly higher than that in Zone 1 (Lower Clear Fork HFS 2.2) and slightly higher than porosity in Zone 2 (Lower Clear Fork HFS 2.1). As shown in figure 10, porosity distributions in W1 and W2 cycles are similar to that in Zone 2. It is best developed in the east half of the north dome and decreases sharply to the south and west. Porosity is much more widely scattered in W4 and W5 cycles. W4 is generally a low-porosity interval over most of the north dome area. Porosity is generally high and evenly distributed in intervals W8 to W11 (Zone 3B). In the north part of the north dome, the Wichita Formation can be separated into two reservoir intervals (W1 to W3 and W8 to W12) by the tight W4 and W5 cycles. In the south half of the north dome, however, this barrier vanishes because W4 and W5 are much more porous.

Permeability (k) and kh Distribution

Lucia (1985) has shown that permeability, for a given porosity, can be an order of magnitude higher for a carbonate grainstone (Class I) than that for a mud-dominated rock (Class III). Therefore, permeability values are significantly lower in the mud-dominated, inner-ramp Wichita Formation than those in the Lower Clear Fork (fig. 11). Permeability

values were calculated from porosity and rock fabric (see Kane, this report; Lucia and others, this report, respectively, for details) and upscaled vertically to resolutions of the 3-D model using the arithmetic averaging technique before being mapped into 3-D space.

Figures 12 and 13 show permeability and kh distributions in operator reservoir Zones 1, 2, Wichita, 3, 3B, and 4. Because permeability and kh are better displayed in a logarithmic scale, special procedures were taken for generating these averaged permeability and kh maps in logarithmic scale. Permeability and kh in the fine-grid model were upscaled to a seven-layer zone model using arithmetic mean. Permeability and kh maps were generated on the logarithmic values of upscaled permeability and kh.

Average permeability and kh (figs. 12 and 13) in the Fullerton reservoir are significantly higher in the Lower Clear Fork Formation (reservoir Zones 1 and 2) than in the Wichita Formation (Zones Wichita, 3, 3B, and 4). With highest permeability and kh, Zone 2 (Lower Clear Fork HFS 2.1) has the highest waterflood recovery efficiency.

Anomalous water production has been reported from the Wichita. Although not predicted or explained by matrix porosity or permeability data, these observations may be due to the presence of zones of karst brecciation in the Wichita. Breccias and related fractures have been reported from reservoir Zones 3 and 3B in several cores in the field (see Ruppel and Jones, this report) and may be the cause of nonmatrix flow.

Alternatively, anomalous water production may be associated with fractures induced by high-pressure water injection, a common problem in high-porosity, low-permeability reservoir zones like the Wichita.

S_w and S_oφh Distribution

One of the petrophysical problems in FCU is that the resistivity log response to grain-dominated rock fabrics in Zone 1 (Lower Clear Fork HFS 2.2) and in the Abo are higher than expected, according to Archie equation calculations. As a result, water saturations derived from resistivity logs are very low. In other words, oil saturations derived from resistivity log data are too high for low-porosity rocks. Water saturation values derived from capillary-pressure data (Lucia and others, this report) are generally much higher than those derived from resistivity data (fig. 14). These observations suggest that water-saturation estimates from the Archie equation are not reliable when porosity is less than 5 percent. Figure 15 shows water-saturation distribution in the full-field 3-D model.

Figures 16 and 17 show water saturation and S_oφh distributions by reservoir zones. These plots reveal that the greatest volume (39 percent) of original-oil-saturated pore volume is in Lower Clear Fork HFS 2.1 (reservoir Zone 2). Although not apparent from figure 18, the Lower Clear Fork HFS 2.2 (reservoir Zone 1) is the second-richest oil reservoir zone in the field (among four Wichita reservoir zones), with 18 percent of the oil, and the Wichita with 42 percent of the oil.

Figures 19 through 21 show S_oφh distribution by cycle. Although 18 percent of the original oil in place (OOIP) was in Zone 1 (Lower Clear Fork HFS 2 L 2.2), it is not apparent in S_oφh maps, and most of the oil is in the south dome. Instead, highest hydrocarbon pore volumes are found in porosity belts in L2140, L2130, L2120, L2110, L2105, W1, and W5 cycles.

VOLUMETRICS

One of the purposes of 3-D geologic models is to provide an accurate and flexible way for making original-oil-in-place (OOIP) estimates. OOIP is calculated from 3-D models by

$$V_o = 0.1781B_o \sum_{k=1}^{kk} \sum_{j=1}^{jj} \sum_{i=1}^{ii} A_{ijk} h_{ijk} \phi_{ijk} (1 - S_{w,ijk}) pay_{ijk} \quad (1)$$

where

- V_o : original oil in place (BSTB)
- B_o : formation volume factor (bbl/STB)
- A_{ijk} : area (ft²)
- h_{ijk} : thickness (ft)
- ϕ_{ijk} : porosity (fraction)
- $S_{w,ijk}$: water saturation (fraction)
- pay_{ijk} : pay flag, 0 or 1

Figure 22 shows two types of oil with formation volume factors of 1.615 and 1.36 documented in the reservoir (Exxon Field Study Group, 1973). The second type of oil was found in the Lower Wichita in the north dome area. Because areal and vertical coverage of the second oil type is not clearly determined and thought to be relatively small, a formation volume factor of 1.6 (table 4) was used in this study for the entire reservoir.

In Equation 1, the pay flag is determined by cutoff values. Major sources of error in volumetric estimations are wireline-log data (porosity and water saturation),

limitations of petrophysical models, water-oil contact, mapping parameters, and vertical resolution of 3D models.

Sensitivity Analysis

Cutoff values are used to reduce errors in wireline logs, to reduce uncertainties in petrophysical equations at low porosity intervals, to eliminate high water-bearing intervals, and to remove non-reservoir-quality rocks from averaging petrophysical properties such as permeability, water saturation, etc.

For mature hydrocarbon fields such as Fullerton Clear Fork field, many wells were drilled before the arrival of modern porosity and resistivity tools. Accordingly, accurate modern porosity logs are of limited availability, and OOIP estimates can thus vary significantly. A sensitivity analysis was performed to determine the most likely range of OOIP of Fullerton Clear Fork field and unit. Parameters studied include

- (1) search radius in mapping,
- (2) grid vertical resolution,
- (3) water-oil contact,
- (4) porosity,
- (5) water saturation, and
- (6) permeability.

Search Radius in Mapping

As discussed in the petrophysical property section, search radius affects OOIP estimates by controlling the smoothness and coverage of petrophysical properties. In areas with close well spacing, a small search radius will not leave significant acreages unmapped (fig. 4). On the other hand, in areas or intervals with wide spacings and, thus,

high uncertainties, large search radii will overestimate OOIP. As shown in table 5, increasing the search radius from 2,500 to 5,000 ft resulted in 5- to 15-percent increases in OOIP. The largest (15 percent) increase in OOIP was in the Abo, where well control is scarce. With high uncertainties in the Abo, a search radius of 2,500 ft could reduce the risk of making too-optimistic predictions.

Grid Resolution

The vertical resolution of the 3-D model also has a significant impact on OOIP estimates. The optimal vertical resolution of the 3-D model needs to be determined as the coarsest resolution of the 3-D model with the least effect on OOIP estimate. We tested the effect of vertical resolution of 3-D models on OOIP using a zone-based model, a cycle-based model, and a 380-layer, fine-grid model. The calculated OOIP values are 1.19, 1.405, and 1.582 BSTB for zone-base, coarse-grid cycle-base, and fine-grid cycle-base models, respectively. The 20-percent difference in OOIP suggests that fine-grid models are necessary for OOIP calculations.

Water-Oil Contact

Similar to those for Zone 1 Lower Clear Fork HFS 2.2, resistivity values in the Abo are consistently high. This high resistivity is caused by the low water salinity. These high resistivity values, in turn, result in calculations of lower initial water saturations than are estimated from capillary-pressure data. They also make it difficult to determine true water-oil contact (WOC) from wireline-log data. Accordingly, four water-oil contacts (-3,940, -4,000, -4,050, and -4,100 ft) were tested to study the effect of WOC on OOIP. The -3,940 ft WOC is the shallowest reported in previous studies (by the operator). A WOC of -4,100 ft was used in this study to estimate original water saturation from

capillary curves. This value is supported by core saturation data in a downdip core in the field (Amoco FM-1). OOIP values (total pore volume) range from 1.582 BSTB for the WOC case at -3,940 ft to 1.917 BSTB for the WOC case at -4,100 ft (tables 6).

Figures 23 and 24 show vertical and area coverages of Wichita Zones 3B and 4 and the Abo (Zone 5). In the case of the WOC at -4,100 ft, the Abo (Zone 5) is included in the hydrocarbon volume calculations. A WOC of -3,940 ft reduces hydrocarbon volumes about 13 percent in Zone 3B and 46 percent in Zone 4 and eliminates almost all oil in the Abo (figs. 23 through 25). The main difference in OOIP among these cases is OOIP in the Abo unit. With a WOC at -4,100 ft, estimated OOIP in the Abo is 236 MMSTB. Because wells completed in the Abo unit are limited and the salinity of formation water in Abo is much lower than that in lower Clear Fork and Wichita, porosity and water saturation cannot be properly estimated as well as mapped, and uncertainty in this OOIP estimate in Abo is thus high.

Porosity Cutoffs

Four porosity cutoff values were studied: 3, 5, 7, and 10 percent. Fig. 26.a to c shows effects of porosity cutoffs of 3, 5 and 10 percent on volumetrics on 380-layer fine-grid and cycle-based models. Table 7 lists OOIP estimates in the unit and model areas for WOC at -3,940 and -4,100 ft. In unit and model areas at WOC of -3940 ft, detailed OOIP estimates by ExxonMobil zonations (tables 8 and 9) and by high-frequency cycles (tables 10 and 11) are also listed. In figure 27a, OOIP is plotted against the porosity cutoff value. The OOIP value decreases gradually with porosity cutoff values from 0 to 5%, and the rate of decrease increases sharply when the porosity cutoff value is greater than 5%.

It is important to understand that the porosity cutoff value should vary with rock fabric. For a specific porosity value, water saturation is lower in grain-dominated fabrics than in mud-dominated fabrics. Therefore, porosity cutoff values for the Lower Clear Fork should be lower than that for the Wichita. Instead of using porosity, water saturation and permeability can be used to resolve this rock-fabric-dependent issue.

Water Saturation Cutoffs

Water saturation is another commonly used parameter for cutoff in OOIP estimates. The purposes of water saturation cutoff are to remove errors and uncertainties in porosity, resistivity, and water saturation models in low-porosity intervals and to remove nonproductive, high-water-saturation transition-zone intervals. OOIP estimates for WOC at -3,940 and -4,100 ft in the unit and model areas are listed in tables 7-11. Results for the unit with a WOC at -3,940 ft are plotted in figure 27b. OOIP values increase with water saturation cutoff from 0.84 BSTB at 50 percent to 1.4 BSTB. OOIP value is pessimistically reduced when a 50-percent water saturation cutoff is used. Although intervals with less than 50-percent oil saturation can be considered nonproductive for waterflooding, oil in these intervals is part of the OOIP. The trade-off is that the recovery factor increases with decreasing OOIP.

Permeability Cutoffs

Three permeability cutoff values were calculated: 0.1, 0.5, and 1 mD. As shown in figure 28, the equivalent porosity cutoff values for Classes I, II, and III rocks are 0.055, 0.07, and 0.09, when 0.1-mD permeability is used; 0.065, 0.09, and 0.12, when 0.5 mD permeability is used; and 0.07, 0.10, and 0.14, when 1.0 mD permeability is used. Permeability cutoffs provide an easy way to determine rock-fabric-dependent porosity

cutoff values. This is clearly shown in figure 26.c with 10% porosity cutoff and figure 26.f with 1-mD permeability cutoff. Most of the low-porosity, high-permeability Zone 1 excluded by 10% porosity cutoff (fig. 26.c) is kept by 1-mD permeability cutoff (fig. 26.f), and vice versa for the high-porosity, low-permeability Wichita.

OOIP values for the entire Fullerton Clear Fork Unit at a WOC of –3,940 ft are 1.537, 1.342, and 1.139 billion barrels (Bbbl) for 0.1, 0.5, and 1.0 mD permeability cutoff values (table 7). Detailed OOIP estimates by ExxonMobil zonations and high-frequency cycles are listed in tables 8-11. Figure 27c shows that OOIP estimates decrease with permeability cutoff value linearly. The selection of permeability cutoff value is field-specific, depending on rock and fluid properties and operation considerations.

Compound Effects of Vertical Resolution and Cutoff Values

Discussed in the section of grid resolution, when no cutoff was applied the OOIP estimate decreases from 1.582 BSTB in the 380-layer high-resolution model to 1.405 BSTB in the cycle-based model. Since petrophysical properties are smoothed with the increase of vertical resolution of 3D grid, effects of cutoff values on OOIP are expected to vary significantly with the vertical resolution. This hypothesis is studied in details using a simple ten-layer model. Shown in figure A.3, this 10-layer model was upscaled into a two-layer flowunit model, and subsequently into a single-layer model. Fig. A.4 reveals that at 5% porosity cutoff volumetric estimate from the single-layer model is higher than the 10-layer model, and volumetric estimate is lowest from two-layer model. This simple example shows that the compound effects of grid vertical resolution and cutoffs on OOIP are complex and unpredictable. Hence, the same cutoff values used for the high-resolution model were performed on a coarser cycle-based model (table 3).

Figures 29 and 30 show changes in porosity and permeability coverages at Row 350 in fine-grid and cycle-based models with cutoffs. Most thin porosity and permeability layers in the fine-grid model are either excluded or averaged into thicker layers. Table 12 compares OOIP values calculated from high-resolution fine-grid and cycle-based model for porosity cutoffs from 0.0 to 10%, water saturation cutoffs from 50% to 100% and permeability cutoffs from 0 to 1 mD. The percent change in OOIP (5th column in table 12) was calculated by the difference in OOIP between high-resolution and cycle-based model divided by the OOIP from the high-resolution model. In figure 31, percent changes in OOIP are plotted with respect to porosity, water saturation and permeability cutoffs. The effect of vertical resolution on OOIP varies significantly with the cutoff criteria. Changes in OOIP between two models increase from 11 to 30 percent with the increase in porosity cutoff from 0 to 0.1 and with the decrease in water saturation cutoff from 100 to 50% but decrease slightly from 11 to 8% with the increase in permeability cutoff from 0.1 to 1 mD. The change in OOIP is highly sensitive to porosity and water saturation cutoffs but not sensitive to the permeability cutoff because arithmetic-mean permeabilities in stratified reservoirs are higher than those calculated from k - ϕ correlations and not very sensitive to grid vertical resolution (discussed in Appendix A). This special advantage in stability makes permeability a better cutoff parameter than porosity and water saturation.

Among parameters studied, vertical grid resolution and WOC have much greater effects on OOIP than search radius and areal coverage (table 13), and high-resolution models should be use for volumetric calculations.

PRODUCTION-TREND ANALYSIS

3-D modeling is an iterative process involving analyses of geology, geophysics, petrophysics, production data, and volumetrics calculations (fig. 2). Problems with geological or structural interpretations are normally detected during the construction of static models. Problems in petrophysical properties in well logs and static models can be identified using production data, production trends, and volumetrics.

Primary- and waterflood-recovery data are shown as bubbles in figure 32. During primary recovery, production from the north-dome area (outlined by three ellipsoids) was significantly higher than in other parts of the field and was generally highest along a NNW-SSE trend (fig. 32a).

Oil recovery from waterflooding has been complicated by the use of widely varying injection patterns through time and episodes of infill drilling. Waterflood operations have been dominated by an early 3:1 line-drive pattern (fig. 32). Oil recovery from such a pattern is expected to be higher at wells in the middle row (red circles in fig. 33) than wells in the other two rows that are closer to injectors (green circles in fig. 33). Four 3:1 line-drive patterns (colored boxes in fig. 32b) were created in the north-dome area during the initial phase of waterflooding (fig. 32b). The expected higher recovery from the middle row of producers was observed in the three 3:1 line-drive patterns in the east (outlined by the orange, green, and purple boxes in fig. 32b), but not in the pattern in the west (outlined by the blue box in fig. 32b).

Figure 34 shows the porosity and $S_o\phi_h$ maps in Zone 2, Wichita, and Zone 3 overlaid with production trends. The high-production areas during primary and waterflooding coincide well with the high porosity and $S_o\phi_h$ trends. Best productions

from the nose- area stem from the fact that it has highest $S_{o\phi h}$ values in all three zones. The drastic changes in petrophysical properties to the west have complicated recovery from patterned waterflooding (blue-colored polygon in fig. 34). The waterflooding recovery in this area decreases to the west.

FLOW-UNIT MODEL AND RESERVOIR SIMULATION

To develop an early understanding of the geology and petrophysics, a 2,000-acre area (fig. 35), containing the highest density of cores and best suites of wireline logs, was selected for detailed, integrated, geologic, petrophysical, and simulation study. After more than forty year waterflooding and extensive infill drillings, the area is currently under complex waterflooding patterns with 10 to 20-ac spacing (fig. 35). Reservoir simulation was performed on a 1600-ac area (red outlined box in fig. 35). Bubble maps of primary and waterflooding recoveries (fig. 36) shows that oil production from the east has been significantly higher than the west area. Because study in this reservoir simulation area was performed in the initial phase of the project, geologic framework, petrophysical models and methods used in 3D modeling were slightly different from those used in full-field models, and results of this study are only briefly discussed here.

Flow-unit Model

Distributing petrophysical properties within a geologic model is one of the most difficult tasks in building a simulation model. In this study, as well as in other reservoir studies done at the Bureau of Economic Geology, the basic geological framework within which the properties are distributed is the high-frequency cycle (HFC). Outcrop studies, however, have shown a systematic layering of petrophysical properties within the HFC related to the vertical succession of rock fabrics (Kerans and others, 1994, Lucia and

others, 1995). HFC's tend to show an upward increase in carbonate grains resulting in an ideal vertical succession from mud-dominated fabrics (mudstone, wackestone, mud-dominated packstone) to grain-dominated packstone and grainstone. Each fabric tends to form a geologic bed, and each fabric has a specific porosity-permeability transform. Therefore, each rock-fabric bed should be defined as a layer within the HFC. If this condition is not satisfied low permeability layers will be averaged with high permeability layers and the basic heterogeneity of the system will be compromised.

Values for porosity, permeability, and initial water saturation are calculated from wireline logs and provide the basic data used to populate the geologic model. There are numerous statistical methods for filling the interwell space with the calculated properties. Whatever method is used it must be constrained by the rock-fabric flow layers in order to preserve the petrophysical heterogeneity. The rock-fabric approach to distributing petrophysical properties is illustrated by outcrop results (fig. 37) (Lucia and others, 1992, Lucia, 1999). At Lawyer Canyon, Guadalupe Mountains, New Mexico, a single HFC has been mapped for 2700 ft along an outcrop and about 2000 permeability measurements made. Statistical analysis of the permeability data shows 1) a significant difference between the average permeability in the upper grainstone and the lower mud-dominated fabrics and 2) little or no spatial correlation of the permeability values within a rock-fabric layer, in this case the grainstone layer (Jennings and others, 2000). The implications are that only rock-fabric layers can be correlated between wells, not petrophysical properties, and that petrophysical properties should be statistically distributed within rock-fabric layers, not within HFC's.

In this study the HFC's are correlated using porosity logs calibrated to core descriptions (Ruppel and Jones, this volume). Cycles within the Lower Clear Fork sequences L2.2 and L2.1 are defined by an upward increase in graininess. Wichita cycles are composed of mud-dominated fabrics and are typically capped by tidal-flat fabrics. The cycles are typically dolostone but limestone may be present at the cycle base (Ruppel and Jones, this volume).

The grainy top of the Lower Clear Fork HFC's tend to be more porous than the muddy base, which is true for both limestones and dolostones. As pointed out by Ruppel and Jones in this volume, much of the core-log calibration was done by comparing core descriptions with porosity logs. The calibration can also be done by comparing thin section descriptions with porosity measurements when the thin sections are taken directly from the core plugs. An analysis of rock fabrics and porosity using data from sequences L2.2 and L2.1 (fig. 38) shows that, for dolostones, grain-dominated packstones average 11.5% porosity, mud-dominated packstones 9.4%, and wackestones and mudstones 4.9%. For limestones, grainstones average 14.9% porosity, grain-dominated packstones 8.2%, mud-dominated packstones 7.6%, and wackestone and mudstones 7.0%. Although there is significant overlap in the porosity ranges, there is a clear increase in porosity with increasing graininess in the dolostones. In the limestones the grainstones (moldic grainstones) are clearly more porous than other fabrics. The lime grain-dominated packstones have an average porosity similar to the mud-dominated fabrics. This result may be related to difficulties in distinguishing between grain- and mud-dominated fabrics. The distinction often becomes a matter of judgment by the observer as to whether or not the inter-grain volume is completely or partially filled with mud.

For simplicity, the HFC's are divided into two rock-fabric flow layers, a lower low porosity layer and an upper high porosity layer. In the Lower Clear Fork sequences L2.1 and L2.2, the porosity changes are used as a surrogate for a lower mud-dominated fabric and an upper grain-dominated fabric. Because there is considerable overlap of porosity values for each fabric, a single porosity value can not be used to separate rock fabrics. Instead, the vertical porosity profile must be used and a judgment made as to where a significant change in rock fabric is likely to occur. Seven HFC are defined in sequence L2.1 each with two flow layers except for cycle 2105, which did not appear to have a low to high porosity profile in the simulation area (fig. 39). The cycle types correlate quite well with porosity, grain-dominated fabrics, and tidal flat facies but not with lithology. In most cycles the distinction between low porosity and high porosity is quite clear. The upper two cycles are class 3 fine crystalline dolostones and the porosity is too low to be productive. Three HFC's were originally defined in sequence L2.2 and are illustrated in figure 40. The cycles were defined based on limestone upward-shoaling successions found in the core from well 6122, and were difficult to pick in the dolostone wells because of low porosity values. As such, the flow layers in this sequence are somewhat arbitrary. Sequence L2.2 was later divided into eight HFC based on core descriptions outside of the simulation area (see Ruppel and Jones, this volume). The simulation model has six flow layers whereas the full field model has eight HFC. There is an imperfect match between the flow layers in the simulation model and the new HFC's (fig. 40). There has been no attempt to integrate the eight HFC into the simulation model.

In the Wichita there is no clear relationship between fabric and porosity because the cycles are typically composed of mud-dominated fabrics, either limestone or

dolostone. The limestones, however, have less than 3 percent porosity and are typically found at the base of the cycles that have porous dolostone tops. Many cycles have no limestone, however, and the upper intervals are more porous than the lower intervals. Ten HFC's were picked in the Wichita each with two flow layers (fig. 41). The upper cycles from W1-W5 typically have thin limestones at the base and are easily correlated throughout the simulation area. No cycles were picked between cycle W5 and W8 because the interval is composed of limestone and dolostone, typically has less the 10 percent porosity, and therefore is nonproductive. Cycles W8-W12 are based solely on the porosity profiles and have little relationship to tidal-flat capped cycles or lithology. Therefore, these cycles and flow layers are the most arbitrary of all the layers in the simulation model.

The importance of the flow layers is to preserve layers of high and low permeability (fig. 42). The individual cycles, however, are characterized by a single transform. The Wichita is characterized by a class 3 transform because it is typically a lime wackestone or fine crystalline dolowackestone. The Lower Clear Fork L2.1 sequence is characterized by a class 2 transform in the lower interval and a class 3 transform in the upper interval. The Lower Clear Fork L2.2 sequence is characterized by a class 1 transform. Therefore, the permeability contrast between the upper and lower flow layers is related the difference in porosity, not the difference in rock fabric. A more accurate permeability contrast could be obtained if the different limestone fabrics could be distinguished.

Out of a total of 140 wells in the model area, 85 (fig. 35) were initially selected for detailed geologic and petrophysical characterization. However, early 3-D models

based on these 85 wells revealed that tops of flowunit mapped using only these wells did not match well tops at unselected wells and that there were significant boundary-effect problems at the model's edges. To correct these problems, all wells in the study area and a line of wells immediately outside the study area were subsequently correlated and included, thus affecting the model.

A fine-scale geological model containing 3.165 million cells (table 14) was then constructed for the area, and porosity (from Kane, this report) was mapped through the 3-D space (fig. 43). The layers average 2.2 ft, and the cells are 100 ft square. Permeability and water saturation (figs. 44 and 45) were calculated from porosity on the basis of correlations provided by Lucia and others (this report). Rock-fabric-dependent permeability-porosity relationships are shown in figure 28. The rock-fabric-based water-saturation-porosity relationships used in this 2,000-acre model were the generic relationships, not the new Thomeer model described by Lucia and Kane (this report).

Porosity and $S_o\phi h$ maps (fig. 46) show that reservoir quality is poor in Zone 1 except the northwest corner, is good in the central and southeastern areas in Zone 2 where primary recovery was higher, and increases to the south in Wichita. Careful examination of figures 43 and 44 shows that although ϕh in the model area is higher in the Wichita, kh is greater in the Lower Clear Fork. This is due to the very different rock fabrics in each. Note that oil saturation (fig. 45) is highest in the Lower Clear Fork, again owing to the presence of better quality rock fabrics in this part of the reservoir (see Lucia and Kane, this report).

Following construction of the fine-scale reservoir model, the model was scaled up to the flow-unit thickness for reservoir simulation. The flow-unit model contains 136,656

cells (73 by 48 by 39). Again, porosity was averaged arithmetically, and permeability and water saturation were calculated using correlations to porosity and rock fabric (figs. 47 and 48). In figure 47, the reservoir appears highly compartmentalized in both lateral and vertical directions, because only cells with porosity values greater than 6 percent are shown.

Flow Simulation

The simulation study was divided into two phases: (1) sensitivity analysis and (2) history matching. From the sensitivity study, it is possible to rank the importance of reservoir parameters affecting production performance.

Figure 49 displays simulated oil-saturation distributions in 1960, 1970, 1980, and 2002. Water injection was initiated in 1960. The blue areas in the 1960 image represent high gas saturation. As water injection progressed, water displaced oil from the injectors into these high-gas-saturation areas, as seen in 1970 and 1980 images.

Figure 50 shows simulated oil-saturation distributions in 2002 in two layers of the Lower Clear Fork HGS L2.2 (reservoir Zone 1). Because Zone 1 is a heterogeneous, locally low permeability interval, reservoir continuities between injectors and producers are poor, and sweep efficiency during waterflooding has been low.

The model shows that the Lower Clear Fork HFS L2.1 (reservoir Zone 2) contains the highest ϕ_h , k_h , and oil in place. The area of highest porosity trends through the east part of model area (fig. 50); however, reservoir continuity in this area is somewhat limited, as revealed by the presence of many small areas of very low oil saturation. Simulated oil-saturation distributions in 2002 at layers 11, 13, 15, and 17 (fig. 51) indicate that many areas have not been swept by water.

In the model area, porosity and reservoir continuity are best developed in Wichita cycles W1 to W3. Simulated oil-saturation distributions (fig. 52) in 2002 at layers 20 and 22 (upper flow units in W1 and W2) indicate that W1 and W2 have been fully swept except for the southeasternmost corner of the model area, where the W2 zone is not perforated in wells 1331, 1333, 1431, or 1433.

Wichita Formation reservoir Zone 3, which includes model layers W4 and W5, exhibits very low permeability in the model area. This low-permeability interval separates porosity and oil saturation in the uppermost Wichita (layers W1 and W2) from relatively high porosity, permeability, and oil saturation in Wichita Zone 3B.

Simulated oil-saturation distributions in year 2002 in model layers 30 and 32 (fig. 53) indicate that Wichita layers W8 and W9 (operator reservoir Zone 3B) have been well swept in areas where wells have been perforated. The southeasternmost corner of the model area, however, has not been flooded because many injectors (wells 1326, 1334, 1430, 1432, and 1434) have not been perforated.

Sensitivity Study

The reservoir flow model was used for history matching of production data of the simulation window (shown in fig. 35). History matching was complicated by (1) lack of reliable primary production data, (2) gas injection, (3) upscaling, (3) relative permeability, and (4) karst breccias and fractures.

Because permeabilities in the simulation model was calculated from k - ϕ correlation from porosity which could underestimate cell permeabilities significantly (discussed in Appendix A), permeability data was increased five to thirty folds during history matching. In addition, relative permeability and ratio of k_{vh} , two of the most

dominating factors affecting oil recovery from reservoir simulation, need to be optimized through history matching.

There are six relative permeabilities for gas, oil, and water phases in drainage and imbibition processes. This raises the question as to what the most critical relative permeability is. A good matching on primary recovery is essential for good matches on secondary and tertiary recoveries. A sensitivity study of oil relative permeability for primary recovery was performed by changing Corey's exponent of oil curve from 2 to 5. Fig. 54 shows that oil and water relative permeabilities decrease with the increase in Corey exponent. The bold curves are oil and water relative permeabilities suggested by ExxonMobil FCU team.

Figures 55a through d show effects of oil relative permeability data on matching oil rate, water rate, pressure and oil recovery. Note that oil permeability had no significant effects on oil and water production during primary recovery from 1942 through 1960 but strong effects on production and pressure data during waterflooding. The effect of oil permeability in primary recovery is on pressure rather than oil. Using oil relative permeability curves with Corey exponents of 2.2 and 3 oil production and pressure histories during waterflooding can be matched reasonably well, but water production history cannot. On the other hand, Using oil relative permeability curves with Corey exponents of 4 and 5, simulation runs match water production history during waterflooding but miss oil production and pressure histories significantly.

Because pressure test data measure pressures in connected pores and simulations calculate average pressures of all pores, simulated pressures should be higher than

measured field pressures. Measured field pressures can be corrected by the fraction of connected oil volume over total oil volume using

$$\Delta P = \Delta P_m \frac{V_{o_conn}}{V_o} = \Delta P_m \frac{V_{o_MB}}{V_o} \quad (2)$$

$$P_i - \bar{P} = (P_i - P_m) \frac{V_{o_MB}}{V_o} \quad (2a)$$

$$\bar{P} = P_i - (P_i - P_m) \frac{V_{o_MB}}{V_o} \quad (2b)$$

Where

ΔP : corrected pressure change, psi,

ΔP_m : measured pressure change, psi,

P_i : initial pressure, psia,

\bar{P} : average pressure, psia,

P_m : measured pressure, psia,

V_{o_conn} , V_{o_MB} : connected oil volume (bbl) from material balance,

V_o : total oil volume (bbl).

One of the difficulties in this simulation was to match water production and injection rates. Both water production and injection from the area were found to be significantly higher than those simulated on the basis of matrix permeability in the static model. Nonmatrix flow has been indicated by negative skin factors from -3 to -5 in well-testing data, anomalous water production, and breccias reported from reservoir Zones 3 and 3B in several cores in the field (see Ruppel and Jones, this report). In addition, near-well-bore fractures might have been induced by high-pressure water injection. Hence,

negative skin factors of -3 (or effective well-bore radii) were used to simulate near-well-bore fractures, and permeability values in the Lower Wichita were modified to simulate karst-related breccias. Two simulation runs were performed by increasing permeability values in the Lower Wichita (Zone 3B) by factors of 25 and 30. Figure 55 compares results of these simulations with cumulative water production of the area (crosses in figure 55). Without permeability modification, simulated water production (the black curve in fig. 55) is significantly lower than the field data (crosses). Two cases with increasing permeability values in Zone 3B by a factor of 25 (green curve) and 30 (purple curve) significantly improve the matches between simulated water productions to the field data. Both cases tend to overestimate water production during the early stage of waterflooding from 1960 through 1985.

Simulation results provide an important glimpse into reservoir response in West Texas Clear Fork carbonate reservoirs. Both techniques were used to construct model and results and can serve as a basis for improved modeling and simulation of other shallow-water carbonate-platform reservoirs.

SUMMARY

Fullerton Clear Fork field is a highly heterogeneous reservoir with complex lithology and porosity trends controlled by diagenetic overprints. Porosity is better developed in the mud-dominated inner-ramp Wichita Formation than the subtidal Lower Clear Fork Formation. Although ϕ_h is higher in the Wichita, hydrocarbon volume and k_h are greater in the Lower Clear Fork because of differing rock fabrics.

In Zone 1, reservoir continuity and quality are best in the south dome area and generally poor in the north dome, with scattered, local porosity developments. With the

highest hydrocarbon pore volume, and good ϕ_h and k_h , the high-porosity trends in Zone 2 in the Lower Clear Fork and Zone W in the Upper Wichita are the best units in Fullerton Clear Fork field. Reservoir quality decreases sharply away from these porosity trends.

Zone 3 (W4 and W5) is tight in the north half of the north dome and becomes porous in the south half of the north dome and the south dome. Zone 3B is a more homogeneous unit, with high porosity and continuity. However, karst-related breccias and fractures have complicated production and injection in Zone 3B.

Because OOIP and permeability distribution are functions of vertical resolution, high-resolution static model should be built as the base geological model.

For stratified reservoirs, arithmetic means rather than geometric means should be used in permeability scaling because it is based on the theory of single phase fluid flow through porous media. Geometric means tend to underestimate permeabilities by an order of magnitude or more in highly heterogeneous, stratified reservoirs.

Permeability values in large-scale stratified reservoirs are higher than those derived from permeability-porosity correlations from core data because permeability values in 3D models are controlled by large-scale features such as stratification, stacking patterns, permeability contrasts, fractures, *etc.*

Original oil in place (OOIP) is a complex function of log-data quality, mapping parameters, vertical resolution of the 3-D grid, water-oil contact, and cutoff values in porosity, permeability, and water saturation. Permeability and water saturation are equivalent to rock-fabric-dependent porosity cutoffs.

Using a simple 10-layer test model (in Appendix A), we showed that the compound effects of grid vertical resolution and cutoffs are complicated. Volumetrics from high-resolution models are more realistic but not always higher than that from coarse models.

High-vertical-resolution 3-D models should be used in volumetric calculation. OOIP estimate depends strongly on the selection of cutoff values. With WOC at $-3,940$ ft, the estimated OOIP is 1.58 BSTB without using any cutoff, 1.32 BSTB with a 5-percent porosity cutoff, 1.23 BSTB with a 0.5-mD permeability cutoff, and 1.32 BSTB with a 60-percent water saturation cutoff.

The 380-layer, high-resolution model, calculates higher OOIP than the 36-layer, cycle-based model by 8 to 30%, depending on cutoff criteria. Due to the unique nature of arithmetic mean in stratified reservoirs, permeability cutoffs are less sensitive to grid vertical resolution than porosity and water saturation cutoffs.

In simulation, oil relative permeability for primary recovery has a strong effect on recovery from waterflooding. Because pressure test data measure pressures among connected pores and simulated pressures calculate average pressures of all pores, simulated pressures should be higher than measured field pressures.

Because most high-permeability streaks were averaged out by upscaling, both oil and water relative permeabilities used in simulations were higher than those measured in the lab.

Because fractures and breccias are common in testing and core data, negative skin factors (or effective well-bore radii) were used to simulate near-well-bore fractures, and

permeability values in the Lower Wichita were modified to simulate karst-related breccias. Through history matching, optimal fluid and rock properties were determined.

Simulation results provide an important glimpse into reservoir response in West Texas Clear Fork carbonate reservoirs. Both the techniques used to construct the model and the results can serve as a basis for improved modeling and simulation of other shallow-water carbonate-platform reservoirs.

REFERENCES

- Exxon Company, 1973, Plan for depletion, Fullerton Clearfork Unit, Andrew County, Texas: Internal Report, Field Study Group, Production Department, Midcontinent Division, 70 p.
- Jennings, J. W., Ruppel, S. C., and Ward, W. B., 2000, Geostatistical analysis of permeability data and modeling of fluid-flow effect in carbonate outcrops: SPE Reservoir Evaluation and Engineering, v. 3, no. 4, p. 292–303.
- Kerans, C., Lucia, F. J., and Senger, R. K., 1994, Integrated characterization of carbonate ramp reservoirs using Permian San Andres Formation outcrop analogs: American Association of Petroleum Geologists Bulletin, v. 78, no. 2, p. 181–216.
- Lucia, F. J., 1999, Carbonate reservoir characterization: New York, Springer-Verlag, 226 p.
- Lucia, F. J., Kerans, Charles, and Senger, R. K., 1992, Defining flow units in dolomitized carbonate-ramp reservoirs: Society of Petroleum Engineers, Paper No. SPE 24702, p. 399–406.
- Lucia, F. J., Kerans, Charles, and Wang, F. P., 1995, Fluid-flow characterization of dolomitized carbonate-ramp reservoirs: San Andres Formation (Permian) of Seminole field and Algerita Escarpment, Permian Basin, Texas and New Mexico, *in* Stouidt, E. L., and Harris, P. M., eds., Hydrocarbon reservoir characterization: geologic framework and flow unit modeling: SEPM (Society for Sedimentary Geology), SEPM Short Course Notes, v. 34, p. 129–153.
- Railroad Commission of Texas, 1986, Docket No. 8-87,428: Hearing File, Texas Railroad Commission, May 1986.

Table 1. Geologic and reservoir parameters of Fullerton Clear Fork Unit (Modified from Docket No. 8-87,428, Texas Railroad Commission, 1986).

| Parameter | Value |
|------------------------------|---|
| Reservoir | Clear Fork & Wichita-Albany |
| Discovery Date | December 1941 |
| Unitization Date | 1953 |
| Structure Type | NW-SE-Trending Anticline |
| Rock Type | Dolomite/Limestone |
| Primary Drive Mechanism | Solution Gas |
| Secondary Recovery | Waterflood |
| Original Oil Productive Area | 44,000 ac |
| Unit Area | 29,541 ac |
| Reservoir Temperature | 110°F |
| Porosity | 10.6% ¹ |
| Permeability | 15 mD ¹ |
| Water Salinity | 90,000 ppm |
| API Oil Gravity | 42° at 60°F |
| Oil Gravity | 0.82 |
| Oil Viscosity | 0.43 cP at 110°F and 2940 psi |
| Original FVF | 1.6 RB/STB |
| Gas Gravity | 0.97 |
| Original Reservoir Pressure | 2,940 psi at 7200 ft 2,852 at -3950 ft |
| Original Saturation Pressure | 2,370 psia |
| Original Solution GOR | 1,250 SCF/STB |
| 1986 Reservoir Pressure | 3,100 psia |
| 1986 Solution GOR | 700 SCF/STB |

¹Based on 6% porosity cutoff and 0.1-mD permeability cutoff.

Table 2. Geologic frameworks used in 3-D reservoir models.

| Sequence | ExxonMobil Zones | Phase-I Study Model | | | Field Model | | |
|--------------------------|------------------|--------------------------|--------------|--------------|---------------------|-------------|---|
| | | Horizon | Flow Unit | Subgrid No. | Cycle | Subgrid No. | |
| Lower Clear Fork HFS 2.2 | Zone 1 | LC1 | LC1 | 1 | 2300 (not included) | | |
| | | | LC1a | 2 | 2270 | 1 | |
| | | LC2 | LC2 | 3 | 2260 | 2 | |
| | | | LC2a | 4 | 2250 | 3 | |
| | | LC3 | LC3 | 5 | 2240 | 4 | |
| | | | LC3a | 6 | 2230 | 5 | |
| | | LC4 | LC4 | 7 | 2220 | 6 | |
| | | | LC4a | 8 | 2210 | 7 | |
| | | Lower Clear Fork HFS 2.1 | LC 5 | LC 5 | 9 | 2200 | 8 |
| | | | | LC5a | 10 | | |
| LC 6 | LC 6 | | 11 | 2150 | 9 | | |
| | LC6a | | 12 | 2140 | 10 | | |
| LC 7 | LC 7 | | 13 | 2130 | 11 | | |
| | LC7a | | 14 | | | | |
| LC 8 | LC 8 | | 15 | 2120 | 12 | | |
| | LC8a | | 16 | | | | |
| LC 9 | LC 9 | | 17 | 2110 | 13 | | |
| | LC9a | | 18 | | | | |
| LC 10 | LC 10 | 19 | 2105 | 14 | | | |
| Wichita | Wichita | W1 | W1 | 20 | W1 | 15 | |
| | | | W1a | 21 | | | |
| | | W2 | W2 | 22 | W2 | 16 | |
| | | | W2a | 23 | | | |
| | | W3 | W3 | 24 | W3 | 17 | |
| | | | W3a | 25 | | | |
| | Zone 3 | W4 | W4 | 26 | W4 | 18 | |
| | | | W4a | 27 | | | |
| | | W5 | W5 | 28 | W5 | 19 | |
| | | | W5a | 29 | | | |
| | | W8 | W8 | 30 | W8 | 20 | |
| | | | W8a | 31 | | | |
| | Zone3B | W9 | W9 | 32 | W9 | 21 | |
| | | | W9a | 33 | | | |
| | | W10 | W10 | 34 | W10 | 22 | |
| | | | W10a | 35 | | | |
| | | W11 | W11 | 36 | W11 | 23 | |
| | | | W11a | 37 | | | |
| Zone 4 | W12 | W12 | 38 | W12 | 24 | | |
| | | W12a | 39 | | | | |
| ABO | Zone 5 | ABO | Not included | Not included | ABO | 25 | |
| | | | | | ABO10 | 26 | |
| | | | | | ABO9 | 27 | |
| | | | | | ABO8 | 28 | |
| | | | | | ABO7 | 29 | |
| | | | | | ABO6 | 30 | |
| | | | | | ABO5 | 31 | |
| | | | | | ABO4 | 32 | |
| | | | | | ABO3 | 33 | |
| | | | | | ABO2 | 34 | |
| ABO1 | 35 | | | | | | |
| ABO1+100 ft | 36 | | | | | | |

Table 3. Dimensions of 3-D field models.

| Item Name | Fine-Grid Model | | Cycle-Based Model | |
|-----------|-----------------|------------------|-------------------|-------------------|
| | Dimension (ft) | No. of Cells | Dimension (ft) | No. of Cells |
| X | 150 | 239 | 150 | 239 |
| Y | 150 | 462 | 150 | 462 |
| Z | | 380 | | 36 |
| Total | | 42×10^6 | | 3.7×10^6 |

Table 4. Formation volume factor, oil-gas ratio, and WOC used in OOIP estimates.

| Parameter | Value | |
|-----------------------------------|----------------------|----------------------|
| Formation Volume Factor (bbl/STB) | 1.6 | |
| Gas-Oil Ratio (SCF/STB) | 1,250 | |
| Water-Oil Contact (ft) | ExxonMobil -3,940 | This Study -4,100 |

Table 5. Effect of variable search radius on OOIP estimates of FCU.

| | Search Radius (ft) | 2500 | 5000 |
|--------------|--------------------|---------------|---------------|
| | OOIP (BSTB) | Zone 1 | 0.2591 |
| Zone 2 | | 0.5744 | 0.5995 |
| Wichita | | 0.2114 | 0.2173 |
| Zone 3 | | 0.2672 | 0.2779 |
| Zone 3B | | 0.2038 | 0.2164 |
| Zone 4 | | 0.0777 | 0.0907 |
| Subtotal | | 1.5936 | 1.6810 |
| Zone 5 (ABO) | | 0.1969 | 0.2357 |
| Total | | 1.7905 | 1.9167 |

Table 6. Effect of water-oil contact on OOIP estimates of FCU.

| | | WOC (ft) | | | |
|----------------|-----------------|---------------|---------------|---------------|---------------|
| | | -3940 | -4000 | -4050 | -4100 |
| OOIP (BSTB) | Zone 1 | 0.2791 | 0.2791 | 0.2791 | 0.2791 |
| | Zone 2 | 0.5991 | 0.5995 | 0.5995 | 0.5995 |
| | Wichita | 0.2108 | 0.2170 | 0.2173 | 0.2173 |
| | Zone 3 | 0.2594 | 0.2746 | 0.2773 | 0.2779 |
| | Zone 3B | 0.1849 | 0.2063 | 0.2142 | 0.2164 |
| | Zone 4 | 0.0485 | 0.0737 | 0.0824 | 0.0907 |
| | Subtotal | 0.7036 | 1.6501 | 1.6698 | 1.6810 |
| | Zone 5 (ABO) | 0.0002 | 0.0281 | 0.1048 | 0.2357 |
| | Total | 1.5821 | 1.6783 | 1.7746 | 1.9167 |

Table 7. Effect of cutoff values on OOIP.

| | | OOIP (BSTB) | | | |
|--------------------------|------------------|------------------|-------|-----------------------------------|-------|
| | | WOC at -3,940 ft | | WOC at -4,100 ft Excluding ABO | |
| | | Unit | Model | Unit | Model |
| | No Cutoff | 1.582 | 1.694 | 1.681 | 1.796 |
| Porosity | 0.03 | 1.577 | 1.688 | 1.676 | 1.789 |
| | 0.05 | 1.514 | 1.614 | 1.612 | 1.715 |
| | 0.07 | 1.344 | 1.423 | 1.440 | 1.521 |
| | 0.10 | 0.998 | 1.044 | 1.084 | 1.132 |
| Water Saturation | 0.50 | 1.184 | 1.253 | 1.228 | 1.295 |
| | 0.60 | 1.329 | 1.406 | 1.378 | 1.460 |
| | 0.70 | 1.427 | 1.521 | 1.494 | 1.587 |
| | 0.80 | 1.505 | 1.608 | 1.584 | 1.686 |
| Permeability (mD) | 0.10 | 1.537 | 1.642 | 1.635 | 1.743 |
| | 0.50 | 1.342 | 1.434 | 1.433 | 1.528 |
| | 1.00 | 1.139 | 1.224 | 1.219 | 1.304 |

Table 8. Effect of cutoff values on OOIP in FCU for WOC at -3940 ft summarized by ExxonMobil zonation.

| | | OOIP (BSTB) | | | | | | | | | | | | |
|------------------|-----------------|--------------|-----------------|--------------|--------------|--------------|-------------------------|--------------|--------------|--------------|--------------|---------------------|--------------|--------------|
| | | Base Case | Porosity Cutoff | | | | Water Saturation Cutoff | | | | | Permeability Cutoff | | |
| Zone | | | 0.03 | 0.05 | 0.07 | 0.10 | 0.5 | 0.6 | 0.7 | 0.8 | 0.9 | 0.1 | 0.5 | 1.0 |
| Lower Clear Fork | Zone 1 | 0.279 | 0.277 | 0.245 | 0.157 | 0.048 | 0.212 | 0.240 | 0.259 | 0.270 | 0.277 | 0.264 | 0.229 | 0.205 |
| | Zone 2 | 0.599 | 0.596 | 0.571 | 0.507 | 0.347 | 0.494 | 0.532 | 0.559 | 0.580 | 0.593 | 0.576 | 0.516 | 0.473 |
| | Subtotal | 0.878 | 0.874 | 0.817 | 0.664 | 0.395 | 0.706 | 0.772 | 0.818 | 0.850 | 0.870 | 0.840 | 0.744 | 0.678 |
| Wichita | Wichita | 0.211 | 0.210 | 0.208 | 0.202 | 0.176 | 0.163 | 0.179 | 0.191 | 0.201 | 0.207 | 0.207 | 0.175 | 0.138 |
| | Zone 3 | 0.259 | 0.259 | 0.256 | 0.249 | 0.215 | 0.162 | 0.193 | 0.219 | 0.239 | 0.253 | 0.256 | 0.211 | 0.153 |
| | Zone 3B | 0.185 | 0.185 | 0.184 | 0.183 | 0.172 | 0.131 | 0.149 | 0.163 | 0.174 | 0.181 | 0.184 | 0.168 | 0.135 |
| | Zone 4 | 0.049 | 0.049 | 0.048 | 0.047 | 0.041 | 0.022 | 0.029 | 0.035 | 0.042 | 0.046 | 0.048 | 0.043 | 0.035 |
| | Subtotal | 0.704 | 0.703 | 0.697 | 0.681 | 0.603 | 0.478 | 0.550 | 0.609 | 0.655 | 0.687 | 0.696 | 0.597 | 0.461 |
| | Zone 1-4 | 1.582 | 1.576 | 1.514 | 1.344 | 0.997 | 1.184 | 1.323 | 1.427 | 1.505 | 1.557 | 1.536 | 1.341 | 1.139 |
| Abo | Zone 5 | 0.000 | 0.000 | 0.000 | 0.000 | 0.000 | 0.000 | 0.000 | 0.000 | 0.000 | 0.000 | 0.000 | 0.000 | 0.000 |
| Total | | 1.582 | 1.577 | 1.514 | 1.344 | 0.998 | 1.184 | 1.323 | 1.427 | 1.505 | 1.557 | 1.537 | 1.342 | 1.139 |

Table 9. Effect of cutoff values on OOIP in Fullerton field for WOC at -3940 ft summarized by ExxonMobil zonation.

| | | OOIP (BSTB) | | | | | | | | | | | | |
|------------------|-----------------|--------------|-----------------|--------------|--------------|--------------|-------------------------|--------------|--------------|--------------|--------------|---------------------|--------------|--------------|
| | | Base Case | Porosity Cutoff | | | | Water Saturation Cutoff | | | | | Permeability Cutoff | | |
| Zone | | | 0.03 | 0.05 | 0.07 | 0.10 | 0.5 | 0.6 | 0.7 | 0.8 | 0.9 | 0.1 | 0.5 | 1.0 |
| Lower Clear Fork | Zone 1 | 0.314 | 0.311 | 0.274 | 0.174 | 0.051 | 0.234 | 0.267 | 0.289 | 0.303 | 0.311 | 0.295 | 0.256 | 0.230 |
| | Zone 2 | 0.647 | 0.643 | 0.613 | 0.542 | 0.371 | 0.526 | 0.568 | 0.600 | 0.623 | 0.639 | 0.621 | 0.556 | 0.511 |
| | Subtotal | 0.960 | 0.954 | 0.887 | 0.716 | 0.422 | 0.760 | 0.836 | 0.889 | 0.926 | 0.950 | 0.916 | 0.812 | 0.741 |
| Wichita | Wichita | 0.219 | 0.219 | 0.216 | 0.210 | 0.182 | 0.167 | 0.184 | 0.198 | 0.208 | 0.215 | 0.215 | 0.181 | 0.144 |
| | Zone 3 | 0.272 | 0.271 | 0.268 | 0.259 | 0.222 | 0.167 | 0.200 | 0.227 | 0.249 | 0.264 | 0.268 | 0.220 | 0.161 |
| | Zone 3B | 0.188 | 0.188 | 0.187 | 0.186 | 0.174 | 0.132 | 0.150 | 0.165 | 0.176 | 0.184 | 0.187 | 0.171 | 0.137 |
| | Zone 4 | 0.049 | 0.049 | 0.048 | 0.047 | 0.041 | 0.022 | 0.029 | 0.035 | 0.042 | 0.046 | 0.048 | 0.043 | 0.035 |
| | Subtotal | 0.727 | 0.726 | 0.720 | 0.702 | 0.619 | 0.488 | 0.564 | 0.626 | 0.675 | 0.709 | 0.719 | 0.615 | 0.477 |
| | Zone 1-4 | 1.688 | 1.681 | 1.608 | 1.418 | 1.041 | 1.248 | 1.400 | 1.515 | 1.601 | 1.659 | 1.635 | 1.427 | 1.218 |
| Abo | Zone 5 | 0.007 | 0.007 | 0.006 | 0.006 | 0.004 | 0.005 | 0.006 | 0.006 | 0.007 | 0.007 | 0.007 | 0.007 | 0.007 |
| Total | | 1.694 | 1.688 | 1.614 | 1.423 | 1.044 | 1.253 | 1.406 | 1.521 | 1.608 | 1.666 | 1.642 | 1.434 | 1.224 |

Table 10. Effect of cutoff values on OOIP in FCU for WOC at -3940 ft summarized by high frequency cycles.

| Formation | Sequence | Cycle | OOIP (BSTB) for WOC at -3940 in FCU | | | | | | | | | | | | |
|------------------|----------------|----------------|-------------------------------------|-----------------|-------|-------|-------|-------------------------|-------|-------|-------|-------|---------------------|-------|-------|
| | | | Base Case | Porosity Cutoff | | | | Water Saturation Cutoff | | | | | Permeability Cutoff | | |
| | | | | 0.03 | 0.05 | 0.07 | 0.10 | 0.5 | 0.6 | 0.7 | 0.8 | 0.9 | 0.1 | 0.5 | 1.0 |
| Lower Clear Fork | HSF L2.2 | L2270 | 0.018 | 0.017 | 0.014 | 0.008 | 0.003 | 0.012 | 0.014 | 0.015 | 0.017 | 0.017 | 0.016 | 0.013 | 0.011 |
| | | L2260 | 0.033 | 0.032 | 0.029 | 0.019 | 0.005 | 0.026 | 0.029 | 0.031 | 0.032 | 0.032 | 0.031 | 0.027 | 0.024 |
| | | L2250 | 0.041 | 0.041 | 0.037 | 0.024 | 0.008 | 0.032 | 0.036 | 0.039 | 0.040 | 0.040 | 0.039 | 0.034 | 0.031 |
| | | L2240 | 0.058 | 0.058 | 0.054 | 0.037 | 0.012 | 0.048 | 0.053 | 0.056 | 0.058 | 0.058 | 0.057 | 0.051 | 0.046 |
| | | L2230 | 0.053 | 0.053 | 0.048 | 0.029 | 0.007 | 0.041 | 0.047 | 0.050 | 0.052 | 0.053 | 0.051 | 0.045 | 0.040 |
| | | L2220 | 0.044 | 0.043 | 0.037 | 0.022 | 0.006 | 0.031 | 0.036 | 0.040 | 0.042 | 0.043 | 0.040 | 0.034 | 0.030 |
| | | L2210 | 0.033 | 0.032 | 0.027 | 0.018 | 0.007 | 0.021 | 0.025 | 0.028 | 0.031 | 0.032 | 0.030 | 0.025 | 0.023 |
| | Zone 1 | 0.279 | 0.277 | 0.245 | 0.157 | 0.048 | 0.212 | 0.240 | 0.259 | 0.270 | 0.277 | 0.264 | 0.229 | 0.205 | |
| | HFS L2.1 | L2200 | 0.027 | 0.027 | 0.025 | 0.022 | 0.011 | 0.014 | 0.018 | 0.021 | 0.024 | 0.026 | 0.023 | 0.012 | 0.007 |
| | | L2150 | 0.025 | 0.025 | 0.023 | 0.019 | 0.009 | 0.013 | 0.016 | 0.019 | 0.021 | 0.024 | 0.020 | 0.010 | 0.007 |
| | | L2140 | 0.107 | 0.106 | 0.101 | 0.092 | 0.066 | 0.090 | 0.097 | 0.101 | 0.104 | 0.106 | 0.104 | 0.099 | 0.095 |
| | | L2130 | 0.123 | 0.122 | 0.117 | 0.105 | 0.077 | 0.106 | 0.112 | 0.117 | 0.120 | 0.122 | 0.120 | 0.114 | 0.107 |
| | | L2120 | 0.140 | 0.139 | 0.134 | 0.119 | 0.086 | 0.121 | 0.128 | 0.133 | 0.137 | 0.139 | 0.136 | 0.126 | 0.118 |
| | | L2110 | 0.097 | 0.096 | 0.092 | 0.080 | 0.049 | 0.082 | 0.088 | 0.092 | 0.094 | 0.096 | 0.093 | 0.083 | 0.073 |
| L2105 | | 0.082 | 0.081 | 0.078 | 0.070 | 0.048 | 0.068 | 0.073 | 0.077 | 0.079 | 0.081 | 0.080 | 0.072 | 0.066 | |
| Zone 2 | 0.599 | 0.596 | 0.571 | 0.507 | 0.347 | 0.494 | 0.532 | 0.559 | 0.580 | 0.593 | 0.576 | 0.516 | 0.473 | | |
| Wichita | HFS L1 | W1 | 0.098 | 0.098 | 0.097 | 0.095 | 0.087 | 0.083 | 0.088 | 0.092 | 0.095 | 0.097 | 0.096 | 0.088 | 0.078 |
| | | W2 | 0.055 | 0.055 | 0.054 | 0.053 | 0.045 | 0.041 | 0.046 | 0.050 | 0.052 | 0.054 | 0.054 | 0.044 | 0.032 |
| | | W3 | 0.058 | 0.057 | 0.057 | 0.054 | 0.044 | 0.039 | 0.045 | 0.050 | 0.054 | 0.056 | 0.057 | 0.043 | 0.028 |
| | | Wichita | 0.211 | 0.210 | 0.208 | 0.202 | 0.176 | 0.163 | 0.179 | 0.191 | 0.201 | 0.207 | 0.207 | 0.175 | 0.138 |
| | | W4 | 0.063 | 0.063 | 0.062 | 0.059 | 0.049 | 0.040 | 0.047 | 0.053 | 0.058 | 0.062 | 0.062 | 0.049 | 0.034 |
| | | W5 | 0.196 | 0.196 | 0.194 | 0.189 | 0.166 | 0.122 | 0.146 | 0.165 | 0.181 | 0.191 | 0.194 | 0.162 | 0.118 |
| | | Zone 3 | 0.259 | 0.259 | 0.256 | 0.249 | 0.215 | 0.162 | 0.193 | 0.219 | 0.239 | 0.253 | 0.256 | 0.211 | 0.153 |
| | W8 | 0.064 | 0.064 | 0.063 | 0.063 | 0.060 | 0.048 | 0.054 | 0.058 | 0.061 | 0.063 | 0.063 | 0.059 | 0.048 | |
| | W9 | 0.051 | 0.051 | 0.051 | 0.051 | 0.048 | 0.037 | 0.042 | 0.046 | 0.048 | 0.050 | 0.051 | 0.047 | 0.038 | |
| | W10 | 0.044 | 0.044 | 0.043 | 0.043 | 0.040 | 0.027 | 0.032 | 0.037 | 0.040 | 0.042 | 0.043 | 0.038 | 0.029 | |
| | W11 | 0.026 | 0.026 | 0.026 | 0.026 | 0.024 | 0.018 | 0.021 | 0.023 | 0.024 | 0.026 | 0.026 | 0.024 | 0.019 | |
| | Zone 3B | 0.185 | 0.185 | 0.184 | 0.183 | 0.172 | 0.131 | 0.149 | 0.163 | 0.174 | 0.181 | 0.184 | 0.168 | 0.135 | |
| | W12 | 0.049 | 0.049 | 0.048 | 0.047 | 0.041 | 0.022 | 0.029 | 0.035 | 0.042 | 0.046 | 0.048 | 0.043 | 0.035 | |
| | Zone 4 | 0.049 | 0.049 | 0.048 | 0.047 | 0.041 | 0.022 | 0.029 | 0.035 | 0.042 | 0.046 | 0.048 | 0.043 | 0.035 | |
| | LCF+W | 1.582 | 1.576 | 1.514 | 1.344 | 0.997 | 1.184 | 1.323 | 1.427 | 1.505 | 1.557 | 1.536 | 1.341 | 1.139 | |
| Abo | Abo | Abo12 | 0.000 | 0.000 | 0.000 | 0.000 | 0.000 | 0.000 | 0.000 | 0.000 | 0.000 | 0.000 | 0.000 | 0.000 | 0.000 |
| | | Abo11 | 0.000 | 0.000 | 0.000 | 0.000 | 0.000 | 0.000 | 0.000 | 0.000 | 0.000 | 0.000 | 0.000 | 0.000 | 0.000 |
| | | Abo10 | 0.000 | 0.000 | 0.000 | 0.000 | 0.000 | 0.000 | 0.000 | 0.000 | 0.000 | 0.000 | 0.000 | 0.000 | 0.000 |
| | | Abo09 | 0.000 | 0.000 | 0.000 | 0.000 | 0.000 | 0.000 | 0.000 | 0.000 | 0.000 | 0.000 | 0.000 | 0.000 | 0.000 |
| | | Abo08 | 0.000 | 0.000 | 0.000 | 0.000 | 0.000 | 0.000 | 0.000 | 0.000 | 0.000 | 0.000 | 0.000 | 0.000 | 0.000 |
| | | Abo07 | 0.000 | 0.000 | 0.000 | 0.000 | 0.000 | 0.000 | 0.000 | 0.000 | 0.000 | 0.000 | 0.000 | 0.000 | 0.000 |
| | | Abo06 | 0.000 | 0.000 | 0.000 | 0.000 | 0.000 | 0.000 | 0.000 | 0.000 | 0.000 | 0.000 | 0.000 | 0.000 | 0.000 |
| | | Abo05 | 0.000 | 0.000 | 0.000 | 0.000 | 0.000 | 0.000 | 0.000 | 0.000 | 0.000 | 0.000 | 0.000 | 0.000 | 0.000 |
| | | Abo04 | 0.000 | 0.000 | 0.000 | 0.000 | 0.000 | 0.000 | 0.000 | 0.000 | 0.000 | 0.000 | 0.000 | 0.000 | 0.000 |
| | | Abo03 | 0.000 | 0.000 | 0.000 | 0.000 | 0.000 | 0.000 | 0.000 | 0.000 | 0.000 | 0.000 | 0.000 | 0.000 | 0.000 |
| | | Abo02 | 0.000 | 0.000 | 0.000 | 0.000 | 0.000 | 0.000 | 0.000 | 0.000 | 0.000 | 0.000 | 0.000 | 0.000 | 0.000 |
| Abo01 | 0.000 | 0.000 | 0.000 | 0.000 | 0.000 | 0.000 | 0.000 | 0.000 | 0.000 | 0.000 | 0.000 | 0.000 | 0.000 | | |
| | Zone 5 | 0.000 | 0.000 | 0.000 | 0.000 | 0.000 | 0.000 | 0.000 | 0.000 | 0.000 | 0.000 | 0.000 | 0.000 | 0.000 | |
| Total | | | 1.582 | 1.577 | 1.514 | 1.344 | 0.998 | 1.184 | 1.323 | 1.427 | 1.505 | 1.557 | 1.537 | 1.342 | 1.139 |

Table 11. Effect of cutoff values on OOIP in Fullerton Clear Fork field for WOC at -3940 ft summarized by high frequency cycles.

| Formation | Sequence | Cycle | OOIP (BSTB) for WOC at -3940 in Fullerton Clear Fork field | | | | | | | | | | | | | |
|------------------|---------------|---------------|--|-----------------|-------|-------|-------|-------------------------|-------|-------|-------|-------|---------------------|-------|-------|-------|
| | | | Base Case | Porosity Cutoff | | | | Water Saturation Cutoff | | | | | Permeability Cutoff | | | |
| | | | | 0.03 | 0.05 | 0.07 | 0.10 | 0.5 | 0.6 | 0.7 | 0.8 | 0.9 | 0.1 | 0.5 | 1.0 | |
| Lower Clear Fork | HSF L2.2 | L2270 | 0.020 | 0.020 | 0.015 | 0.009 | 0.003 | 0.013 | 0.015 | 0.017 | 0.019 | 0.020 | 0.018 | 0.014 | 0.012 | |
| | | L2260 | 0.035 | 0.034 | 0.030 | 0.019 | 0.005 | 0.027 | 0.030 | 0.032 | 0.034 | 0.034 | 0.033 | 0.028 | 0.025 | |
| | | L2250 | 0.044 | 0.044 | 0.039 | 0.026 | 0.008 | 0.034 | 0.039 | 0.041 | 0.043 | 0.044 | 0.042 | 0.037 | 0.034 | |
| | | L2240 | 0.066 | 0.065 | 0.060 | 0.041 | 0.013 | 0.054 | 0.059 | 0.063 | 0.064 | 0.065 | 0.063 | 0.057 | 0.052 | |
| | | L2230 | 0.060 | 0.060 | 0.054 | 0.033 | 0.008 | 0.046 | 0.053 | 0.057 | 0.059 | 0.060 | 0.058 | 0.051 | 0.045 | |
| | | L2220 | 0.050 | 0.050 | 0.043 | 0.025 | 0.007 | 0.036 | 0.041 | 0.046 | 0.048 | 0.049 | 0.046 | 0.039 | 0.035 | |
| | | L2210 | 0.039 | 0.038 | 0.032 | 0.021 | 0.007 | 0.025 | 0.030 | 0.033 | 0.036 | 0.038 | 0.035 | 0.030 | 0.027 | |
| | | Zone 1 | 0.314 | 0.311 | 0.274 | 0.174 | 0.051 | 0.234 | 0.267 | 0.289 | 0.303 | 0.311 | 0.295 | 0.256 | 0.230 | |
| | HFS L2.1 | L2200 | 0.028 | 0.028 | 0.027 | 0.022 | 0.011 | 0.015 | 0.018 | 0.021 | 0.024 | 0.027 | 0.024 | 0.012 | 0.007 | |
| | | L2150 | 0.027 | 0.026 | 0.025 | 0.019 | 0.009 | 0.013 | 0.017 | 0.020 | 0.023 | 0.025 | 0.022 | 0.011 | 0.008 | |
| | | L2140 | 0.114 | 0.114 | 0.109 | 0.098 | 0.070 | 0.095 | 0.103 | 0.108 | 0.111 | 0.114 | 0.112 | 0.106 | 0.101 | |
| | | L2130 | 0.138 | 0.137 | 0.131 | 0.118 | 0.087 | 0.119 | 0.125 | 0.130 | 0.134 | 0.136 | 0.134 | 0.127 | 0.121 | |
| | | L2120 | 0.150 | 0.149 | 0.143 | 0.127 | 0.092 | 0.128 | 0.136 | 0.142 | 0.147 | 0.149 | 0.146 | 0.135 | 0.127 | |
| | | L2110 | 0.104 | 0.103 | 0.099 | 0.086 | 0.052 | 0.086 | 0.093 | 0.098 | 0.101 | 0.103 | 0.100 | 0.089 | 0.079 | |
| | | L2105 | 0.086 | 0.085 | 0.082 | 0.072 | 0.049 | 0.069 | 0.075 | 0.080 | 0.083 | 0.085 | 0.083 | 0.075 | 0.069 | |
| | | Zone 2 | 0.647 | 0.643 | 0.613 | 0.542 | 0.371 | 0.526 | 0.568 | 0.600 | 0.623 | 0.639 | 0.621 | 0.556 | 0.511 | |
| | Wichita | HFS L1 | W1 | 0.103 | 0.103 | 0.102 | 0.100 | 0.091 | 0.086 | 0.092 | 0.097 | 0.100 | 0.102 | 0.102 | 0.093 | 0.083 |
| W2 | | | 0.056 | 0.056 | 0.055 | 0.053 | 0.046 | 0.041 | 0.046 | 0.050 | 0.053 | 0.055 | 0.055 | 0.045 | 0.032 | |
| W3 | | | 0.060 | 0.060 | 0.059 | 0.056 | 0.045 | 0.040 | 0.046 | 0.051 | 0.055 | 0.058 | 0.059 | 0.044 | 0.029 | |
| Wichita | | | 0.219 | 0.219 | 0.216 | 0.210 | 0.182 | 0.167 | 0.184 | 0.198 | 0.208 | 0.215 | 0.215 | 0.181 | 0.144 | |
| W4 | | | 0.066 | 0.066 | 0.064 | 0.061 | 0.050 | 0.040 | 0.048 | 0.055 | 0.060 | 0.064 | 0.065 | 0.050 | 0.034 | |
| W5 | | | 0.206 | 0.205 | 0.204 | 0.198 | 0.173 | 0.127 | 0.152 | 0.173 | 0.189 | 0.200 | 0.204 | 0.170 | 0.127 | |
| Zone 3 | | | 0.272 | 0.271 | 0.268 | 0.259 | 0.222 | 0.167 | 0.200 | 0.227 | 0.249 | 0.264 | 0.268 | 0.220 | 0.161 | |
| W8 | | | 0.065 | 0.065 | 0.065 | 0.064 | 0.061 | 0.049 | 0.054 | 0.059 | 0.062 | 0.064 | 0.065 | 0.060 | 0.049 | |
| W9 | | | 0.052 | 0.052 | 0.051 | 0.051 | 0.048 | 0.037 | 0.042 | 0.046 | 0.049 | 0.051 | 0.051 | 0.047 | 0.038 | |
| W10 | | | 0.045 | 0.045 | 0.045 | 0.044 | 0.041 | 0.028 | 0.033 | 0.038 | 0.041 | 0.044 | 0.045 | 0.040 | 0.030 | |
| W11 | | | 0.027 | 0.027 | 0.026 | 0.026 | 0.024 | 0.018 | 0.021 | 0.023 | 0.025 | 0.026 | 0.026 | 0.024 | 0.020 | |
| Zone 3B | | 0.188 | 0.188 | 0.187 | 0.186 | 0.174 | 0.132 | 0.150 | 0.165 | 0.176 | 0.184 | 0.187 | 0.171 | 0.137 | | |
| W12 | | 0.049 | 0.049 | 0.048 | 0.047 | 0.041 | 0.022 | 0.029 | 0.035 | 0.042 | 0.046 | 0.048 | 0.043 | 0.035 | | |
| Zone 4 | | 0.049 | 0.049 | 0.048 | 0.047 | 0.041 | 0.022 | 0.029 | 0.035 | 0.042 | 0.046 | 0.048 | 0.043 | 0.035 | | |
| LCF+W | | 1.688 | 1.681 | 1.608 | 1.418 | 1.041 | 1.248 | 1.400 | 1.515 | 1.601 | 1.659 | 1.635 | 1.427 | 1.218 | | |
| Abo | | Abo | Abo12 | 0.004 | 0.004 | 0.004 | 0.003 | 0.002 | 0.003 | 0.003 | 0.004 | 0.004 | 0.004 | 0.004 | 0.004 | 0.004 |
| | | | Abo11 | 0.003 | 0.003 | 0.003 | 0.002 | 0.001 | 0.002 | 0.002 | 0.003 | 0.003 | 0.003 | 0.003 | 0.003 | 0.003 |
| | Abo10 | | 0.000 | 0.000 | 0.000 | 0.000 | 0.000 | 0.000 | 0.000 | 0.000 | 0.000 | 0.000 | 0.000 | 0.000 | 0.000 | |
| | Abo09 | | 0.000 | 0.000 | 0.000 | 0.000 | 0.000 | 0.000 | 0.000 | 0.000 | 0.000 | 0.000 | 0.000 | 0.000 | 0.000 | |
| | Abo08 | | 0.000 | 0.000 | 0.000 | 0.000 | 0.000 | 0.000 | 0.000 | 0.000 | 0.000 | 0.000 | 0.000 | 0.000 | 0.000 | |
| | Abo07 | | 0.000 | 0.000 | 0.000 | 0.000 | 0.000 | 0.000 | 0.000 | 0.000 | 0.000 | 0.000 | 0.000 | 0.000 | 0.000 | |
| | Abo06 | | 0.000 | 0.000 | 0.000 | 0.000 | 0.000 | 0.000 | 0.000 | 0.000 | 0.000 | 0.000 | 0.000 | 0.000 | 0.000 | |
| | Abo05 | | 0.000 | 0.000 | 0.000 | 0.000 | 0.000 | 0.000 | 0.000 | 0.000 | 0.000 | 0.000 | 0.000 | 0.000 | 0.000 | |
| | Abo04 | | 0.000 | 0.000 | 0.000 | 0.000 | 0.000 | 0.000 | 0.000 | 0.000 | 0.000 | 0.000 | 0.000 | 0.000 | 0.000 | |
| | Abo03 | | 0.000 | 0.000 | 0.000 | 0.000 | 0.000 | 0.000 | 0.000 | 0.000 | 0.000 | 0.000 | 0.000 | 0.000 | 0.000 | |
| | Abo02 | | 0.000 | 0.000 | 0.000 | 0.000 | 0.000 | 0.000 | 0.000 | 0.000 | 0.000 | 0.000 | 0.000 | 0.000 | 0.000 | |
| | Abo01 | | 0.000 | 0.000 | 0.000 | 0.000 | 0.000 | 0.000 | 0.000 | 0.000 | 0.000 | 0.000 | 0.000 | 0.000 | 0.000 | |
| | Zone 5 | | 0.007 | 0.007 | 0.006 | 0.006 | 0.004 | 0.005 | 0.006 | 0.006 | 0.007 | 0.007 | 0.007 | 0.007 | 0.007 | |
| Total | | | 1.694 | 1.688 | 1.614 | 1.423 | 1.044 | 1.253 | 1.406 | 1.521 | 1.608 | 1.666 | 1.642 | 1.434 | 1.224 | |

Table 12. Effect of vertical resolution on OOIP.

| | | OOIP (BSTB) WOC at -3,940 ft | | |
|----------------------|------|---------------------------------|-------|------------|
| | | Fine Grid | Cycle | Change (%) |
| No Cutoff | | 1.582 | 1.405 | 11.2 |
| Porosity | 0.03 | 1.577 | 1.398 | 11.4 |
| | 0.05 | 1.514 | 1.315 | 13.1 |
| | 0.07 | 1.344 | 1.124 | 16.4 |
| | 0.10 | 0.998 | 0.731 | 26.8 |
| Water Saturation | 0.50 | 1.184 | 0.843 | 28.8. |
| | 0.60 | 1.329 | 1.027 | 22.4 |
| | 0.70 | 1.427 | 1.177 | 17.5 |
| | 0.80 | 1.505 | 1.298 | 13.8 |
| | 0.90 | 1.557 | 1.376 | 11.6 |
| Permeability (mD) | 0.10 | 1.537 | 1.39 | 9.6 |
| | 0.50 | 1.342 | 1.23 | 8.3 |
| | 1.00 | 1.139 | 1.05 | 7.8 |

Table 13. Summary of parameters affecting OOIP.

| Parameter | Change (%) |
|---------------------|------------|
| Search radius | 4-7 |
| Vertical resolution | 8-29 |
| Areal Coverage | 6-10 |
| Water-oil contact | |
| -3940 to -4100 ft | 20-25 |
| -3940 to top of Abo | 4-6 |

Table 14. Dimensions of 3-D models of initial 2,000-acre model (simulation area).

| Item Name | Fine-Grid Model | | Simulation Model | |
|-----------|-----------------|---------------------|------------------|--------------|
| | Dimension (ft) | No. of Cells | Dimension (ft) | No. of Cells |
| X | 103 | 140 | 200 | 73 |
| Y | 105 | 90 | 200 | 48 |
| Z | 2.2 (0-16) | 254 | | 39 |
| Total | | 3.165×10^6 | | 136,656 |

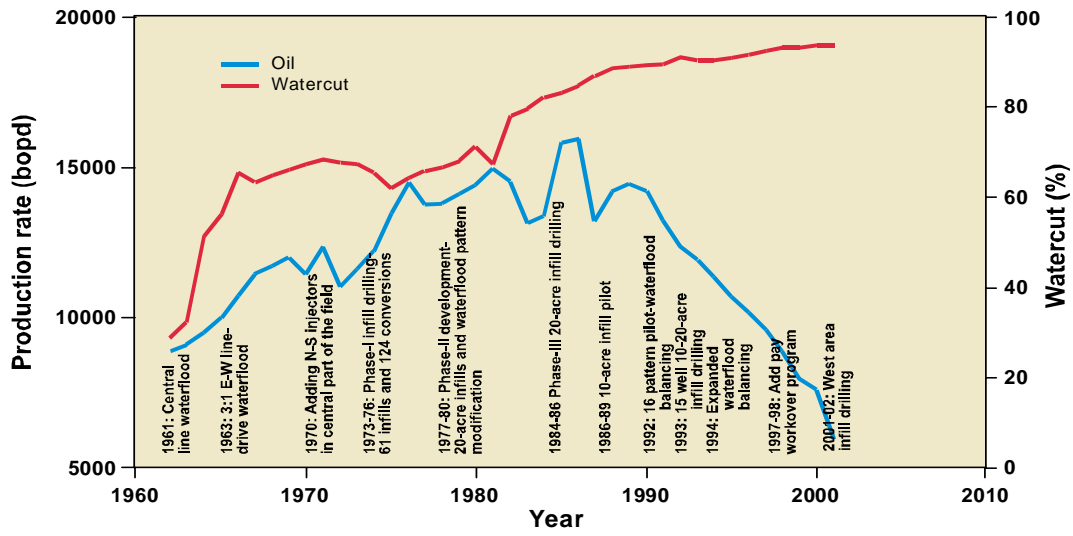


Figure 1. Production history of waterflooding in Fullerton Clear Fork Unit.

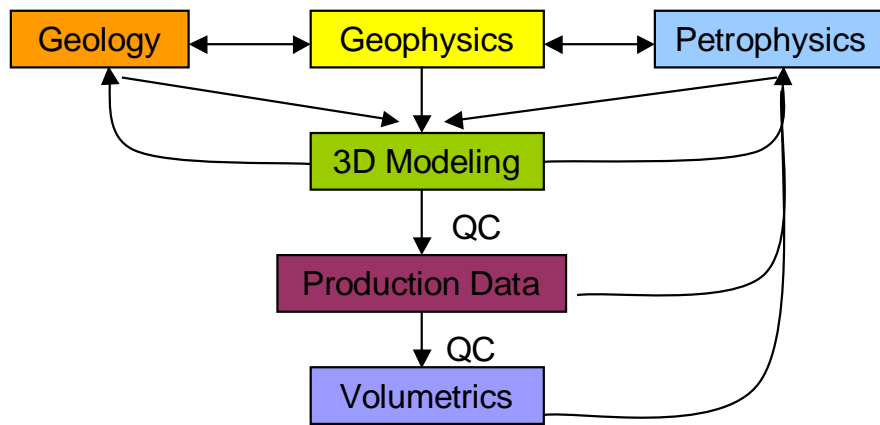


Figure 2. Workflow of 3-D modeling.

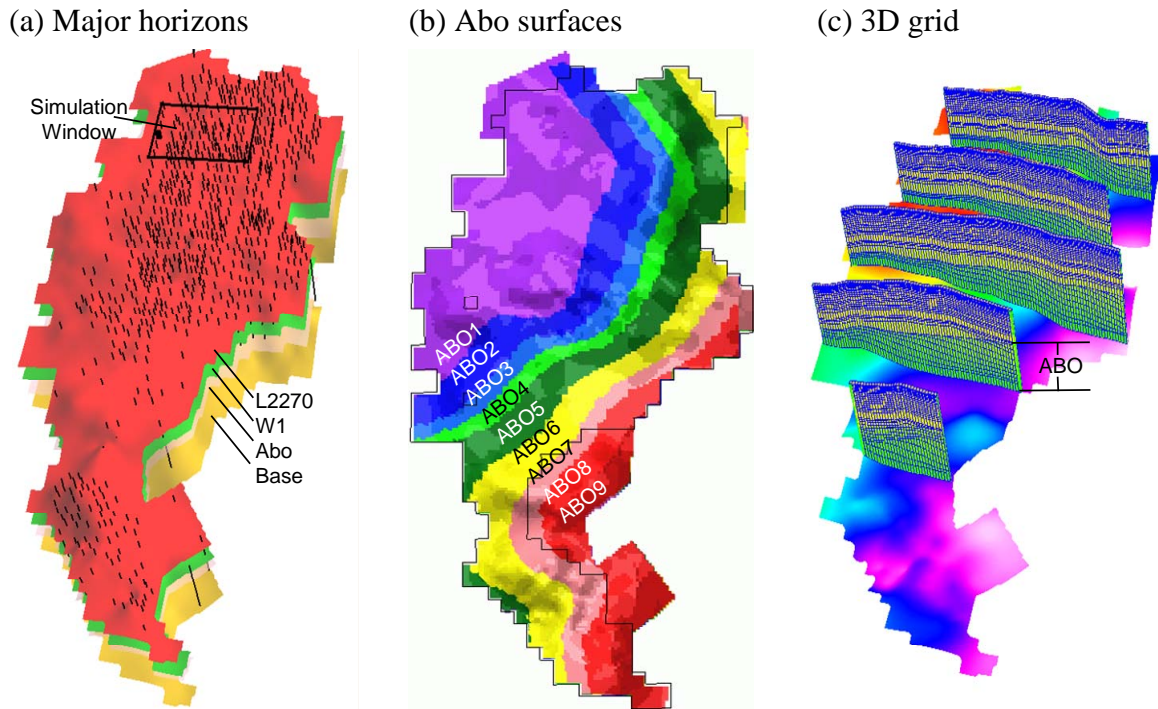


Figure 3. Geologic framework used to build 3-D models of Fullerton Clear Fork field. (a) four major horizons, 730 selected wells, and the simulation window; (b) 9 west-east prograding units used in building Abo model; and (c) sections of 3-D grids showing the prograding Abo unit.

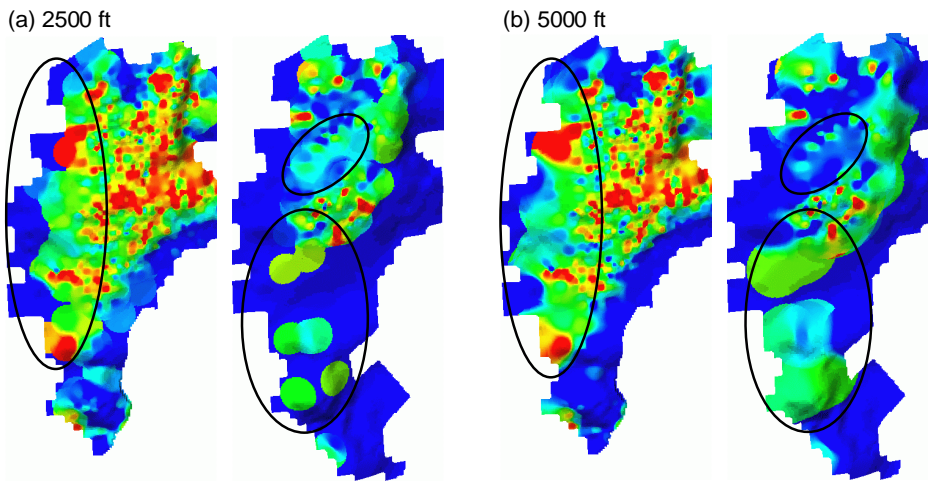


Figure 4. Effect of search radius of (a) 2,500 ft and (b) 5,000 ft on porosity mapping. Circled areas show that a search radius of 5,000 ft improves mapping coverages.

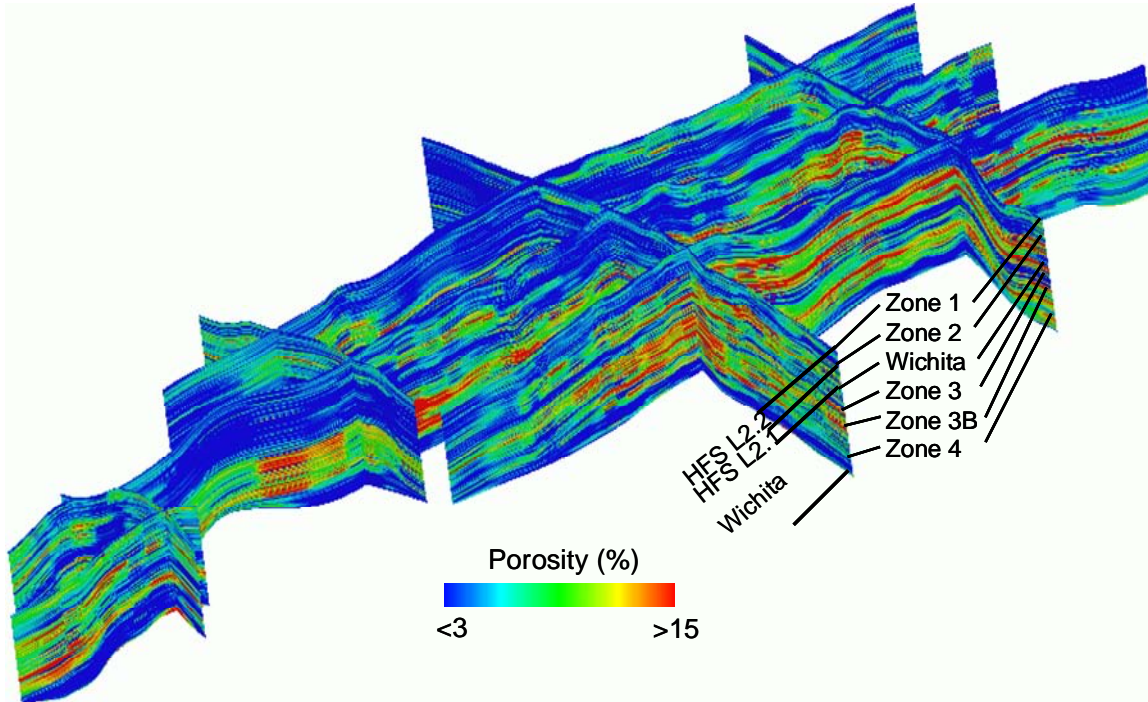


Figure 5. Porosity distribution in fine-grid model.

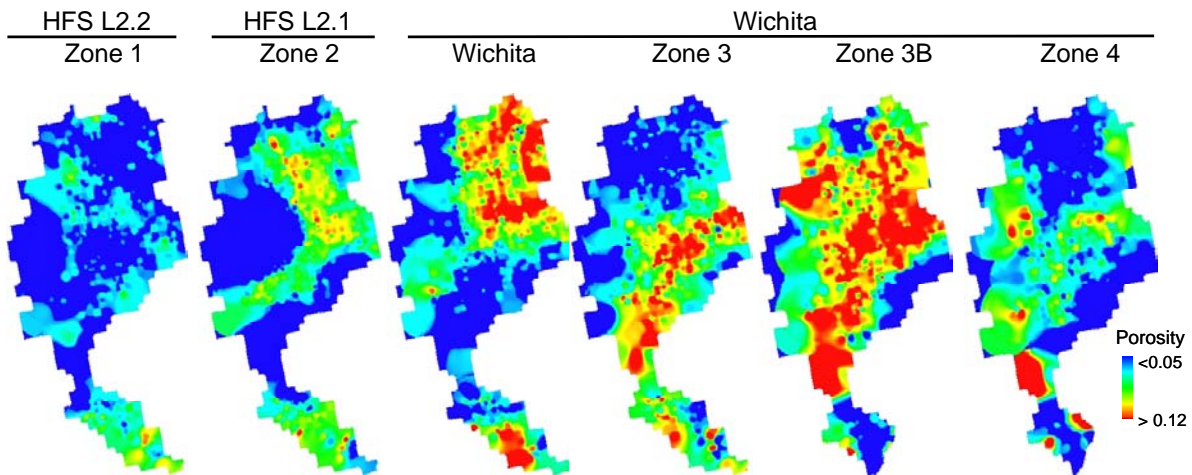


Figure 6. Average porosity distribution, from left to right, in Zone 1, Zone 2, Wichita, Zone 3, Zone 3B, and Zone 4.

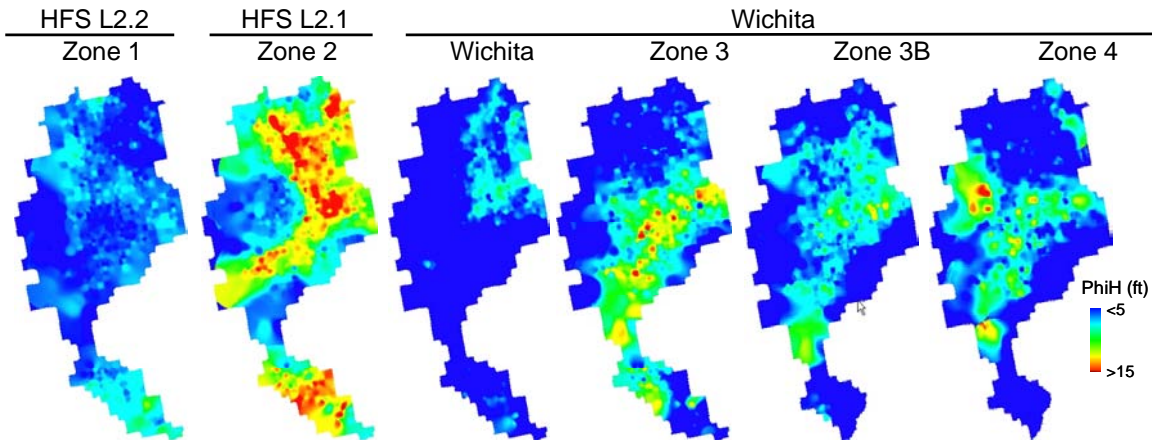


Figure 7. ϕh distribution in reservoir Zone 1 (Lower Clear Fork HFS 2.2) by cycle.

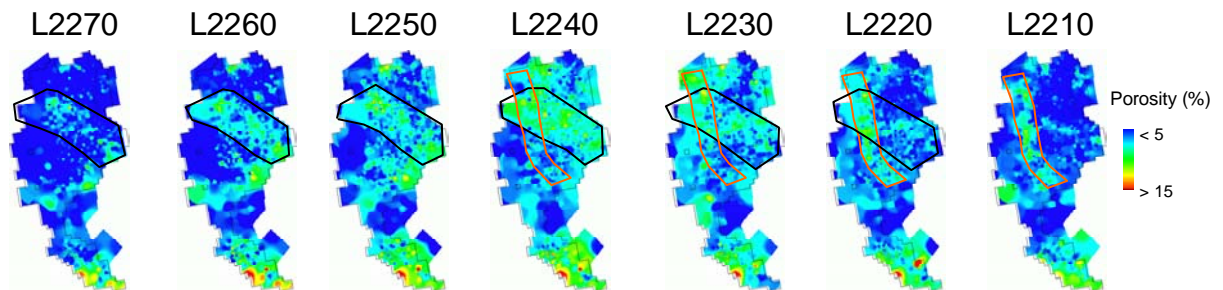


Figure 8. Porosity distribution in reservoir Zone 1 (Lower Clear Fork. HFS 2.2) by cycle.

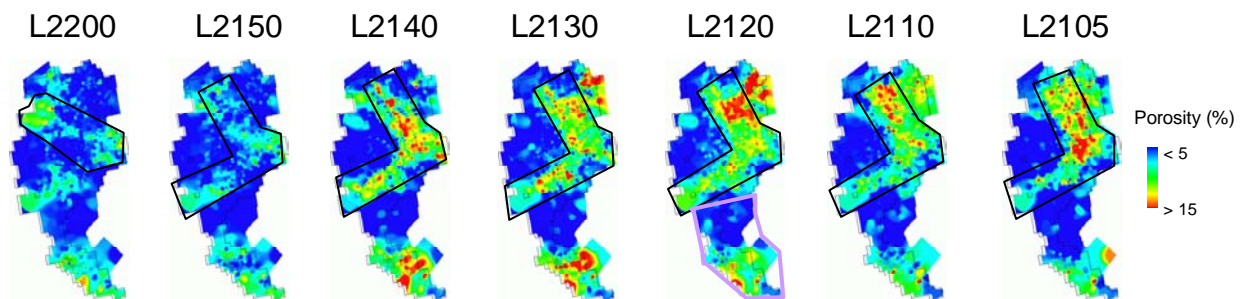


Figure 9. Porosity distribution in reservoir Zone 2, (Lower Clear Fork. HFS 2.1) by cycle.

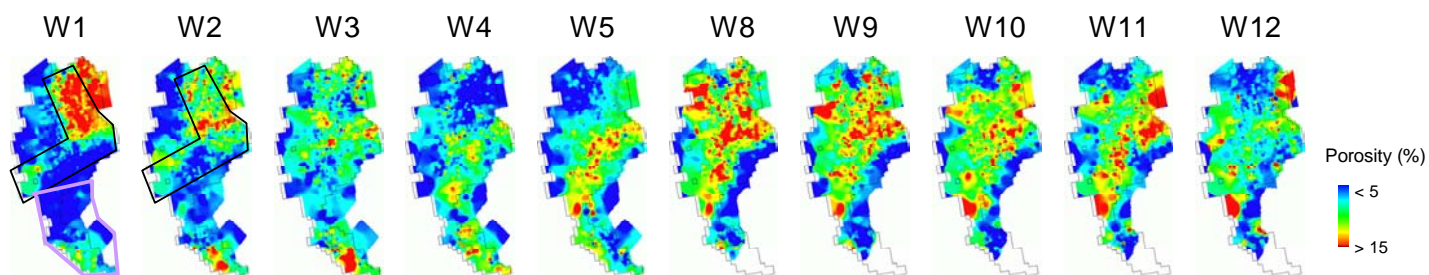


Figure 10. Porosity distribution in Zones Wichita, 3, 3B, and 4, in the Wichita Formation.

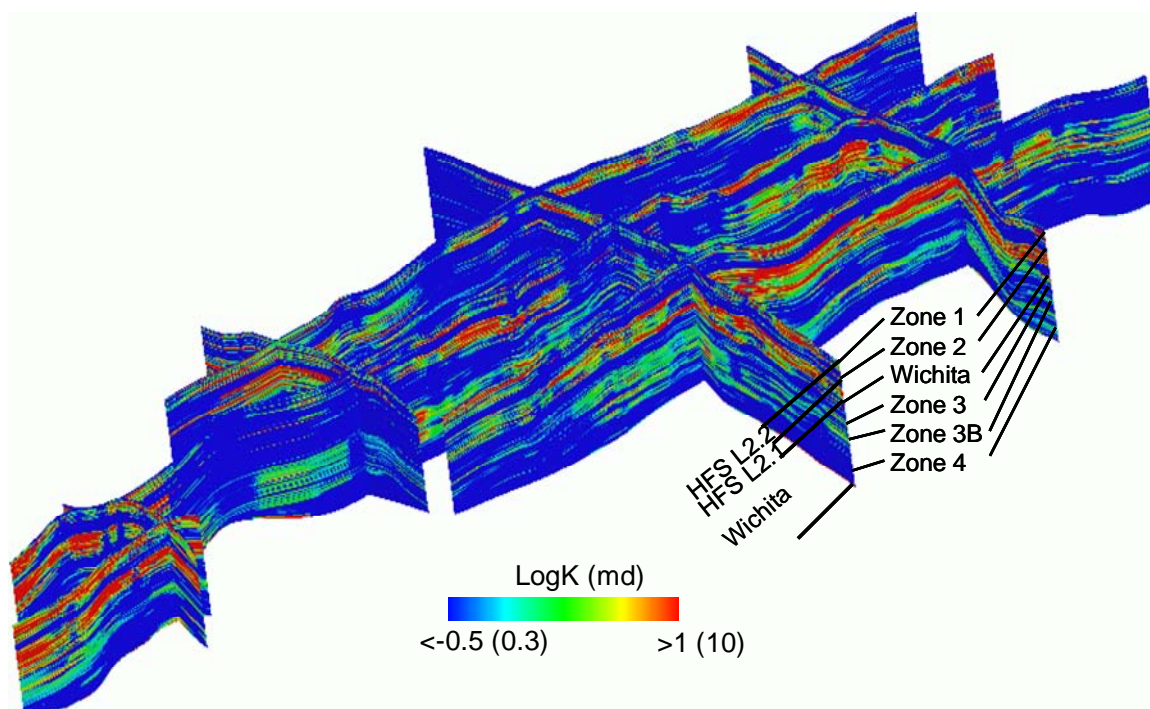


Figure 11. Permeability distribution in 3-D model.

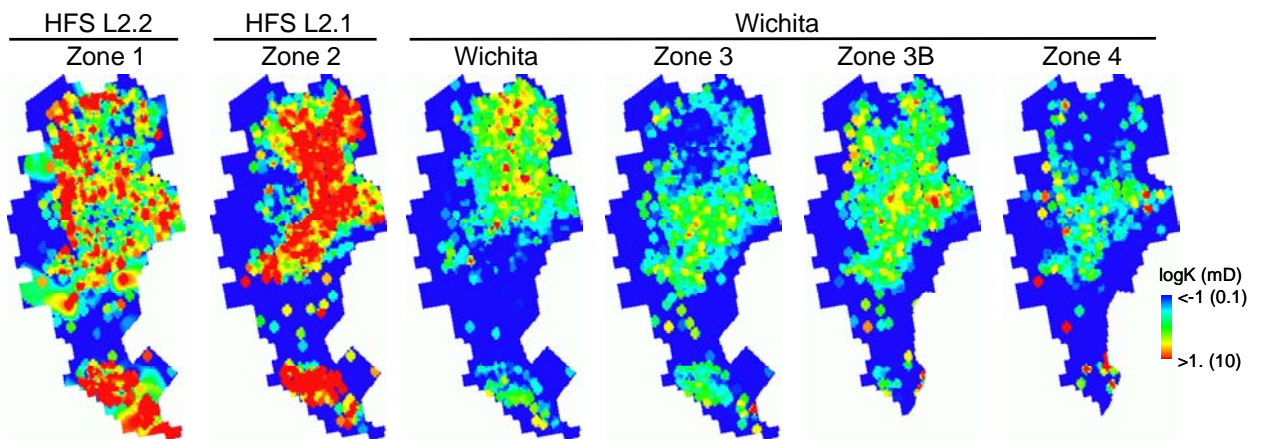


Figure 12. Permeability distribution in reservoir zones 1, 2, Wichita, 3, 3B, and 4.

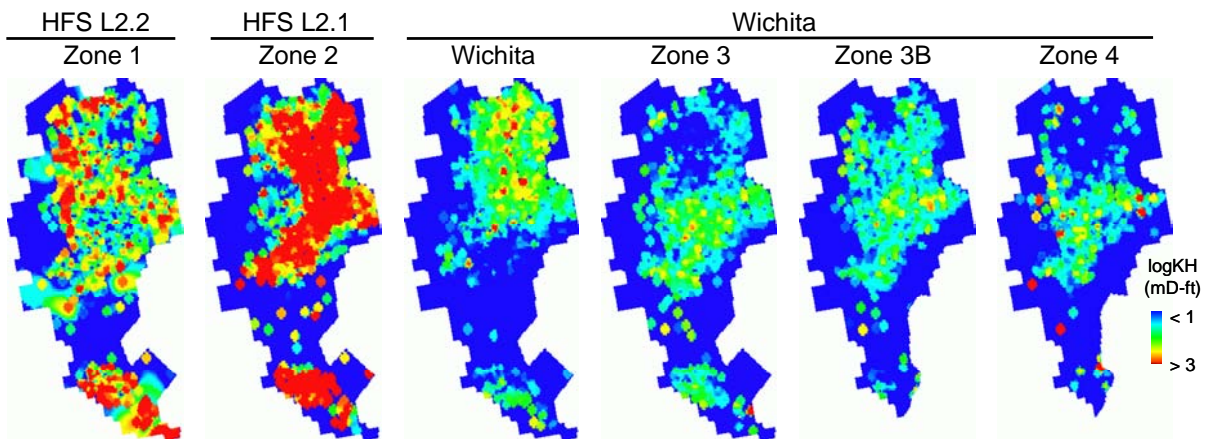


Figure 13. kh distribution in Zone 1, Zone 2, Wichita, Zone 3, Zone 3B, and Zone 4.

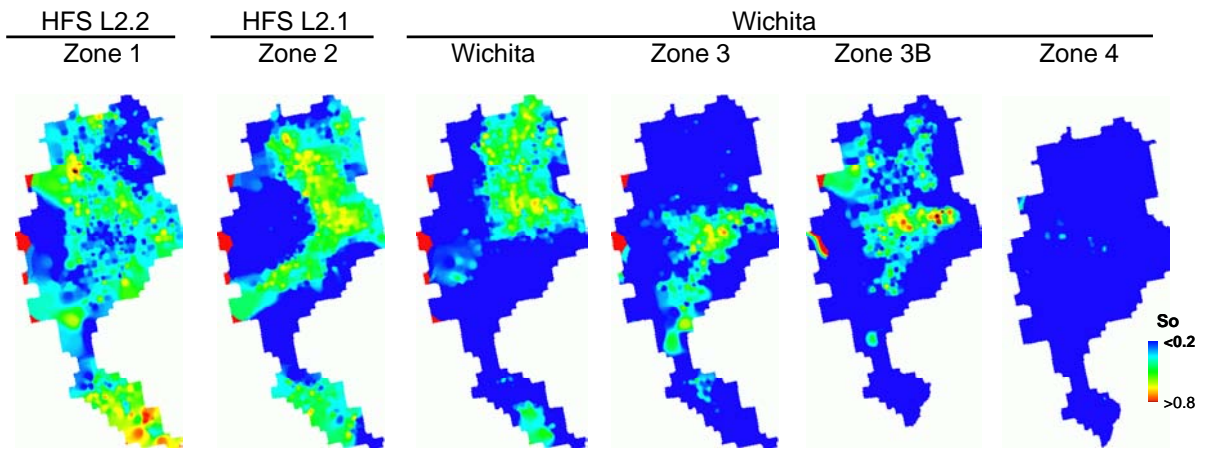


Figure 16. Water saturation distribution in Zone 1, Zone 2, Wichita, Zone 3, Zone 3B, and Zone 4.

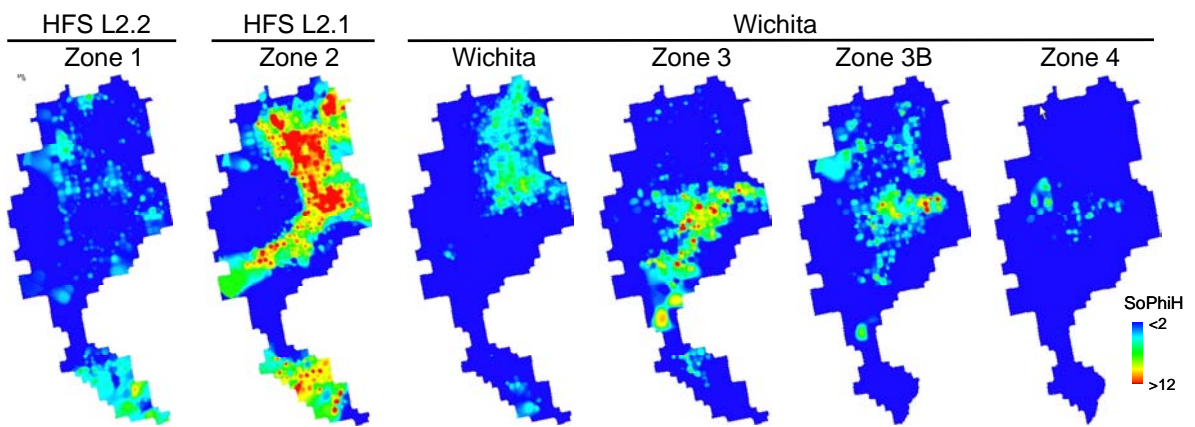


Figure 17. Hydrocarbon volume ($S_o\phi_h$) distribution in Zone 1, Zone 2, Wichita, Zone 3, Zone 3B, and Zone 4.

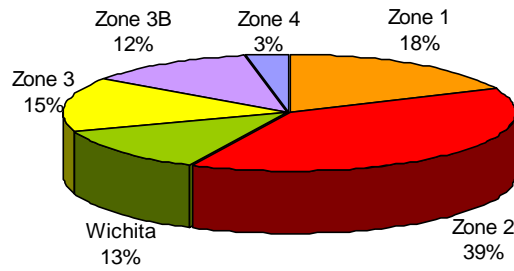


Figure 18. Hydrocarbon volume distribution in six reservoir zones.

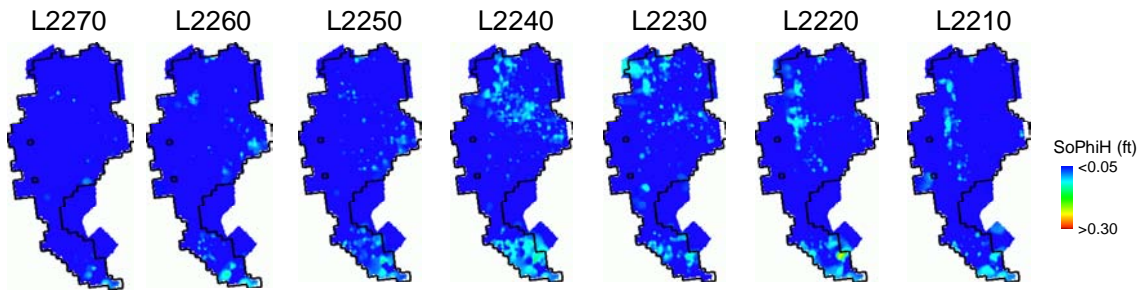


Figure 19. Hydrocarbon volume ($S_o\phi$) distribution in Zone 1 (Lower Clear Fork HFS L 2.2).

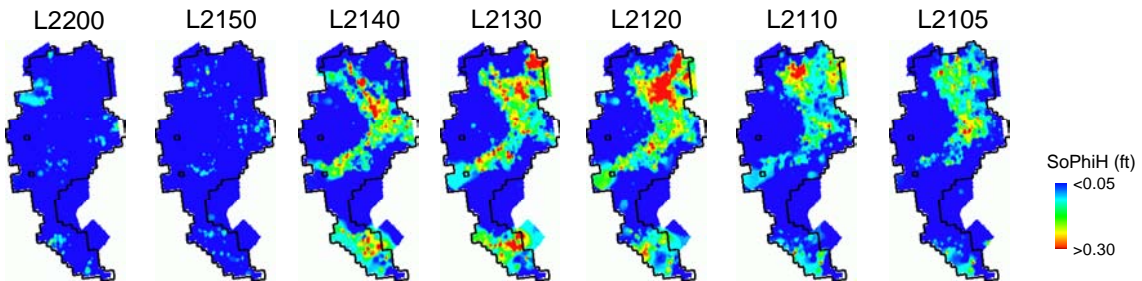


Figure 20. Hydrocarbon volume ($S_o\phi$) distribution in Zone 2 (Lower Clear Fork HFS L 2.1).

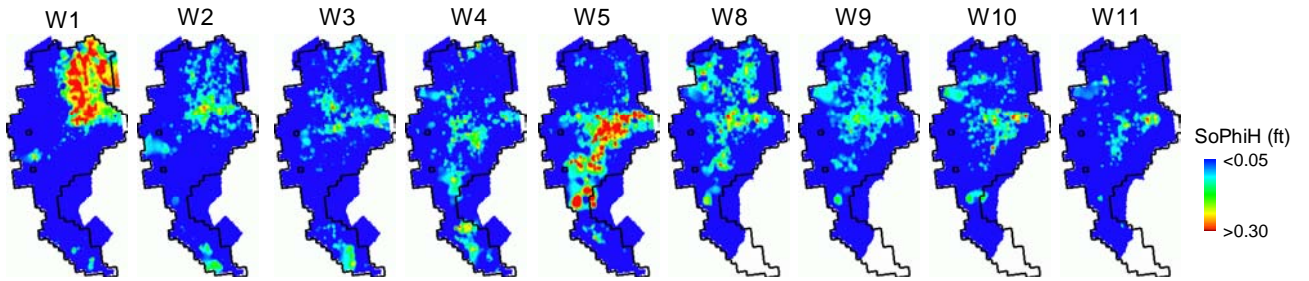


Figure 21. Hydrocarbon volume ($S_0\phi$) distribution in the Wichita Formation.

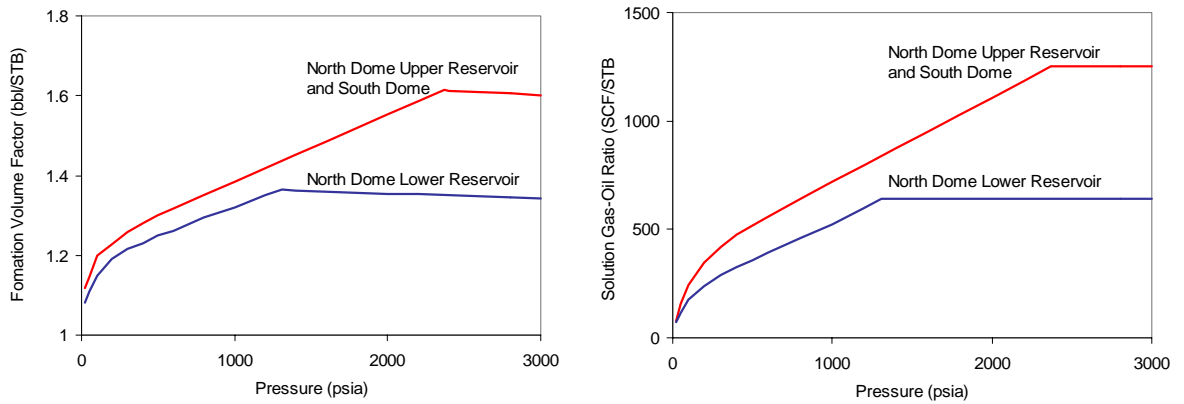


Figure 22. Formation volume factor and oil-gas ratio of two types of crude in FCU (from Field Study Group, 1973).

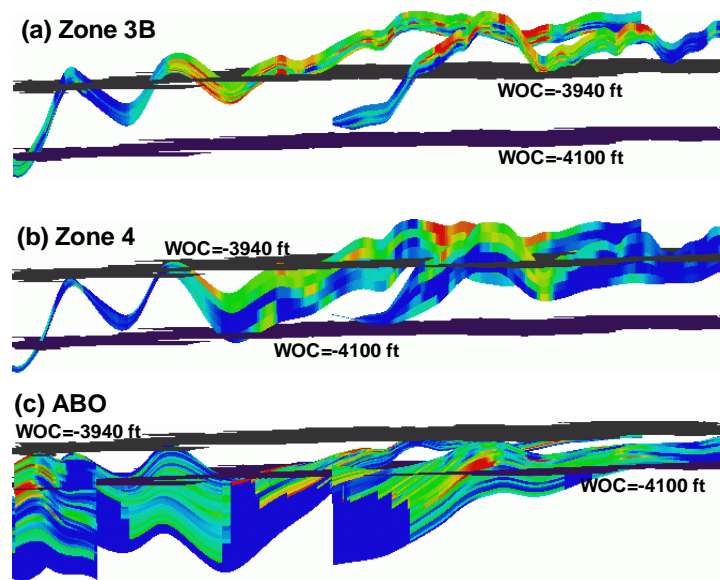


Figure 23. Effect of water-oil contact on vertical coverage in (a) Zone 3B, (b) Zone 4, and (c) Zone 5 (Abo).

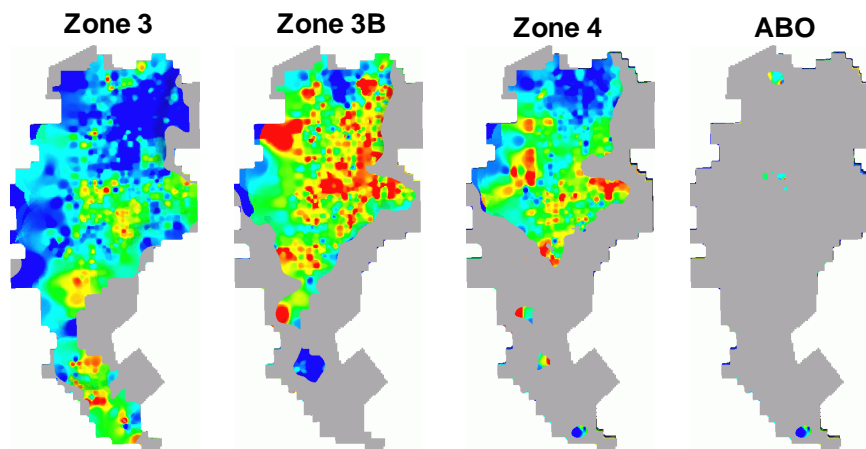


Figure 24. Effect of water-oil contact on areal coverage in Zone 3, Zone 3B, Zone 4, and Zone 5 (Abo).

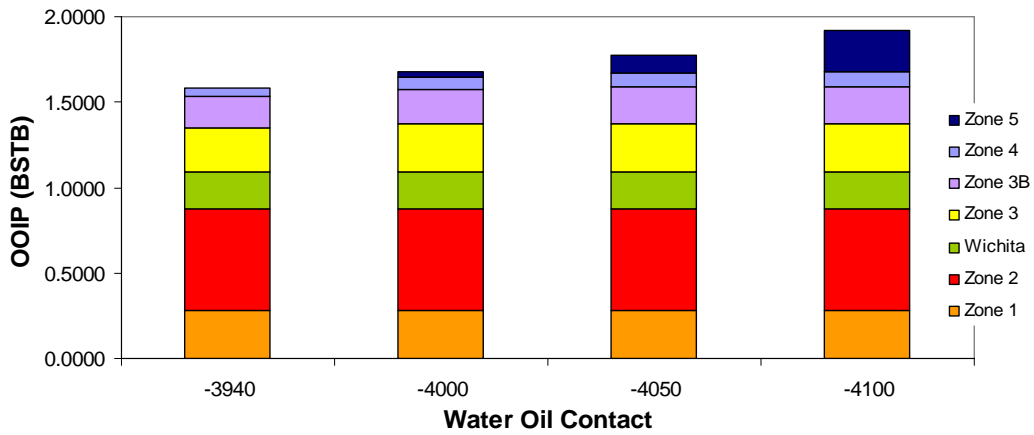


Figure 25. Effect of water-oil contacts on OOIP estimate.

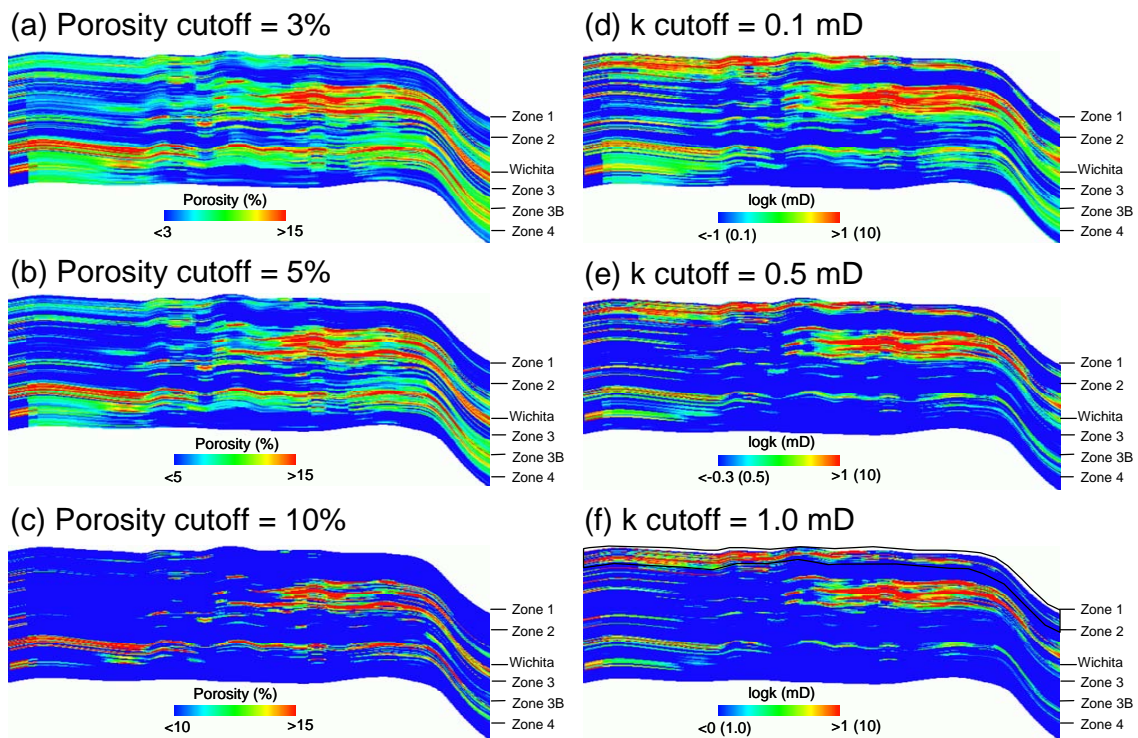


Figure 26. Effects of porosity cutoffs of (a) 3%, (b) 5% and (c) 10%, and permeability cutoffs of (d) 0.1, (e) 0.5 and (f) 1 mD on volumetrics.

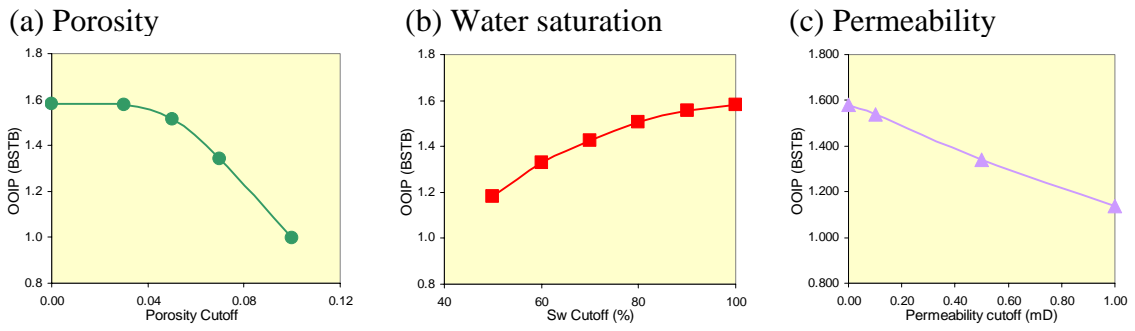


Figure 27. Effects of cutoff values on OOIP estimate: (a) porosity, (b) water saturation and (c) permeability.

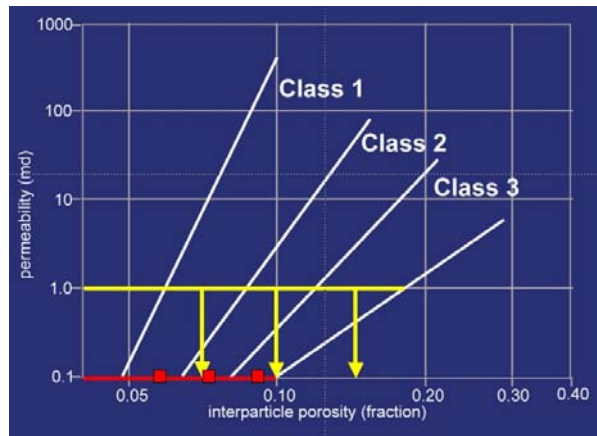


Figure 28. Relationship between permeability and porosity cutoff values. A specific permeability cutoff represents rock-fabric-dependent porosity cutoffs.

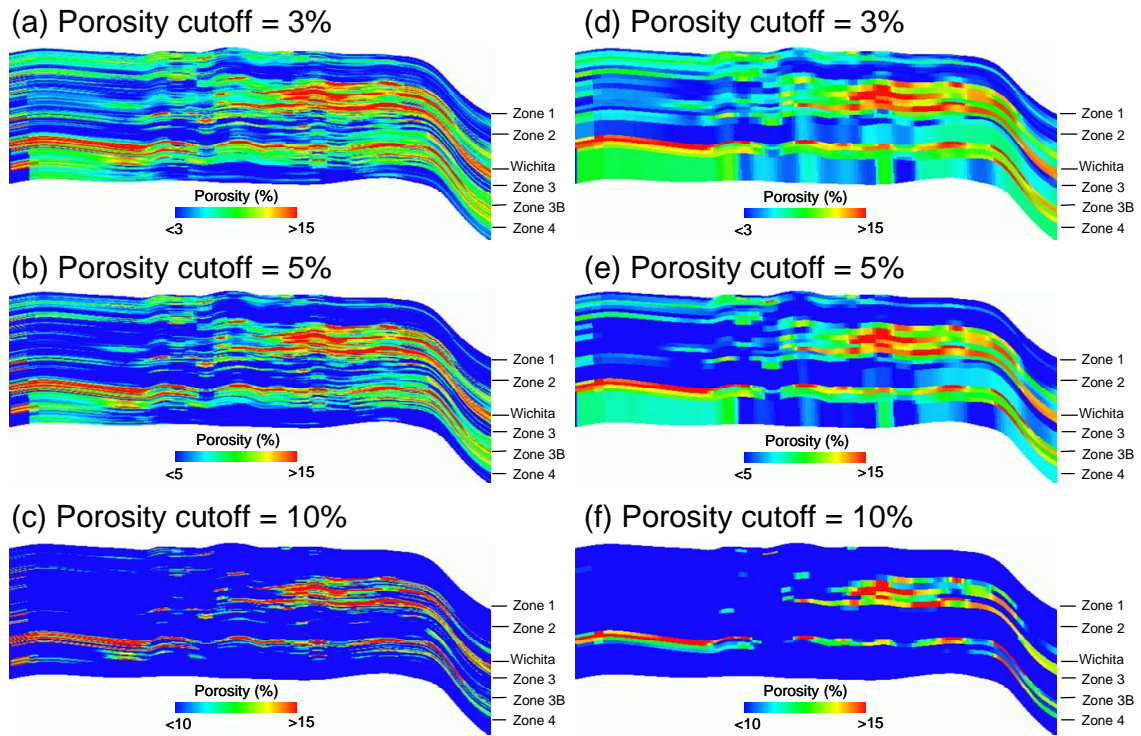


Figure 29. Effects of porosity cutoffs and grid vertical resolution on volumetrics, (a) 3%, (b) 5% and (c) 10% on fine-grid model, and (d) 3%, (e) 5% and (f) 10% on cycle-based model.

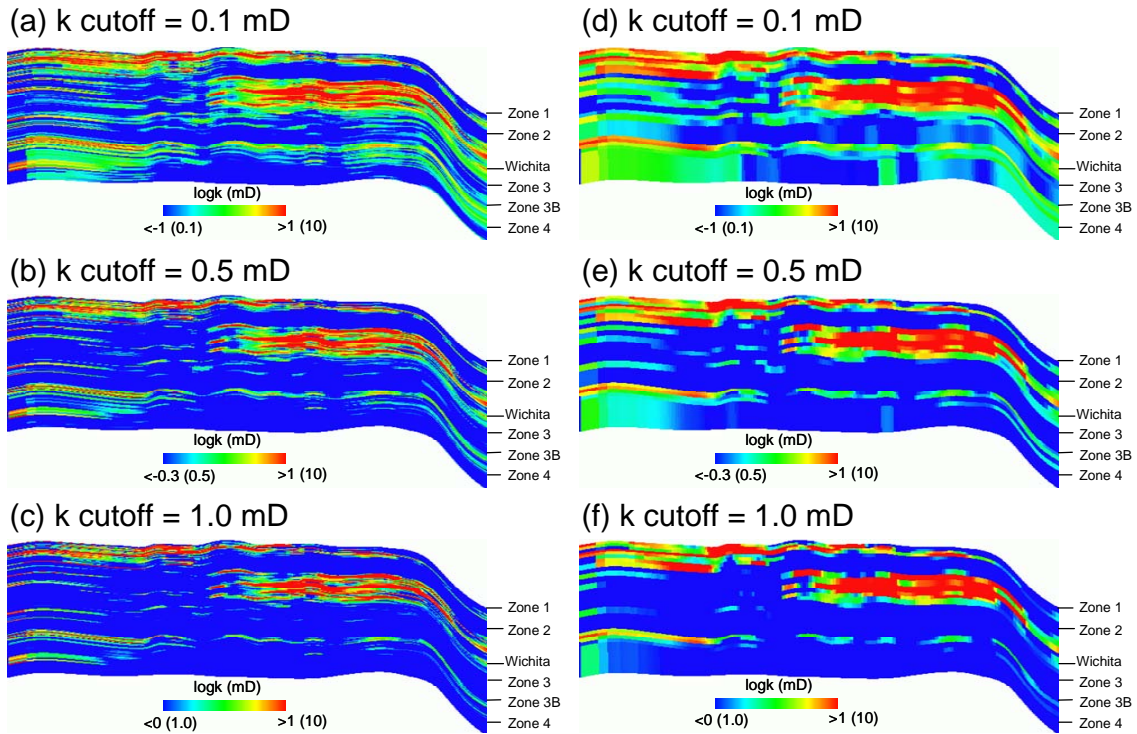


Figure 30. Effects of porosity cutoffs and grid vertical resolution on volumetrics, (a) 0.1, (b) 0.5 and (c) 1.0 mD on fine-grid model, and (d) 0.1, (e) 0.5 and (f) 1.0 mD on cycle-based model.

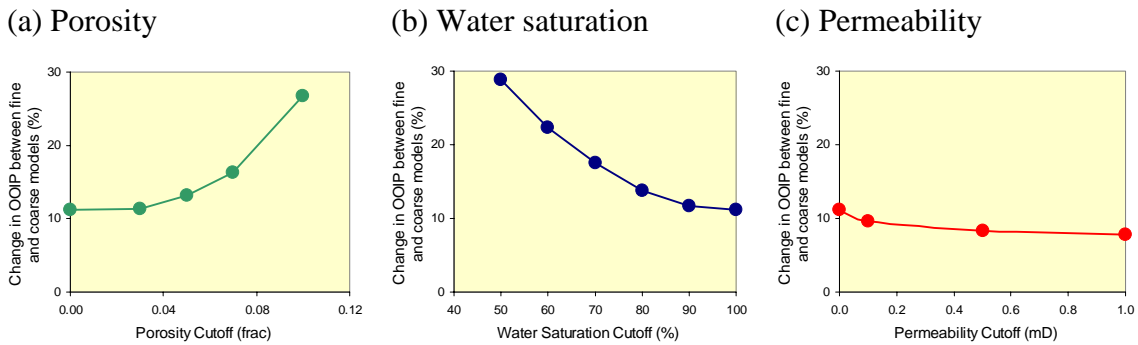


Figure 31. Changes in OOIP between high-resolution and cycle-based models with respect to (a) porosity cutoff, (b) water saturation cutoff and (c) permeability cutoff values.

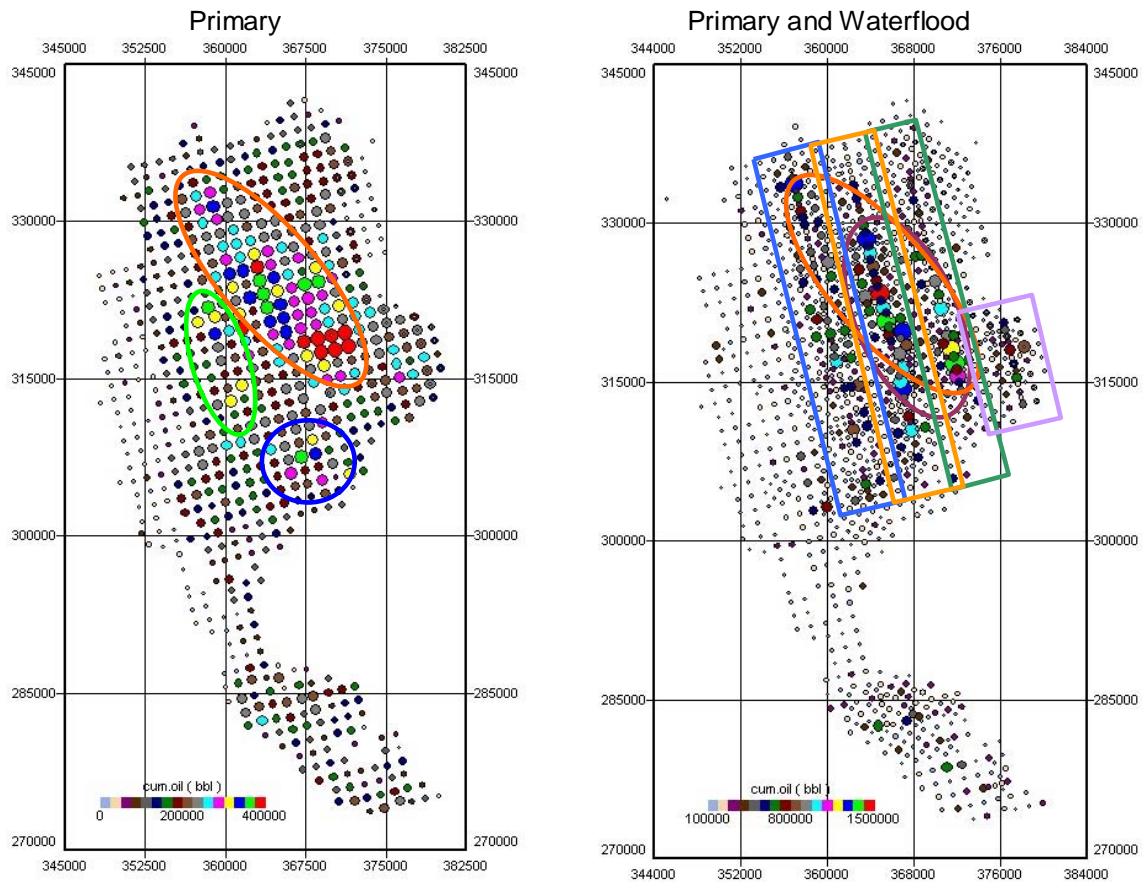


Figure 32. Production data and trends in primary and waterflooding.

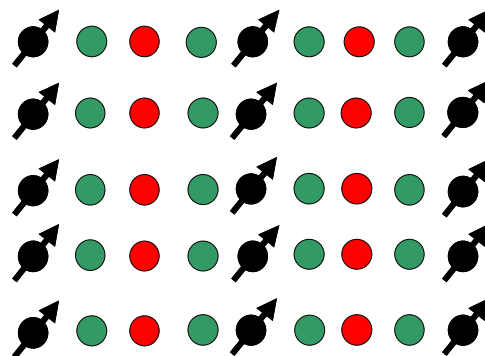


Figure 33. Initial 3:1 line-drive waterflooding pattern. Production is expected to be higher in the middle row of producers (red) than in the other two rows of producers closer to injectors (green).

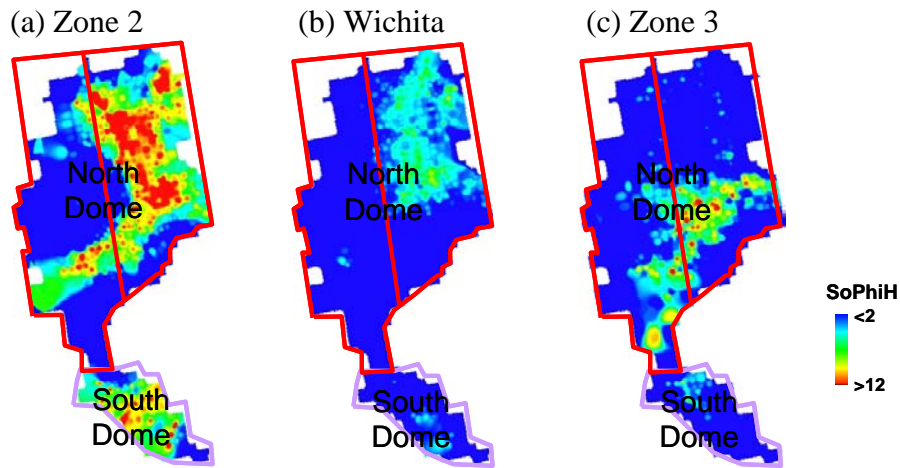


Figure 34. Porosity and $S_0\phi H$ in (a) Zone 2, (b) Wichita, and (c) Zone 3, overlaid with production trends. The best production areas during primary and waterflooding coincide with the high porosity and $S_0\phi H$ trends in zone.

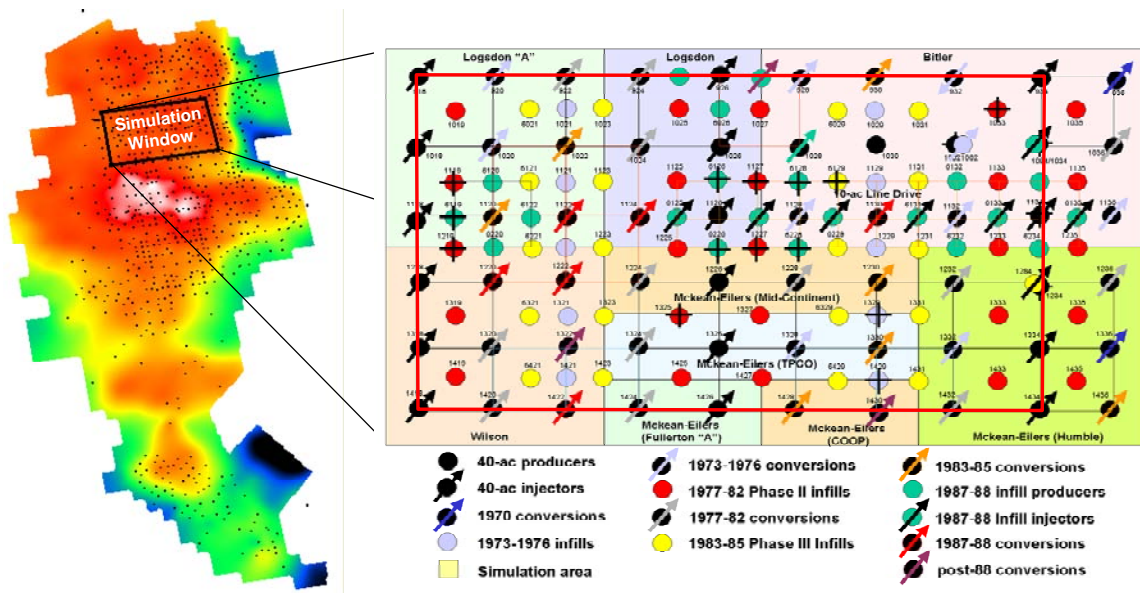
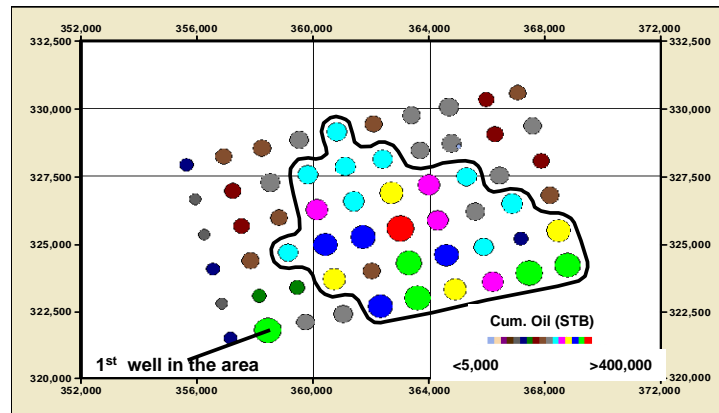


Figure 35. Water-injection patterns in the initial reservoir model area in 2001. The area of reservoir simulation is outlined by the red box. Development history is illustrated by colored symbols.

(a) Primary recovery



(b) Waterflooding recovery

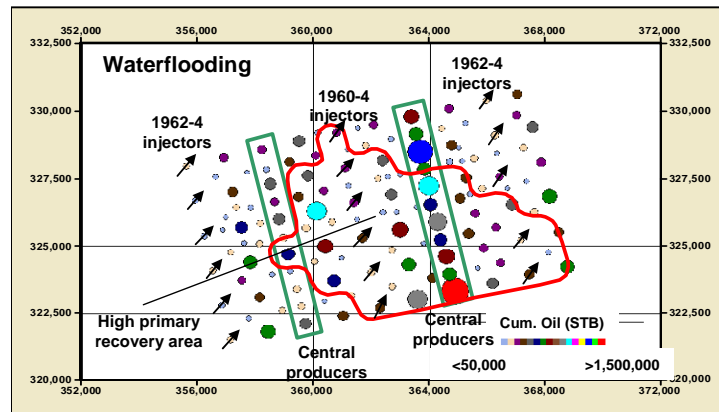


Figure 36. Production data and trends in (a) primary and (b) waterflooding in simulation area.

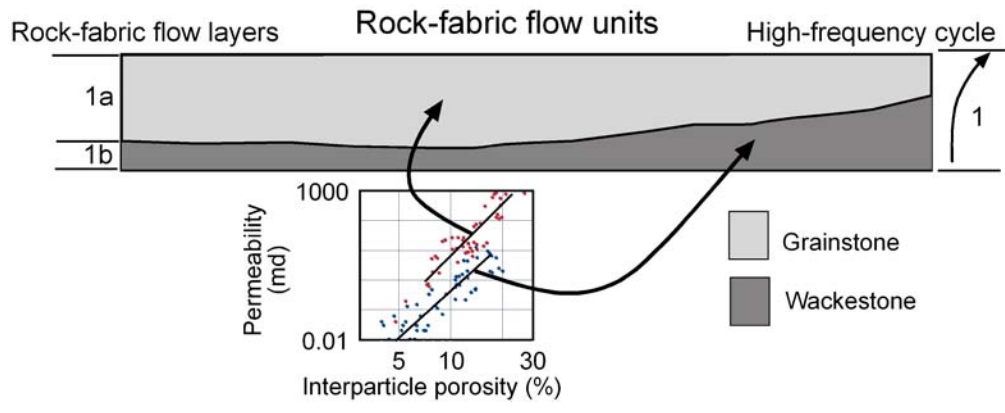
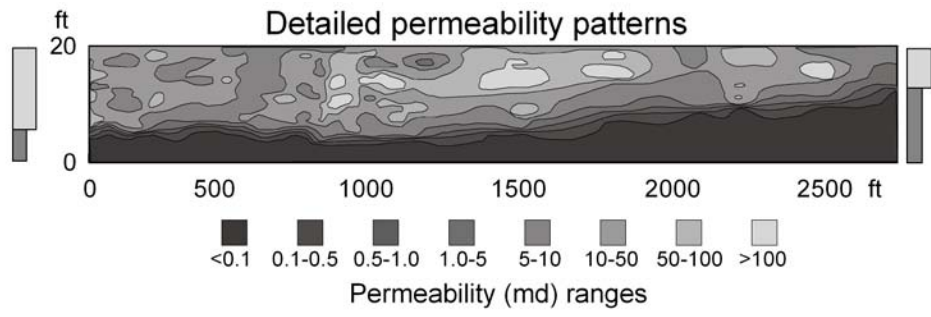


Figure 37. Lawyer Canyon cycle 1 flow-layer model.

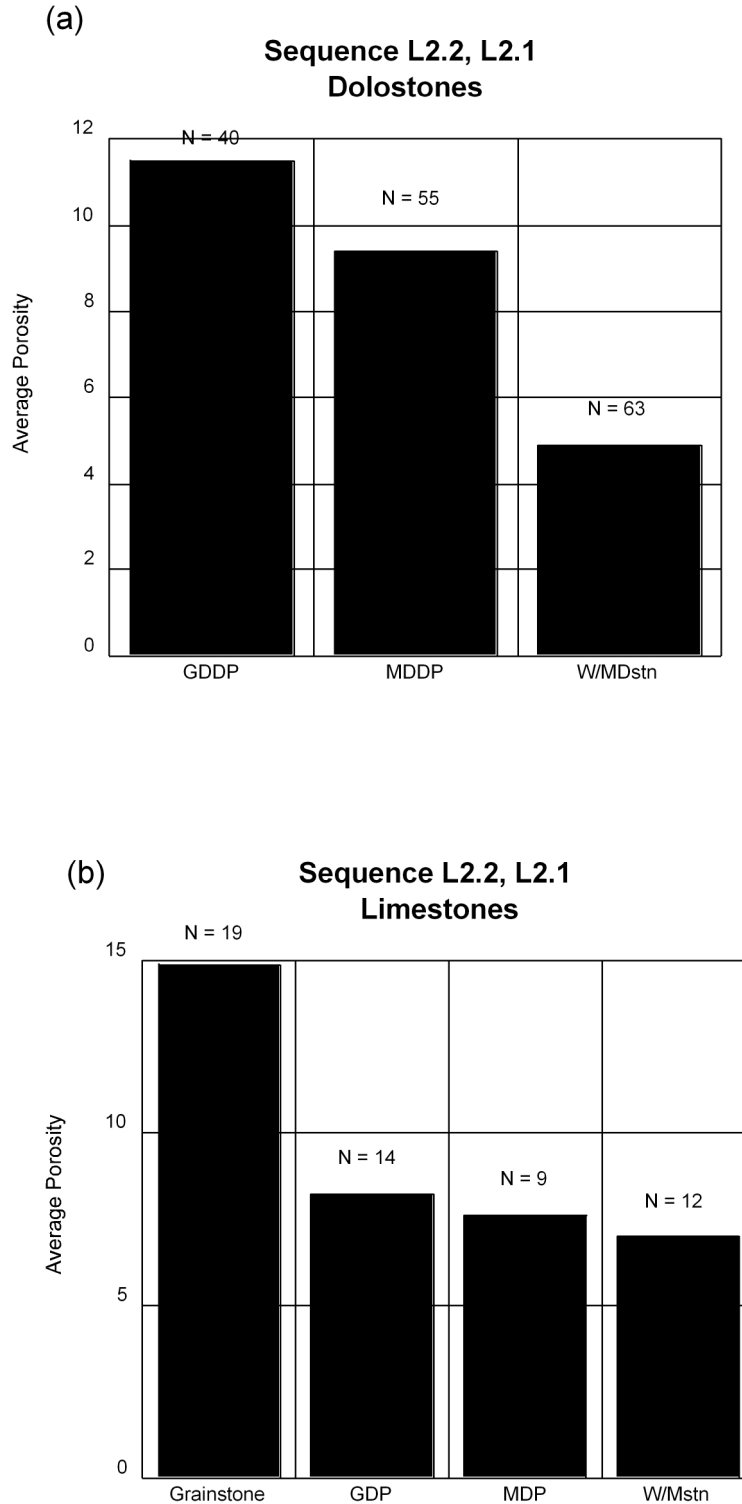


Figure 38. Average porosity for various rock fabrics in sequences L2.1 and L2.2. (a) Dolostone rock fabrics showing decrease in porosity with increasing lime mud. (b) Limestone rock fabrics showing high porosity correlated with grainstones. Grain-dominated packstones (GDP) may have sufficient lime mud to be described as mud dominated packstones (MDP).

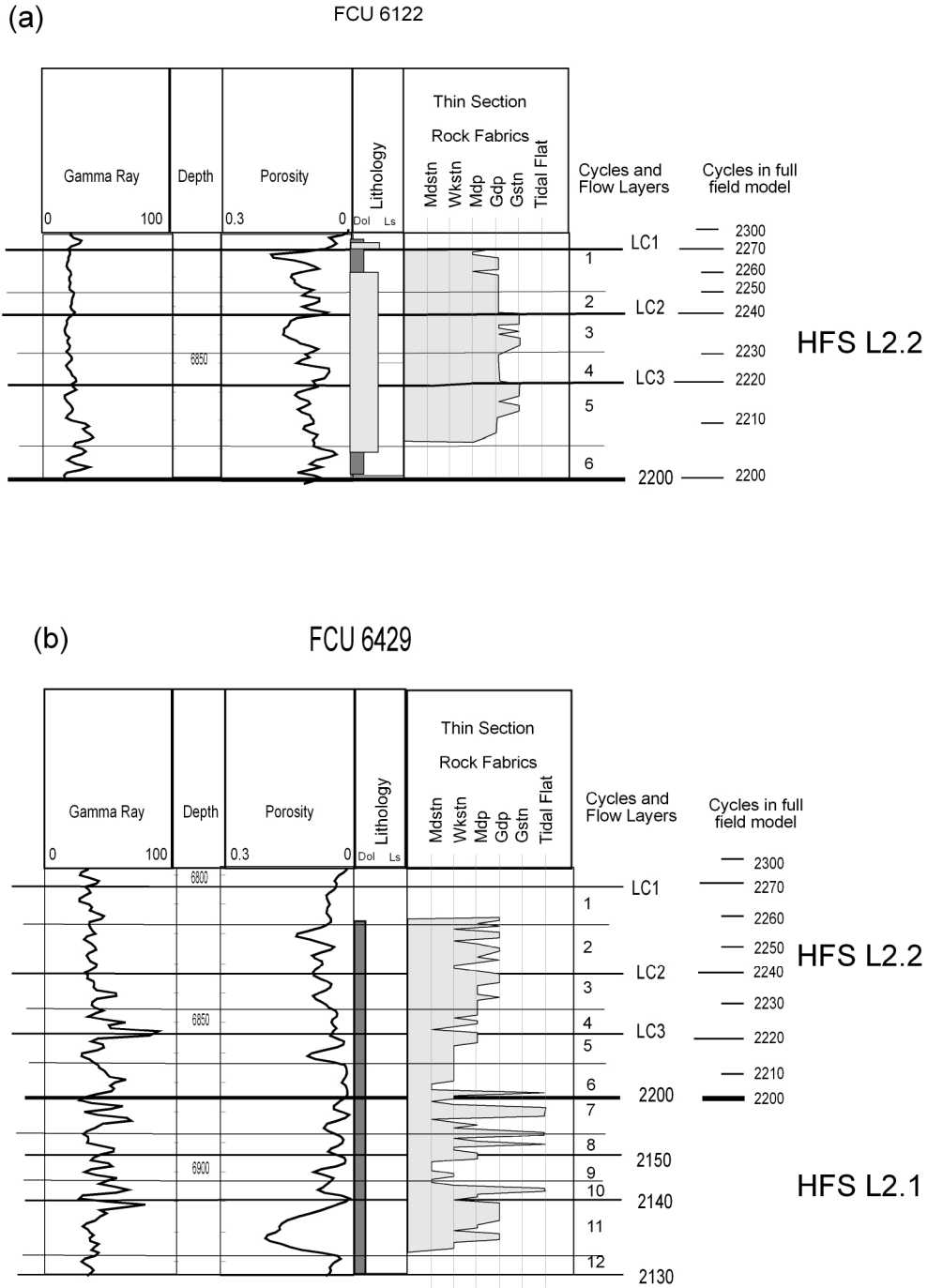


Figure 40. Flow layers in sequence L2.2. The cycles and flow layers in the simulation model are compared with the cycles in the full field model. (a) In the limestone area there is a reasonable correlation between cycles, flow layers, and porosity. (b) In the dolostone area the correlation between cycles, flow layers, and porosity is less apparent.

Wichita FCU 5927

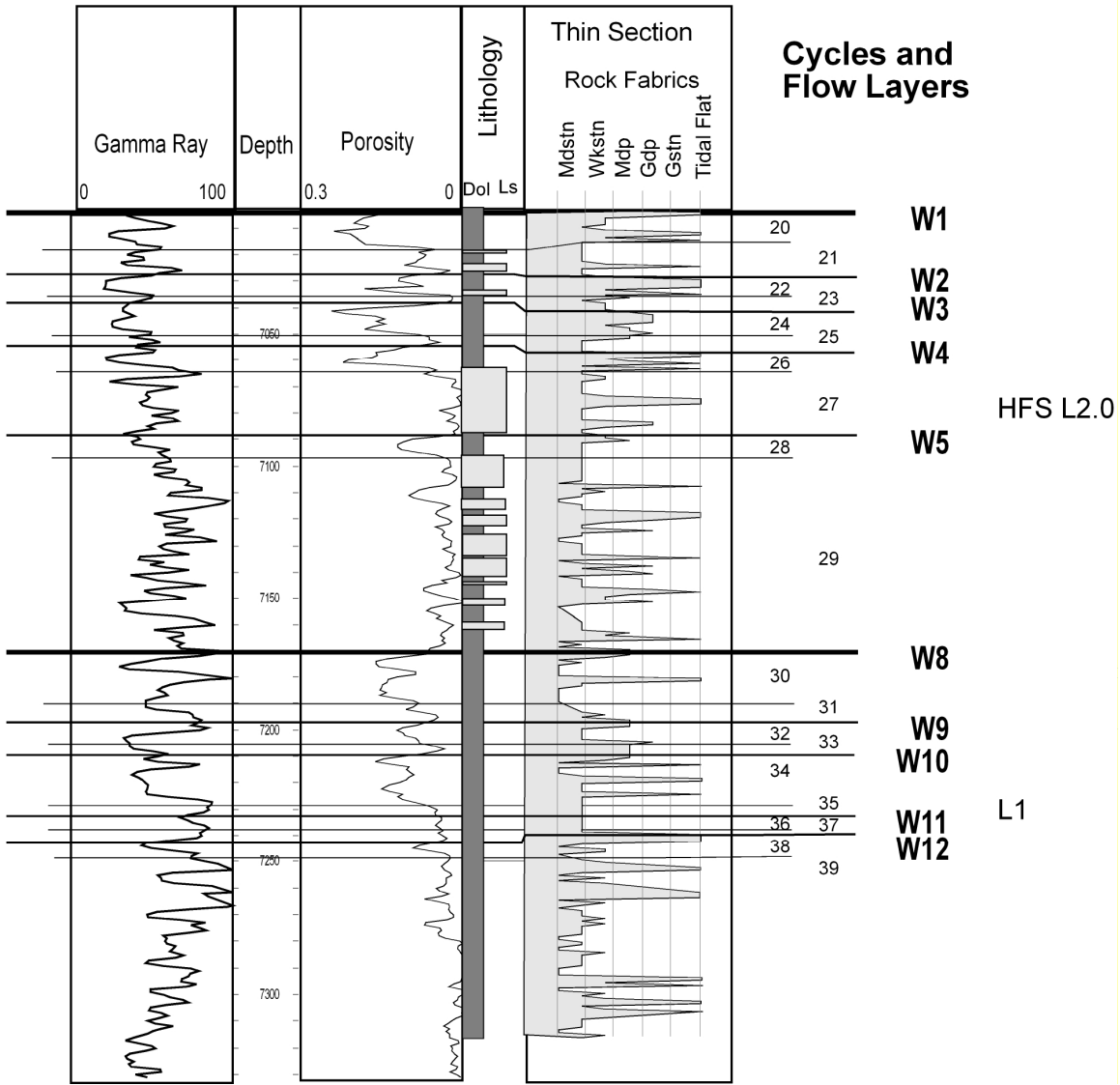


Figure 41. Flow layers in the Wichita.

Flow Unit Architecture

Fullerton Clear Fork/Wichita Reservoir

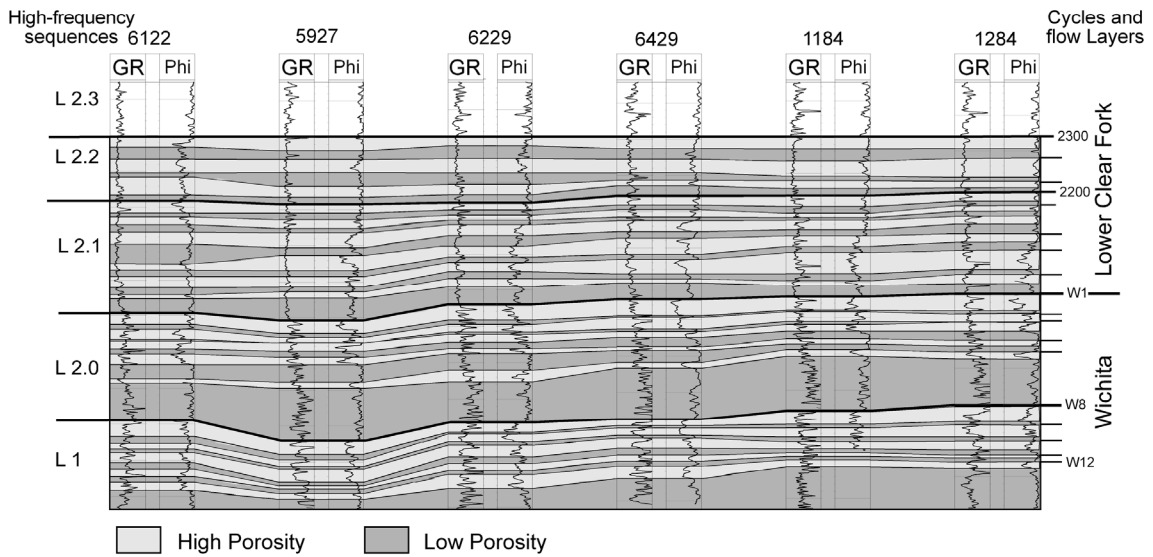


Figure 42. Lower Clear Fork and Wichita flow layers in cored wells of simulation area illustrating the use of porosity to build a flow model.

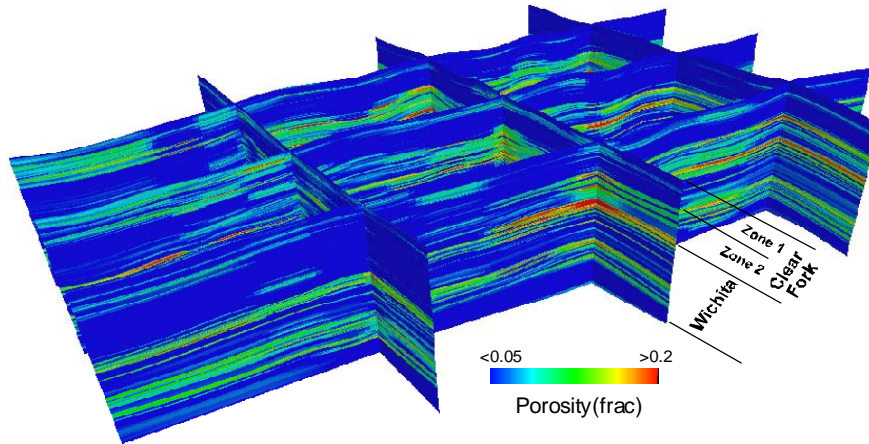


Figure 43. Porosity distribution in the simulation area.

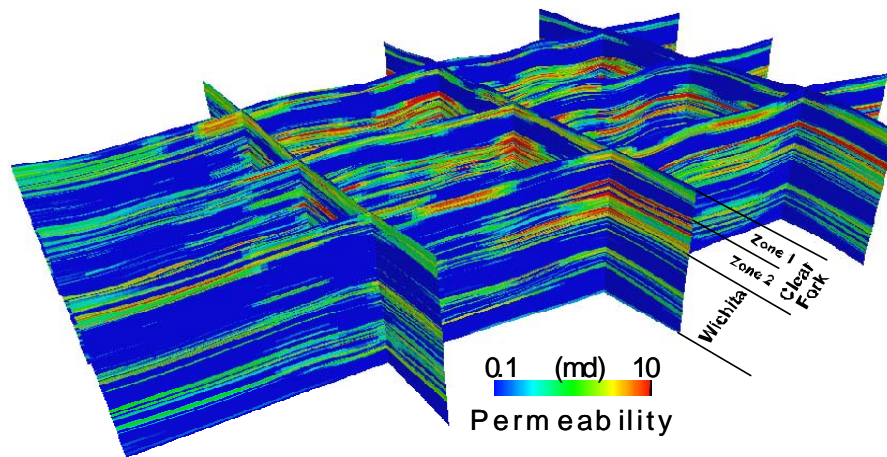


Figure 44. Permeability distribution in the simulation area.

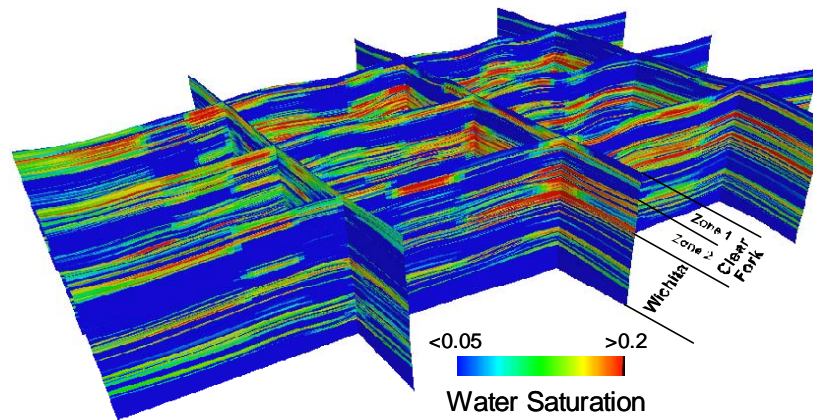


Figure 45. Water saturation distribution in the simulation area.

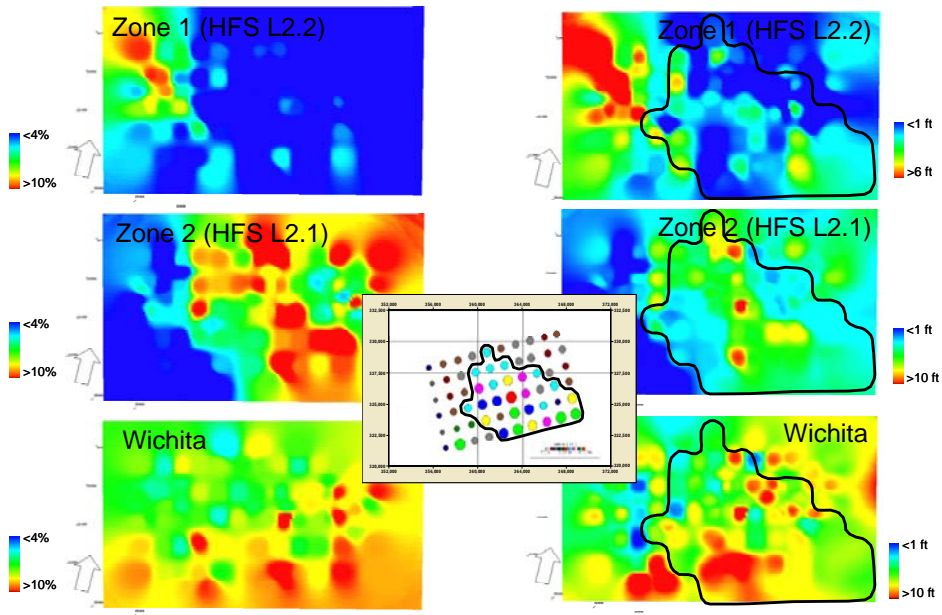


Figure 46. Porosity and $S_o\phi h$ trends in the simulation area.

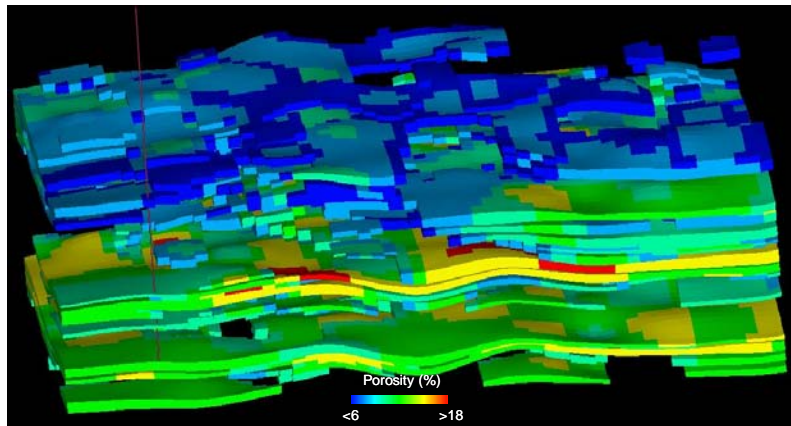


Figure 47. Porosity distribution in simulation model.

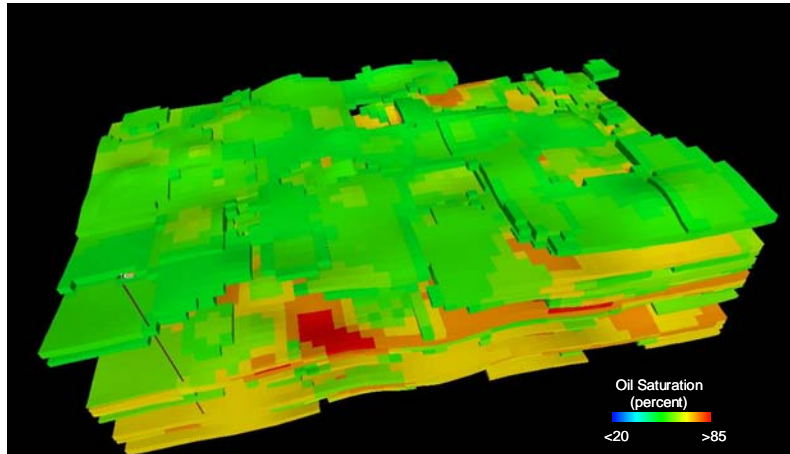


Figure 48. Initial oil saturation in simulation model.

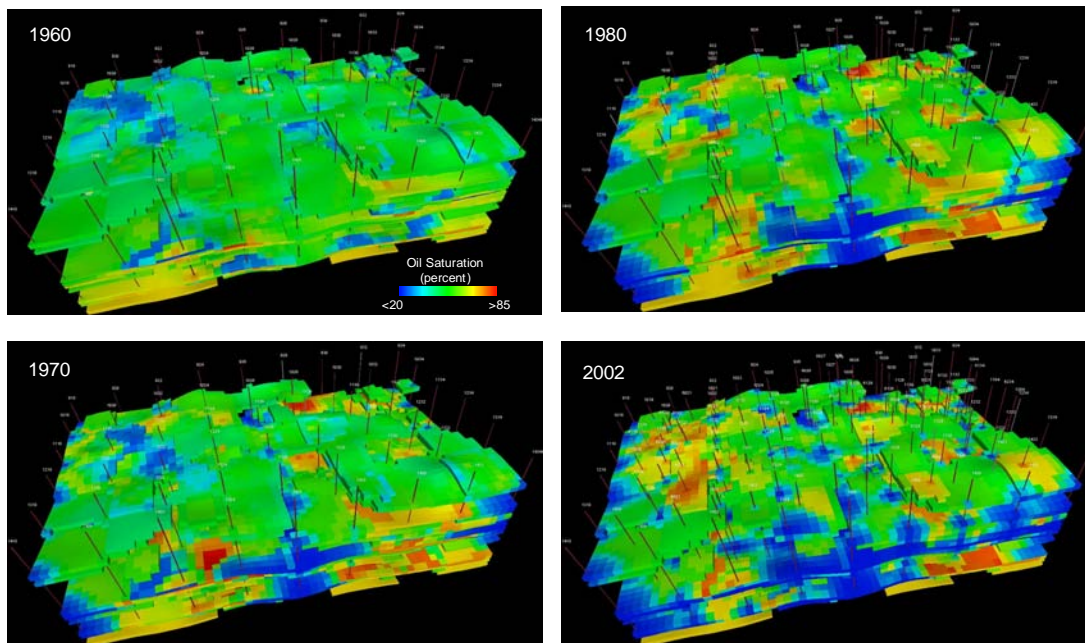


Figure 49. Simulated oil saturation in 1960, 1970, 1980, and 2002, simulation area.

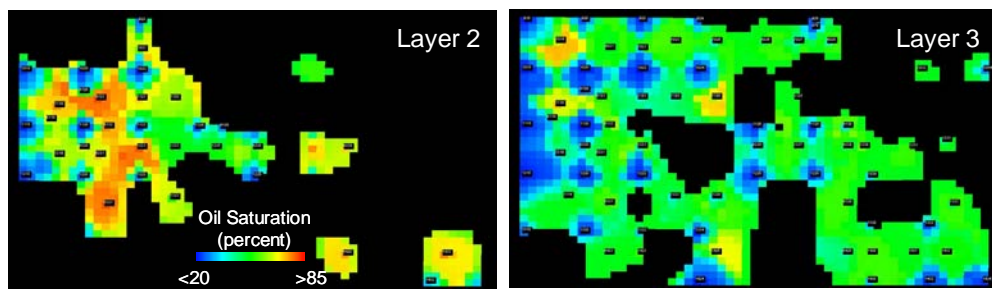


Figure 50. Simulated oil saturation in 2002, in Zone 1.

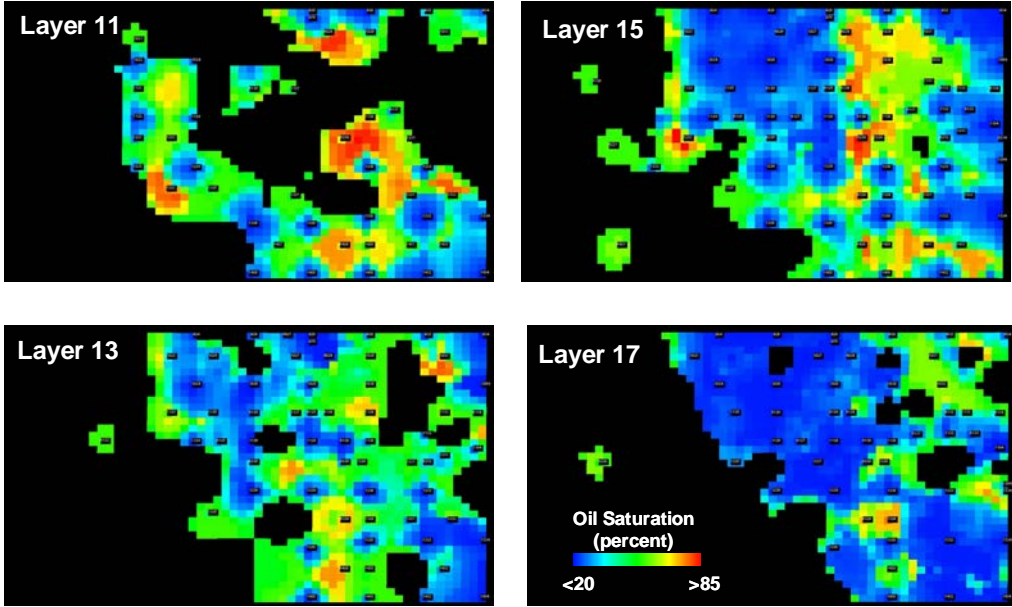


Figure 51. Simulated oil saturation in 2002, in selected model layer slices of the Lower Clear Fork HFS L2.1 (reservoir Zone 2).

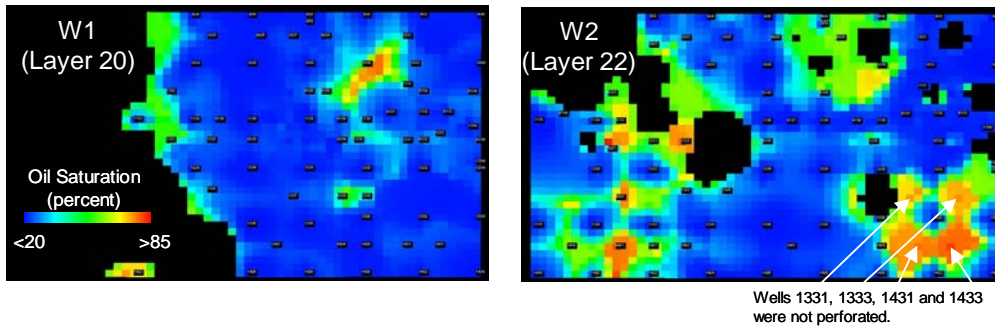


Figure 52. Simulated oil saturation in 2002, in upper model layers of the Wichita.

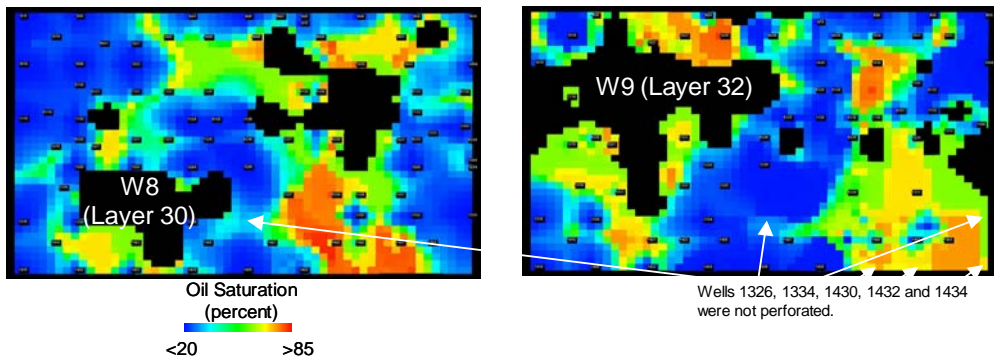


Figure 53. Simulated oil saturation in 2002, in model layers of Wichita reservoir Zone 3B. Note that the oil has not been produced or swept from the southeasternmost part of the model area.

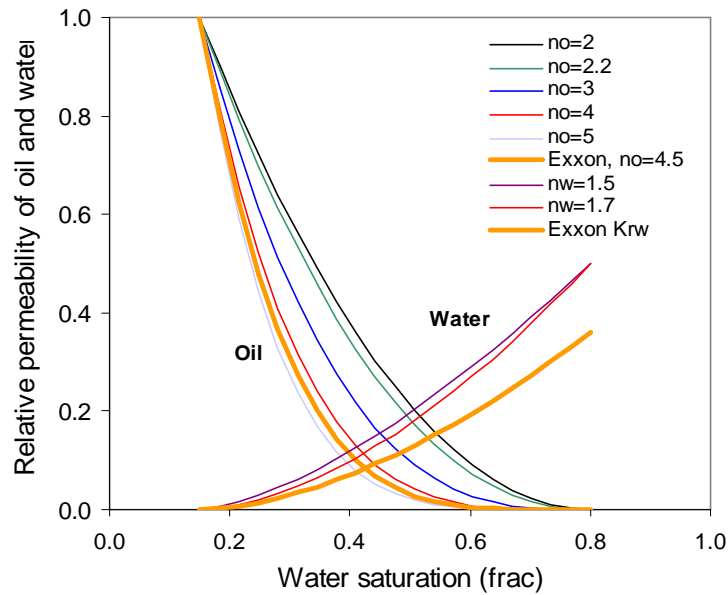
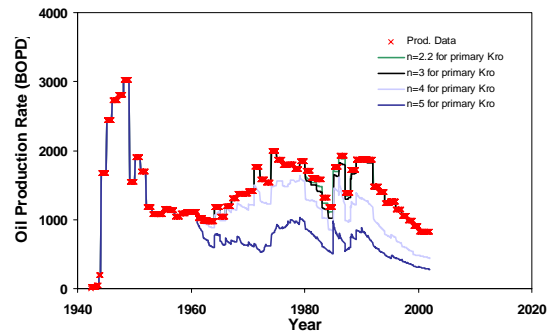
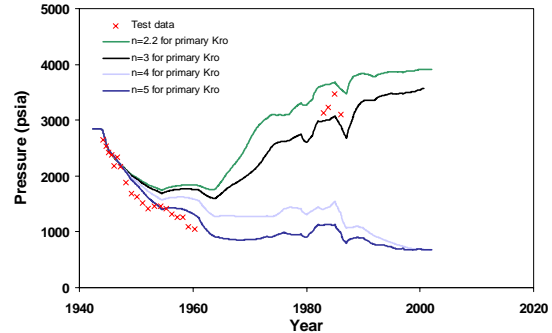


Figure 54. Corey correlations for relative permeability.

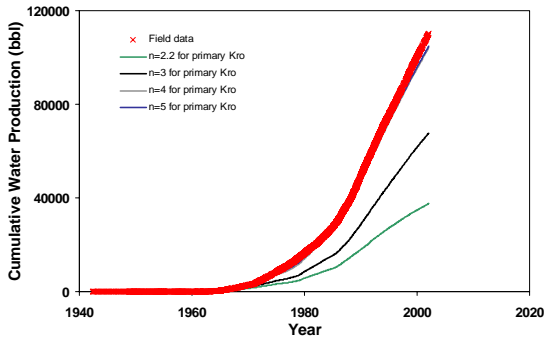
(a) Oil rate



(c) Pressure



(b) Water rate



(d) Oil recovery

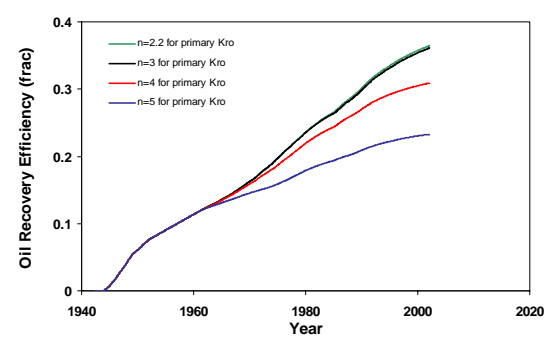


Figure 55. Effect of relative permeability on simulated (a) oil rate, (b) water rate, (c) pressure and (d) oil recovery.

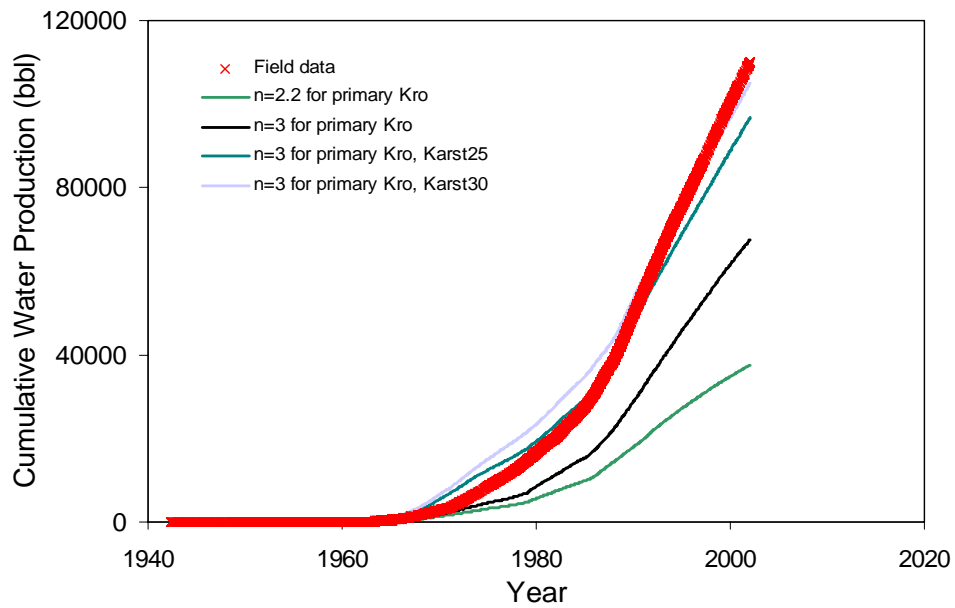


Figure 56. Effect of permeability multiplication on simulated water production.

APPENDIX A: UPSCALING

Permeability Upscaling in Vertical Direction

Because the vertical resolution of 3D static models is commonly much coarser than that of wireline logs, upscaling is an issue encountered in several stages in 3D modeling. The arithmetic mean is normally used in porosity and water saturation upscaling. Permeability upscaling in vertical direction, the frequently debated issue between geologists and engineers, should be resolved in the early stage of 3D modeling. The argument for geologists is that because permeability data are commonly log-normally distributed, geometric mean should be used according to the statistical theorem; the argument for engineer is that upscaling is a process of averaging based on the theory of fluid flow through porous media rather than the geometric mean based on the statistical theory.

The differences in permeability among arithmetic, geometric means and a k - ϕ correlation (Lucia, 1999) can be demonstrated by simple two-layer models shown in table A.1 and fig. A.1. Permeabilities for class 2 rock-fabric carbonates is given by Lucia (1999)

$$k_{rf2} = 10^{6.1736\log(\phi/100)+6.1606} \quad (\text{A.1})$$

Where

k_{rf2} : permeability (mD) for class 2 rock-fabric carbonate

ϕ : porosity (percent)

Layer 1 is a 2-ft thick layer with a porosity of 20 percent and a permeability of 70.06 mD. Layer 2 is 5-ft thick layer with porosity values varying from 19 to 7.5%, and permeability values of 11.86 and 0.164 mD in case 1 to 14. The two different thicknesses for layer 1

and 2 are to show the effect of thickness-weighting on averages and the fourteen cases in layer 2 are to show the effect of permeability contrast on different averages. Unweighted and thickness weighted average porosities are calculated by

$$\varphi_{unw} = \frac{\sum_{i=1}^n \varphi_i}{n} \quad (\text{A.2})$$

$$\varphi_w = \frac{\sum_{i=1}^n \varphi_i h_i}{\sum_{i=1}^n h_i} \quad (\text{A.3})$$

unweighted and weighted arithmetic-mean permeabilities are calculated by

$$k_{AM_unw} = \frac{\sum_{i=1}^n k_i}{n} \quad (\text{A.4})$$

$$k_{AM_w} = \frac{\sum_{i=1}^n k_i h_i}{\sum_{i=1}^n h_i} \quad (\text{A.5})$$

unweighted and weighted geometric-mean permeabilities are calculated by

$$k_{GM_unw} = \sqrt[n]{k_1 \dots k_n} = 10^{\frac{\sum_{i=1}^n \log k_i}{n}} \quad (\text{A.6})$$

$$k_{GM_w} = 10^{\frac{\sum_{i=1}^n h_i \log k_i}{\sum_{i=1}^n h_i}} \quad (\text{A.7})$$

where

φ_{unw} : unweighted average porosity (percent)

φ_w : thickness weighted average porosity (percent)

| | |
|-----------------|--|
| φ_i : | porosity (percent) of layer i |
| h_i : | thickness (ft) of layer i |
| k_{AM_unw} : | unweighted arithmetic-mean permeability (mD) |
| k_{GM_unw} : | unweighted geometric-mean permeability (mD) |
| k_{AM_w} : | thickness weighted arithmetic-mean permeability (mD) |
| k_{GM_w} : | thickness weighted geometric-mean permeability (mD) |
| k_i : | permeability of layer i (mD) |

In table A.2, arithmetic and geometric means in permeability were compared to the permeabilities derived from the permeability-porosity correlation (eq. A.7). Because the porosity in the thicker 2nd layer is lower than the 1st layer, thickness-weighted porosities and permeabilities are lower than the unweighted. According to the theory of single-phase fluid flow through porous media, permeabilities of the two-layer systems are the thickness-weighted arithmetic means (highlighted in table A.2). Three averaged permeabilities are plotted with respect to the permeability contrast between two layers in figure A.2.a. This figure shows that permeabilities derived from the permeability-porosity correlation are closer to those from geometric mean than arithmetic mean, and permeabilities from geometric mean and from k - ϕ correlation tend to underestimate the average permeability. Differences in permeability between arithmetic mean and geometric mean or derived from the permeability-porosity correlation (figure A.2.a and b) increase with permeability contrasts between two layers. This difference can be in an order of magnitude or higher in highly heterogeneous, stratified systems.

In figure A.2.c, thickness-weighted arithmetic and geometric means were plotted with respect to thickness-weighted average porosity. Note that in stratified systems permeability values from arithmetic mean do not follow permeability and porosity correlations derived from core data (the curve in figure A.2.c). Arithmetic means (crosses in figure A.2.c) shift from the k - ϕ correlation (curve in figure A.2.c) to the vertical line for fractured systems with the permeability contrast between two layers. The effect of high-permeability layer on permeability in stratified system, similar to the effect of fracture on fractured systems, is to increase permeability sharply compared to the increase in porosity.

To determine general porosity and permeability trends, additional four two-layer models with porosity in layer 1 of 14, 16, 18 and 22 percent were studied. Each model includes seven to ten cases with different porosities in layer 2. Figures A.3.a and b show average permeability from arithmetic mean and ratio of arithmetic mean to geometric mean as functions of permeability contrast between layer 1 and 2. Arithmetic-mean permeabilities of two-layer models decline exponentially from permeability ratio between layers 1 and 2 from 1 to about 50, and then gradually leveled off to asymptotic values (fig. A.3.a). It is interesting to note in fig. A.3.b that ratios of arithmetic to geometric means of five models fall into a single curve as a function of permeability contrast between layers 1 and 2. In reality, the geometric mean will overly underestimate the permeability of the lumped model (which is the arithmetic mean) when the permeability contrast between two layers is great than 10. Figure A.3.c compares average porosity and permeability trends in five two-layer models to the trend from core data (curve in figure A.3.c). Permeabilities in layered systems (figure A.3.c) are dominated by the high-

permeability layers and shift towards fractured systems when the permeability contrast increases. Permeabilities in most 3D models with vertical scales greater than scales of log and core data are commonly controlled by large-scale features such as stratifications, stacking patterns, permeability contrasts among strata, fractures, *etc.*, and are much higher than those calculated from geometric mean and k - ϕ correlations. This explains one of the reasons why permeability values in upscaled simulation models based on geometric average or k - ϕ correlations often need to be increased by an order of magnitude or more during history matching.

Volumetrics

The compound effects of grid vertical resolution and cutoffs on OOIP are complicated and unpredictable. This can be demonstrated using a ten-layer model shown in fig. A.4. This model is to simulate a typical cycle in carbonate which can be divided into two flow unit with a high-porosity unit at the top and low-porosity unit at the base. The 10-layer model is first upscaled to a two-layer flow unit model, and then to a single-layer cycle model. Porosity and permeability values are upscaled using the arithmetic averaging method.

When porosity cutoff of 0.05 is used (fig. A.5.a), two layers with porosity of 0.04 are excluded from the 10-layer model and 80 percent of bulk volume used in volumetrics; the lower flow unit is excluded from flow unit model and only 50 percent of bulk volume is used in volumetrics; and 100 percent of bulk volume is used in volumetrics in the single-layer cycle model. That is to say, among three models the single-layer cycle model calculates the higher volumetrics than the high-resolution ten-layer, and the two-layer flow unit model calculates the least volumetrics. Although OOIP from the high-

resolution is the most realistic but OOIP from the single-layer cycle model can be slightly higher than that from the 10-layer high-resolution model and the two-layer flow-unit model calculates lowest OOIP.

When porosity cutoff of 0.1 is used (fig. A.5.b), five low-porosity layers in the ten-layer model, the lower flow unit in the two-layer model and the entire cycle model are excluded from volumetric calculation.

OOIP is a complex function of grid vertical resolution, petrophysical properties and cutoff values, and how the grid vertical resolution and cutoffs affecting OOIP cannot be predicted. OOIP from high-resolution models are more realistic but not always higher than that from the coarse models.

Table A.1. Parameters used in a two-layer model for the case study.

| Case No. | Layer No. | Thickness (ft) | Porosity (%) | Permeability (mD) | Permeability ratio |
|----------|-----------|----------------|--------------|-------------------|--------------------|
| | 1 | 2 | 20 | 70.055 | |
| 1 | 2 | 5 | 19 | 51.040 | 1 |
| 2 | 2 | 5 | 18 | 36.555 | 2 |
| 3 | 2 | 5 | 17 | 25.686 | 3 |
| 4 | 2 | 5 | 16 | 17.667 | 4 |
| 5 | 2 | 5 | 15 | 11.861 | 6 |
| 6 | 2 | 5 | 14 | 7.747 | 9 |
| 7 | 2 | 5 | 13 | 4.903 | 14 |
| 8 | 2 | 5 | 12 | 2.991 | 23 |
| 9 | 2 | 5 | 11 | 1.748 | 40 |
| 10 | 2 | 5 | 10 | 0.971 | 72 |
| 11 | 2 | 5 | 9 | 0.506 | 138 |
| 12 | 2 | 5 | 8.5 | 0.356 | 197 |
| 13 | 2 | 5 | 8 | 0.245 | 286 |
| 14 | 2 | 5 | 7.5 | 0.164 | 426 |

Table A.2. Results of average porosities and permeabilities of fourteen cases of a two-layer model.

| Case No. | Permeability ratio | Porosity (frac) | Permeability (mD) | | | Permeability ratio | |
|------------|--------------------|-----------------|-------------------|-------|--------|--------------------|-------------|
| | | | AM | GM | k-poro | AM/GM | AM/(k-poro) |
| unweighted | 1 | 19.50 | 60.55 | 59.80 | 59.92 | 1.01 | 1.01 |
| | 2 | 19.0 | 53.31 | 50.61 | 51.04 | 1.05 | 1.04 |
| | 3 | 18.5 | 47.87 | 42.42 | 43.29 | 1.13 | 1.11 |
| | 4 | 18.0 | 43.86 | 35.18 | 36.56 | 1.25 | 1.20 |
| | 5 | 17.5 | 40.96 | 28.83 | 30.72 | 1.42 | 1.33 |
| | 6 | 17.0 | 38.90 | 23.30 | 25.69 | 1.67 | 1.51 |
| | 7 | 16.5 | 37.48 | 18.53 | 21.36 | 2.02 | 1.75 |
| | 8 | 16.0 | 36.52 | 14.48 | 17.67 | 2.52 | 2.07 |
| | 9 | 15.5 | 35.90 | 11.07 | 14.52 | 3.24 | 2.47 |
| | 10 | 15.0 | 35.51 | 8.25 | 11.86 | 4.31 | 2.99 |
| | 11 | 14.5 | 35.28 | 5.96 | 9.62 | 5.92 | 3.67 |
| | 12 | 14.3 | 35.21 | 4.99 | 8.64 | 7.05 | 4.07 |
| | 13 | 14.0 | 35.15 | 4.14 | 7.75 | 8.49 | 4.54 |
| | 14 | 13.8 | 35.11 | 3.39 | 6.93 | 10.35 | 5.07 |
| h-weighted | 1 | 19.3 | 56.47 | 55.87 | 55.97 | 1.01 | 1.01 |
| | 2 | 18.6 | 46.13 | 44.02 | 44.33 | 1.05 | 1.04 |
| | 3 | 17.9 | 38.36 | 34.21 | 34.80 | 1.12 | 1.10 |
| | 4 | 17.1 | 32.63 | 26.19 | 27.05 | 1.25 | 1.21 |
| | 5 | 16.4 | 28.49 | 19.70 | 20.80 | 1.45 | 1.37 |
| | 6 | 15.7 | 25.55 | 14.53 | 15.81 | 1.76 | 1.62 |
| | 7 | 15.0 | 23.52 | 10.48 | 11.86 | 2.24 | 1.98 |
| | 8 | 14.3 | 22.15 | 7.36 | 8.78 | 3.01 | 2.52 |
| | 9 | 13.6 | 21.26 | 5.02 | 6.39 | 4.24 | 3.33 |
| | 10 | 12.9 | 20.71 | 3.30 | 4.58 | 6.28 | 4.52 |
| | 11 | 12.1 | 20.38 | 2.07 | 3.22 | 9.84 | 6.33 |
| | 12 | 11.8 | 20.27 | 1.61 | 2.68 | 12.59 | 7.57 |
| | 13 | 11.4 | 20.19 | 1.23 | 2.21 | 16.39 | 9.12 |
| | 14 | 11.1 | 20.13 | 0.93 | 1.82 | 21.72 | 11.07 |

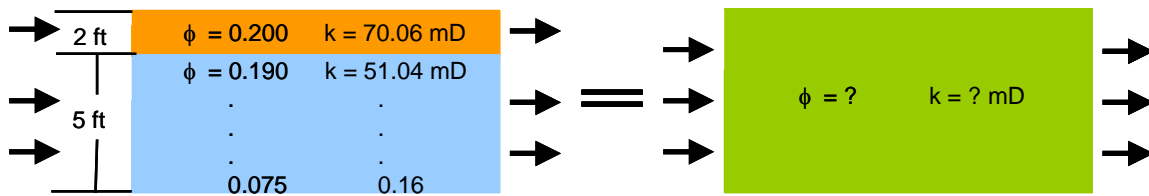


Figure A.1. Schematic diagram showing upscaling of two-layer models and associated layer properties.

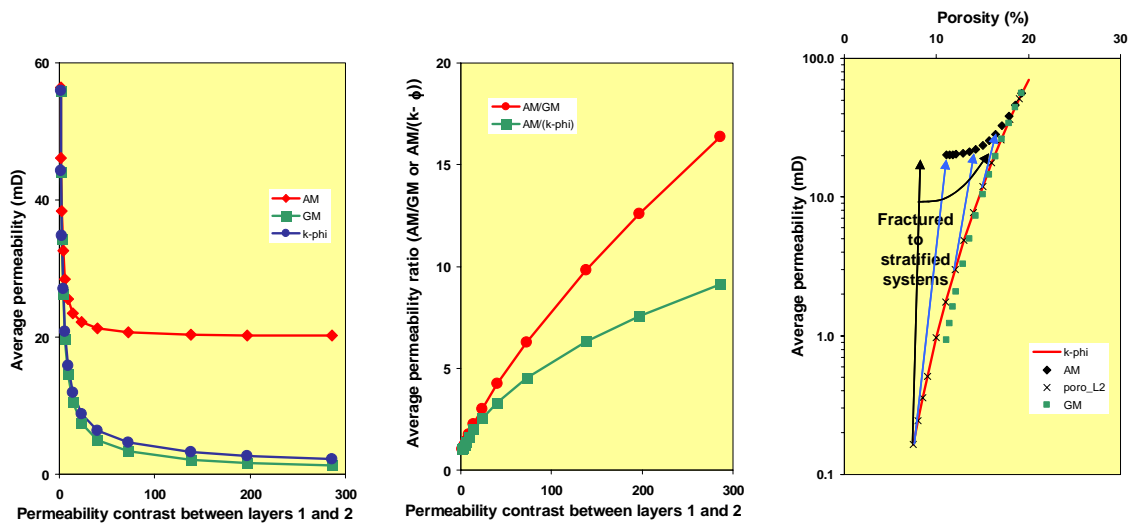


Figure A.2. Relationships among average permeability values of a two-layer system: (a) average permeabilities calculated by arithmetic mean, geometric mean and k-porosity correlation vs. permeability contrast between layer 1 and 2, (b) average permeability ratio between arithmetic and geometric means (red curve) and between arithmetic mean and permeability derived from k-porosity correlation as a function of permeability contrast between two layers, and (c) average permeability vs. average porosity.

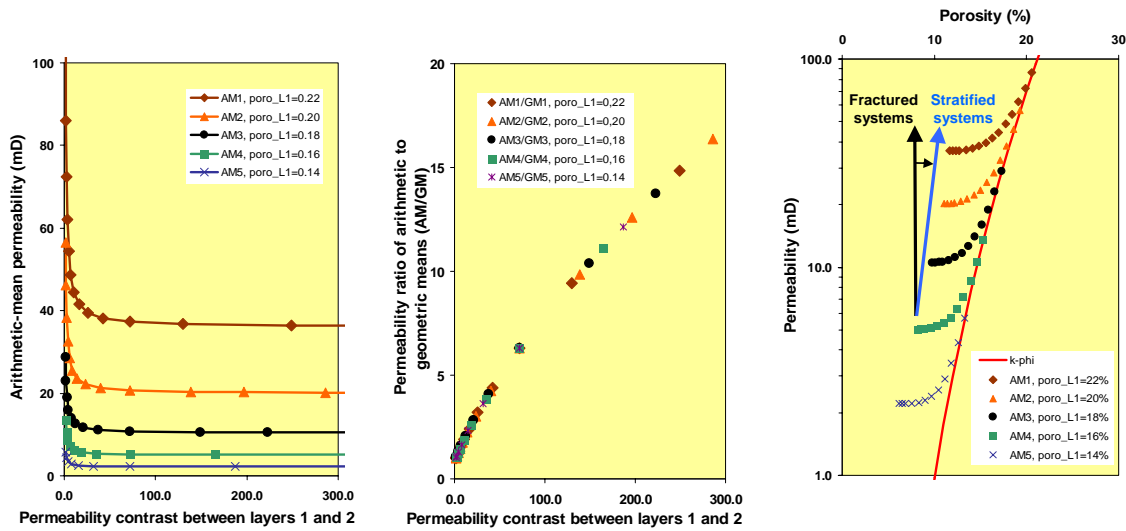


Figure A.3. Average permeabilities in two-layer systems: (a) average permeability vs. permeability contrast between layer 1 and 2, (b) average permeability ratio between arithmetic and geometric means (red curve) and between arithmetic mean and permeability derived from k-porosity correlation as a function of permeability contrast between two layers, and (c) average permeability vs. average porosity.

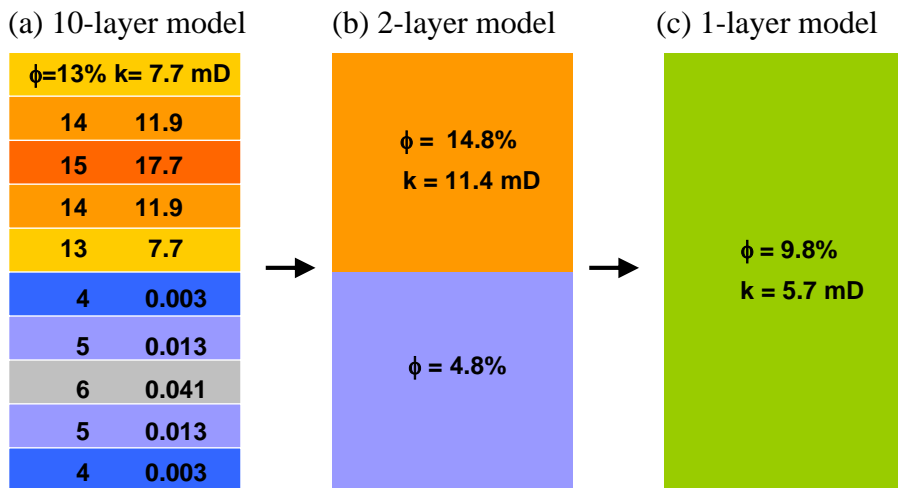


Figure A.4. Schematic diagram showing upscaling associated layer properties of ten-layer model to a two-layer flow unit model, and to a single-layer cycle model.

(a) Porosity cutoff = 5%



(b) Porosity cutoff = 10%

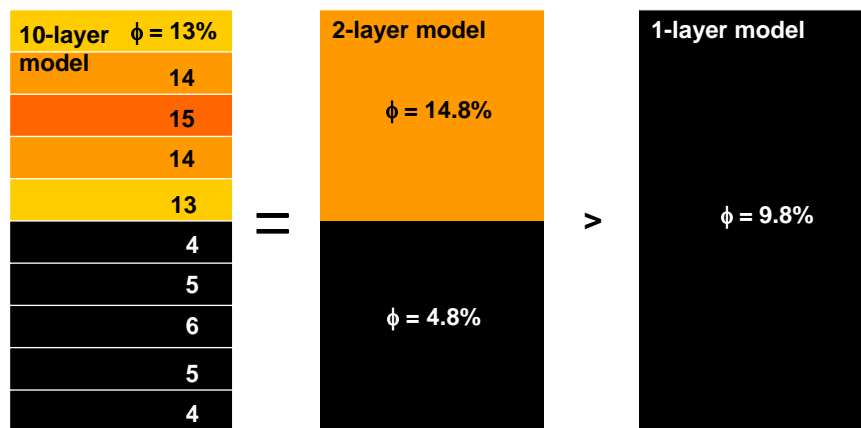


Figure A.5. Schematic diagram showing effect of porosity cutoffs of (a) 0.05 and (b) 0.10 on upscaling associated layer properties of ten-layer model to a two-layer flow unit model, and to a single-layer cycle model.

CONSTRUCTION AND ANALYSIS OF 3-D SEISMIC
POROSITY INVERSION MODELS

Hongliu Zeng

Bureau of Economic Geology
Scott W. Tinker, Director
John A. and Katherine G. Jackson School of Geosciences
The University of Texas at Austin
Austin, Texas 78713-8924

| | |
|--|-----|
| ABSTRACT..... | 309 |
| INTRODUCTION | 309 |
| METHODOLOGY | 311 |
| DATA AND TIE..... | 313 |
| IMPROVEMENT OF SEISMIC DATA INTERPRETABILITY | 314 |
| 90°-phasing | 314 |
| High-frequency Signal Enhancement | 315 |
| WELL-BASED AI MODEL..... | 316 |
| MODEL-BASED SEISMIC INVERSION..... | 317 |
| Why Model-based? | 317 |
| How Well and Seismic Data Are Integrated | 319 |
| PROGRESSIVE INVERSION..... | 320 |
| Problems in Model-based Inversion | 320 |
| Solution..... | 322 |
| Blind Test..... | 324 |
| CONCLUSIONS..... | 325 |
| REFERENCES | 326 |

Figures

| | |
|--|-----|
| 1. Location of well and seismic data in Fullerton field, Andrews County, Texas, and 3-D seismic inversion area around Phase 2 area..... | 327 |
| 2. Synthetic seismogram of lower Clear Fork and Wichita and surrounding formation in well Cal/Mon 1 across 2-D seismic line 0123 | 328 |
| 3. Linear relationship between AI and log porosity of carbonate rocks in the lower Clear Fork and Wichita, Fullerton field, Andrews County, Texas..... | 328 |
| 4. A 0°-phase seismic section (trace 2382) in the 3-D survey area showing poor tie between high-porosity/low-AI units and amplitude/polarity and difficulty in picking high-frequency sequence boundaries..... | 329 |

| | |
|---|-----|
| 5. A 90°-phase seismic section (trace 2382) in the 3-D survey area showing improved tie between high-porosity/low-AI units and amplitude/polarity | 330 |
| 6. A high-frequency-enhanced (spectral-balanced) version of Figure 5 showing improvement in seismic resolution | 331 |
| 7. Wireline log-based AI models for reservoir characterization and seismic inversion..... | 332 |
| 8. Procedure of a model-based inversion..... | 333 |
| 9. Model based inversion from background model, blocky model, smoothed log model, and log model..... | 334 |
| 10. Differences of AI inversion corresponding to different initial model inputs | 335 |
| 11. Initial models for progressive inversion | 336 |
| 12. Progressive inversion..... | 337 |
| 13. Differences of stratigraphic framework used in initial model construction | 338 |
| 14. Difference in AI estimation through progressive inversion..... | 339 |
| 15. Blind test showing value and limit of progressive inversion (example 1)..... | 340 |
| 16. Blind test showing value and limit of progressive inversion (example 2)..... | 341 |
| 17. Blind test showing value and limit of progressive inversion (example 3)..... | 342 |

Construction and Analysis of 3-D Seismic Porosity Inversion Models

Hongliu Zeng

ABSTRACT

Geology-guided reconditioning of seismic data is the key to improve extraction of relevant geologic information. At Fullerton field, the most convenient and useful tools for data reconditioning are phase shifting and high-frequency enhancement. A simple seismic phase rotation (to 90°) reconditions seismic data for impedance representation, roughly linking seismic amplitude directly to log lithology and porosity and making stratigraphic correlation more accurate. High-frequency enhancement raises the dominant frequency of 3-D seismic data from 30 to 50 Hz, significantly improving seismic resolution. More accurate and finer scale seismic mapping of reservoir parameters is achieved from model-based, progressive inversion that seamlessly integrates the geologic interpretation of well-seismic data and model-based seismic inversion for high-resolution (2 ft) impedance models.

INTRODUCTION

Post-stack seismic data contain rich information about reservoir stratigraphy, sedimentology, and physical properties. The value of seismic interpretation and well-seismic integration has long been recognized. Higher purposes of interpretation include (1) to establish a direct link between subsurface geology and seismic signal by making seismic expression resemble to geologic section (structure, stratigraphy, lithology, rock properties, etc.), and (2) to extract the highest possible resolution information from seismic processing and from integration of well data. However, our current seismic interpretation strategies fall short for these higher

purposes by emphasizing more on structural mapping and less on stratigraphic evaluation. Stratigraphic information in seismic data is far from being fully utilized because of the lack of thorough understanding of the relationship between stratigraphy and its seismic responses, regularly poorly conditioned seismic data that fail to express the stratigraphy in a way geologists can understand, and the gap in well and seismic resolution and difficulties in data integration. Better methods of stratigraphy-oriented data reconditioning and integration are the goal of this study.

In this report we describe a systematic approach to the better seismic stratigraphic interpretation. The first step in this approach is basic data reconditioning within seismic frequency range (5-70 Hz in this study) to improve seismic data interpretability. Two key techniques were applied: phase rotation and high-frequency enhancement. A simple seismic phase rotation (to 90°) reconditions seismic data for impedance representation, roughly linking seismic amplitude directly to log lithology and porosity. High-frequency enhancement raises the dominant frequency of 3-D seismic data from 30 to 50 Hz, significantly improving seismic resolution.

However, there is a limit to the improvements that can be achieved in seismic data interpretability possible from basic data reconditioning. For example, the 90°-phasing does not eliminate the wavelet effect. To remove wavelet sidelobes for truer representation of geology it is also necessary to perform a seismic inversion. Furthermore, there are limits to the resolution obtainable from the high-frequency enhancement. A high-frequency enhancement processing does not result in the resolution high enough for reservoir flow model construction. To reach the levels of high resolution needed for flow modeling, it is necessary to employ well data. Inversion without use of constraining well data will not provide reservoir details beyond seismic

resolution. To solve this problem, we developed a more advanced data reconditioning method called progressive inversion. With this approach which is described in this report, more accurate and log-resolution (2 ft) seismic mapping of reservoir parameters can be achieved.

METHODOLOGY

We emphasize on stratigraphy-oriented 3-D seismic data interpretation by addressing the use of following three techniques:

1. Seismic phase adjustment to layer-based event expression. Standard seismic processing usually produces (or at least attempts to produce) 0°-phase seismic data as the final product. Interpretive advantages of 0°-phase data include wavelet symmetry, center lobe (maximum amplitude) coincidence with reflection interface, and higher resolution (Brown, 1991). However, those advantages of 0°-phase data are realized only if the seismic reflection comes from a single reflection interface. More often we have to deal with seismically thin beds where reflection amplitudes are composite seismic responses from the top and the base. In this situation, the observed waveform is a peak-trough couplet. Because seismic events do not necessarily coincide with bed geometry, it can be difficult tying lithology/porosity logs in wells to seismic data, especially when multiple thin beds co-exist in a stratigraphic interval. Ninety-degree-phase data are more suitable for geologic interpretation of seismically thin beds (Zeng et al., 1996, 2003, 2004; Zeng, 2003). The use of a 90°-phase wavelet overcomes the shortcomings of the 0°-phase wavelet by shifting the main lobe (maximum amplitude) of the seismic response to the center of the thin bed. The seismic response is symmetrical to the thin bed, instead of to the top and base of the bed, which makes the main seismic event (a trough, in this case) coincide with the geologically defined high-frequency sequences and flow units. As a

result, seismic polarity/amplitude is uniquely tied to stratigraphy. These improvements, when applied to real data, can make seismic interpretation easier.

2. High-frequency enhancement. By relatively suppressing low-frequency components and enhancing high-frequency components in the data, seismic resolution can be further improved. However, the processing will inevitably reduce the signal-to-noise ratio of the data. As a result, there are still arguments on whether and how useful the technique is. Our experience indicates that the technique is valuable in enhancing the thin-bed imagery if without over-boosting high-frequency noise beyond effective signal bandwidth. There are several methods to achieve high-frequency signal enhancement, such as frequency filtering and deconvolution (Yilmaz, 1987), and spectral balancing (Tufekcic et al., 1981). For this study, spectral balancing was used to relatively enhance the high-frequency energy in the data without over-whitening the spectrum.
3. Combine well and seismic data for full spectrum reservoir modeling. Well data integration is necessary to build a high-resolution reservoir simulation model from seismic data. The difficulty is how to calibrate data of different scale and different resolution in both geologically and computationally reasonable and seamless way. Departing from current trend of concentrating on geophysical algorithms, we emphasize the role of geologists in interpretation-oriented processing such as seismic inversion. With a close involvement of geologists, integration (in the form of inversion) is typical not one-time process. Zeng et al. (2003) demonstrated that a progressive (or repeated) inversion can considerably improve the quality of reservoir modeling. By upgrading initial model from previous inversion and geologic knowledge for subsequent inversion,

the progressive inversion can combine and calibrate well and seismic data more efficiently and accurately.

DATA AND TIE

Data for this study come from the Fullerton Clear Fork field in Andrews County, Texas (Figure 1). The Fullerton Clear Fork reservoir comprises shallow water carbonates of Lower Permian (Leonadian) age at a depth of about 6,600 to 7,500 ft. Available data for the field study include wireline logs ($\pm 1,400$ wells), cores (approximately 15,000 ft), 3-D seismic (26 mi^2) and 2-D seismic data (30 lines). This study focused on the central part of the field and utilized approximately 5 mi^2 3-D seismic and 66 well log suites.

Well to seismic ties using synthetics is straightforward at Fullerton field. For example, in well Cal/Mon 1, a seismogram was generated with a sonic log (Figure 2). The seismogram ties very well to a 2-D seismic line across the well (line 0123). From well-log interpretation, we can easily pick Tubb and Abo reflectors from the seismic data, which form the top and base of the lower Clear Fork and Wichita reservoir section, respectively. Synthetics in other wells in the field (both in 2-D and 3-D seismic area) exhibit similar results.

Petrophysical analysis of wireline logs shows a linear relationship between acoustic impedance (AI) and calculated porosity. Although a spectrum of limestones and dolostones—from grain-dominated to mud-dominated dolostones—and anhydrate have been observed in conventional cores, the log AI steadily decreases with log porosity at fairly high correlation ($\rho=0.88$) in a depth range of 6,600 to 7,300 ft (Figure 3). This close relationship between AI and porosity implies that seismic amplitude should be a good indicator of porosity, provided that amplitude tuning effects can be reasonably estimated with well control.

However, the observed excellent well log-to-seismic tie and the simple acoustic relationship do not automatically lead to an easy interpretation of seismic data, especially in terms of stratigraphy and porosity. Figure 4 shows a standard, 0°-phase seismic section tied to well logs. Note that only major stratigraphic boundaries (Tubb, Wichita, and Abo, solid lines, Figure 4) are linked to prominent seismic events. High-frequency sequence boundaries (HFS2.1-HFS2.3, Wichita 8, Figure 4) are not resolved by seismic and cannot be correlated based on seismic phase. Low-AI or high-porosity zones in high-frequency sequences (dashed lines, Figure 4) recognized in sonic/density and porosity logs tie neither to polarity nor to amplitude. A similar situation is seen in other seismic data volumes (2-D and 3-D) in the project area. This observation suggests that the seismic data are not in the best form for stratigraphic interpretation and must be reconditioned and reprocessed before being put into use.

IMPROVEMENT OF SEISMIC DATA INTERPRETABILITY

Simple post-stack processing tools are available in various seismic interpretation packages (e.g., Poststack in Landmark). A quick improvement of data interpretability can be achieved by applying appropriate data processing techniques for better stratigraphically-oriented seismic interpretation. Our tests show that seismic phase adjustment and high-frequency enhancement are two of the most useful tools.

90°-phasing

As seen in Figure 4, standard 0°-phase seismic data is not optimal for stratigraphically oriented, thin-bed interpretation. To improve the data interpretability, the 0°-phase seismic data in Figures 4 were reprocessed by applying a 90° phase shift (Figure 5). In this reprocessed seismic section, the important stratigraphic boundaries (Tubb, Wichita, and Abo) are tied to

seismic events with a 90° phase shift (zero crossings, Figure 5). Although the high-frequency sequence boundaries still fail to correlate to specific seismic phase characters, high-porosity zones (low AI) associated with some of them (dashed lines, Figure 5) tend to tie to seismic trough events (negative amplitude). The resolution, though, is dominated by the low dominant frequency of the data (around 30 Hz), which causes some thinner porosity zones to be imaged as merged seismic events without clear separation.

Apparently, the 90° phasing of seismic data reconditions seismic traces to better resemble an impedance profile so that the interpretability of the data is improved. The procedure is simple, reliable, and not data damaging.

High-frequency Signal Enhancement

Although 90° phasing significantly improves the visual correlation between seismic events and stratigraphic units (Figure 5), the resolution of seismic data is still not satisfactory. It is still difficult to map individual thin porosity zones in high-frequency sequences because of the frequent merging of seismic events following these closely spaced units. To improve the seismic resolution, a spectrum balancing processing was applied to the data (Figure 6). After the processing, the dominant frequency of 3-D seismic data was raised from about 30 to 50 Hz. As a result, seismic events are shorter in time and are better separated on seismic sections. Eventually, seismic separation between thin porosity zones becomes more clear (compare Figure 5 and Figure 6).

Even though a high-frequency enhancement processing raises the noise level in the data to a certain degree so that the signal-to-noise ratio of the data is somewhat reduced, the new seismic data set provides better definition of major reservoir units in the field. With this increased resolution, structural mapping for major stratigraphic boundaries (Tubb, Wichita, and

Abo) and attribute extraction for thin porosity zones in high-frequency sequences can be performed in the entire study area. However, seismic resolution is still not enough for seismic correlation of high-frequency sequence boundaries and flow-unit level reservoir units because of the lack of seismic information beyond 70 Hz.

WELL-BASED AI MODEL

To further improve reservoir interpretation and modeling, well data must be integrated. Cores and wireline logs provide not only measurements of lithology, facies, and rock properties, but also high-resolution (down to 0.5 ft) correlation of geologic and flow units that is beyond seismic control. It is important to use well information to the fullest extent possible. At current stage of seismic reservoir characterization, this means to construct the best possible high-frequency sequence stratigraphic and high-resolution AI models from well data to guide data integration (inversion).

Based on construction methods and output model resolution, there are four basic model types (Figure 7),

1. Background model (Figure 7a). Only a low-frequency AI trend is calculated from well AI logs. High-frequency sequence boundaries and all details in well AI logs are omitted.
2. Blocky model (Figure 7b). AI values are averaged for each layer defined by horizons (high-frequency sequence boundaries) picked from well and seismic data. In this model, horizons are usually seen as sharp AI boundaries because of the blocky effect. Unpicked, internal geologic surfaces are omitted in AI mapping. Resolution depends on horizon density and is typically lower than seismic resolution.

3. Smoothed log model (Figure 7c). AI values between wells follow filtered well log trends within the interpreted stratigraphic framework. Resolution is variable. In this case, the model resolution is adjusted to seismic resolution (<70 Hz).
4. Log model (Figure 7d). AI values are modeled in log resolution (down to 1.25 ft). Thin beds between wells are linearly interpolated between successive pairs of horizons. As a result, modeled reservoir geometry and architecture are very sensitive to the stratigraphic framework provided.

These models (Figure 7a to 7d) utilize increasingly detailed well data information. The degree of geologist's involvement, through interpretation of stratigraphic framework and reservoir architecture used in the models, also increases. For best possible integration, it is important to construct and use well-based AI models at log-resolution level.

MODEL-BASED SEISMIC INVERSION

To achieve the integration of well and seismic data in reservoir modeling is equivalent in geophysical terms to completing three tasks: (1) remove wavelet effect, (2) restore low-frequency AI trend, and (3) combine high-frequency (high-resolution) well AI information. An appropriate seismic inversion can accomplish all three in a seamless and efficient manner.

Why Model-based?

From the geophysical literature, there are four main types of inversion:

1. Recursive inversion. Assuming a seismic trace as a reflection coefficient series, AI can be calculated by recursively solving the reflection coefficient equation. In this process, the wavelet effect is not removed and well data are not involved except to provide a low frequency trend. The results are commonly poor.

2. Sparse spike inversion. This method finds major reflection interfaces (spikes) that have a significant contribution to a seismic trace by inserting reflection interfaces at proper positions for the best fit of synthetics and real seismic traces. Minor reflection interfaces are ignored. As a result, inversion is low frequency in nature. Wavelet effect is reduced. The detailed well data, however, cannot be combined into output in this process.
3. Neural network inversion. An artificial neural network can be trained to find nonlinear correlations between seismic attributes and AI (or an appropriate rock property of interest). With this process, wavelet effect can be reduced by forced calibration of seismic traces to wireline logs. The resolution, though, is still limited to the seismic frequency range.
4. Model-based inversion. Also called Generalized Linear Inversion (GLI), this approach requires input of an initial (or guess) AI model. The initial model is typically constructed from available well and seismic data. If the initial model is built such that the full spectrum (low frequency, seismic frequency, and high frequency) of information is included, the inversion process will modify the model at the seismic frequency range by minimizing error functions between synthetics and seismic traces and let the low frequency trend and the high frequency details from well interpretation carry through to the final model. Model-based inversion is the most popular inversion package in the industry (e.g., Hampson-Russell, Jason, and CGG).

Only the model-based inversion offers us a platform to build a full-spectrum reservoir model in a single process that combines all available information. The model-based inversion method is the approach used at Fullerton field study.

How Well and Seismic Data Are Integrated

A model-based inversion (e.g., in Hampson-Russell Strata) is typically an iterative process (Figure 8):

1. Construct an initial AI model trace;
2. Create synthetics using the estimated AI trace and extracted wavelet;
3. Calculate the difference between the synthetics and real seismic trace. If the error is within the tolerance level, output the AI trace as inversion model; otherwise compute objective function and model perturbation, update the AI trace, and go back to step 1.

Because the initial model is seldom perfect, the process must commonly be repeated multiple times.

The optimization aims at fitting a model-generated synthetic seismogram to its real seismic counterpart. The process is restricted to the seismic frequency range in the real data. Any frequency components beyond seismic in the initial model (both low and high frequencies) are filtered out in the synthetics by the extracted wavelet, and cannot influence the optimization. If the restraints to output AI are set loosely enough, those model components beyond seismic frequency range tend to carry through to updated AI models and the final inversion.

As an example, Figure 9 shows four versions of inversion results from the four different initial models in Figure 7. Although the same seismic line and well data were used to build the initial models, the inversion can be quite different. A background model (Figure 7a) brings the least geologic information (low-frequency trend only) and inversion is mainly controlled by seismic frequency (Figure 9a). A blocky model (Figure 7b) introduces major geologic layering controlled by high-frequency sequence-scale horizons. The inversion (Figure 9b) emphasizes horizontal continuity at and near the sharp impedance boundaries at these geologic boundaries

and can be biased. A smoothed log model (Figure 7c) better follows AI trend defined by well logs and therefore better honors geologic knowledge (both stratigraphic framework and AI distribution). The inversion, however, still lacks details beyond seismic frequency range. Differences in inverted AI for the first three inversions are shown in Figure 10. In some intervals (e.g., intervals between HFS2.2 and HFS2.3 and between Wichita and Wichita 8) 25% variation in inverted AI is observed among the three inversions, although all the inversions fit seismic data equally well. Finally, an introduction of high-frequency log data to the initial model (Figure 7d) leads to a high-resolution inversion (Figure 9d). The similarity of the model and the inversion is a result of carry-through of high-frequency AI components from the model to the inversion. The inversion, however, still incorporates a seismic signal at the seismic frequency range, which modifies size, continuity, and AI value for many of the thin reservoir units in the initial model.

PROGRESSIVE INVERSION

Problems in Model-based Inversion

Assuming good-quality well and seismic data and a correct implementation of inversion software, many factors can still influence the quality of inversion because of the nonuniqueness of inverse problems. Geophysicists tend to concentrate more on improving optimization algorithms. Vigorous model testing indicates that when a good, geologically-constrained model is used, a regular optimization algorithm (e.g., conjugate-gradient algorithm in Hampson-Russell) should yield satisfactory results. On the other hand, model quality is equally important. A bad model will lead to a bad inversion, even if a most sophisticated optimization algorithm is applied. In this study, model quality is our major concern.

From the geologist's point of view, a high-quality initial model is created by deriving the most detailed and the most accurate stratigraphic framework possible from available well and

seismic interpretation, and then spatially populating AI within the framework in a geologically and statistically reasonable way. In this study, the accuracy of the stratigraphic framework was the key issue. Although varying approaches to interwell mapping can play an important role in model construction, a discussion of attribute mapping is beyond the scope of this study. All well data were mapped between and beyond wells following inverse square distance rule, a popular choice in the industry.

In the final analysis, the task of performing a good model-based inversion is reduced to a surface picking issue. The biggest challenge is that it is very difficult, if not impossible, to build an accurate high-resolution initial model by interpreting closely spaced stratigraphic surfaces between and beyond the wells from low-resolution seismic data (Figure 4-6). In this seismic data volume, good horizons that can be at least approximately tied to geologic surfaces are limited (e.g., Top Tubb, Tubb, and Wichita, Figure 11). However, these surfaces alone are typically not enough to accurately define the stratigraphic model. Picked geologic surfaces (e.g., Wichita, Figure 6) may offset seismic events (in this case, a peak-to-trough zero crossing) because of seismic interferences or misperception in interpretation. High-frequency and cycle boundaries commonly are not resolved and cannot be picked directly from low frequency seismic section (e.g., HFS2.1, 2.2, and 2.3, and Wichita 8, Figure 6). Without sufficient good-quality surfaces mapped, the initial model is almost always oversmoothed and poor in quality. To make things worse, most people use this poor initial model once and only once in the inversion process and never revisit. As a result, significant error/uncertainty in model building tends to carry through to the final inversion product.

Solution

Progressive inversion improves model-based inversion by progressively building multiple initial models and performing multiple inversions (Figure 8). The first initial model should be a low-resolution model based on a small number of prominent and reliable geologic boundaries and seismic horizons. The first inversion is performed on the basis of this initial model, which reduces wavelet effect and usually reveals more geologic detail than the original seismic data. Horizons are then reinterpreted by comparing seismic data and the first inversion. Additional horizons are then added from interpretation of the seismic data and the first inversion to create a new and more accurate initial model that fits geologic expectations. A new inversion based on this improved initial model will provide yet more accurate geologic details. This process may be repeated until inversion is satisfactory for reservoir model building applications.

For this study, a progressive inversion was performed with Hampson-Russell inversion software (Figures 11-13). The first inversion was done using an initial impedance model (Figure 11a) made from a single seismic horizon, Top Tubb, one of the most prominent geologic boundaries in the wells that show the best tie to the seismic data (Figure 6). By using only one horizon, we assume a sheet-like formation without lateral thickness variation. The result (Figure 12a), as expected, is less than desired because of the poor geologic control on the initial model. However, compared to seismic data (Figure 6) the inversion does a better job of resolving other geologic boundaries. A second horizon, Wichita, was added to build a new initial model (Figure 11b). Improving stratigraphic control, this two-horizon-based model was used to perform a second-round inversion (Figure 12b). Following the same procedure, another two rounds of inversion were completed. The fourth-round inversion (Figure 12c) was performed by using a seven-horizon-based initial model (Figure 11c), which utilized all high-frequency sequence

boundaries recognizable from interpretation of well data, seismic amplitude data, and intermediate inversion results as far.

A key improvement achieved from progressive inversion is the introduction of increasingly more accurate stratigraphic framework by using more and more horizons. As shown in Figure 13, the seven horizons used in the final-round inversion provide the most detailed stratigraphic correlation based on wireline log, core, and seismic analysis. As a result, thickness variations in each of the high-frequency sequences are easily modeled, which potentially has significant influence on definition of reservoir architecture and flow units in the model. In this study, the use of fewer control horizons in the first- and second-round inversions (Figure 13 a, b) introduced a correlation error ranged at 0-50 ft that is more than enough to produce the mis-correlation of flow units between wells. Some of the mis-correlation can be identified by comparing the early-generation model to a later-generation model (Figure 11, AA', BB', CC' and DD'). These mis-correlations, unfortunately, carried through to inversions (Figure 12, AA', BB', CC' and DD'). The mis-correlation can also be illustrated by the AI differences in successive rounds of inversion (Figure 14). At or near the wells, the models generated similar results (white, vertical strips in Figure 14a, b). Away from the wells, however, improvements in thin-bed definition from fine-tuning geologic surface picking and adding more geologic surfaces lead to significant changes of AI distribution (high-frequency bands in Figure 14a, b), although all three inversions fit seismic data equally well. The final (fourth round) inversion provides the best fit between geologic interpretation and seismic signal.

Progressive inversion is a seamless way to integrate geologic knowledge and seismic processing for reservoir characterization purpose. It requires an intimate involvement of geologists in seismic inversion. A sequence stratigraphic model provides guidance on how

seismic correlations should be carried out between and beyond wells for initial guess model construction using well impedance logs. In the study area, the geologic model indicates that all HFS-level seismic picks in the lower Clear Fork and Wichita should be relatively flat because the succession was deposited on a flat shallow-water platform (Ruppel, 2003). A comprehensive study of core, logs, and seismic data further established a high-frequency sequence stratigraphic framework at all well locations (Ruppel and Jones, this report). Initial and intermediate inversion results allow correlation of high-frequency sequence boundaries between and beyond well locations that honor both well picks and seismic trends. Multiple seismic/geologic picks in a short time window (in this case seven horizons in 100 ms) transfer detailed *a priori* stratigraphic information to seismic inversion, achieving impedance models that exceed expectations if using well or seismic data alone.

Blind Test

To demonstrate the value and limit of seismic signal and progressive inversion, nine wells were withheld from the 66-well data base to recreate the seven-horizon initial AI model. A new inversion was then done following the same procedure and parameter setup. Results of these tests are displayed in Figures 16-18. In each case, the original inversion is compared with inversions made after wells have been removed. There are two major observations,

1. Seismic can supply important missing geologic information between and beyond well control. Figure 15a and 15b show the effect of removing a well from model. Note that a high-porosity zone (A) and a low porosity zone (B) (Figure 15a) are not imaged by the model when the well is removed (Figure 15b). By contrast, the inversion does an excellent job of imaging the high-porosity zone (A) and the low porosity zone (B) despite the missing well. Figure 15d (the inversion with a missing well) compares quite well with

both the original log model (Figure 15a) and the inversion based on the original log model (Figure 15c). In other words, the inversion can provide a good image of reservoir character where well control is missing. Figures 16 and 17 show two more examples of the ability of inversion to define porosity in areas of less well control.

2. High-resolution details in the inversion are imperfect. Seismic signal is low frequency in nature, with a resolution no better than a quarter wavelength (approximately 20 m in this case). The high-resolution layering (1 ft in the initial model and 2 ft in the inversion) is defined by well AI logs within stratigraphic framework between and beyond wells. Seismic inversion adjusts AI distribution without changing the thickness architecture. Unfortunately, in this study, only the simplest attribute mapping was conducted between and beyond wells: thin-bed thickness is proportional to interval thickness between horizons; AI distribution in each bed is predicted by inverse square distance rule. As the result, the error in thin-bed thickness and AI mapping is not trivial, leading to an imperfect AI estimation. As a result, inversions with or without missing wells show somewhat different details near the well location (Figures 15-17). Some isolated thin beds are totally unrepresented without using of the missing wells. To further improve the inversion, an effort has to be made to develop more advanced mapping algorithms beyond the proportional layering and inverse square distance rule.

CONCLUSIONS

1. Post-stack seismic data are commonly not in optimal form and require reconditioning before they can be used for stratigraphic analysis and reservoir characterization.
2. Basic data conditioning applies do-it-yourself poststack processing tools to improve data interpretability and resolution. A 90°-phasing adjusts seismic traces to resemble

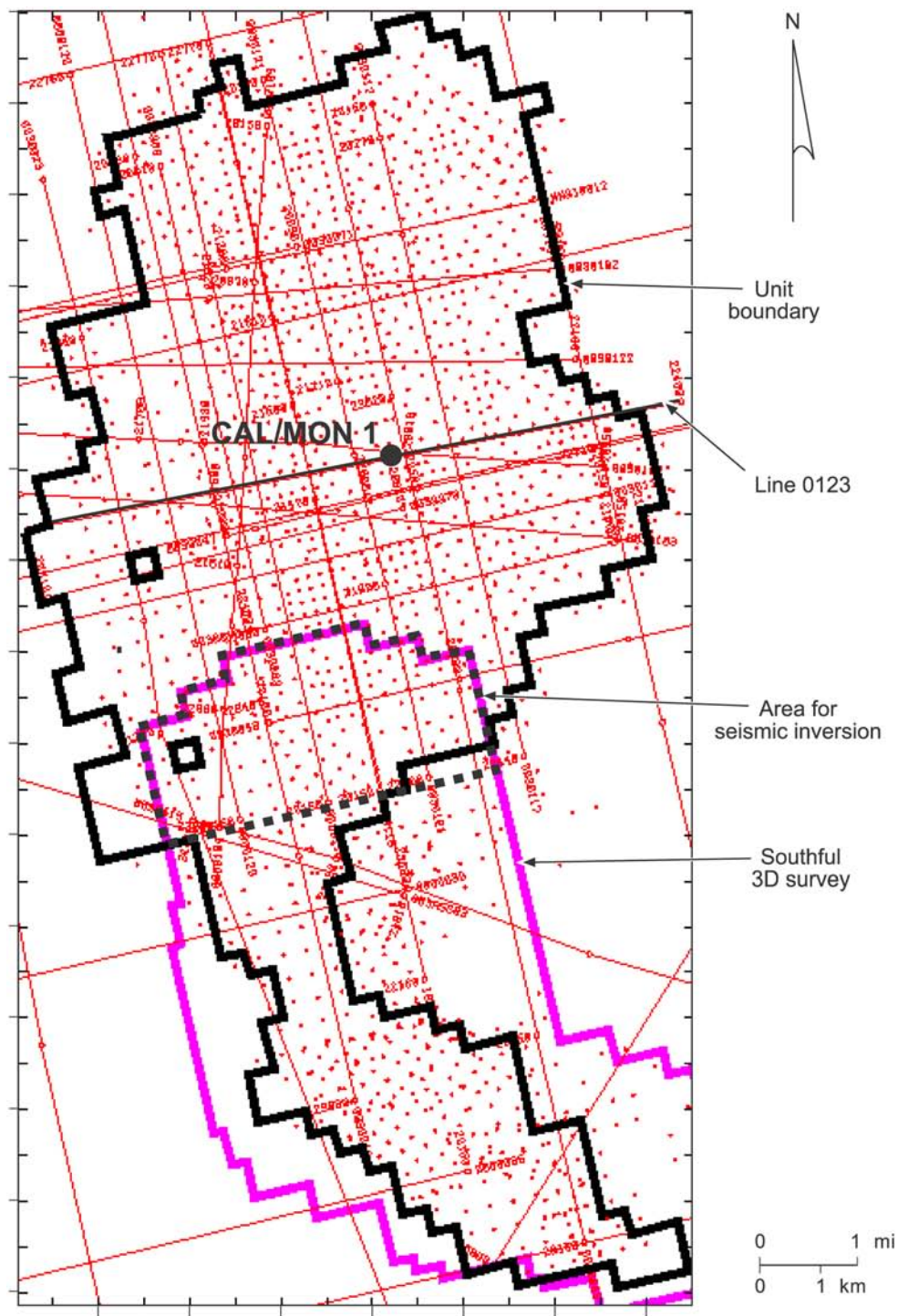
impedance logs; a high-frequency enhancement enables interpreters to identify more and thinner geologic units (at 100-ft resolution level).

3. Progressive seismic inversion can provide a good representation of reservoir porosity in areas of missing or poor quality log data.
4. Progressive seismic inversion requires involvement of geologists by providing a geologic model and quality-checking seismic picking of high-resolution geologic boundaries.

Progressive inversion promises to seamlessly integrate geologic knowledge and seismic data for detailed impedance modeling down to wireline log resolution.

REFERENCES

- Brown, A. R., 1991, Interpretation of three-dimensional seismic data: Tulsa, Oklahoma, AAPG Memoir 42, 3rd edition.
- Ruppel, S. C., 2003, Lower Leonardian (Clear Fork – Abo) Reservoir Architecture: Insights From Outcrops And Fullerton Clear Fork Field, West Texas: WTGS Fall Symposium, Back to Basics: : West Texas Geological Society Fall Symposium: West Texas Geological Society Publication #03-112, p.45-46.
- Tufekcic, D., J. F. Claerbout, and Z. Rasperic, 1981, Spectral balancing in the time domain: Geophysics, v. 46, no. 8, p. 1182–1188.
- Yilmaz, O., 1987, Seismic data processing: Society of Exploration Geophysicists. 526 p.
- Zeng, Hongliu, 2003, Significance of seismic phase in interpretation of stratigraphy and sedimentology (abs.), *in* Partners in a new environment: CSPG/CSEG Convention, June 2–6, Calgary, Alberta, Canada, unpaginated, CD-ROM.
- Zeng, Hongliu, Backus, M. M., Barrow, K. T., and Tyler, N., 1996, Facies mapping from three-dimensional seismic data: potential and guidelines from a Tertiary sandstone-shale sequence model, Powderhorn field, Calhoun County, Texas: AAPG Bulletin, 80, no.1, 16-46.
- Zeng, Hongliu and Hentz, T. F., 2004, High-frequency sequence stratigraphy from seismic sedimentology: applied to Miocene, Vermilion Block 50-Tiger Shoal Area, offshore Louisiana: AAPG Bulletin, 88, no. 2, 153-174.
- Zeng, Hongliu, Ruppel, S. C., and Jones, R., 2003, Reconditioning seismic data for improved reservoir characterization, lower Clear Fork and Wichita, Fullerton field, West Texas, *in* T. J. Hunt and P. H. Lufholm, eds., The Permian Basin: back to basics: West Texas Geological Society Fall Symposium: West Texas Geological Society Publication #03-112, 67-78.



QAd4045x

Figure 1. Location of well and seismic data in Fullerton field, Andrews County, Texas, and 3-D seismic inversion area around Phase 2 area.

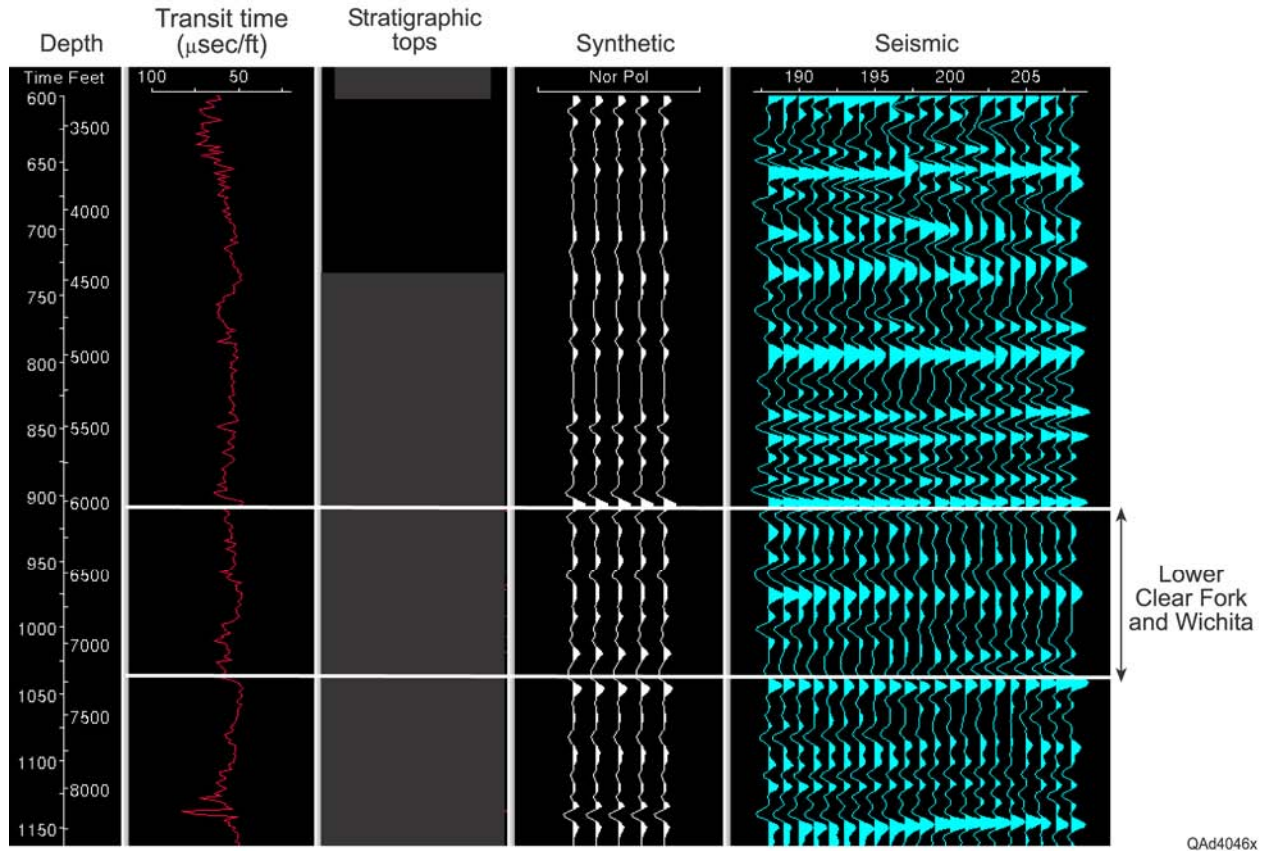


Figure 2. Synthetic seismogram of lower Clear Fork and Wichita and surrounding formation in well Cal/Mon 1 across 2-D seismic line 0123.

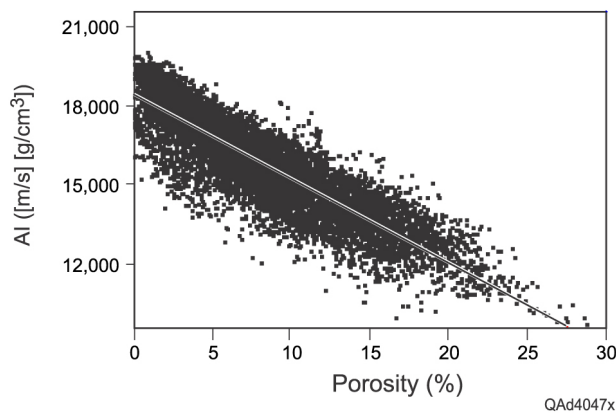


Figure 3. Linear relationship between AI and log porosity of carbonate rocks in the lower Clear Fork and Wichita, Fullerton field, Andrews County, Texas. AI was computed from transit time and bulk density logs in eight wells, whereas porosity was calculated by neutron-density cross-plotting, with a sample rate of 0.5 ft. Correlation coefficient between AI and porosity=0.88.

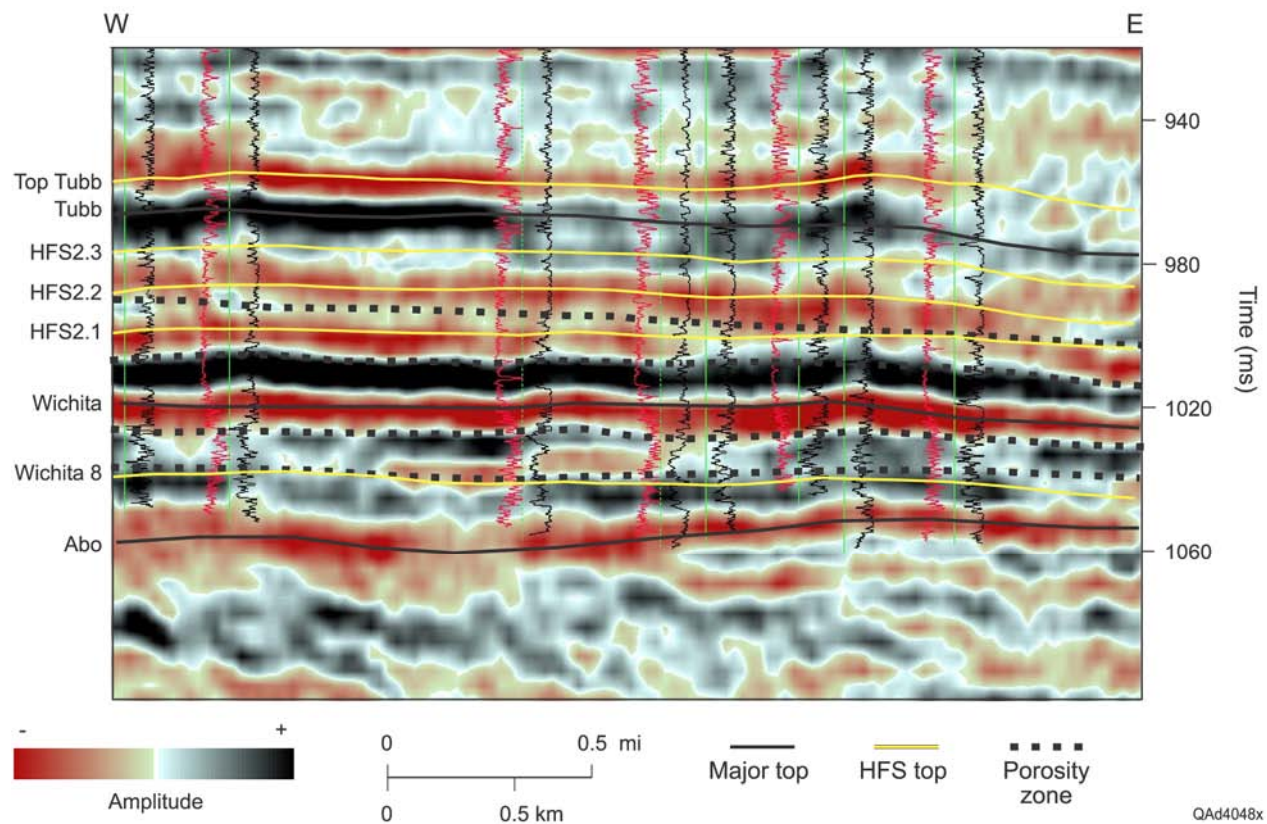


Figure 4. A 0° -phase seismic section (trace 2382) in the 3-D survey area showing poor tie between high-porosity/low-AI units and amplitude/polarity and difficulty in picking high-frequency sequence boundaries. Dashed lines highlight porosity zones in high-frequency sequences and flow units.

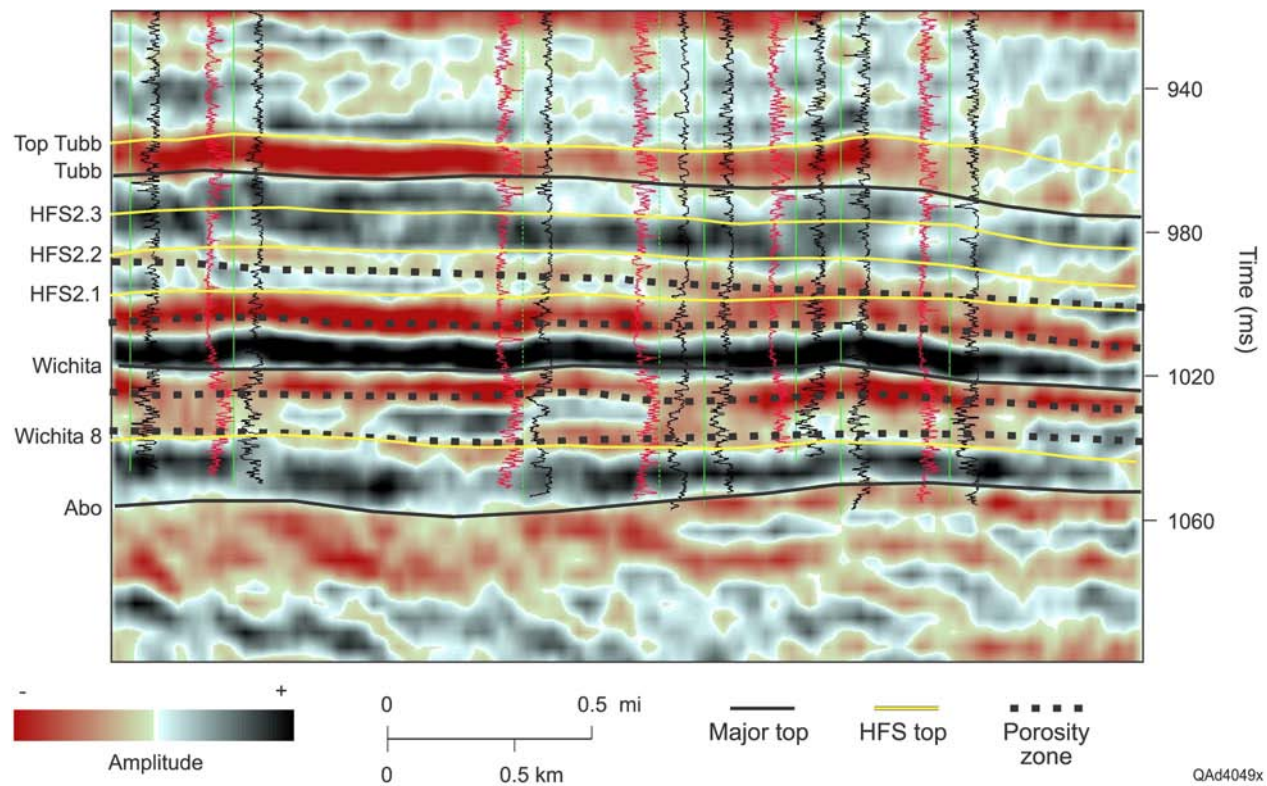


Figure 5. A 90°-phase seismic section (trace 2382) in the 3-D survey area showing improved tie between high-porosity/low-AI units and amplitude/polarity. The picking of high-frequency sequence boundaries, however, is still difficult.

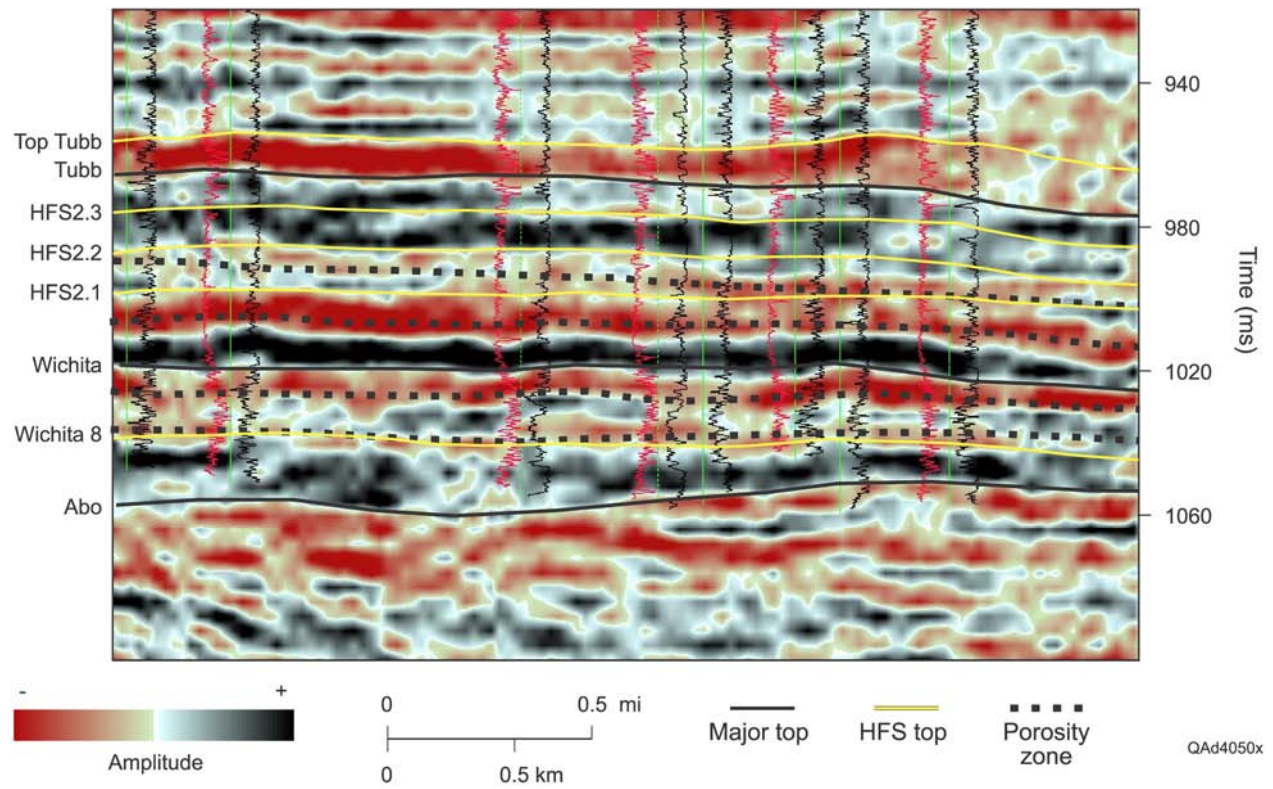


Figure 6. A high-frequency-enhanced (spectral-balanced) version of Figure 5 showing improvement in seismic resolution. Though not accurate, the high-frequency sequence boundaries can be partially interpreted by following top and bottom of the porosity zones.

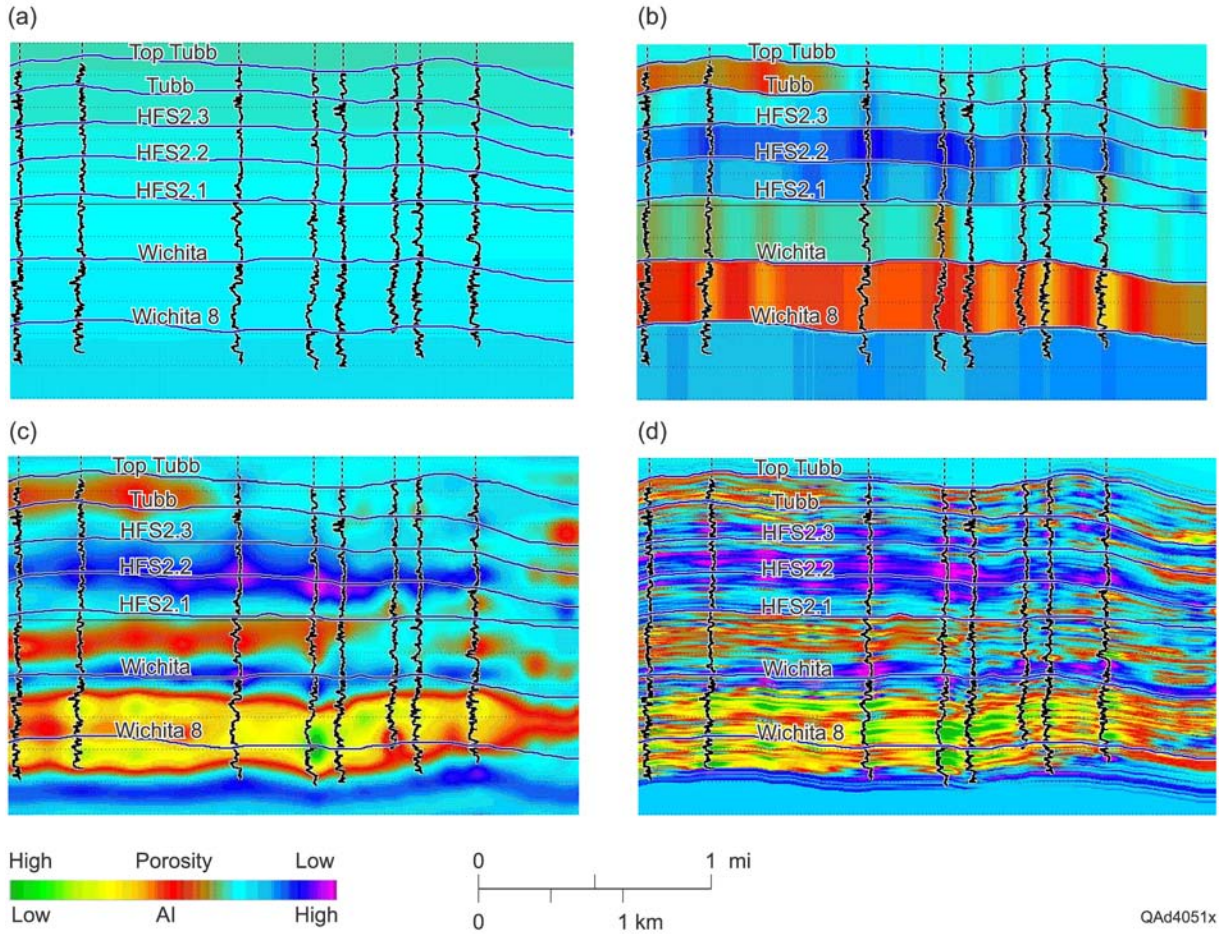


Figure 7. Wireline log-based AI models for reservoir characterization and seismic inversion. A total of seven high-frequency sequence boundaries were used for stratigraphic control of the modeling. (a) Background model. (b) Blocky model. (c) Smoothed log model up to seismic frequency (0-70 Hz). (d) Log model sampled to 0.125 ms (1-1.2 m). Logs are pseudo-AI calculated from porosity. From (a) to (d) the use of geologic information is increased.

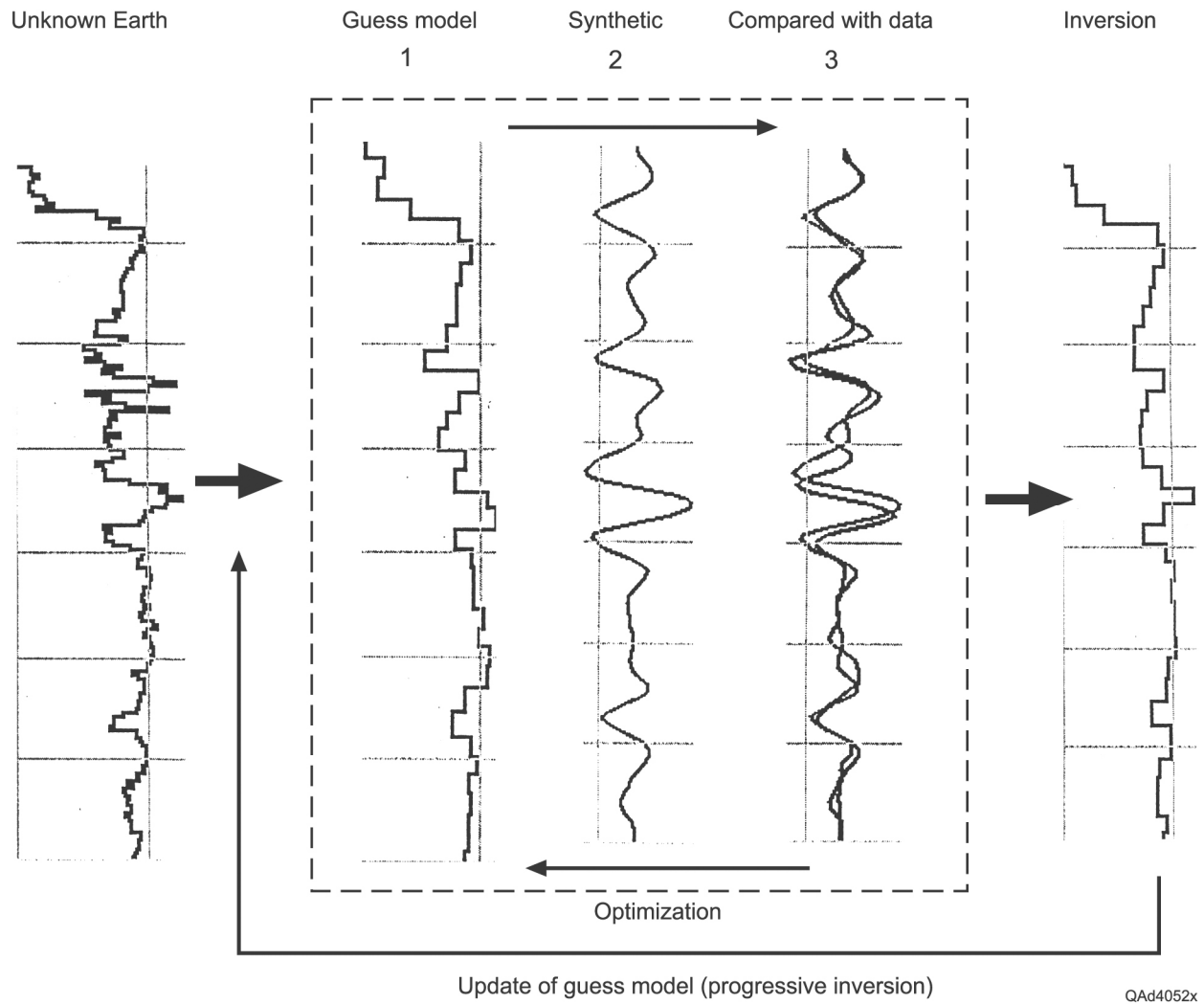


Figure 8. Procedure of a model-based inversion.

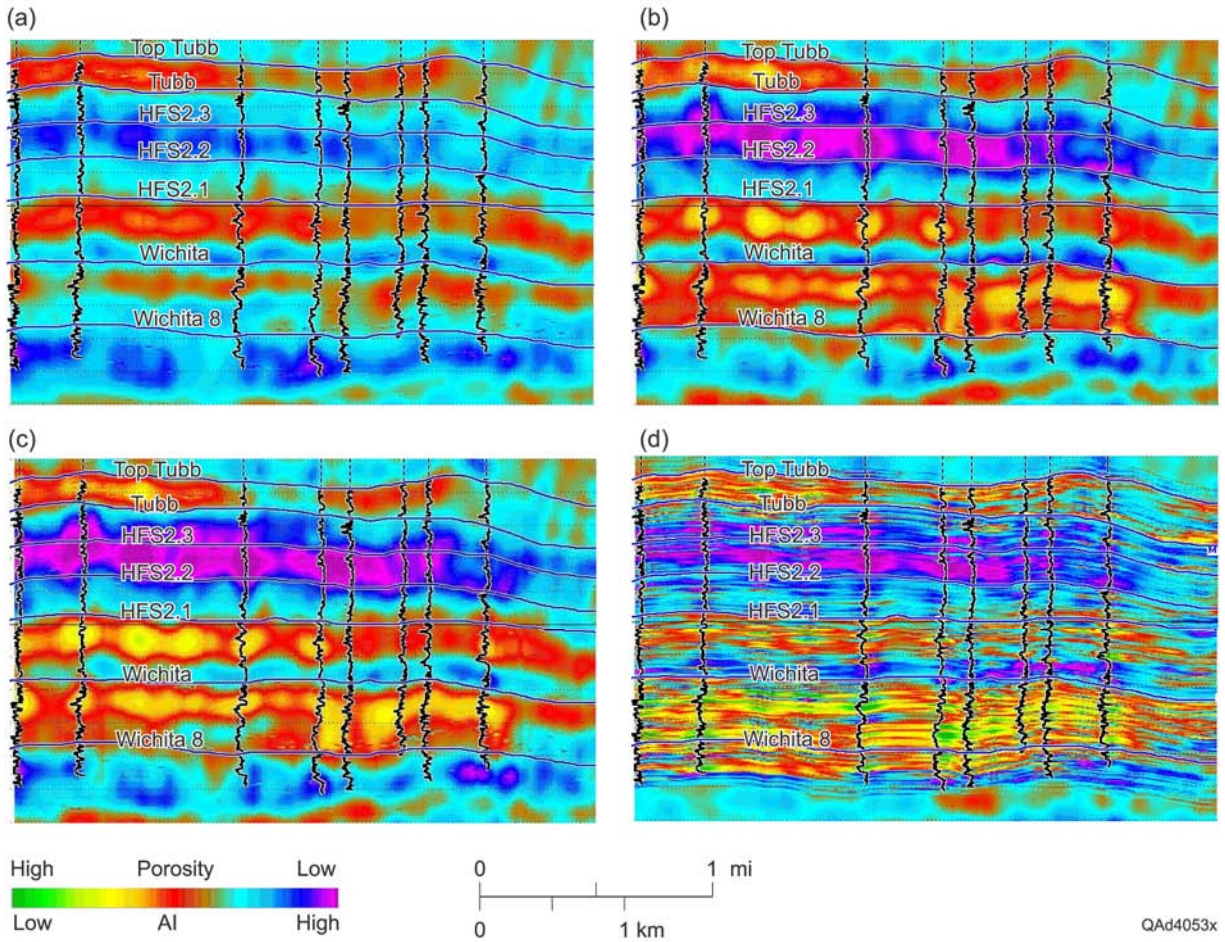


Figure 9. Model based inversion from (a) Background model, (b) Blocky model, (c) Smoothed log model, and (d) Log model in Figure 7. Section follows same seismic line (trace 2382).

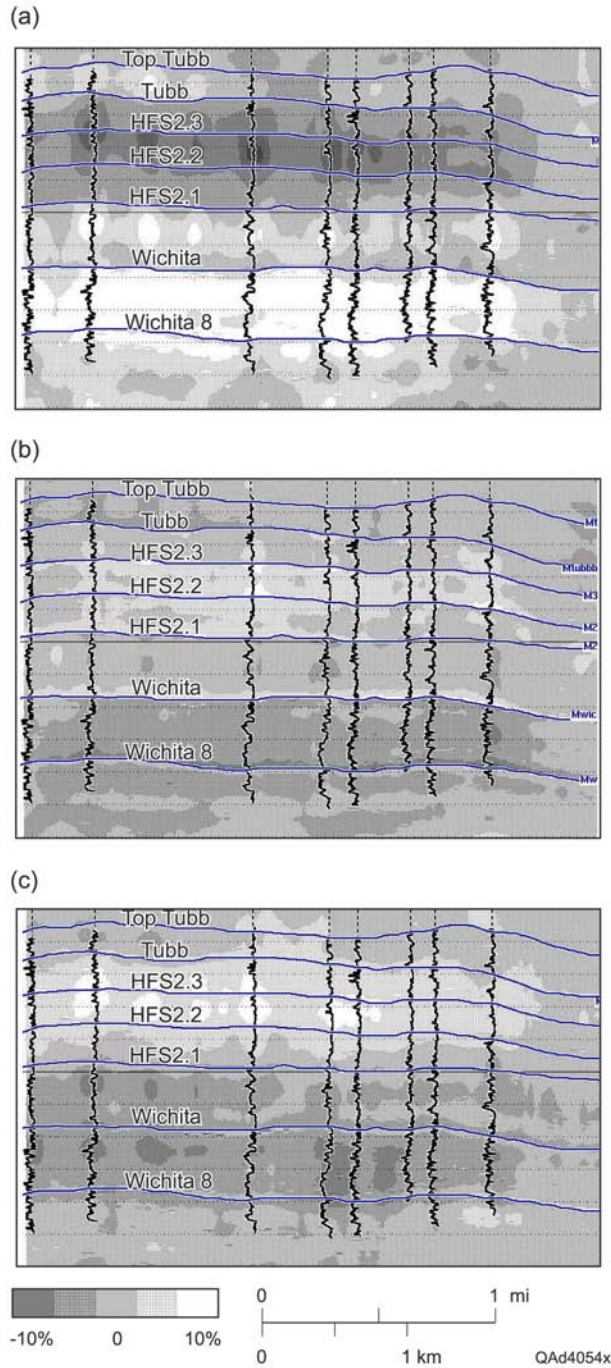


Figure 10. Differences of AI inversion corresponding to different initial model inputs. (a) Difference between the background model inversion (Figure 9a) and the average value of models a, b, and c in Figure 9. (b) Difference between the blocky model inversion (Figure 9b) and the average value of models a, b, and c in Figure 9. (c) Difference between the smoothed model inversion (Figure 9c) and the average value of models a, b, and c in Figure 9.

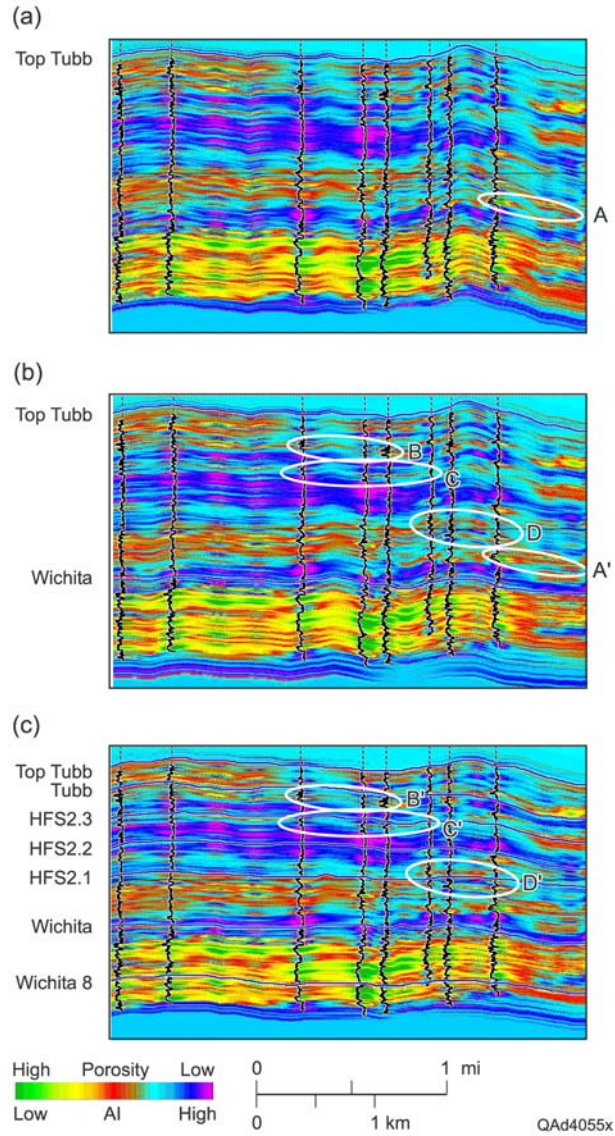


Figure 11. Initial models for progressive inversion. (a) Model based on one horizon. (b) Model from two horizons. (c) Model based on seven horizons. Logs are pseudo-AI calculated from porosity.

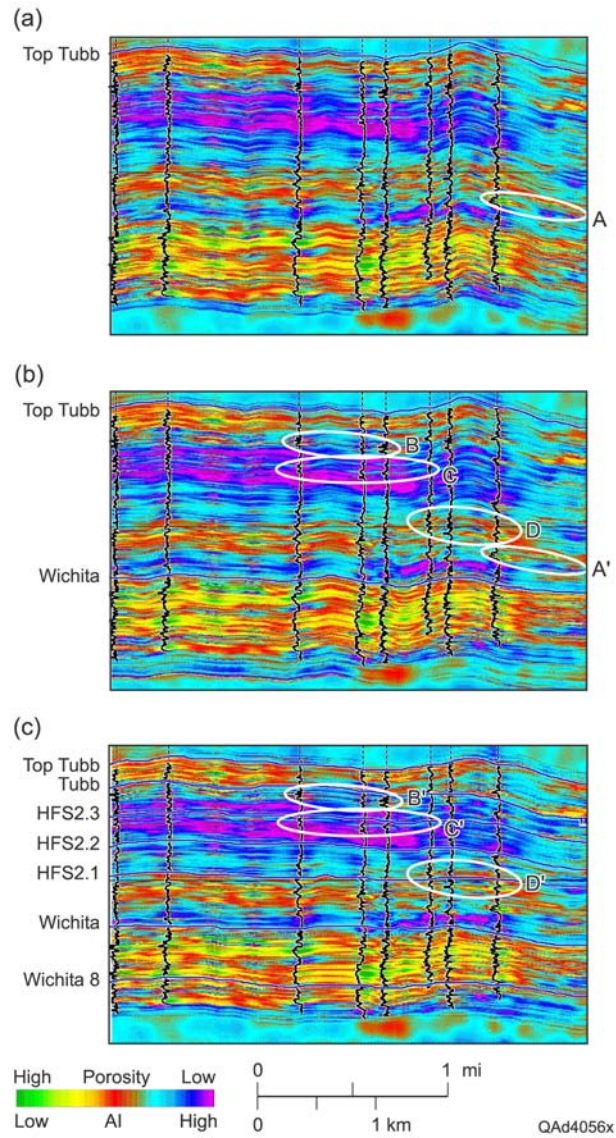


Figure 12. Progressive inversion. (a) Inverted AI based on one-horizon model (Figure 11a). (b) Inverted AI based on two-horizon model (Figure 11b). (c) Inverted AI based on seven-horizon model (Figure 11c).

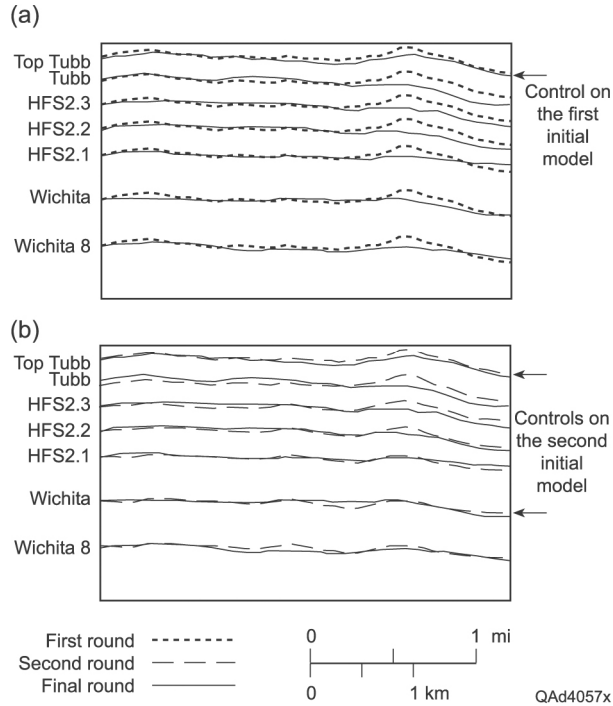


Figure 13. Differences of stratigraphic framework used in initial model construction. (a) One-horizon model (the first round) versus seven-horizon model (the final round). In the one-horizon model, high-frequency sequence boundaries were extrapolated parallel from the single control surface (top Tubb). (b) Two-horizon model (the second round) versus seven-horizon model (the final round). In the two-horizon model, high-frequency sequence boundaries Tubb and HFS2.1-2.3 were linearly interpolated between control surface top Tubb and Wichita. High-frequency sequence boundary Wichita 8 was extrapolated parallel from control surface Wichita.

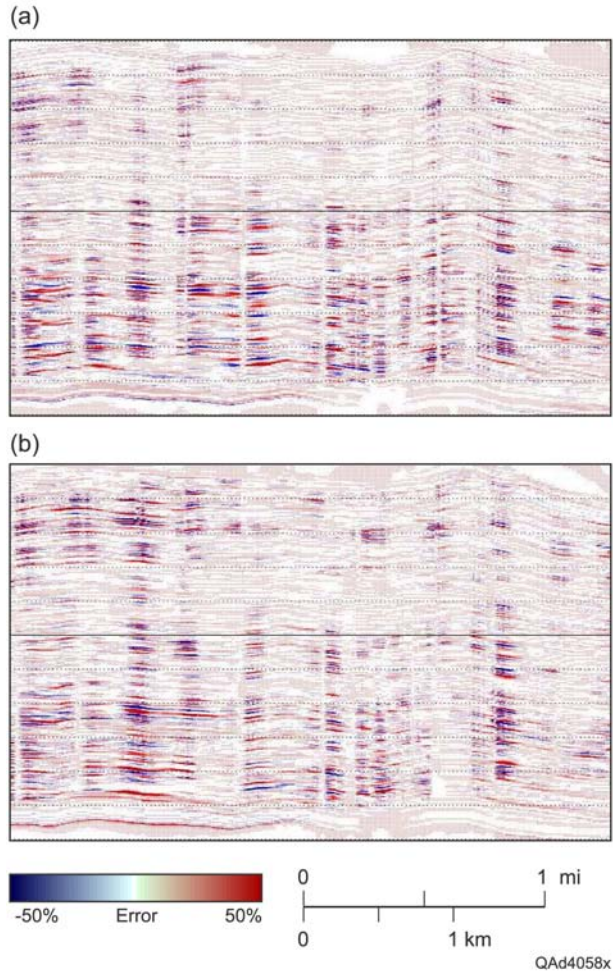


Figure 14. Difference in AI estimation through progressive inversion. (a) Difference between the second-round inversion (Figure 12b) and the first-round inversion (Figure 12a). (b) Difference between the final-round inversion (Figure 12c) and the second-round inversion (Figure 12b).

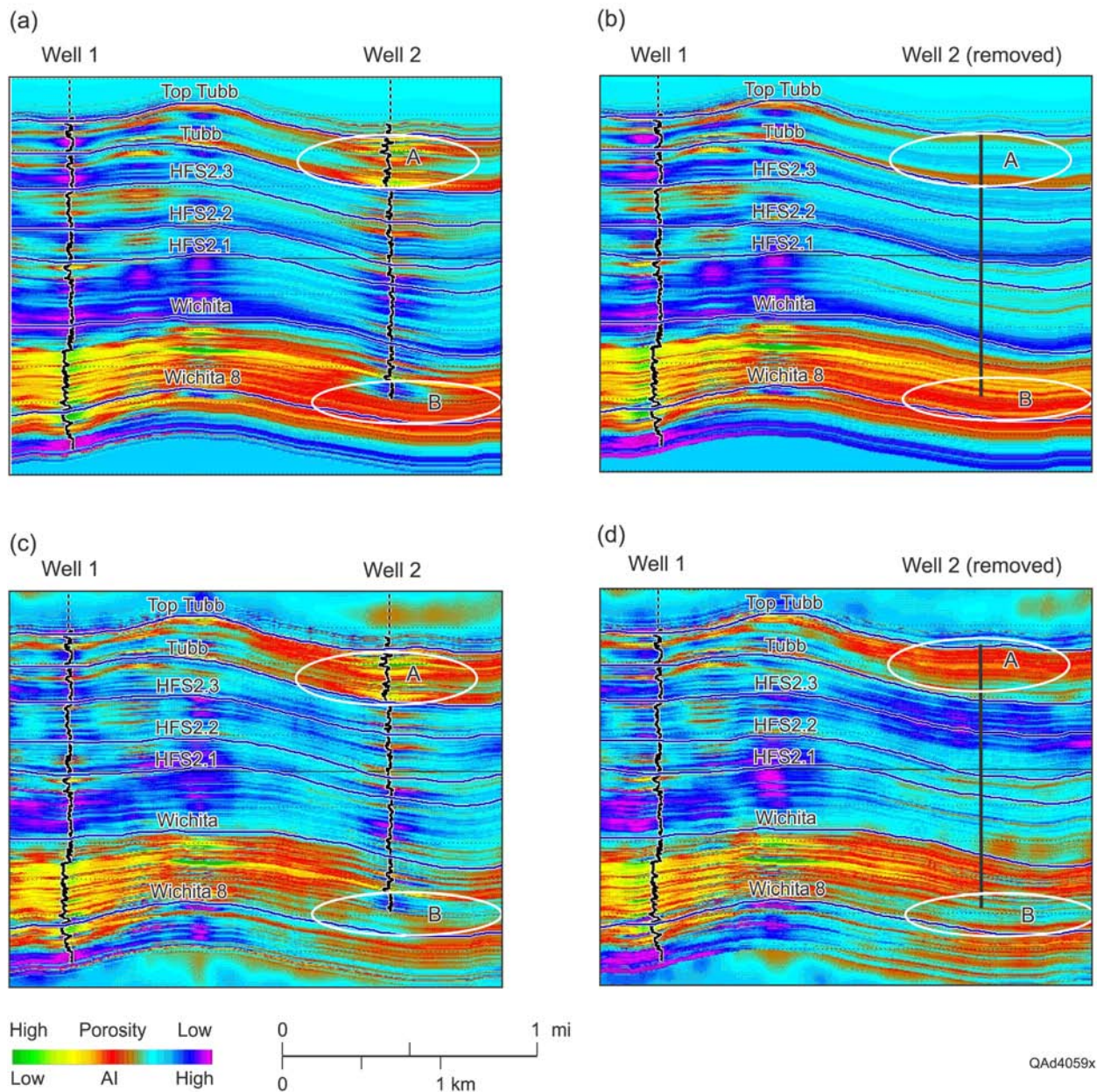


Figure 15. Blind test showing value and limit of progressive inversion (example 1). (a) Initial model. (b) Initial model made after removing a well. A high-porosity zone (A) and a low-porosity zone (B) in the model are misrepresented as a low-porosity zone (A) and a high-porosity zone (B). (c) Inversion from model (a) revealing recovered zone A and zone B. (d) Inversion from model (b) managed to recover zone A and zone B with subtly different details compared to (c).

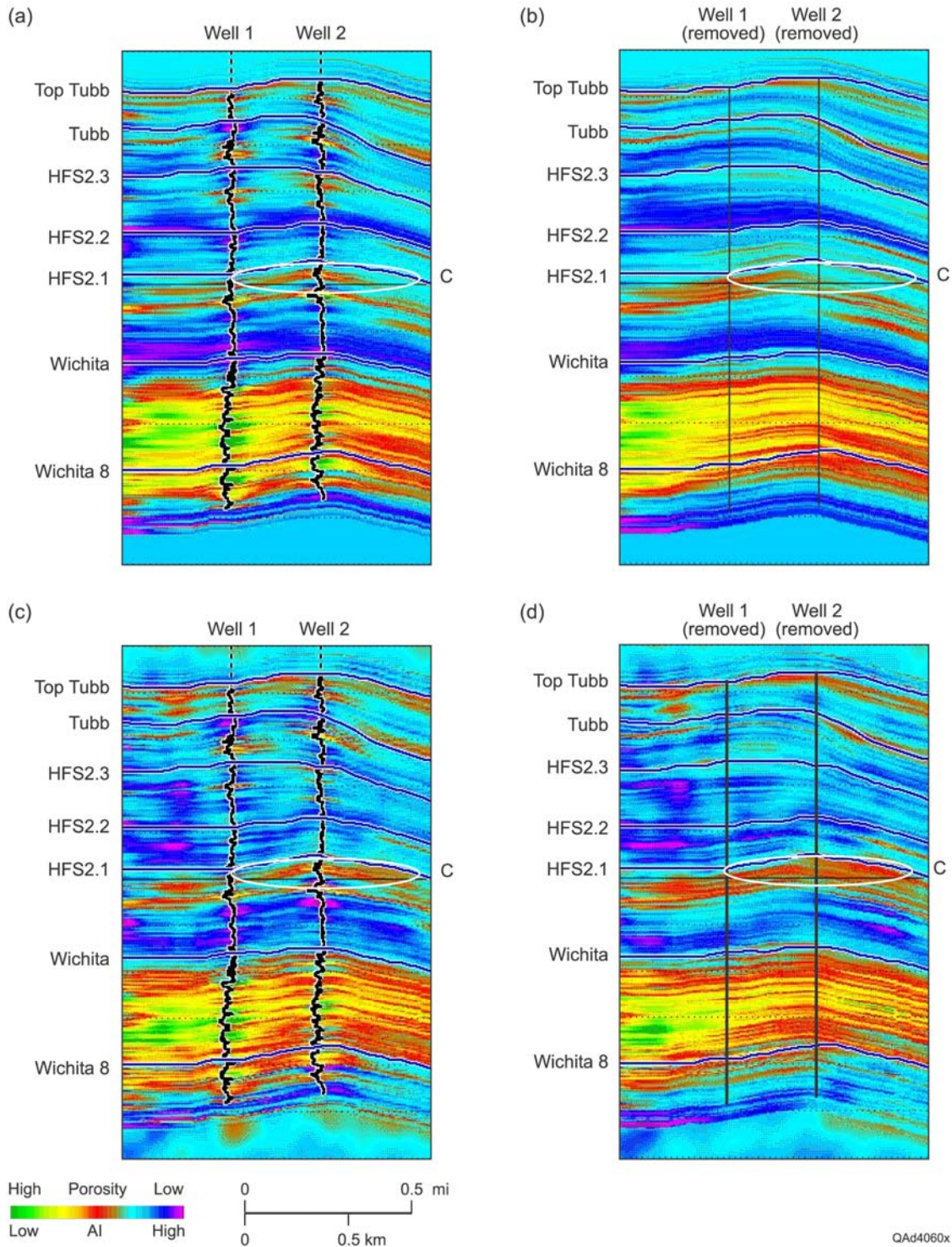


Figure 16. Blind test showing value and limit of progressive inversion (example 2). (a) Initial model. (b) Initial model made after removing two wells. A high-porosity zone C is misrepresented. (c) Inversion from model (a) revealing recovered zone C. (d) Inversion from model (b) attempted to recover zone C with subtly different details compared to (c).

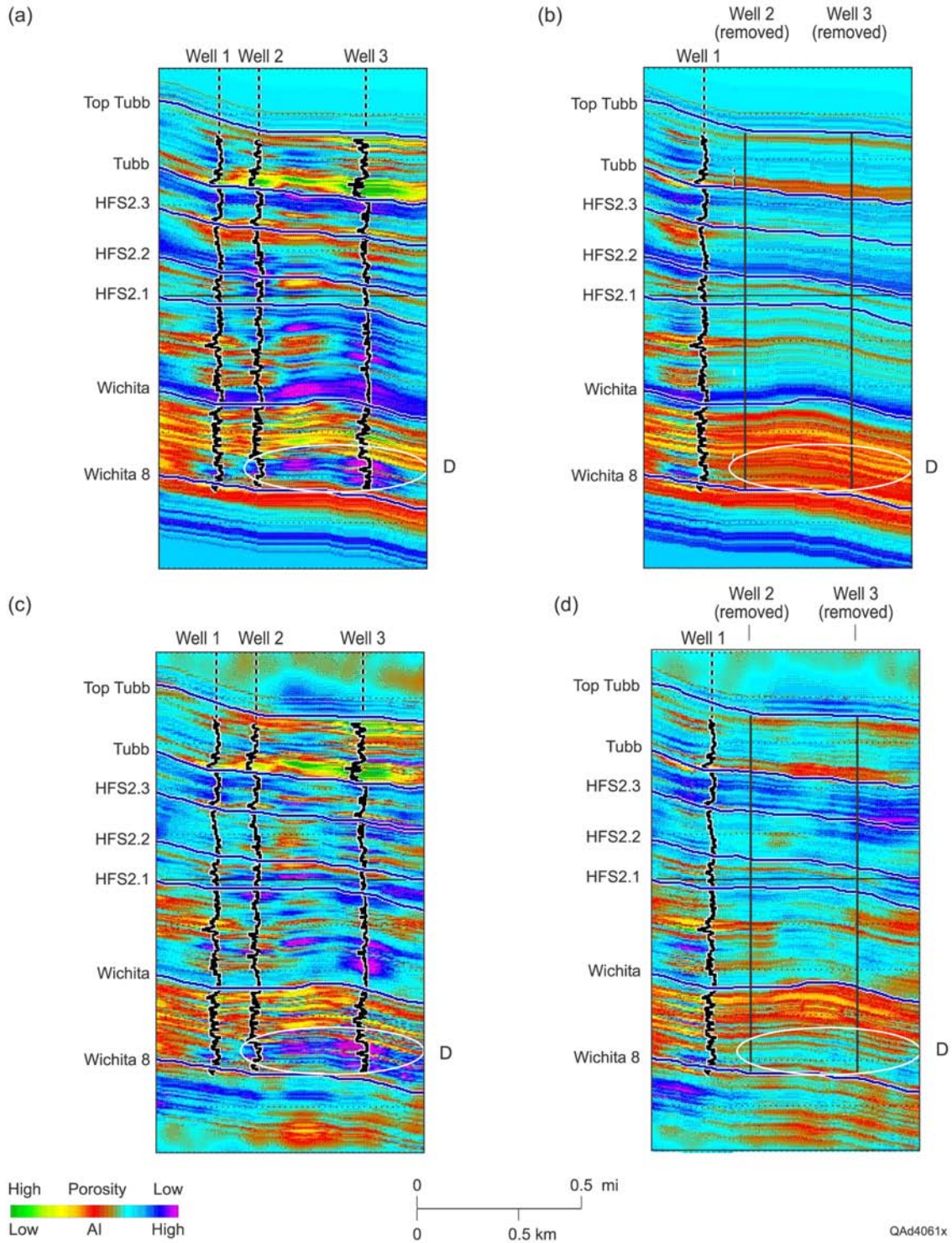


Figure 17. Blind test showing value and limit of progressive inversion (example 3). (a) Initial model. (b) Initial model made after removing two wells. A low porosity zone D is misrepresented. (c) Inversion from model (a) revealing recovered zone D. (d) Inversion from model (b) that recovers zone D with subtly different details compared to (c).